OPTIMIZATION OF DEEP BOREHOLES
FOR DISPOSAL OF HIGH-LEVEL NUCLEAR WASTE

By

Ethan Allen Bates

B.S., Nuclear Science and Engineering, Massachusetts Institute of Technology (2011)
S.M., Nuclear Science and Engineering, Massachusetts Institute of Technology (2011)

SUBMITTED TO THE DEPARTMENT OF NUCLEAR SCIENCE AND ENGINEERING IN
PARTIAL FULFILLMENT OF THE REQUIREMENTS FOR THE DEGREE OF

DOCTOR OF PHILOSOPHY IN NUCLEAR SCIENCE AND ENGINEERING
at the
MASSACHUSETTS INSTITUTE OF TECHNOLOGY

FEBRUARY 2015

Signature of Author: **Signature redacted**

Department of Nuclear Science and Engineering
December 1, 2014

Certified by: **Signature redacted**

Michael J. Driscoll – Thesis Supervisor
Professor Emeritus of Nuclear Science and Engineering

Certified by: **Signature redacted**

Emilio Baglietto – Thesis Supervisor
Assistant Professor of Nuclear Science and Engineering

Certified by: **Signature redacted**

Jacopo Buongiorno – Thesis Reader
Associate Professor of Nuclear Science and Engineering

Accepted by: **Signature redacted**

Mujid S. Kazimi
TEPCO Professor of Nuclear Engineering
Chairman, Department Committee on Graduate Students

OPTIMIZATION OF DEEP BOREHOLES
FOR DISPOSAL OF HIGH-LEVEL NUCLEAR WASTE

By Ethan Allen Bates

Submitted to the Department of Nuclear Science and Engineering on December 1st, 2014 in partial fulfillment of the requirements for the degree of Doctor of Philosophy in Nuclear Science and Engineering

Abstract

This work advances the concept of deep borehole disposal (DBD), where spent nuclear fuel (SNF) is isolated at depths of several km in basement rock. Improvements to the engineered components of the DBD concept (e.g., plug, canister, and fill materials) are presented. Reference site parameters and models for radionuclide transport, dose, and cost are developed and coupled to optimize DBD design. A conservative and analytical representation of thermal expansion flow gives vertical velocities of fluids vs. time (and the results are compared against numerical models). When fluid breakthrough occurs rapidly, the chemical transport model is necessary to calculate radionuclide concentrations along the flow path to the surface. The model derived here incorporates conservative assumptions, including instantaneous dissolution of the SNF, high solubility, low sorption, no aquifer or isotopic dilution, and a host rock matrix that is saturated (at a steady state profile) for each radionuclide. For radionuclides that do not decay rapidly, sorb, or reach solubility limitations (e.g., I-129), molecular diffusion in the host rock (transverse to the flow path) is the primary loss mechanism.

The first design basis failure mode (DB1) assumes the primary flow path is a 1.2 m diameter region with 100x higher permeability than the surrounding rock, while DB2 assumes a 0.1 mm diameter fracture. For the limiting design basis (DB1), borehole repository design is constrained (via dose limits) by the areal loading of SNF (MTHM/km^2), which increases linearly with disposal depth.

In the final portion of the thesis, total costs (including drilling, site characterization, and emplacement) are minimized ($/kgHM) while borehole depth, disposal zone length, and borehole spacing are varied subject to the performance (maximum dose) constraint. Accounting for a large uncertainty in costs, the optimal design generally lies at the minimum specified disposal depth (assumed to be 1200 m), with disposal zone length of 800-1500 m and borehole spacing of 250-360 meters. Optimized costs range between $45 to $191/kgHM, largely depending on the assumed emplacement method and drilling cost. The best estimate (currently achievable), minimum cost is $134/kgHM, which corresponds to a disposal zone length of ~900 meters and borehole spacing of 272 meters.

Thesis Supervisor: Michael J. Driscoll
Title: Professor Emeritus of Nuclear Science and Engineering

Thesis Supervisor: Emilio Baglietto
Title: Assistant Professor of Nuclear Science and Engineering

Thesis Reader: Jacopo Buongiorno
Title: Associate Professor of Nuclear Science and Engineering

Acknowledgments

I would like to express my deep gratitude (and grazie mille) to Mike, Emilio, and Jacopo for their resolute dedication, attention, and support during this thesis. Together they generated a seemingly limitless source of energy, enthusiasm, and advice on diverse scientific issues, while remaining patient, empathic, and understanding as mentors. They taught me how to make rapid but highly effective calculations, the importance and joy of discipline and daily progress, and the ability to solve complex problems systematically.

Special thanks go to Richard Lester for showing me the art of precise and impactful writing. I also appreciate the effort Tom McKrell, who was always there to help with experimental work and Eugene Shwageraus for providing radionuclide inventory data. The NSE administrative staff (Heather, Clare, Peter, Jennifer...) made studies and travels run smoothly. My office and class mates (John, Andrew, Alex, Enrique, Nick, Josh) helped elevate my spirits during this long journey.

I am very grateful for the advice of Patrick Brady and Bill Arnold at Sandia National Laboratories (SNL). Their experience in modeling geologic repositories and ability to identify important variables and analyses was invaluable to the progress of this research. Pat's positive suggestions helped motivate me to achieve things I did not initially see as possible. The Department of Energy's (DOE's) Nuclear Energy University Program (NEUP) program deserves a large credit for recognizing the importance of this research and for funding this collaboration with SNL.

Most importantly, this thesis is dedicated to my family for encouraging and shaping me as a person. I would not be here without the influence of my father Chris, who imparted to me a spirit of scientific curiosity, creativity, and a desire to improve the world. My mother Ling-Li gave me focus, perseverance, and drive that allowed me to succeed. My sister Diana showed me how to be persuasive and the importance of context and world issues. My twin brother Richard is the best friend and source of support that I could ask for.

Table of Contents

List of Figures

12

1. Introduction

1.1. Objective of the Thesis

This thesis develops a comprehensive radionuclide performance assessment model for spent nuclear fuel disposed in deep boreholes drilled up to 5 km into crystalline rock. The integrated model accounts for thermal, hydraulic, and chemical transport phenomena with an emphasis on analytical, conservative, and transparent methods. The thesis opens with a review of the available geoscience data and proposes baseline site parameters required as realistic inputs for the purpose of performance assessments. Secondly, the deep borehole concept is updated with respect to new plug, canister, and gap filling material designs. Finally, with a set of assumed site parameters and failure pathways, the radionuclide performance model is incorporated with economic and feasibility constraints to illuminate key design tradeoffs to provide a new and optimized design for deep borehole disposal.

1.2. Topic Motivation

1.2.1. Sustainable energy

The byproducts of electricity generation, whether they be combustion or fission, must be managed and contained responsibly to avoid undue consequences to future generations. With either - CO_2 or spent nuclear fuel (SNF)- it is accepted that deep geologic sequestration on (unprecedented) scales will be required to meet climate change targets and maintain intergenerational equity of resources. Table 1-1 summarizes the United States' electricity generation and waste production from coal, natural gas, and nuclear electricity production in 2013.

Table 1-1. Comparison of electricity generation and waste resulting from the three major forms of electricity production in the U.S in 2013[1], with a population of 317 million.

	Electricity production *GWhr(s)/yr {W/person}	Total waste/yr	Mass of waste/GW-hr	Volume/GW-hr
Coal	1,585,998 {571}	1.575×10^9 tons CO_2	993 tons CO_2	1.34×10^6 liters
Natural gas	1,113,665 {401}	0.442×10^9 tons CO_2	396 tons CO_2	534,169 liters
Nuclear	789,017 {284}	2000 MTHM[2]	2.78 kgHM	0.290 liters
Total (with other sources)	4,058,209 {1460}			

*GW-hr: The amount of electrical energy produced by a 1 billion Watt powerplant in 1 hour.
**MTHM: metric tons of heavy metal

Extrapolating the current per capita electricity usage (~1.46 kW) across the average lifetime (~80 years), the average American will demand a total of ~1 GWhr of electricity. By this logic, the waste produced during the generation of 1 GWhr (shown on the last column of Table 1-1) essentially provides a per person waste "footprint" (assuming all electricity is obtained from that source). The volumes and characteristics of each byproduct differ vastly, creating unique challenges for the geologic disposal of each of these wastes. While the CO_2 emitted from a coal or natural gas plant is produced at an extremely low density (<1 kg CO_2/m^3 of flue gas), here it has been assumed that the CO_2 has been separated, captured and compressed to a supercritical density (~743 kg/m^3) and pressure ideal for deep geologic sequestration (~100 atmospheres).

For each waste form, special geologic formations must be studied, characterized, and licensed to safely contain and isolate the waste, essentially permanently (>1000 years). Transporting the waste is difficult and costly, which favors disposal in nearby geologic formations (assuming they can be proven suitable). Each form of confinement utilizes the same principles of geoscience, benefits from a robust geologic sealing unit (one that retards the flow of fluids), and must be carefully engineered to maintain sufficient storage capacity (for the scale and type of project under consideration) without causing unwanted rock disturbances or contamination of groundwater supplies. By any estimate, the volume of isolated and licensable geologic media required for CO_2 sequestration applied on the large scale necessary for climate change mitigation is staggering, as shown in Table 1-2.

Table 1-2. Comparison of areal estimates for CO_2 sequestration.

Source	Injected mass of CO_2	Areal extent of subsurface CO_2 plume and pressurization	Areal density (km^2/GT CO_2)	Lifetime footprint of 317×10^6 GWhr (using natural gas): 126 GT
Barnes et. al. 2009 [3]	1.2×10^7 tons	3.8 km radius (45.36 km^2)	3780	476,000 km^2
Stauffer et. al, 2009 [4]	3.65×10^8 tons (1.2 MT/yr for 50 years)	12-18 km radius (452- 1,017 km^2)	1239-2788	351,000 km^2
Birkholzer and Zhou, 2009 [5]	5 GT (100 MT/yr for 50 yrs) injected into Mt. Simon formation	(241,000 km^2)	48,200	6,000,000 km^2

MT: Million metric tons of CO_2

Birkholzer and others[6] are beginning to acknowledge that high-level estimates of regional or global storage capacity in deep saline formations probably need to be revised (downwards) based on pore pressure buildup limits, seismic concerns, and environmental impacts. Thus, although CO_2 sequestration may initially appear to make coal and natural gas sustainable and "clean" technologies, a basic analysis of the land requirements for this technology show that it cannot be scaled up and sustained for more than a few generations.

On the other hand, geologic disposal of nuclear wastes requires much less land area. When the approximate SNF loading density of Yucca mountain is used (87 MTHM/acre or 21,750 MTHM/km^2)[7], the total area required is ~20 km^2, at least a factor of 10,000 less than for CO_2 sequestration. Limiting our consideration to the volumes of permanently isolated geologic pore space that must be obtained and characterized, it is clear that SNF is far better suited to permanent disposal than CO_2. Thus far, this may seem to be a restricted or biased discussion of the land requirements and feasibility of CO_2 vs. SNF disposal. However, the entirety of the thesis is dedicated to discussing the latter: the challenges, requirements, and predicted performance of SNF disposal in deep geologic formations.

1.2.2. Accumulated SNF

From a technical perspective, geologic disposal of SNF may be relatively easier to achieve than CO_2 sequestration, but that is not to say it is a simple or easy task. The regulated time period of confinement is 1 million years and the allowable harm of 15-100 mRem/yr to a future individual is very small- this is a fraction of the annual doses received from natural sources and background radiation. Figure 1-1 shows the projected radioactivity of the potentially harmful components of ~10 years of fuel discharged from a pressurized water reactor (PWR), vs. time after discharge.
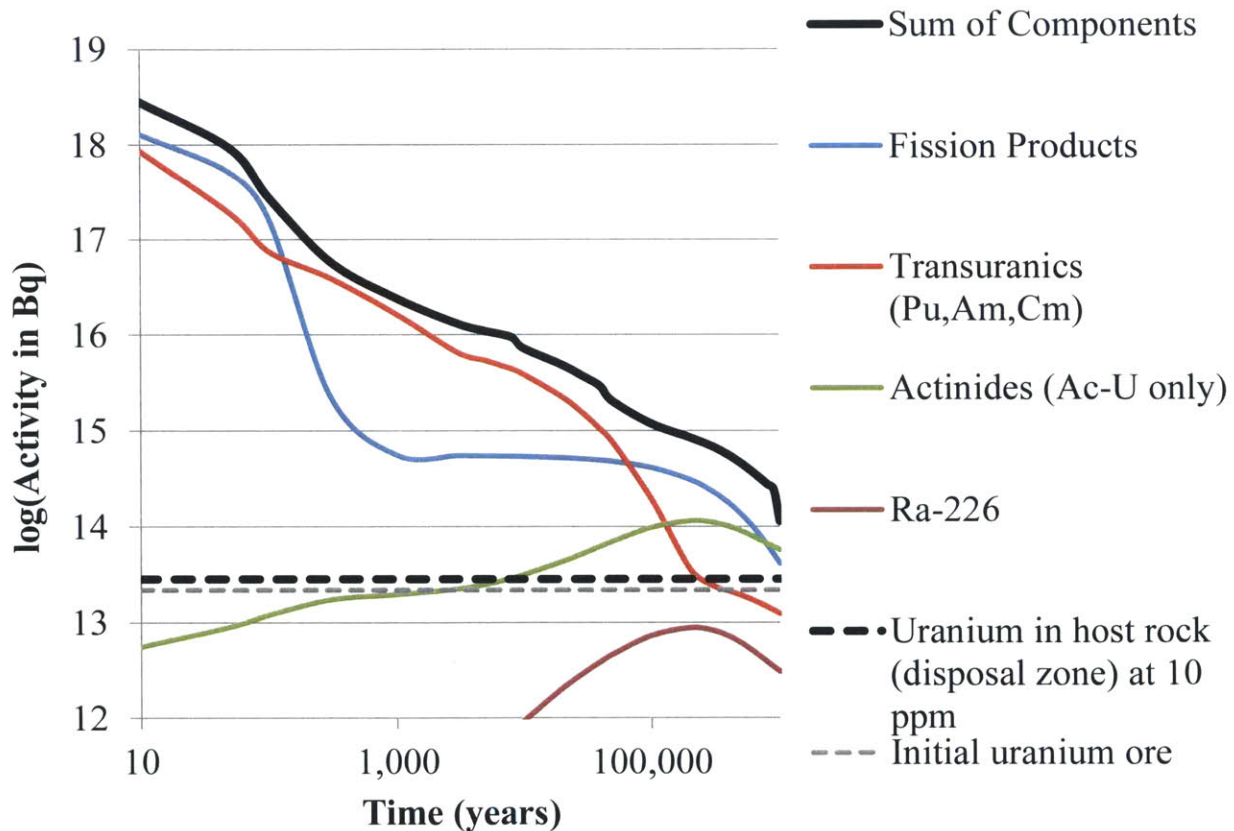
Figure 1-1. Log-log plot of radioactivity vs. time of 200 MTHM of spent nuclear fuel (SNF), at a burnup of 50 GWd/MTHM. [8]

Predicting conditions and events on these time scales is challenging, particularly for geologic disposal options that show sensitivity to changes in climate, hydrologic cycles, glaciation, and water tables. Accomplishing geologic disposal will be a truly interdisciplinary feat of science, involving geologists, chemists, civil, and nuclear engineers. In addition to the technical

challenge of designing and projecting the performance of an underground facility for 1 million years, there are considerable political and social barriers that must be overcome for deep geologic disposal to be viable. The issue of nuclear waste disposal has become highly politicized; to such an extent that the successful expansion of the nuclear industry in the U.S is threatened unless a safe and socially acceptable solution can be developed. Without Yucca Mountain operating as planned, 66,000 MTHM of SNF has accumulated at reactor sites across the country in spent fuel pools and dry cask storage facilities, as shown in Figure 1-2.
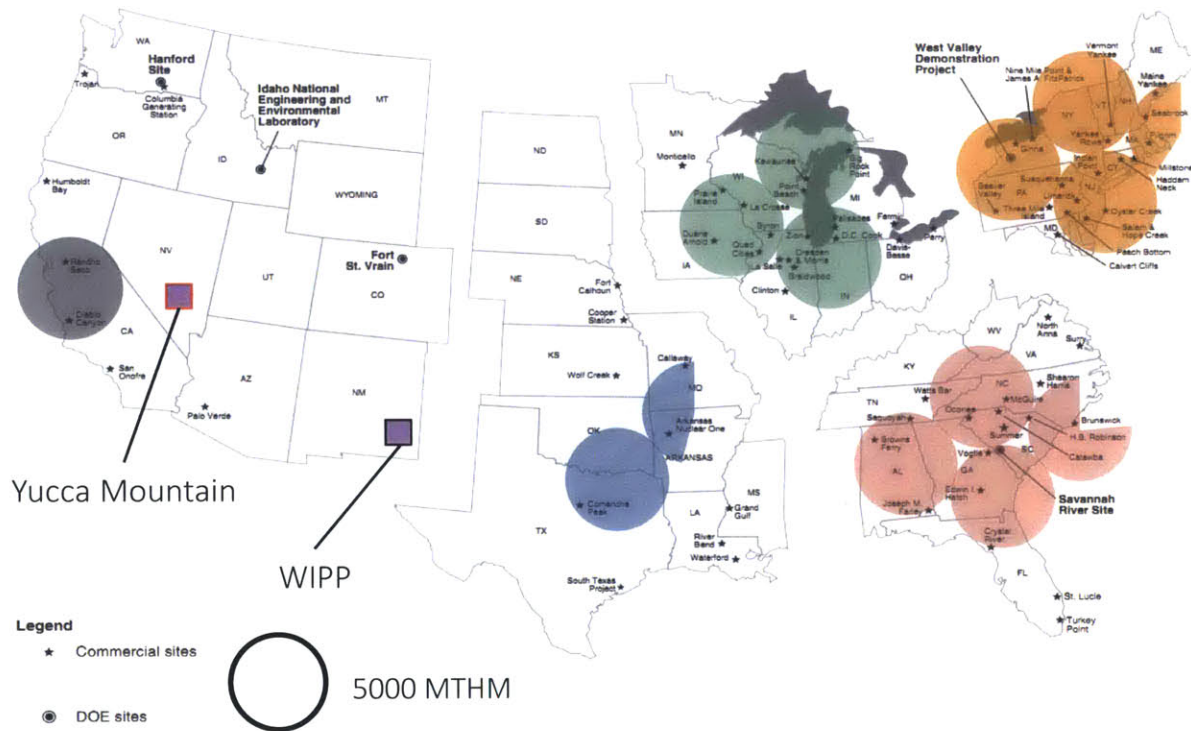
Figure 1-2. Approximate distribution of discharged spent nuclear fuel and operating or planned nuclear waste disposal facilities in the U.S, subdivided across 5 regions[9].

1.3. Overview of deep borehole disposal (DBD)

Fortunately, in the years since Yucca Mountain was selected as the nation's sole repository, scientific advancements have expanded the range of geologic disposal concepts that can be considered. Over 30 years ago, the Department of Energy (DOE) reviewed and downselected options for disposal of high-level wastes[10]. Out of the dozen or so options, only two were explicitly recommended for further research and development as promising alternatives to mined

geologic repositories: disposal of nuclear waste in deep boreholes and under the seabed. Since then, the legality of subseabed disposal has come into question[11] , and the initially selected mined repository of Yucca Mountain has been deemed unworkable by the current administration. The deep borehole alternative remains as a promising possibility. In 2012 the Blue Ribbon Commission (BRC) reconsidered options again [10] and echoed the DOE's original conclusions, noting a need for flexibility the U.S waste management strategy. The BRC went further by recommending demonstration of deep borehole disposal (DBD). The added political and economic flexibility of the borehole concept comes from:

1. The greater availability of suitable bedrock granite at depths of 2-5 km.
2. A modular approach which allows for additional capacity as needed.
3. Potentially lower costs for characterizing each site.

DBD's technical feasibility benefits from the petroleum, geothermal, and drilling industries which are constantly improving techniques to reach depths and diameters not conventionally considered feasibly or possible. Figure 1-3 shows the drilling depth and diameter profile achieved 20 years ago by the KTB scientific drilling project, almost entirely in crystalline rock.
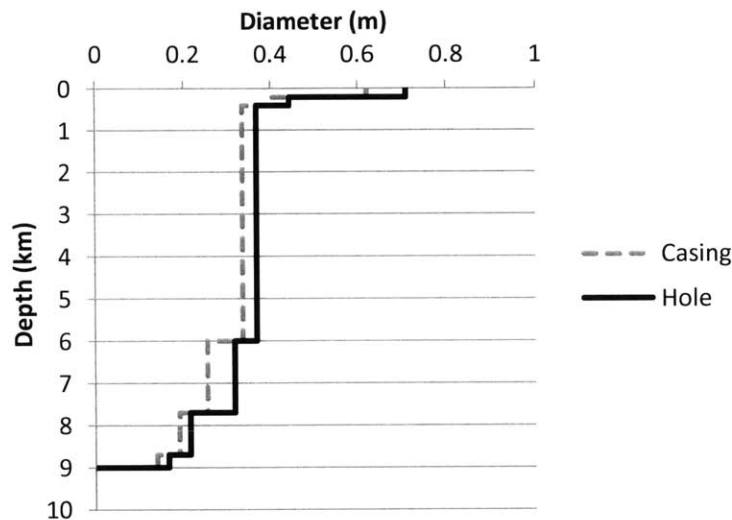
Figure 1-3. Casing and borehole profile of the KTB-HB main hole, drilled in 1990-1994[12]

The depths and diameters achieved by the KTB project approached those necessary to implement DBD and accommodate an intact PWR assembly (0.303 m width). In addition to generating a number of advancements in drilling technologies (such as automated systems to maintain verticality, handle drill liners, coring), the KTB project also improved techniques to assess fluid

19

mobility, residence time, and history [13], [14]. These data and methods bolster a central component of the geologic disposal strategy: predictions of future performance should be based on a strong record of past containment on a time scale exceeding that required for UNF isolation is available and understood. Advancements in understanding of subsurface flows and water residence times has also improved in North America, where isolated pore waters in deep crystalline rock have been well-studied [15], [16] . Figure 1-4 describes a section of the continental lithosphere called the North American craton in which the basement rocks are extremely old, tectonically stable, and may contain deep-seated fossil pore fluids.
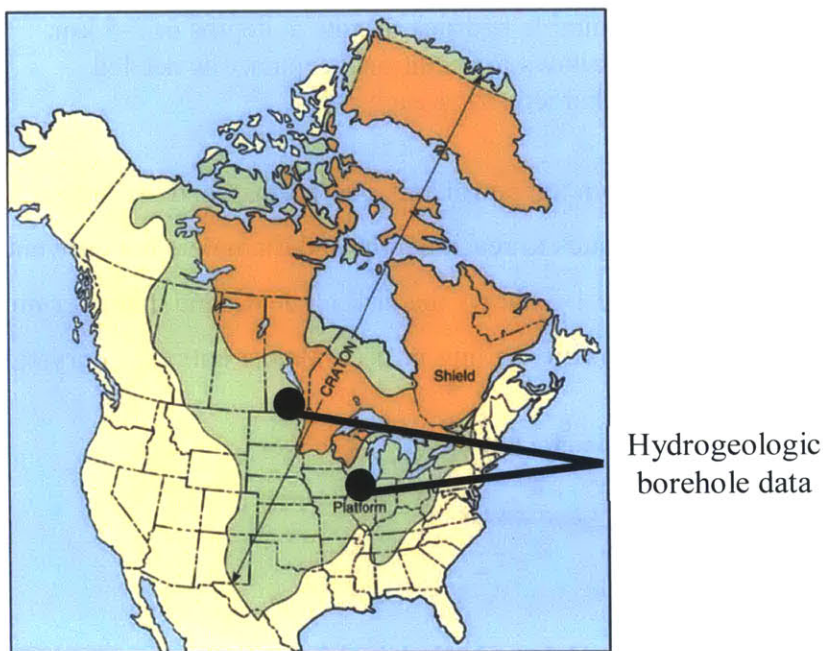
Figure 1-4. Locations of major scientific studies improving understanding of deep crystalline basement rock fluids in North America [15], [16]

At both sites, the deep pore fluids (>1000 m) were shown to have distinct chemical compositions from the overlying waters, implying that little flow and transfer of chemicals to the surface had taken place in many millions of years. At the UPH-3 borehole shown in Illinois, the concentration profile of saline fluids was consistent with an extremely slow diffusive process. Advancements in isotopic analysis (e.g., spread of accelerator mass spectrometry since 1980's) has facilitated analysis and understanding of potentially mobile, highly soluble, and conservative fission and neutron absorption products such as I^{129} and Cl^{36}. Elevated levels of these radionuclides in pore fluids indicates that they must have grown in concentrations (without

significant losses to the surface) for extremely long periods of time. The deep borehole disposal (DBD) is the only form of deep geological disposal that can take advantage of these highly favorable conditions for radionuclide isolation.

Deep borehole performance and design have been previously evaluated by a number of organizations, mostly in the U.S., Sweden and the U.K. However, rigorous justifications (i.e., based on repository performance and cost) for fundamental design parameters such as borehole array spacing, borehole depth, and capacity have never been presented. This is primarily because a fully coupled, rapidly evaluated, performance and cost model for trade study and design optimization has never been developed. In addition, the results depend on site (model input) parameters, which in the past have been treated in a generic fashion and without leveraging the most recently available data. This thesis develops improved inputs and models (with a focus on analytical methods to provide transparency and speed) to give an updated and optimized borehole design. A detailed schematic of the most recent reference DBD concept developed at MIT in 2006 is shown in Figure 1-5. Figure 1-6 compares the previous borehole designs with the one developed in this thesis.

Figure 1-5. Schematic and key parameters of the deep borehole disposal concept [17].

Diagram labels:

Hole 1   Hole 2

Diameter (Hole, Casing OD, Casing ID) in cm

≤1 km Overburden Zone, Sedimentary Rock — Upper (66.04, 50.8, 48.9)

1 km Plug Zone, Basement Rock — Mid-Zone (60.96, 45.72, 43.82)

2 km Waste Emplacement Zone — Lower (50.8, 40.6, 38.7)

Hole Spacing= 200 m
Square array
(Not to Scale)
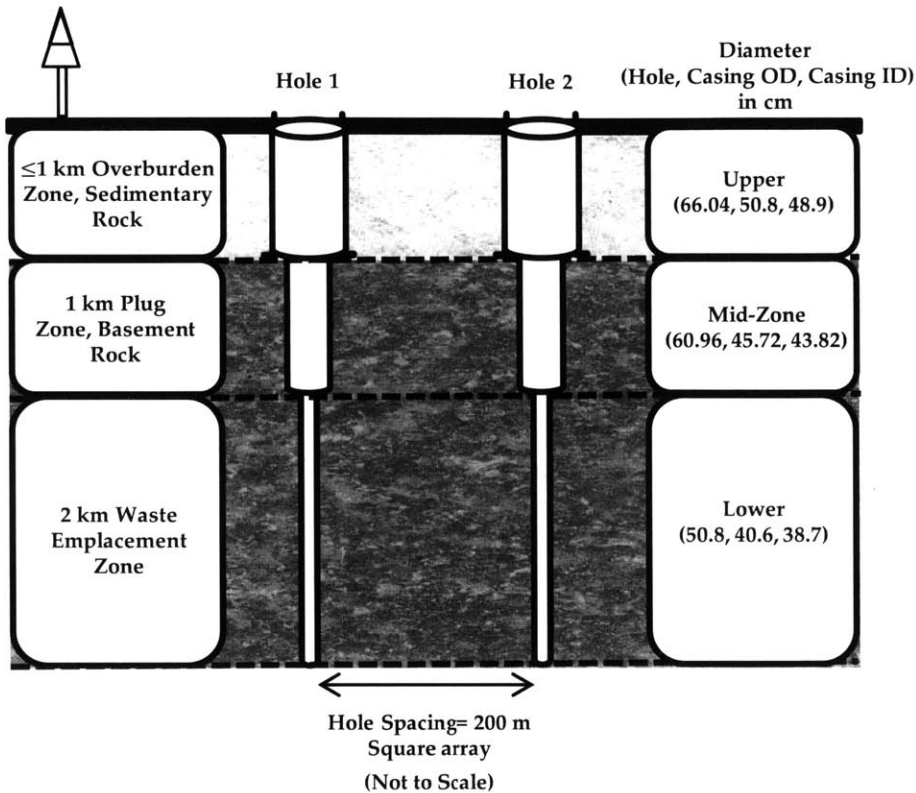
Waste Canister
34 cm OD, 31.5 cm ID*, 5 m   length
Capacity: One PWR Assembly
Weights, kg:
Casing**   600
Spent Fuel*** 700
Sand Fill   700
Total   2000
*To accommodate 21.4 cm. width assemblies (30.3 cm diag.)
**Including end plugs
***Of which ~500 kg is (as-loaded) heavy metal

Borehole Repository Field
400   Canisters (assemblies) per hole
200   MTHM/Hole (ten reactor years' worth)
Hole Array: 20 x 20 = 400 Holes, i.e. 4 km x 4 km field
Capacity: ≥70,000 MT (~Yucca Mountain)

Figure 1-6. Evolution of borehole designs from Woodward and Clyde, SKB, MIT, and SNL [17]–[21] (disposal zone depth and length are on the left axis while borehole spacing is indicated by the arrows and the right axis).

1.4. Arrangement of the Thesis

Chapter 2: Reference Site Parameters

This chapter discusses site characterization methods and objectives. Generic, reference values for the thermal, hydraulic, chemical, and mechanical parameters affecting the performance and behavior of deep borehole disposal are proposed. The site specific parameters of a particularly well characterized site at the UPH-3 borehole are also outlined.

Chapter 3: Reference Design

In this chapter, the deep borehole reference concept is updated with respect to plug, canister and fill material designs. Based on experimental results with a MgO-based expansive cement and a review of the existing data on clays, representative plug hydraulic properties are proposed. The canister design is improved to withstand the simultaneous effects of both hydrostatic and crushing stresses. In addition, a high thermal conductivity graphite based drilling mud is experimentally tested and proposed to improve heat transfer from the canister.

Chapter 4: Transport Model

This chapter develops a comprehensive thermal/hydraulic/chemical performance model of a borehole and its surrounding cell of host rock, accounting for both bulk and gap flows. The model is based on a conservative (radially closed) representation of the system where thermal expansion caused by heat generation drives fluids towards the surface (a process that is accelerated through failed high permeability regions). The analytical thermal/hydraulic model is compared against a numerical code, and the results for velocity are shown to be conservative. In the second portion, a chemical model is outlined, beginning with data on the radionuclide inventory, solubility, sorption, and dose conversion coefficients. A chemical transport model accounts for advection, dispersion and diffusion transport through a preferential, cylindrical flow path. For radionuclides that do not decay rapidly or sorb onto the host rock, a key loss mechanism occurring during flow to the surface is diffusion into the adjacent host rock. A maximally exposed receptor is assumed to consume all fluids exiting the failed flow path at the time of breakthrough.

Chapter 5: Integrated Performance and Economic Model

This chapter begins by defining a set of design basis failure pathways and properties by which the borehole design may be evaluated and optimized. Radionuclides from the disposal zone are assumed to flow through either a large (~1.2 m diameter) elevated permeability pathway or a cylindrical fracture (0.1 mm diameter). Economic assumptions on the costs of drilling, site characterization and canister emplacement are presented, which allow for a trade study on the design variables of borehole disposal depth, disposal zone length, and borehole spacing. Combining the economic and performance models, the design is optimized to minimize costs while meeting the specified dose limits.

Chapter 6: Summary, Conclusions, and Recommendations

Appendices A and B: These sections provide supporting analyses and derivations for models used in the prior chapters.

2. Reference Site Parameters

2.1. Chapter Introduction

Deep borehole disposal (DBD) relies primarily on passive geologic properties and phenomena to provide containment of radionuclides. To develop confident predictions of regional fluid pressurization and migration, a site characterization and data review of deep formations on the scale of kilometers will be necessary; the extent, geology, hydrology, and hydraulic connectivity of the deep hydrogeologic system needs to be well understood. A vast catalog of inputs, each of which may vary by many orders of magnitude with depth is required to support DBD performance. Ideally, these parameters are measured at the specific site where performance is evaluated. However, a detailed study of deep crystalline rock properties (>1 km) -specifically for nuclear waste disposal- has yet to be completed in the U.S.

Fortunately, over the past three decades, highly relevant hydrogeologic data and characterization methods for basement rocks were produced by other scientific interests and borehole projects- most notably the KTB project[22] but also geothermal[23], [24], CO_2 sequestration[25] and energy storage[26]. The purpose of this chapter is to review the most relevant data and propose conservative yet realistic and defensible geologic parameters for evaluation of deep borehole disposal performance. The chapter opens with a review of site characterization methods on the lab, borehole, and regional scale. Drawing primarily from the regional scale methods, generically applicable values for permeability, porosity, and other mass and heat transfer properties are proposed. These may be used as the basis of parametric studies or generic performance models where site specific data is unavailable. The chapter concludes by detailing boreholes that have been studied in the United States, with a focus on the UPH-3 borehole, the most well documented borehole (found thus far) with properties favorable to deep borehole disposal. Mainly using site specific properties obtained through boreholes and other sources (aquifer, CO_2 sequestration characterizations), a realistic deep borehole site is defined, which could be used in future work moving beyond generic models.

Experience at Yucca Mountain suggests that site characterization for nuclear waste disposal can be extremely costly and lengthy ($3.8 billion between 1987 and 2002) [27]. Over 450 boreholes were drilled and 25 wells were instrumented[28]. Although the actual footprint of 70,000 MTHM theoretically only covers ~ 3 km^2 (based on an areal loading of 87 MTHM/acre [7]), faults were surveyed over a site covering more than 170 km^2[29]. For the total area of land

surveyed this amounts to $22,000/km^2 and for the total mass of fuel planned for disposal, a specific cost of $54/kgHM. DBD could have a considerable advantage over shallow mined repositories such as YM and provide flexibility if it significantly reduces this characterization effort in terms of cost and time.

2.2. Site Characterization

2.2.1. Surface methods

Before presenting geologic parameters to be used in deep borehole disposal evaluations, it is important to discuss how these parameters are measured. The basic goal of site characterization for nuclear waste disposal is to measure hydrologic properties and features such as faults, porosity, and permeability which together determine the ability of the medium to store and transmit fluids and radionuclides.

The first step is to map the thickness, structure, and rock characteristics (i.e., stratigraphy, lithography) which serve as indicators of geologic history and stability. At a very large scale (over 100's of km) and without drilling a borehole, measurements of small deviations in gravity (anomalies) and thus rock density (< 0.1 g/cc) can be used to outline Precambrian basement bodies that underlie sediments [26]. Gravity measurements can also be used to reconstruct the region's block tectonic history and behavior [30], [31]. Positive gravity anomalies are caused by a high density lithosphere that has moved downwards, while negative anomalies are caused by a low density lithosphere that has moved upwards. Earthquake epicenters tend to be located near the edges and closures between gravity anomalies[30]. Gravity maps of the U.S. have been made since 1912 [32] and detailed maps are available from the United States Geological Survey (USGS)[33]. An even more detailed set of measurements was completed and compiled for Nye county and surrounding nuclear bomb test sites to provide an updated geologic framework and support groundwater flow models at Yucca Mountain [34] . Whereas gravity measurements quantify local variations resulting from density differences, magnetic anomalies result from variations in the magnetic properties of rocks. Thus, magnetic anomaly maps can also be used to identify major structural trends and features of the Precambrian basement, in particular ore bodies (ferri-magnetic minerals)[35].

The mapping of basement topography can also be achieved using seismic reflection profiles [36]. Reflections of compressional body waves (or P waves) traveling along near-

vertical paths are recorded as a source and receiver are moved along a line[37]. By recording information somewhat off vertical as well, information on velocity structure can also be obtained and used to convert the time section to a depth section. While in principle it is similar to echo location, in practice seismic profiling is more complex and involves multiple sources and receivers, great redundance of information, highly sophisticated data processing, and a substantial field effort. However, of all geophysical methods discussed thus far, seismic-reflection provides the highest resolution of structural details and information [37]. For example, at the KTB drill hole a 3-D seismic experiment covering 19×19 km correlated strong seismic wave reflectors and contrasts in seismic impedance with major fault systems, showing the effects of brittle faulting and creating an image of the young deformation pattern of the upper crust [22].

Furthermore, by comparing the relative velocity of compressional (P) waves and shear (S) waves in different lithologic layers, the rock's poroelastic properties can be obtained, as seen in Eq. (2-1) and Eq. (2-2)[38],

$$V_P = \sqrt{\frac{(\beta_u^{-1} + 0.75G)}{\rho}}$$ (2-1)

$$V_S = \sqrt{\frac{G}{\rho}}$$ (2-2)

Thus, if the density, V_P and V_s are known from measurement, the elastic shear modulus (G) in Pa and undrained compressibility (β_u) of the rock can be determined. Since seismic velocity is dependent on the density and effective and confining pressure on the rock, anomalously low seismic velocities can be indicative of high porosity rock containing overpressured fluids[39]. In addition, a higher velocity ratio (V_S/V_P) is indicative of lower crack densities[40]

2.2.2. Borehole methods

After surface investigations and pre-existing data have narrowed down possible sites, one or more test boreholes will have to be drilled to obtain detailed information on the hydrogeologic properties of the specific site. The diversity and complexity of down-hole logging and borehole/reservoir testing methods (which have been continually advanced by the oil and gas

27

industry) exceeds surface techniques, and it is not possible to fully explain all methods in detail here.

A key complexity of characterizing basement rock properties is that some properties tend to increase by orders of magnitude with the scale on which they are measured. This phenomena was recognized for permeability by Brace [41], subsequently receiving support with large compilations of data by Clauser [42]and theoretical and stochastic models by Neuman[43], [44]. Generally, measurement techniques and the data they collect are applicable on three scales:

1. Laboratory or core, ~10 cm
2. Drill hole or borehole - ~100 meters
3. Crustal, regional, reservoir: 0.5-5 km.

Permeability was noted to increase by three orders of magnitude from the laboratory scale to borehole scale, but stabilized from the borehole to the regional scale. The same scale dependence occurs for other important parameters such as the diffusion coefficient; for example, Liu, Zhou, and others [45], [46] determined that diffusion coefficients increase by 3 orders of magnitude as the scale of measurement increases from 5 to 2000 meters. Fundamentally, this occurs because:

1. The rock has low permeability and flow occurs through random fracture networks[44].
2. As the volume of rock that is investigated increases, the probability that conductive fractures will be intersected increases as well[47].
3. More mass transfer processes occur as a result of the heterogeneous nature of flow in fractured systems [45].

It is not feasible (or necessary) to collect and model the fine scale variability of the fractured rock system[45]; as a result, large scale transport is effectively modeled using large blocks with varying hydraulic transport parameters. The transport parameters of each element or block represents the lumped transport features of the small scale mass transfer processes. Thus, field scale diffusion (pressure, solute) is an upscaled transport process, and it is believed that a field scale diffusion coefficient can accurately simulate the local scale processes.

Rather than attempt to describe all measurement techniques at all possible scales, Table 2-1 and the following corresponding list briefly outline each method, at which boreholes they have been used, the parameters they can measure, and the general scale over which those

measurements are applicable. A greater emphasis is placed on the borehole or reservoir scale measurements, as they provide the most applicable data to large scale transport modeling. Details on each of the methods can be obtained from the references organized in Table 2-1.

Table 2-1. Summary of borehole characterization methods and inferred parameters. Length scale is indicated by dashes, (-) laboratory (---) borehole , and (-----) regional.

	Permeability	Fractures/ faults	Porosity	Diffusion coefficient	Mechanical	Scale
Core	[48]*UPH [49]*CP [50]*KTB [51]*CLX	[52]*CP [22]*KTB [53]*UPH	[54]*CS [15], [48], [55]*UPH	[56][57]	[58]*KTB	(-)
Neutron log		[53]*UPH	[59] [60]*UPH			(-)
Caliper log/televiewer		[53]*UPH ***[61]			(see chapter on structural modeling)	(-)
Electrical resistivity		[62], [63]*CP [60]*UPH [22]*KTB				(---)
Tracer tests		[64]*SW		[54]*CS [45]*** [64]*SW		(---)
Head test, drawdown test, packer test	[47]*CP [54]*CS [50]*KTB [53]*UPH ***[61]	[47]*CP				(---)
Isotope analysis		[16], [65]*CS [66]*KTB		[15]*UPH		(-----)
Models/ calibrations	[67]*CP [22], [68]*KTB [69]*KLA					(-----)
Injection and induced seismicity	[70]*FH [71], [72]*KTB [73]*SZ ***[74]	[47]*CP			[75]*MC [76]*KTB	(-----)

*denotes the site at which techniques have been documented; CP-Cajon Pass, CA, USA; CLX- Climax, NV, USA; FH- Fenton Hill, NM, USA; CS- Canadian Shield; KLA- Kola, Russia; KTB, Germany; MC- Monticello Reservoir, SC, USA; SW- Sweden; SZ- Soultz, France; UPH, IL, USA.
***Summarizes tests at multiple sites.

2.2.2.A. Laboratory and core scale

Core: Rock samples, typically obtained in the form of small cylindrical cores similar in diameter to the borehole, can provide highly detailed and fine scale chemical and mechanical rock properties. Core permeability (as measured in laboratories) is frequently reported [48]–[51] and is typically extremely small for crystalline rocks (10^{-21} to 10^{-19} m^2). Stress relief and thermal cracking occurring during or after the coring process can affect the measured physical properties of cores including permeability[48], porosity and microfractures [61], [77]. Water accessible porosity (relevant to hydraulic and molecular flow) is typically measured by comparing the water saturated and vacuum dry masses of cores [15], [48], [55], [78]. Core porosity measurements on granitic rocks vary between 0.2% to 0.7%[54], [61], [78], and have a significantly smaller spread of values than permeability.

Comparison of core samples with depth improves the detail of lithologic profiles and homogeneity of the rocks with depth. If multiple boreholes and core samples are available, the lateral extent of the rock layers can also be confirmed. Interpretation of core mineralogy through X-ray diffraction[52], pore fluids[15], and fracture filling minerals can also be used to support the chemical and hydraulic flow history at a site[13], [63].

One advantage of core samples is that a wide range of temperatures and pressures can be simulated in the laboratory. Therefore, the change of the physical properties (in particular, those related to thermal expansion) of the repository rock in response to waste emplacement can be understood. [51].

Neutron log: The neutron log primarily measures the water content (specifically, low Z elements such as hydrogen) of the rock. The probe consists of a neutron source and detector. The number of scattered (and thermalized) neutrons is an inverse function of the hydrogen content of the rock surrounding the borehole. The measurements are affected by both chemically bound water and pore water, and therefore are a less accurate measure of porosity within hydrated clay minerals. However, the data can be useful for detecting fractures, which are frequently filled with such hydrated minerals.

2.2.2.B. Borehole scale

Resistivity: Electrical resistivity of a rock is a function of the porosity, fluid resistivity, and grain resistivity of the rock. Considering that the crystalline rock typically has a higher resistance than the fluid, low resistivity is associated with fractures and interconnected fluid

conduits while higher and uniform values for resistivity are associated with fewer fractures. The electrical conduction is thus either electrolytic along the pores and fluid filled fractures, or through cation exchange on clay surfaces for altered parts of the rock[62]. At the KTB borehole site, an innovative electric dipole experiment successfully detected an anomalously low resistance fracture (filled with graphite)[22].

Caliper log/televiewer- The borehole wall can be measured and imaged accurately, providing a means to resolve the texture of the rock and quantify fracture frequency with depth [53]. The extent of compressive borehole breakouts can also be used to infer in-situ stresses. The caliper and electrical resistivity logs are frequently interpreted in parallel to build a complete picture of fractures in the borehole.[61]

Tracer tests- conservative tracers are elements which are not typically sorbed onto rock or react with minerals (e.g., Cl, I⁻, fluorescein[64]) can be used to measure the diffusion coefficient at boreholes. Since diffusion coefficients measured on these smaller scales can be so low in granitic rocks ($\sim 10^{-12}$ m/s), experiments can take many weeks or even years to conduct [54].

Drawdown, well, packer tests: With packer tests, inflatable rubber seals are used to isolate portions of the borehole while a pump injects fluids and measures the pressure response in the borehole. The decay of pressure can then be related to the permeability of the formation [53]. Another variation is to hold pressure constant and measure the flow into the formation (i.e., constant head). Drawdown tests work on the same principles, but only the bottom is sealed so the permeability of the entire borehole- rather than isolated sections- is measured. Thus, the tested interval can vary in length from a few meters to kilometers. Fundamentally, the lower the permeability of the rock, the longer a given test will take- thus in some cases (when the rock permeability was $\sim 10^{-18}$ m^2) drawdown tests lasted 6 months [47].

2.2.2.C. Regional scale

Isotope analysis: Isotope analysis is essentially the natural analogue of the artificial tracer tests that have been previously discussed. Rather than analyzing tracers that are introduced at the time of the experiment, preexisting isotopes are measured- their distributions (or presence) can be related to various major chemical events that have occurred in the site's past. These are arguably the best methods to obtain site parameters that would be considered valid on the timescales and length scales for geologic disposal. Groundwater tracing is a vast discipline and many isotopes

have been analyzed to estimate groundwater flow rates and residence times[79]. A key example is the comprehensive series of isotope analyses at a site including 53 boreholes in the Canadian shield, which allowed for a detailed determination of residence time vs. depth. Figure 2-1 shows the inferred bounds for residence time vs. depth using tritium (H^3), carbon-14 (C^{14}), iodine-129 (I^{129}), chlorine-36 (Cl^{36}), and others not discussed in detail here.
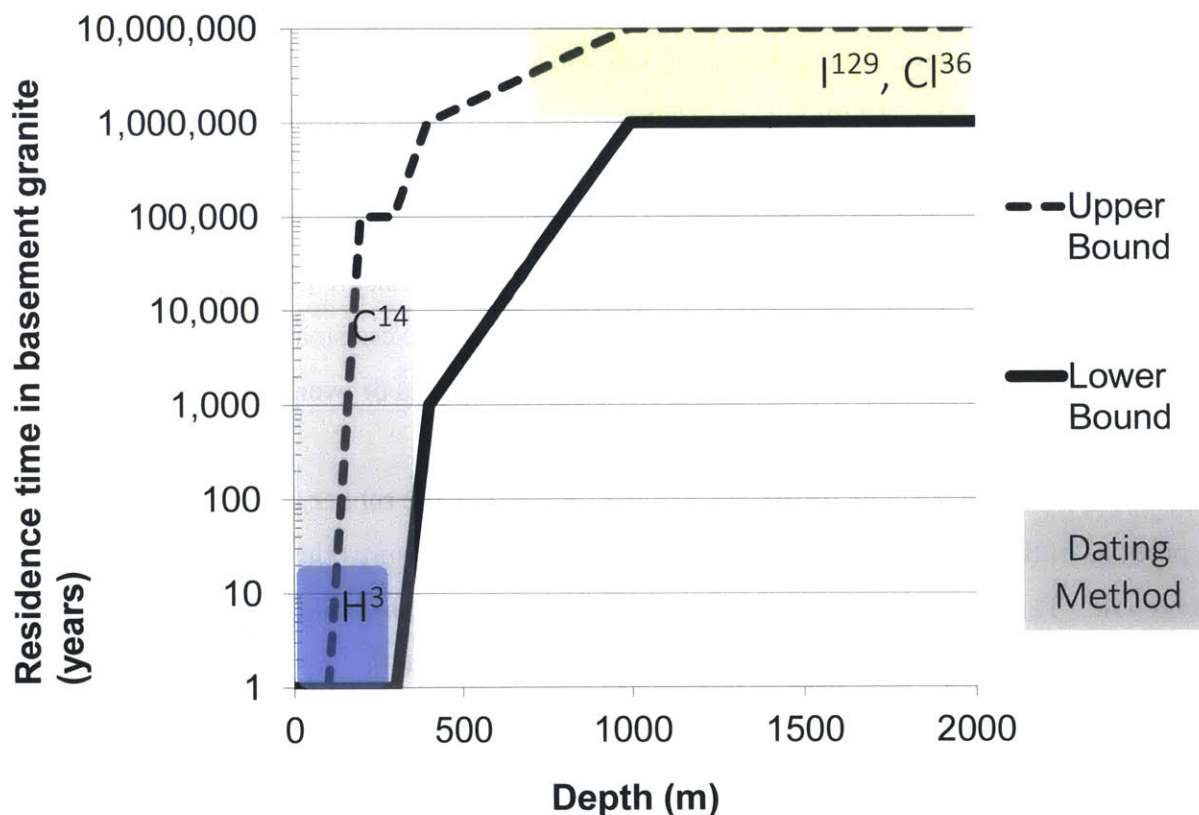
Figure 2-1. Pore fluid residence time at a southern site in the Canadian Shield as inferred by various isotope analysis methods. Data obtained from Table 7 of [16].

The intrusion and presence of H^3 (produced in major quantities in the atmosphere within the last 60 years) down to ~200 meters indicates that the near surface bedrock is in rapid communication with young meteroric surface waters) and has a residence time only on the order of 10-100 years. Within a deeper transition zone (200-400 meters), the estimated residence time is between 1000 to 10,000 years, as indicated by low C^{14} and lack of H^3. In the deep and stagnant groundwater and brines at 400-1000 meters, the high ratio of Cl^{36}/Cl indicates that uranium fission has produced neutrons which have been absorbed by Cl^{35} to produce Cl^{36} (with a half-life of 0.3 Ma),

which must have accumulated in the porewaters for a million years or more. I^{129} is produced directly from spontaneous uranium fission, and its very long halflife (15.7 Ma) allows it to be used as a long term groundwater tracer. Similar isotopic analyses have been completed at the KTB site [66] and in Sweden[80]. Comparison with the preanthropogenic I^{129}/I ratio of 1.5 $\times 10^{-12}$ (identical for all reservoirs in exchange with the atmosphere or ocean) signifies how long water has been separated from meteoric waters[66]. At one mine in the Canadian shield, the concentration is so high that it is consistent with secular equilibrium of I^{129}, a process that requires stagnant conditions and buildup for >80 Ma[65]. At another deep mine drilled into the African craton, similar radiogenic isotope dating methods provided minimum subsurface residence times for the water ("minimum bulk age") ranging from 1.5 to 23 Ma, but recently developed neon based dating methods improved these estimates and showed that the water has been trapped for >2 billion years [81]. Thus, groundwater age techniques are continually advancing and many of the radiogenic methods discussed may only provide lower bound estimates. Note that the age of the rock is also frequently determined via isotope analysis (Zircon, U-Th-Pb [22], [52]), but this does not necessarily give any direct information of the pore fluid history. These analyses help rule out the existence of highly conductive fractures from the surface, but have not been used to infer values for permeability or diffusion coefficients.

A good example of chemical analysis being used to quantify diffusion coefficients on a reservoir scale (~1 km) comes from the UPH-3 borehole drilled in Illinois. Couture and Seitz showed that the salinity profile between the deep granite and the surface is consistent with a very slow diffusion of solutes (towards overlying sandstone that had been depleted of solutes) over 10's of millions of years[15]. The upper bound diffusion coefficient for Cl^- below a depth of 700 meters was bounded to be $<3 \times 10^{-10}$ m^2/s. This compares with the value of 2×10^{-10} m^2/s obtained via I^- borehole tracer tests in Sweden[64].

Numerical models/calibrations: By creating numerical models of the entire region, simulating heat and mass transfer throughout the domain and comparing the results to measurements, bounding estimates can be made on rock properties and the dominant methods of heat transfer (advection or conduction) can be characterized. Temperature vs. depth profiles that are seriously disturbed (do not follow a typical linear profile) are indicators of advection due to a combination of high heat flow, high permeability, or topographic effects at a site [69], [82]. Thus, the methods are sensitive, and can help separate topographic and paleoclimactic effects

(changes in surface temperature) on heat flow. In general, climatic effects on rock temperatures have been found to extend not much deeper than 500 m [22]. Heat flow variations may also result from heat refraction effects due to lateral variations in thermal conductivity (e.g. with steeply dipping layers of rocks [68]). Manning and Ingebritsen [83] and Stober and Bucher [84] interpreted geothermal heat flow and metamorphic data at many sites to come up with a convenient expression for permeability with depth, but cautioned using their correlation for actual simulations.

Large numerical models were used to investigate and explain heat flow measurements at the San Andreas fault[67], KTB boreholes[22] and Kola borehole[69]. The thermal model at the Kola borehole constrained kilometer scale permeability to be 10^{-14} m^2 and 10^{-17} m^2 for the depth intervals of 0-2 km and 6-8 km, respectively. An important result of numerical models is to identify the depth at which heat flow is purely diffusive (e.g., 400 meters depth at the KTB site [68]). Calibrated numerical models are generally important to developing confidence in the validity of approximating crystalline rocks as homogenous porous media on long time scales.

Injection and seismicity: Injection tests provide the most applicable and representative hydraulic data on field or reservoir scale properties. They have been used to characterize geothermal sites (Fenton Hill[70], Soultz[73]), but were also used multiple times at the KTB borehole[71], [76] over a decade. The fundamental principles and working method of seismic injection measurements (i.e., hydraulic diffusion) are directly tied to every important hydraulic property (porosity, permeability, fractures, pore pressures, mechanical state of rocks). Thus, the following section on hydrologic properties begins with a description of the governing equations, assumptions inherent with seismic injection testing, and the results obtained at various test sites.

2.3. Mass Transfer (Hydrologic, Chemical)

Based on a large number of borehole injection tests, stress analyses, and permeability studies, Zoback and Townend came to the conclusion that the shallow crust to ~10 km depth (including basement rock) is in a state of frictional failure along preexisting faults[85], [86]. While the mechanical equations and stress analysis are discussed in greater detail in Section 2.7, the basic reasons for and effects on diffusion of pressure and fluids will be described here. When pore fluid pressure is increased significantly above hydrostatic, the effective stress in the rock is increased. When the stress is increased beyond a certain threshold (determined by frictional

slipping along a preexisting fault), fractures will open, causing permeability to increase and allowing pressure to equalize close to hydrostatic. Zoback and Townend summarize a number of stress measurements which indicate that basement rocks are usually at or near this failure point (therefore small increases in pore pressure result in small seismic events and increases in permeability).

This approach, termed seismicity based reservoir characterization (SBRC) has been used to infer the permeability of large rock masses in the KTB borehole[71] and other boreholes drilled into crystalline rock in the U.S. and France [70]. Large changes in pressure are made at a borehole, and the spatial and temporal seismic responses (i.e., associated with equilibration of pore pressures) are recorded. For example, with the KTB injection tests, pressure increases of ~1 bar (above hydrostatic) were required to trigger microseismic events [76]. An interesting result of the series of KTB injection tests was that a pore fluid volume approximately equal to that which had been extracted in a previous test had to be injected before any microseismicity resulted[76]. This suggests that at a deep borehole site, borehole durability could be improved by initially removing a set amount of pore fluids (i.e., achieving sub-hydrostatic pressures), which would allow for expansion of the pore fluids after waste emplacement without inducing seismicity.

Townend argues that hydrostatic pore pressures existing to great depths are both an indicator and result of this rock failure equilibrium. In this way, shallow crustal scale permeability far below $10^{-17} m^2$ is ruled out[87], unless pore pressures are maintained significantly above hydrostatic. Secondly, if temperature profiles suggest a conductive regime and thermal gradient (discussed more in the chapter on natural convection), permeabilities significantly greater than $10^{-15} m^2$ [69], [87] may be ruled out (discussed more in chapter on stability of convection). Thus, with two arguments and types of data (pressure diffusion, heat diffusion) the permeability of the crystalline basement can be bounded to be between the range of 10^{-17} to $10^{-15} m^2$.

2.3.1. Hydraulic diffusivity

To allow for analytical models to be used, the transport of pressure is typically modeled as a diffusive process in pressure (P) which is written as Eq. (2-3) [71], [73], [76], [85],

$$\frac{\partial P}{\partial t} = \nabla^2 (D_{hydr} P) \tag{2-3}$$

In some situations, the diffusivity could be changed by the pressure increase, which means that the equation becomes non-linear. Shapiro argues that this only happens locally in restricted regions around the borehole (~100 meters), and thus the equation remains valid for measuring diffusivity on a large rock volume on the order of 1 km [73]. Assuming that the borehole injection process can be modeled as diffusion of pressure from a point source, Shapiro and others[71], [85] calculate a characteristic diffusive pressure response time curve which is written as Eq. (2-4),

$$l = \sqrt{D_{hydr} t} \tag{2-4}$$

where l is the distance that the pressure perturbation travels in a given time t and D_{hydr} is the hydraulic diffusivity. By analyzing the temporal and spatial distribution of seismic events induced by the pore pressure increase from fluid injection experiments, the hydraulic diffusivity can be calculated. A simplified and widely used form of hydraulic diffusivity takes the form of Eq. (2-5)[38],

$$D_{hydr} = \frac{k}{\mu(\phi \beta_w + \alpha c')} \tag{2-5}$$

where k is the permeability of the rock (m^2), μ is the dynamic viscosity of the fluid (Pa-s), ϕ is the porosity, and β_w is the fluid compressibility (Pa^{-1}). Furthermore, α is defined as Eq. (2-6)

$$\alpha = 1 - \frac{\beta_g}{\beta_d} \tag{2-6}$$

where β_g and β_d are the compressibilities of the grain (solid phase) and drained matrix frame respectively. Also called the 'effective stress coefficient', α indicates the change in pore volume per unit change in bulk volume, under drained conditions. It generally varies between ϕ and 1. Up to this point, the terms presented thus far are the simplified equations used in SBRC [71],

with slight differences in terminology. Lastly, c' is called the vertical compressibility, and is defined by Kumpel [38] as Eq. (2-7),

$$c' = \frac{(1 + v_P)(\beta_d - \beta_g)}{3(1 - v_P)}$$

(2-7)

where v_P is the dry or drained Poisson ratio of the rock. In Shapiro et. al [71]and Townend and Zoback's[85] simplified equations, the term c' is approximated with β_g (equivalent to $1/K_g$, the bulk modulus of the grain by Shapiro), which is written as Eq. (2-8),

$$D_{hydr} = \frac{k}{\mu(\phi\beta_w + \alpha\beta_g)}$$

(2-8)

Other models of large geological domains including the Precambrian basement (for CO_2 sequestration) approximate hydraulic diffusivity using a slightly different form shown in Eq. (2-9) [25],

$$D_{hydr} = \frac{k}{\mu\phi(\beta_w + \beta_r)}$$

(2-9)

where β_r is defined as the rock compressibility. This expression may be invalid for very low porosity rocks (because it predicts that hydraulic diffusivity increases without bound as porosity decreases). This may be a conservative approximation for CO_2 sequestration modeling, as it tends to maximize the pressure buildups in the system (the basement rocks effectively become impermeable boundaries in this case). Thus, although different authors use different formulations to calculate the compressibilities, we may compare them all on a similar basis by calculating values for c_r, as shown in Eq. (2-10),

$$D_{hydr} = \frac{k}{\mu(\phi\beta_f + c_r)}$$

(2-10)

where c_r, is a term with units of Pa^{-1} that generally encompasses the effective capacity of the rock to compress and absorb pressure perturbations (similar to the role of heat capacity in thermal diffusion). This single term can then be used to calculate the permeability of the rock from the measured hydraulic diffusivity. Table 2-2 presents a comparison of poroelastic parameters used by various authors analyzing measured seismic emission data.

Table 2-2. Comparison of poroelastic properties and estimates for hydraulic diffusivity and permeability from SBRC and models.

Source of Data	ϕ	μ (Pa-s)	β_f (Pa^{-1})	β_g (Pa^{-1})	β_d (Pa^{-1})	α	c_r (Pa^{-1})	Measured D_{hydr} (m^2/s)	Calculated permeability (m^2)
SBRC Measurements									
KTB borehole, 1994- 2005, 5-9 km depth [71] [76]	0.003	1×10^{-3}	4.35×10^{-10}	1.43×10^{-11}	2.00×10^{-11}	0.286	4.08×10^{-12}	0.01 to 2 (fractured zones)	5.38×10^{-17} to 1.12×10^{-14}
Soultz [73]	0.003	1.9×10^{-4}	4.55×10^{-10}	1.33×10^{-11}	2.04×10^{-11}	0.347	4.62×10^{-12}	0.05	5.69×10^{-17}
Fenton Hill[70]	0.003	1.9×10^{-4}	4.55×10^{-10}	1.33×10^{-11}	2.04×10^{-11}	0.347	4.62×10^{-12}	0.17	1.93×10^{-16}
Models								**Calculated D_{hydr} (m^2/s)**	**Permeability (m^2)**
Townend and Zoback [85]	0.02	1.9×10^{-4}	5×10^{-10}	2.00×10^{-11}	Not given	1	2×10^{-11}	0.0017- 0.017	10^{-16} to 10^{-17}
Zhou et al. [25]	0.05	5×10^{-4}	3.4×10^{-10}	-	-	-	1.48×10^{-8}	3.7×10^{-6}	10^{-19}

*grey cells indicate values that are shown or assumed directly in the papers. Other cells are calculated using equations given.

With respect to the first row of Table 2-2 summarizing KTB measurements, the choice of 1×10^{-3} Pa-s (viscosity at room temperature) for water at 5-9 km is unrealistic (calculated permeability should be lower by ~ 5×). In general, the fluid properties would be more accurately treated in numerical models (where the viscosity and compressibility are evaluated at the specific conditions of that node). The Soultz and Fenton Hill rock material values are identical (second and third row of data) and appear to be suitably adopted for estimating hydraulic diffusivity at deep bedrock sites where such data is unavailable (i.e., $c_r=4.62 \times 10^{-12}$).

Townend and Zoback's porosity value of 0.02 might be high (vs. measured values which lie between 0.002- 0.007), but at such low porosities, the rock compressibility starts to determine the hydraulic diffusivity in Eq. (2-9). Overall, Townend and Zoback's crustal hydraulic diffusivities on the order of 10^{-3} to 10^{-2} m^2/s are used to infer a rock permeability range of 10^{-17} to 10^{-16} m^2: a reasonable range that encompasses the measured seismic data. With the assumed (modeling) data used in Birkholzer and Zhou [25], the combination of very low permeability and large values for c_r results in what appears to be an unrealistically small crystalline rock hydraulic diffusivity of 3.7×10^{-6} m^2/s. However, this tends to maximize pressure buildups, and may be considered an appropriate and conservative assumption for their modeling simulations of CO_2 plume transport and capacity in a sandstone formation that overlies the Precambrian basement.

As a side note, Shapiro et al. [71] has computing errors that could not be reconciled (there is a difference between the poroelastic properties given and the reported vs. calculated diffusivities). Also note that the diffusivity calculated here is associated with the speed at which the pressure wave travels, which is significantly faster than the speed at which the fluid itself travels- thus, the characteristic time shown in Eq. (2-4) is not the transport time of the fluid.

While different estimates for permeability and porosity could result in identical values for D_{hydr}, the two systems will behave in very different ways. A smaller permeability (and proportionally smaller c_r and porosity) results in greater pore pressure buildups[5], which could be more problematic due to microseismicity, geomechanical damage, and permeability increase associated reasons which have been previously discussed. A larger c_r and porosity with proportionally higher permeability could have the same overall diffusivity but would result in a much smaller pressure buildup due to higher capacity of the rock to absorb pressure perturbations. As Kumpel puts it, deformation of the rock matrix slows the settling of a pore pressure change[38]. Thus, a sensitivity study which varies hydraulic diffusivity by changing

permeability alone is clearly insufficient to capture this effect. Furthermore, varying the porosity (which would also have other effects on the transport velocity of the fluid) will not change the total diffusivity proportionally. Therefore the rock compressibility is clearly a key and independent input parameter (neglected in previous deep borehole simulations) which should be included. This is especially true for simplified methods or models which assume closed boundaries that allow pressures to build up[88].

The second general conclusion is that obtaining a site with extremely low rock permeability may not necessarily be beneficial to the safety case, as it increases the potential for large pore pressure buildup and requires more complex geomechanical models to be developed. Alternatively, this raises the possibility of searching for sites (or intentionally engineering them) to have isolated regions of high hydraulic diffusivity, which would allow the pressure buildup in the system to be relieved in a more controlled location and manner.

2.3.2. Chemical diffusion

With regard to (molecular) diffusion transport, it might seem intuitive that a high value (associated with faster rates of diffusion) would be considered conservative. However, there are some scenarios (e.g., flow along a single vertical fracture) where larger diffusion coefficients could actually reduce the total vertical radionuclide transport rate [89]. An Archie's law expression developed from experiments (which gives the effective diffusion coefficient (D_{eff}) vs. porosity) is described by Eq.(2-11),

$$D_{eff} = \phi^{n-1} D_w \tag{2-11}$$

where n= 2.93 for granite [46] and D_w could be (conservatively) evaluated at the lowest possible value (2×10^{-9} m^2 at room temperature, higher for higher temperatures). An Archie's law based expression such as this could also be used to evaluate the diffusion coefficient in other sedimentary layers [90] which may exist as important components of a realistic deep borehole performance model. Note an important distinction between the "effective" diffusion coefficient and the apparent matrix diffusion (D_m) coefficient used more frequently throughout this thesis, which are related by Eq. (2-12),

$$D_{eff} = \phi_m D_m \qquad\qquad (2\text{-}12)$$

Combining Eq.(2-11) and Eq. (2-12) gives Eq. (2-13),

$$D_m = \phi^{0.93} D_w \qquad\qquad (2\text{-}13)$$

Inserting a matrix porosity of 0.01, we obtain an apparent matrix diffusion coefficient of 2.76 $\times 10^{-11}$ m^2/s. A similar parameter measured by SKB in Swedish bedrock [91] (capturing the reduced diffusion coefficient of species due to the tortuous flow path) is defined as Eq. (2-14),

$$D_m = D_w \left(\frac{\delta_{SKB}}{\tau_{r,SKB}^2} \right) = D_w (9 \times 10^{-3}) \qquad\qquad (2\text{-}14)$$

which would give a matrix diffusivity (D$_m$) of 1.8 $\times 10^{-11}$ m^2/s. Yet another definition of the apparent rock matrix diffusion coefficient is given by Eq. (2-15) [54],

$$D_m = \frac{D_w}{\tau_r^2} \qquad\qquad (2\text{-}15)$$

where τ_r is the tortuosity of the flow paths in the rock, which has been experimentally measured to be 5-15 for in-situ measurements on Precambrian crystalline bedrock in Canada [54]. This reduces the diffusion coefficient by a factor of 25-125 and therefore gives matrix diffusivities ranging from 8.9 $\times$ 10^{-12} m^2/s to 7.17 $\times$ 10^{-10} m^2/s. Thus the value of 8.9 $\times 10^{-12}$ m^2/s may be taken as a lower bound for the apparent matrix diffusion coefficient (D$_m$).

The temperature dependence of the diffusion coefficient (which could also be important, particularly at sites with larger geothermal gradients) can be modeled as an Arrhenius dependence[92]; with the diffusion coefficient of 2.26 $\times 10^{-9}$ m^2/s activation energy of 17.6 kJ/mol (at 25 °C)[93] we obtain Eq. (2-16),

$$D_w = 2.98 \times 10^{-6} exp \left(-\frac{17600}{8.314 \times T} \right) \qquad\qquad (2\text{-}16)$$

The increase of diffusion coefficient with temperature is thus quite strong, as displayed in Figure 2-2.
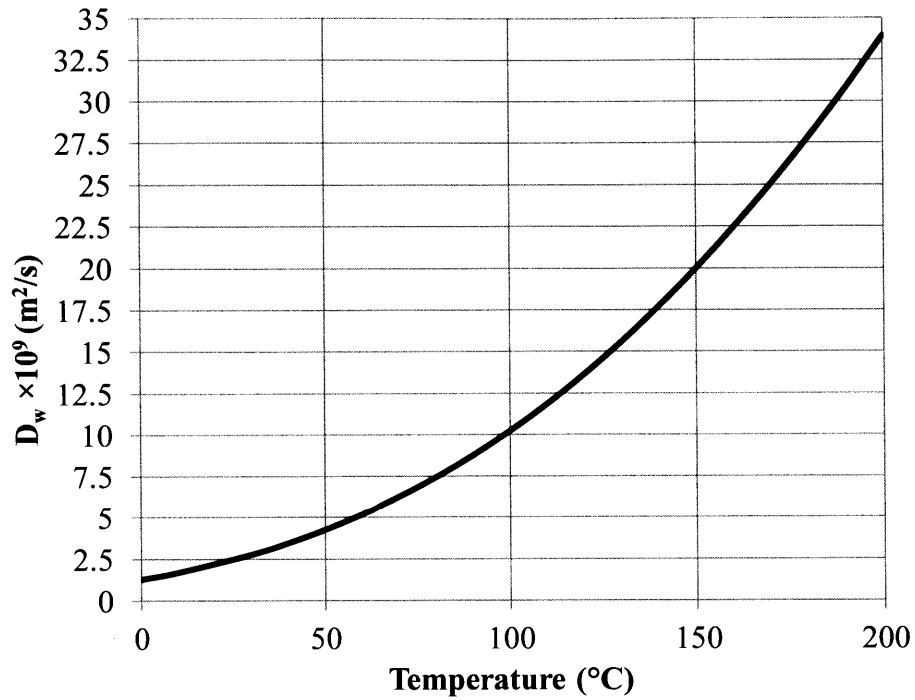
Figure 2-2. Diffusion coefficient of free water vs. temperature.

2.3.2.A. *Summary of mass transfer properties*

Table 2-3 summarizes the suggested mass transfer properties of crystalline basements as discussed so far, along with comparisons against major previous models of deep borehole performance.

Table 2-3. Summary of mass transfer properties of crystalline basement rock for generic use with deep borehole performance assessment.

Parameter	Suggested value or range	Previous measurement or range	Previous model assumptions
Permeability (k in m^2)	10^{-17} to 10^{-16}	(see Table 2-2) 10^{-14} (0-2 km depth)[83] 10^{-17} (6-8 km depth) 3.5×10^{-18} (500 m depth)[94]	10^{-17} [95] Varies with depth[95] 10^{-18} (>500 m depth) [96]
Porosity (ϕ)	0.002 to 0.01	0.0012 to 0.007[78] 0.002 to 0.007[61] 0.002 to 0.003[54] 0.002 [97] 0.006 to 0.01[51] (also see Table 2-2)	0.01 [98] (also see Table 2-2)
Effective rock compressibility (c_r in Pa^{-1})	4.62×10^{-12}	(See Table 2-2)	Not modeled
Diffusion coefficient, rock matrix (D_m in m^2/s)	8.9×10^{-12} to 3×10^{-10}	$<3 \times 10^{-10}$ (UPH) [15] 2×10^{-9} (Mirror Lake) [99] Summarized in [45], [46]	$D=2.8 \times 10^{-10}(\phi)$[100, p. 27]

Note that an uncertainty range of hydraulic diffusivity (and thus permeability) over one order of magnitude is considered reasonable for such large scale characterizations[5] (even if site specific tests and data were available, this might still be true). Thus, it does not seem necessary to apply more detail than this (e.g., detailed permeability functions vs. depth), especially for a generic performance assessment. Porosity can be generically bounded within less than one order of magnitude in range, as seen by comparison with the compilation of measured porosities. As stated before, rock compressibility has never been included in previous deep borehole models, and could have a significant effect on the diffusion of pressure and thus mass transport.

2.4. Heat Transfer

In general, thermal properties are simpler to measure and report compared to the previously discussed hydraulic properties due to the fact that thermal conductivity and density do not exhibit complex "scale" effects. Thus, measurements made in laboratory core samples are much more characteristic of the in-situ values. In addition, they tend to vary much less than hydraulic values (such as permeability), and their variability is likely to be less important to the outcome of

radionuclide transport calculations. However, some thermal properties (such as geothermal gradient) are site specific, and could have an appreciable effect on radionuclide transport (in particular if significant convection is associated with the geothermal heat flux).

Table 2-4. Summary of thermal properties of crystalline basement rock for generic use with deep borehole performance assessments.

Parameter	Suggested value	Previous measurement or range	Previous model assumptions
Density (kg/m^3)	2750	2600 to 2830[78] (UPH, IL) 2600 to 2800[61] (Outokumpu, Finland) 2630[94] (Auriat, France)	2700[95], 2750[98]
Thermal Conductivity $(W/m-°K)$	3.0	2.5 (Auriat, France) [94] 2.93 to 3.47 (UPH, IL) [78] 2.5 to 3.0 (Outokumpu, Finland) [61] 2.6 to 3.0 (KTB, Germany) [101] 3.1 (Climax, NV) [51]	3.0 [98] and [95] 2.6 [96] (SKB) 3.0 [86] 3.6(FEBEX)[102]
Specific heat $(c_p$ in $J/kg-°K)$	790	880[94]	790[98] 790 [95] 780(SKB)[96] 793 (FEBEX)[102]
Geothermal heat flux (mW/m^2)	45	50-80 (KTB) [101] 65 (global continental avg.)[103] 28.4 (North American craton) [104]	45 [95] 40 [87] 60 [86]

2.5. Chemistry

Porewater chemistry plays an important role in determining corrosion rates, radionuclide solubility limits, and fluid density profiles. Parameters for porewater chemical conditions (potential, pH, etc.) for evaluating corrosion in deep boreholes were investigated by Anderson and Dozier at MIT [105], [106]. One current design goal of the deep borehole concept is a greater reliance on passive (geologic) barriers, and less reliance on the performance of engineered barriers[107], such as corrosion resistant packages. As such, rather than focusing on (difficult to validate) models of waste and package degradation, this thesis strives to improve the detail and understanding of a frequently mentioned[108] but as yet uncredited passive geologic barrier: stratified saline pore waters. Pore water salinity has been treated generically with past borehole models[109] and this work contributes by gathering and analyzing realistic site and salt specific data and density effects, respectively. In cooperation with DeMaio [110], an extensive

review of salinity vs. depth and density vs. salinity correlations was completed. The highest quality and most applicable data (for evaluating salinity effects in North American deep boreholes) was obtained from Canadian mines and research facilities [16], [111], [112], most of which are within ~200 km of the U.S. border. Based on this data, a generically applicable (with uncertainty) density vs. depth profile is obtained by combining the best fit (polynomial) for total dissolved solids (TDS) vs. depth (>344 m) shown in Eq. (2-17) with the density vs. TDS relation shown in Eq. (2-18),

$$TDS \left[\frac{mg}{l}\right] = 0.1234 \times \left(Depth\ (m)\right)^2 - 59.42 \times Depth(m) + 5844.6 \tag{2-17}$$

$$\rho \left[\frac{kg}{m^3}\right] = (7.08 \times 10^{-4} \pm 1.5 \times 10^{-4}) \left(TDS \left[\frac{mg}{l}\right]\right) + \rho_{ref} \tag{2-18}$$

where ρ_{ref} is a reference density at the temperature and pressure evaluated by other means (e.g., numerical lookup tables, existing correlations). Thus, this assumes that the effects of salinity can be treated separately from temperature and pressure, which is typical in numerical models[113] . Equation (2-17) begins with non-negative TDS values starting at a depth of 344 m and is valid to 1930 m, where a TDS of 350 g/l is reached (the highest values of salinity seen in the borehole studies considered). Although salt saturation would not be reached until ~3700 m, the density is conservatively assumed to stay constant at $\rho(kg/m^3) = \rho_{ref} + 200.44 \pm 53.88$ for depths below 1900 meters. Uncertainty bounds in Eq. (2-18) are created by model variations for salinity vs. density. Figure 2-3 shows other methods of evaluating saline water density by Kukkonen[114] and Millero[115] and curve fits (exponential, power) to the Canadian shield data, compared to the proposed curve[110] (generated by Eq. (2-17) and Eq. (2-18)).
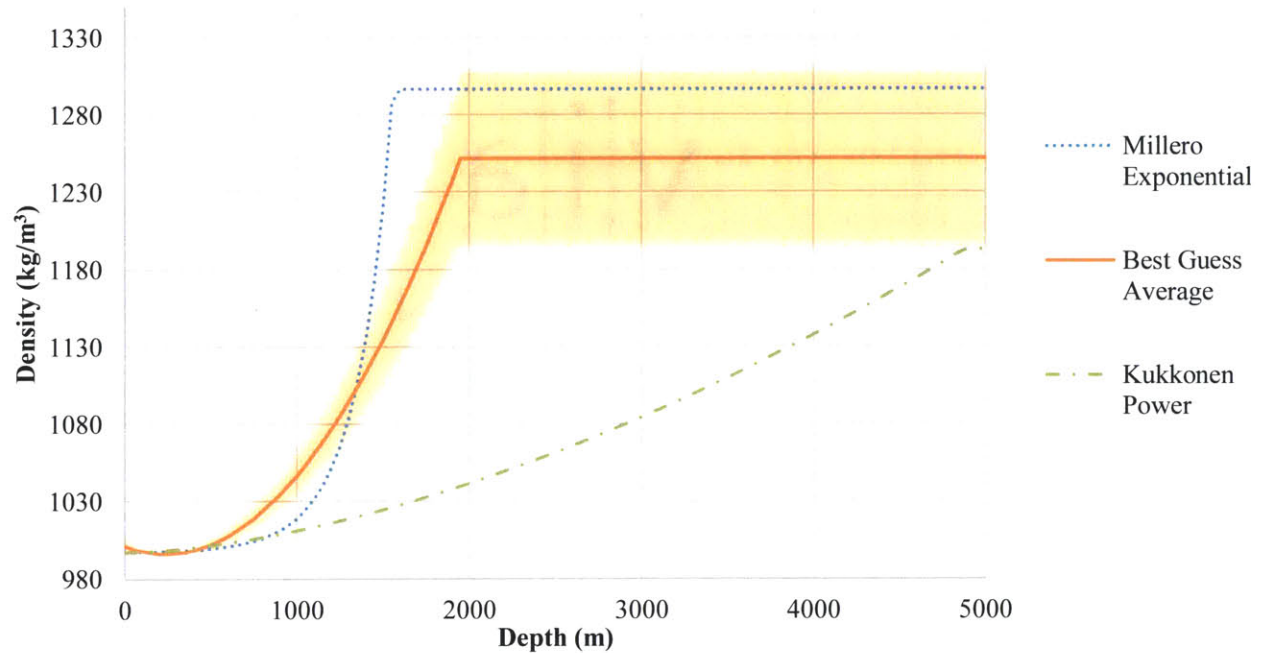
Figure 2-3. Maximum, minimum and best guess density vs. depth curve[110], created by curve fitting (exponential, polynomial, power) and salinity vs. density modeling variations (e.g., models by Kukkonen[114] and Millero[115])

2.6. Previously studied deep boreholes in the U.S.

Existing databases created by the oil and gas industry could provide additional and valuable site specific data, prior to drilling a test borehole. Figure 2-4 shows the locations of oil and gas wells through the U.S., developed through 2005.
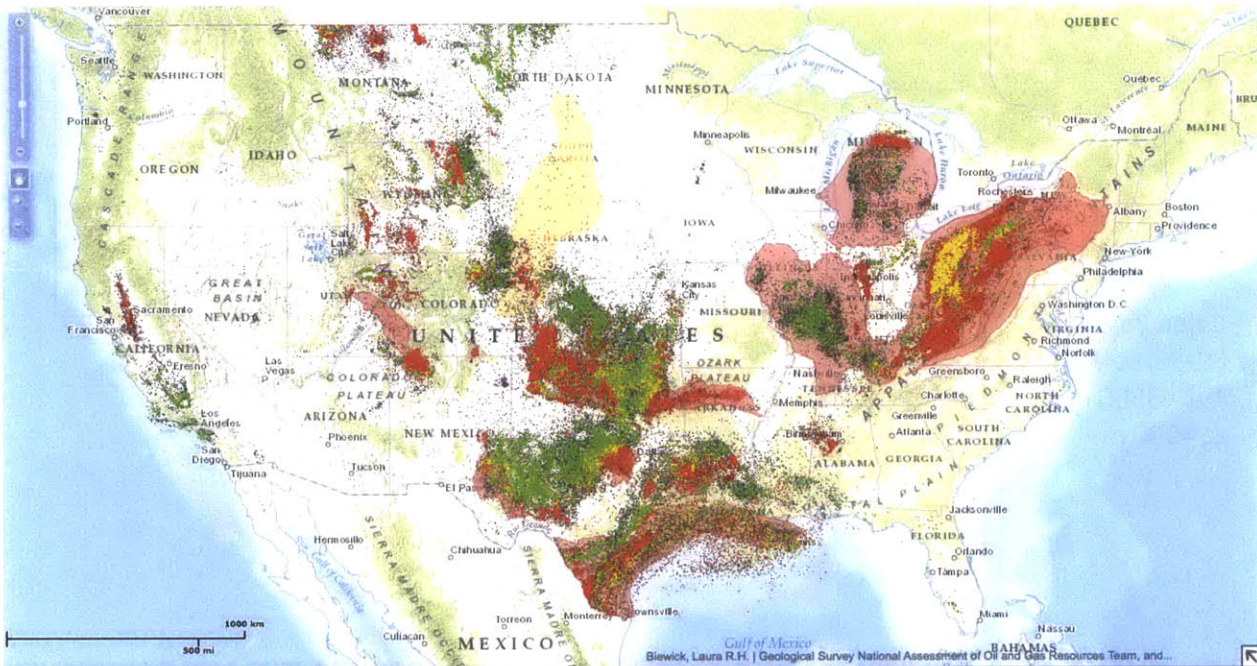
Figure 2-4. Locations of historical oil (red dots), gas (green dots) oil and gas (yellow) and shale gas (shaded regions) development in the U.S., through 2005/2006 [116].

In addition to the vast amount of data produced by the oil and gas industries, there are a few very well studied (and more relevant) boreholes drilled into the basement rock in the United States Figure 2-5 summarizes the locations and important properties of these boreholes.
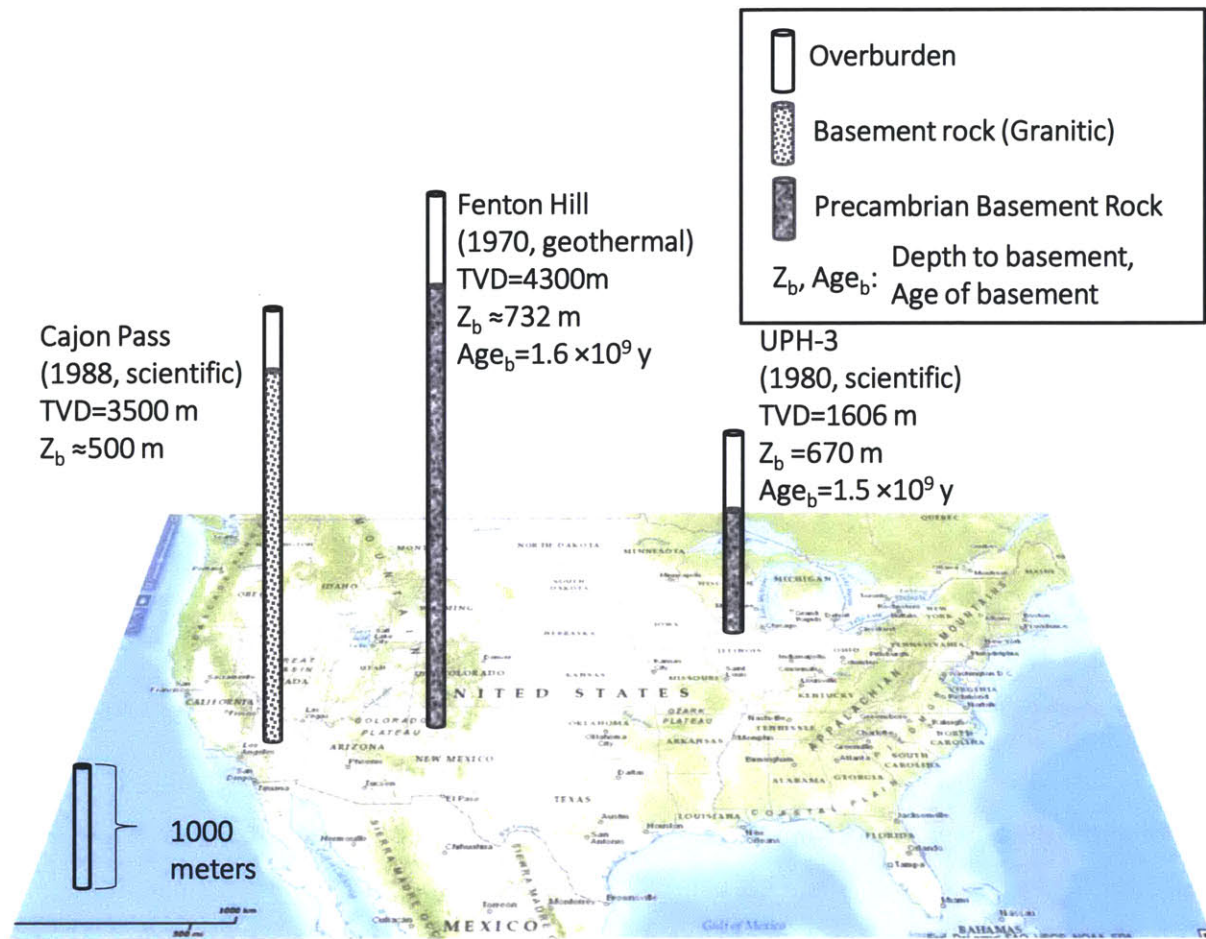
Figure 2-5. Locations of important scientific boreholes drilled in the U.S. Underlying map is tilted (and distorted) to allow for comparison of borehole depths and approximate locations [116].

The Cajon Pass scientific drill hole (far left of Figure 2-5) penetrated 3.5 km into basement rocks of low permeability granites and granodiorites near San Bernardino, California; 4 km from the San Andreas fault. An overview of the geology at the Cajon Pass drill hole is given by Zoback et al [117] and Silver and James[52]. A number of important heat flow and mechanical studies were documented [49], [62], [118], [119], but because of the proximity to a major fault and regional seismic activity, it would likely be ruled out as a suitable site for deep borehole disposal.

The Fenton Hill scientific drill hole (center of Figure 2-5), was drilled in the 1970's at the onset of enhanced geothermal system (EGS) feasibility studies. In EGS, low permeability, high temperature crystalline rock formations are stimulated (via pressure injection) to allow for extraction of deep geothermal heat. Of all the boreholes in the U.S., the Fenton Hill drill hole

penetrated the deepest into the Precambrian basement (~3.5 km), and the borehole was also very well studied and provided valuable insights into the mechanical and hydraulic behavior of basement rocks.[24], [120]. Due to the large geothermal gradient and high temperatures, this site is also not fully representative of what would be used for deep borehole disposal.

2.6.1. UPH-3 borehole

To evaluate the feasibility of underground pumped hydroelectric (UPH) storage, Commonwealth Edison drilled three deep boreholes UPH-1, UPH-2 and UPH-3 (0.6, 1.6 and 1.6 km total depth, respectively) into the Precambrian basement[26], as shown on the right of Figure 2-5. Cores were obtained from all holes and fortunately the UPH-3 hole was not sealed at the end of initial tests and was converted into a project that yielded many scientific studies improving knowledge of the basement geology[55], [48], [60], [121] . Borehole scale permeability [53], diffusion coefficients [15], stress history and formation [55], [77], [122], thermal conductivity, mineralogy [78], and pore fluid composition [123] were extensively measured. The site is part of the North American craton (connected to the Canadian Shield, but overlain by younger sediments), and exhibits favorable rock stresses (not critically stressed) and relative tectonic stability [53].

The Illinois basin (in which the UPH holes were drilled) and the shallow subsurface has also become understood as a result of studies of water resources [124], oil and gas exploration[36], and more recently CO_2 sequestration tests and evaluations[25]. Precambrian rocks occur at depths from 610 m (2000 ft) in the northernmost part of Illinois to more than 4300 m (14,000 ft) below the surface in the southern part of the Illinois Basin.

Figure 2-6 and Figure 2-7 show vertical and cross sectional maps of the basement topology of the northern region of the basin, as obtained from UPH[26] and regional aquifer studies [124].
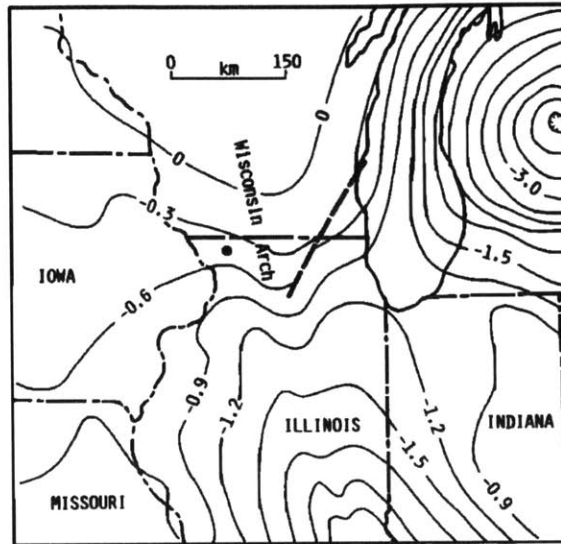
Figure 2-6. Depth to Precambrian basement for region surrounding the UPH holes (signified by the black dot). Numbers give elevation in km relative to sea level [26].
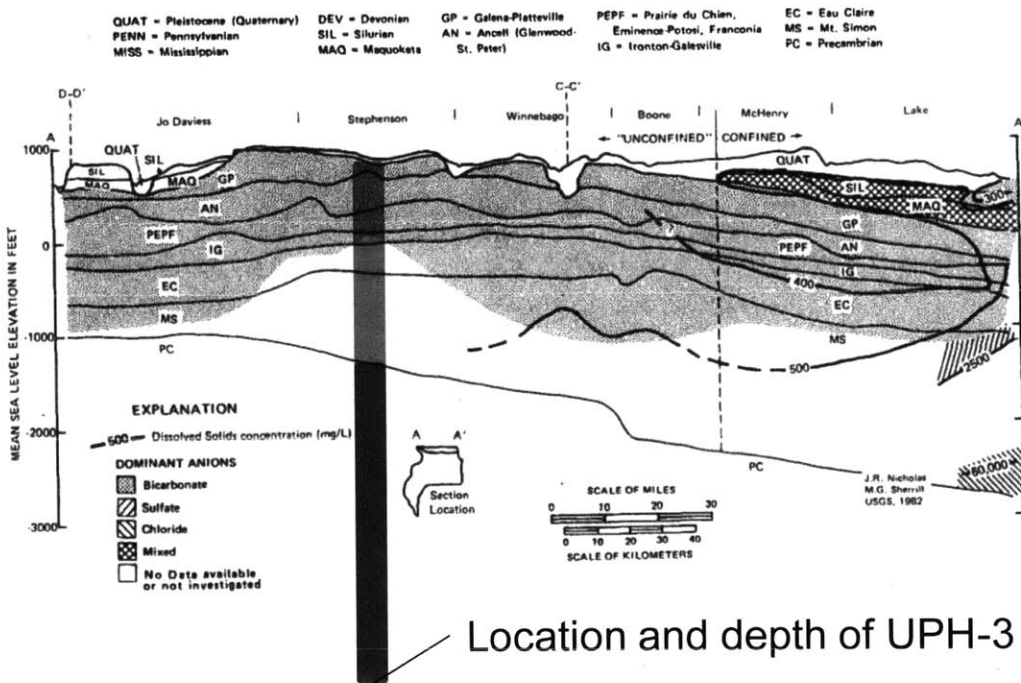
Figure 2-7. Cross section of geology and pore fluid chemistry of the overlying saline aquifers and Precambrian basement in Northern Illinois. Modified from [124]. The approximate location and depth of the UPH-3 borehole in Stephenson county is shown.

Note that the surface elevation is ~300 meters above sea level. The lithologic profile shown in Figure 2-7 is consistent with that measured at the UPH-3 borehole [26]. Precambrian basement highs (i.e., in the northern area where UPH holes were drilled) have been avoided by oil and gas

prospectors (see Figure 2-5). This area would also be avoided by prospective CO_2 injectors because a high Precambrian basement reduces the thickness of overlying Mt. Simon sandstone (hence, capacity of CO_2) and because CO_2 must be injected at a depth >700 m to be supercritical. A low permeability and confining unit called the Eau Claire formation (EC) (composed primarily of a shale and siltsone in northern Illinois) overlies the Mt. Simon sandstone [36] and forms the basal bedrock immediately adjacent to the crystalline basement. The top of this basal bedrock is approximately at sea level. Above the sealing Eau Claire (EC) layer, the Ironton-Galesville aquifer has low dissolved solids concentrations, very large permeability, and short travel times for water moving from the recharge area compared to other Cambrian and Ordovician aquifers in the areas (e.g., those located further east) [124]. By combining all the data obtained from the UPH-3 studies and CO_2 modeling efforts, it is possible to obtain a detailed and realistic description of the UPH-3 site, as presented in Table 2-5. The large heterogeneity of and layers in the aquifer above the basal bedrock may not need to be explicitly modeled (a simplification used by CO_2 sequestration modelers[25]). The aquifer behavior could be captured in a biosphere and uptake model which can be developed in the future using existing detailed data on the aquifers [124] (but this may also depend on currently non-existent regulations and standards for deep borehole facilities).

Table 2-5. Detailed geologic, thermal, hydraulic, and chemical description of the UPH-3 borehole site.

Depth (m)	Formation	Graphic	Permeability (m²)	Porosity	Rock compress.	Diffusion coefficient (m²/s)	Density (kg/m³)	Thermal conductivity (W/m- °K)	Temp. gradient and heat flux	Specific heat (J/kg- °K)
304	Ironton/ Galesville aquifer and others (limestone, sandstone)								$T=12.5°C$ /km [26]	
399	Eau Claire (Shale, siltstone)		10^{-18} [5]	15% [5]	$\beta_r=7.42\times10^{-10}$ [5] w/Eq. (2-9)	2.05×10^{-10} Eq. (2-13)*	2530 [121]	1.5 [125]		1047 [121]
663	Mt. Simon (Sandstone)		5×10^{-13} [5]	17% [5]	$\beta_r=3.71\times10^{-10}$ [5] w/Eq. (2-9)	2.4×10^{-10} Eq. (2-13)	2480 [121]	4.5 [125]		1255 [121]
1607	Precambrian basement (crystalline rock)		2.7×10^{-17} [53] Max. value obtained from a pulsed packer test over entire interval.	0.37% [15] Avg. value of core samples over interval	$c_r=4.62\times10^{-12}$ w/Eq. (2-10) See Table 2-2	$<3\times10^{-10}$ [15]	2750 [78]	3.31 [78] Avg. value of core samples over interval.	Heat flux= 75 mW/m² [26]	880 [121]

*Diffusion coefficient in shale is conservatively high, calculated using Eq. (2-13), not accounting for clay.

In addition to rock properties summarized in Table 2-5, pore fluid chemistry data are available from the UPH-3 borehole studies conducted by Couture and others [15], [123]. The pore fluid is primarily NaCl, with a Ca/Na ratio of 0.05 to 0.1 [123], and salinity increases with depth, up to concentrations of 2.4 M Cl⁻ for the deepest core samples. Using a Ca/Na mol ratio of 0.075 and converting from molar concentrations to mass concentrations, it is possible to compare the Illinois data with the generic TDS vs. depth curve fit previously discussed in Section 2.5. Figure 2-8 compares the generic fit with the site specific data.
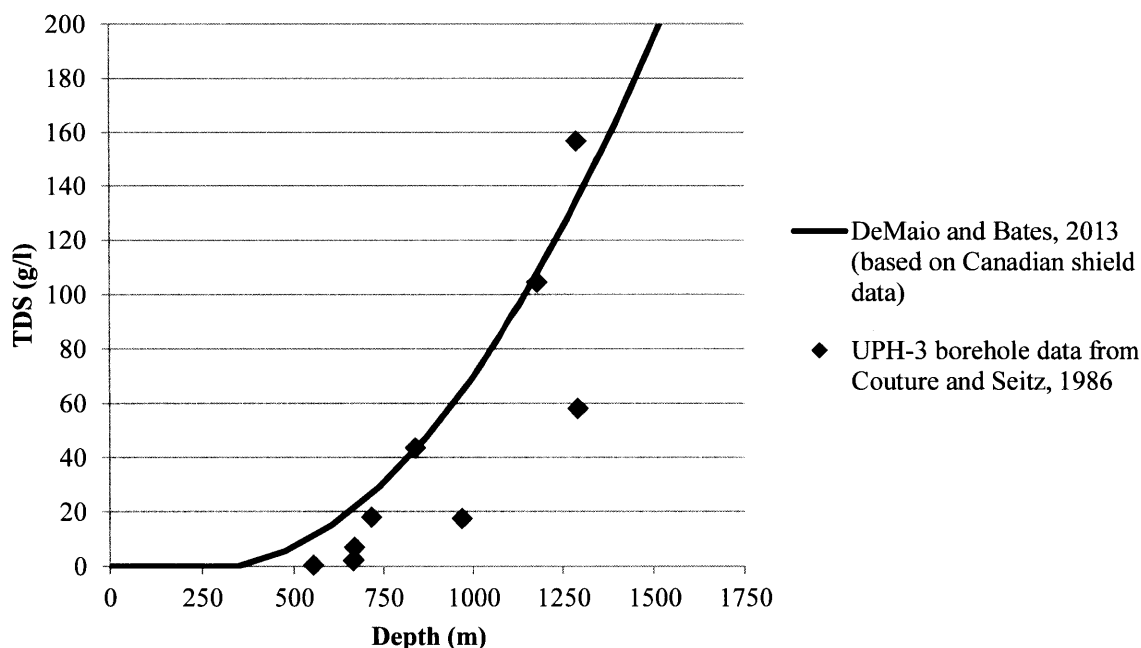
Figure 2-8. Comparison of generic salinity vs. depth curve [110] Eq. (2-17) with the site specific data obtain from UPH-3 core samples [123].

The good fit between the site specific data and the generic model (which was developed independently from the UPH-3 data) supports the validity of the generic model for the North American craton (and suggests that it may be used for a UPH-3 site specific evaluation as well). The closeness suggests that salinities in relatively proximate deep North American craton sites tend to have similar depth dependencies.

2.7. Mechanical

Continental cratons have not experienced major tectonic disruptions over a timescale of ~1 billion years, and by definition, have attained stability (e.g., not deformed) since the Precambrian period [126]. Tectonic disruptions and fracturing are typically associated with pathway creation for fluid and chemical transport [87]. It is thus important to understand the mechanical processes, forces, and limits, that could potentially cause faulting or permeability increases at a DBD site. Mechanical stresses significantly affect the feasibility and performance of deep borehole disposal, specifically in terms of the:

1. Effect of stresses on the drilling process and cost, as discussed in [127].

2. Effect of stresses on long-term rock behavior and parameters (in particular, surrounding the borehole plug).
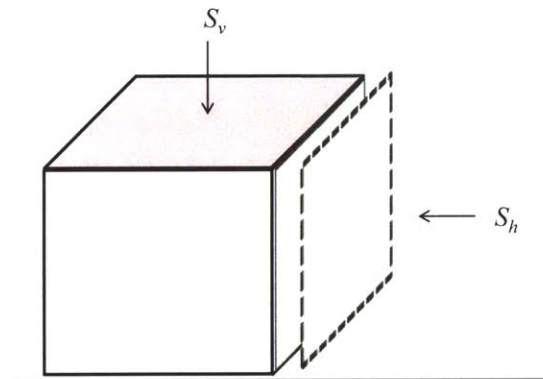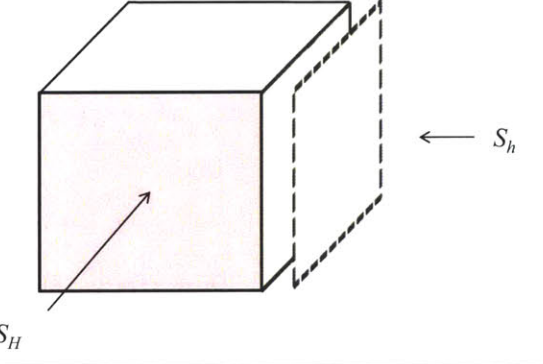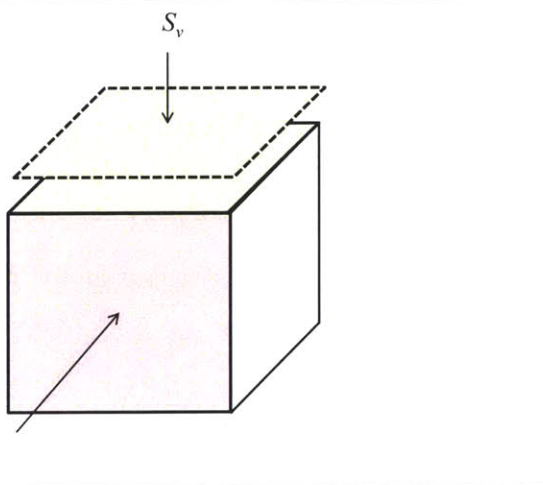
A few modeling efforts of deep boreholes have accounted for mechanical effects [128], [129]; however, they did not establish or use realistic stress profiles (i.e., consistent with preexisting data). Extensive stress field data are available from crystalline rock boreholes drilled in France (Soultz), Germany (KTB), and the USA (Cajon Pass, Monticello Reservoir), Canada and Sweden. In a previous paper [127], based on the most relevant data, values of stress fields and rock strength properties were proposed for generic assessment of deep borehole disposal. Vertical principal stresses (S_v), minimum horizontal stresses (S_h) and maximum horizontal stresses (S_H) are summarized in Table 2-6.

Table 2-6. Summary of estimated stress profiles developed for basement rocks from borehole data in Germany, U.S. and Canada (where Z is depth in km).

Description	Rock Type	Regime	S_h (MPa)	S_H (MPa)	S_V (MPa)
Data applicable from deep borehole studies					
KTB Borehole Data [130], 3-7 km	Crystalline basement, amphibolite,	SS	20Z	45Z	28Z
KTB Borehole Data, [131] 3-7 km	(Same as above)	SS	-20+22.5Z	92+22.8Z	27.7Z
Canadian shield, [132] 0-2.1 km	Precambrian basement	RF	5.37+30Z	10.08+41Z	26.5Z
UPH-3 borehole 0.6-1.6 km [53]	Precambrian basement	RF, SS at 1.4 km	8.7+19Z	20.5+23Z	-1.3+26Z
Models					
Bates et. al, 2014 0-5 km[127]	Granite	SS	23.2Z	43.1Z	27.5Z

The principal stresses govern how the rock responds to pore fluid pressure changes[85], [133], which occurs due to fluid pumping and injection (as in the case of CO_2 sequestration or liquid waste disposal) or fluid thermal expansion (as in the case of nuclear waste disposal). The faulting regime and failure mode is determined by the relative magnitude of the principal stresses in the rock. Table 2-7 depicts conditions and planes of slipping possible for each of the three faulting regimes.

Table 2-7. Description of normal, strike slip, and reverse faulting regimes.

Faulting regime	Relative magnitude of principal stresses	Failure plane during pore pressure increase
Normal (NF)	$S_h \leq S_H \leq S_v$	
Strike Slip (SS)	$S_h \leq S_v \leq S_H$	
Reverse (RF)	$S_v \leq S_h \leq S_H$	

Drilling data suggests that in general, the upper crust is at or close to a state of failure equilibrium [85]. In other words, a (purely) frictional force between preexisting faults is in equilibrium with the maximum and minimum principal stresses. This is based on the assumption that faults have no cohesive strength[134] and that a fault preexists as a plane along which failure is most likely to occur (i.e., the plane orthogonal to the minimum principal stress). An important outcome at sites satisfying failure equilibrium is that continual faulting and fracturing (on small scales) causes the permeability to remain relatively high (10^{-16} to 10^{-17} m^2), and thus pore pressures do not build up significantly above the hydrostatic pressure. There are sections of the crust or particular seismically stable sites where the rock is not at failure equilibrium (or faults are not oriented in the optimal direction[95]), it is possible for the pore pressure to build up significantly above hydrostatic without failure and permeability increase occurring [130]. The threshold for frictional failure [134] is described by Eq. (2-19),

$$\frac{(S_{max} - P_p)}{(S_{min} - P_p)} \leq \left[(\mu^2 + 1)^{\frac{1}{2}} + \mu \right]^2 = F_c \qquad (2\text{-}19)$$

where S_{max} and S_{min} are the maximum and minimum principal stresses, respectively, P_p is the pore fluid pressure, μ is the coefficient of friction (varying between 0.6-0.8), and F_c is a frictional failure criterion constant (varying between 3.1- 4.3, respectively) . Intuitively, the lower the assumed coefficient of friction, the easier it is to induce frictional slipping/failure. The terms may be reorganized to obtain an upper bound on the pore pressure that precludes frictional/seismic events (and thus prevents significant increases in permeability and flow), as shown in Eq. (2-20),

$$P_p < \frac{F_c S_{min} - S_{max}}{(F_c - 1)} \qquad (2\text{-}20)$$

Another proposed limit on pore pressure (actually imposed by the EPA on companies injecting fluids into subsurface formations) is based on the fracture opening/closure pressure[135]. The regulation states that the maximum injection (pore fluid) pressure should be less than the measured fracture closure pressure (FCP), as determined through principal stresses. The (FCP) is equivalent to the minimum principal stress [134] (which may either be the vertical stress S_v or

the minimum horizontal stress S_h). If pore pressure exceeds the FCP, a fracture opens and conducts flow in a plane perpendicular to the least principal stress. Thus, just as with the frictional failure described in Table 2-7, when S_v is the minimum stress, fractures occur in horizontal planes. When S_h is the minimum stress (corresponding to a normal faulting or strike slip regime), the fractures occur in vertical planes. Ideally when the regulation is satisfied, existing fractures cannot open and no new fractures can form, and no additional migration of waste fluids out of the injection intervals occurs [88]. In general, the maximum pore fluid pressure gives a measure of the seismic stability of a site and the ability of a site to store injected fluids without compromises in permeability. Figure 2-9 shows the maximum pore fluid overpressure as calculated by two failure criteria (frictional failure and fracture closure), for the generic stresses proposed in Table 2-6 [127].
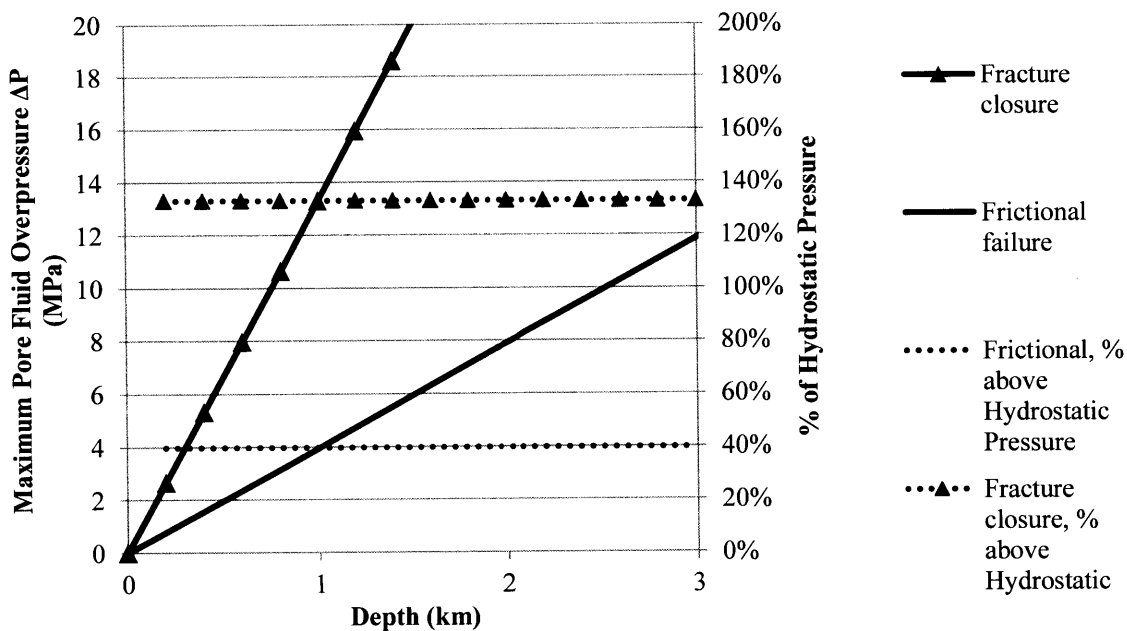
Figure 2-9. Comparison of maximum pore fluid pressures obtained through different failure criterion using the generic stress profile from [127]. Frictional failure assumes a coefficient of friction of 0.6, while FCP is equal to S_h.

The maximum allowable pore overpressure (i.e., P_p-P_{hydr}) can be expressed as a percentage of the hydrostatic pressure (P_{hydr}). In this particular case, since all of the stresses and failure criteria increase linearly with depth, the percentage is a constant. These percentages are indicated by the

right vertical axis and dotted lines in Figure 2-9. Clearly, the FCP (133% of hydrostatic in this case) is would be a much less stringent limitation than the frictional failure limit (40% of hydrostatic). This is expected, because the frictional failure assumes that a favorably oriented fracture pre-exists, while the fracture closure pressure assumes that the injection pressure creates a new fracture. This analysis indicates that using the generic stress profiles, pore overpressures of 4-10 MPa could be safely be sustained between the depths of 1-3 km (i.e., 40% of hydrostatic) without adverse slipping along existing fractures (i.e., seismic events). A similar analysis may be applied to the site specific data from the UPH-3, as shown in Figure 2-10.
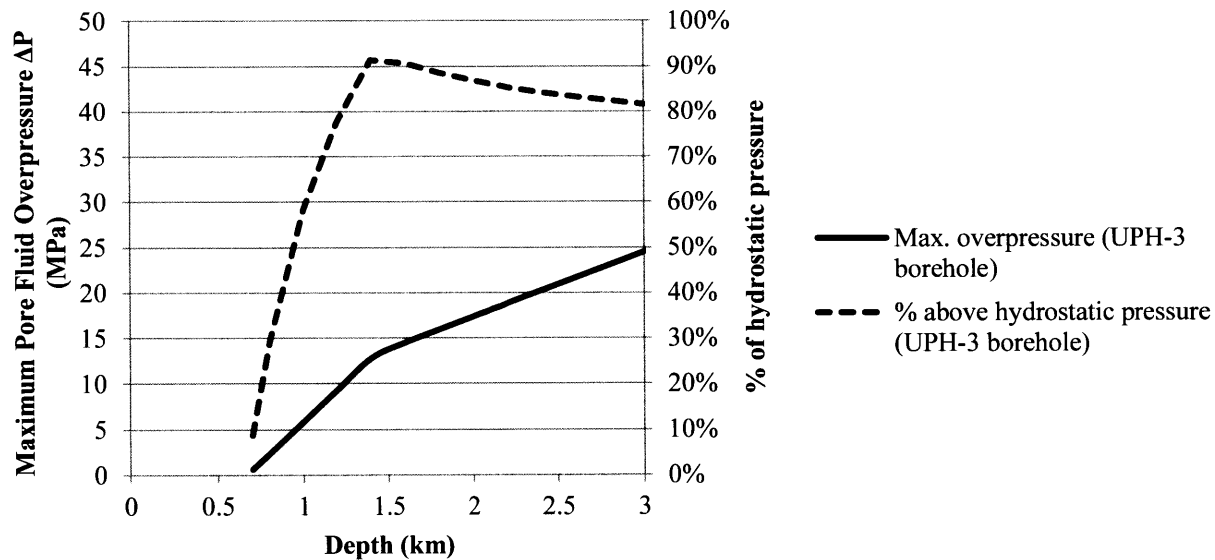
Figure 2-10. Maximum pore fluid pressures vs. depth (0.7-3 km) obtained through frictional failure criterion using the site specific UPH-3 stress profile from [127]. Frictional failure assumes a coefficient of friction of 0.6.

Note that the shift in slope at 1.4 km is due to a change in the regime from strike slip to a reverse faulting. At this particular site, only the top of the granite interval (at 700 m) would be close to a critical stress (assuming a coefficient of friction as low as 0.6, although previous authors expected it to be 0.85) [127]. Using the calculated maximum pore overpressure at 700 meters (0.6 MPa), we obtain a conservative frictional failure pressure gradient of 0.85 MPa/km, or ~8.5% of hydrostatic. This frictional failure gradient is similar to that derived by Zhang et. al.

58

who concluded that pore pressures greater than 0.7-1.5 MPa at crystalline basement rock depths of 1-4 km would induce mechanical failure. Note that since rock is in a strike slip regime at that depth, the preexisting fracture planes would have to be oriented vertically to favor such a failure mechanism.

Note that at the adjacent, shallower depths (<600 m), the host rock is composed primarily of Mt. Simon sandstone and shale, which according to the EPA has a failure limit determined by an FCP (overpressure) of 0.57 psi/ft [135] (12.8 MPa/km) which is >100% of the hydrostatic pressure. An extremely high, sustainable pore pressure (along with higher porosity of sandstone) is the fundamental basis for CO_2 sequestration (discussed more in Appendix B.2). The effects of simultaneous mechanical failure in the (underlying) crystalline basement have only recently been considered important in CO_2 sequestration evaluations [136].

2.8. Chapter Summary

This chapter attempts to resolve the issue that deep borehole performance, modeling and optimization cannot fully begin unless the problem and reference properties are clearly defined. It begins with a brief summary of site characterization techniques, their working principles and limitations. Due to the scale dependence of many parameters, the most applicable and relevant data comes from large scale, in-situ experiments, calibrations to numerical models, or isotope analysis. Overall, a simplistic criteria of obtaining minimum permeability (e.g., $<10^{-18}$ m^2) host rock on a reservoir scale (~1 km) is probably not realistic or even desirable (as it tends to increase both characterization time and the potential for excessive pressurization and geomechanical damage).

Mass transport via advection is cast in terms of hydraulic diffusivity, instead of permeability and porosity, which on their own do not fully capture the poroelastic behavior of the rock. The governing equations indicate that at very low porosities (<0.01), rock compressibility (in addition to water compressibility) determines hydraulic diffusivity and thus transport of pressure and mass. Therefore rock compressibility is a key parameter that should be included in future deep borehole performance models, especially ones that include domains with closed boundaries in which pressure buildups occur.

In the second portion of the chapter, highly detailed reference parameters for thermal, hydrologic, and chemical of modeling deep boreholes (both generic and site specific) are

presented. The site described here (UPH-3 borehole) was chosen on the basis that it is the most well characterized deep crystalline rock in the U.S. to date (in a seismically stable region). The goal of presenting specific site properties is to facilitate more realistic estimates for the performance of deep boreholes.

2.9. Future Work

On the basis of hydraulic diffusivity, a number of interesting methods to improve borehole confinement assurance could be investigated. One involves increasing the hydraulic diffusivity in a controlled manner (e.g., fracking), or deliberately searching for sites in which the expansion of pore fluids occurs into a desired location. In fact, the UPH-3 borehole site might present these properties and behavior, with a high hydraulic diffusivity layer of sandstone above the Precambrian basement, sealed from groundwater by a (low hydraulic diffusivity) layer of shale. The other possibility is to initially depress pore pressures by initially extracting pore fluids, such that microseismicity is not induced by the pore pressure volume increase created by the decay heat of the waste.

In addition, the discrepancies between poroelastic modeling approaches should be addressed-the basic question apparent in Eq. (2-8) and Eq. (2-9) is whether rock compressibility is affected by porosity.

3. Reference Design

3.1. Chapter Introduction

This chapter reviews the reference deep borehole disposal facility design, which serves as the starting point for evaluating performance and design variations. A major emphasis of this chapter is on evolutionary improvements to key engineered components of the system, such as the plug design, gap filler, and canister design. Other modifications to the reference borehole design, such as disposal depth, disposal zone length, and borehole spacing, may only be justified with radionuclide release and economics estimates, and are thus discussed after the transport and performance models are presented in Chapter 4.

3.2. Plug Design

The materials that seal the borehole above the waste disposal zone comprise what is perhaps the most important engineered barrier in deep borehole design. The purpose of the plug is to prevent vertical fluid transport through the borehole, which can occur through thermal expansion driven mechanisms. Concerns about plug performance originate from the consideration that the borehole seal is the shortest pathway from the nuclear waste to the biosphere, and the intruding fluids (directly from the disposal zone) would contain the highest concentrations of radionuclides. Section 3.2 summarizes the key improvements to plug design [137] that have been developed during this thesis.

3.2.1. Plug bypass routes

A key finding of [137] is that gaps and cracks in the plug (developed via chemical and/or mechanical means) provide preferential flow paths to the surface, thereby compromising the leak-tightness of the system. Thus, although the plug material may have extremely low bulk permeability, the overall or effective permeability of the plug may be orders of magnitude higher if a gap or crack develops between the plug and borehole wall. Figure 3-1 shows the relevant hydraulic and geometric parameters of an idealized annular gap between a borehole plug and a borehole wall.
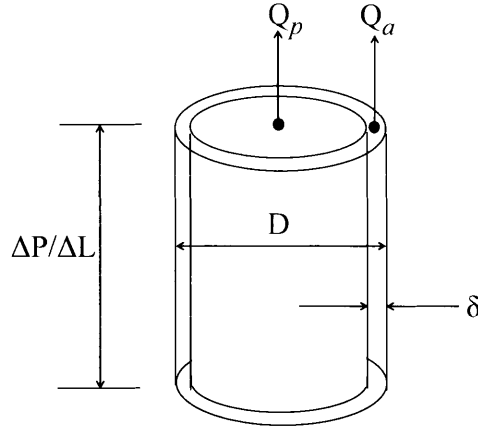
Figure 3-1. Description of fluid flow through an annular gap with thickness δ around a porous plug in a borehole with diameter (D)

The total flow through the gap Q_a is given by Eq. (3-1),

$$Q_a = \frac{\pi}{12} \frac{D}{\tau_{or}} \frac{\delta^3}{\mu} \left(\frac{\Delta P}{\Delta L}\right)$$

(3-1)

where D is the borehole diameter and τ_{or} is the assumed tortuosity of the flow path (~1-2). When the gap size (annular or cylindrical) is larger than a few microns and the bulk permeability of the plug is very low (10^{-18} m^2), the total flow through the plug region is dominated by Q_a (annular gap flow rates), as opposed to Q_p (the bulk porous plug flow rate). In this case, the effective permeability of the failed plug zone may be calculated from the properties of the gap alone. The effective permeability ($k_{eff,a}$) of the annulus-plug system (where the area for Darcian flow is defined by the entire plug) in this case has been derived to be Eq. (3-2) [137] ,

$$k_{eff,a} = \frac{\delta^3}{3D_p\tau_{or}}$$

(3-2)

Figure 3-2 shows the effective permeability of the plug vs. the annular gap size.
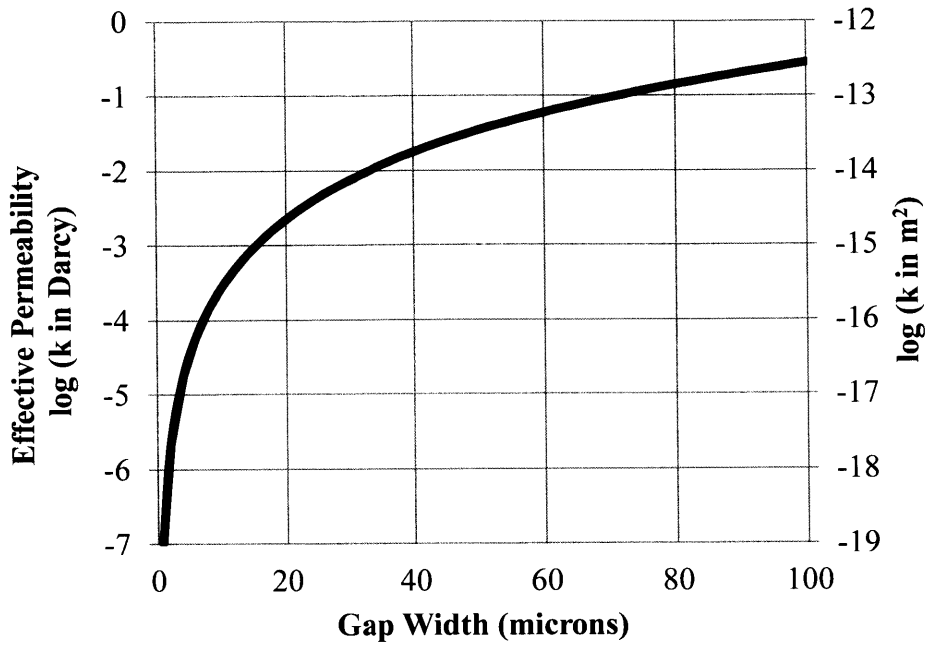
Figure 3-2. Semi-log plot of the effective permeability of a plug vs. annular gap width, for a plug diameter of 0.6 m and tortuosity of 2.

Even for gaps that are only 20 μm in size, the effective permeability is $2.22 \times 10^{-15} \, \text{m}^2$, which is an order of magnitude higher than the upper bound permeability of the host rock ($10^{-16} \, \text{m}^2$). Assuming that the plug and host rock are subjected to an arbitrary vertical pressure gradient across the plug length ($\Delta P/L_p$) allows for some instructive comparisons to be made. The advection velocity in a porous plug (v_p) is the Darcy velocity (v_D) divided by the porosity, and is written as Eq. (3-3),

$$v_p = \frac{v_D}{\phi_p} = \frac{Q_p}{A_p \phi_p} = \frac{k_p \Delta P}{\mu \phi_p L_p}$$

(3-3)

where Q_p is the volumetric flow rate (m^3/s) ϕ_p is the plug porosity, k_p is the plug permeability, A_p is the total area of the plug, and μ is the dynamic viscosity of the fluid. For a plug with an annular gap, the gap advection velocity (v_a) is written as (3-4).

$$v_a = \frac{Q_a}{A_a} = \frac{\dfrac{\pi}{12}\dfrac{D}{\tau}\dfrac{\delta^3}{\mu}\left(\dfrac{\Delta P}{L_p}\right)}{\dfrac{\pi}{4}(4D\delta)} = \frac{\delta^2 \Delta P}{12\mu\tau_{or}L_p}$$

<div align="right">(3-4)</div>

The time required to traverse the plug (e.g., reach the surface) is calculated by dividing the total distance (L_p) by the advection velocity. The results for an ideal case and two other cases representative of a plug (highly porous or with an annulus creating the same effective permeability) are shown in Table 3-1.

Table 3-1. Comparison of advective transport times (t_v) for various plug conditions.

Case	Permeability (m^2)	Flow area (m^2)	t_v (in years) for L_p= 2 km	t_v (in years) for L_p= 3 km
A) Ideal plug, ε=0.4	k $\leq$1×10^{-16}	A$_p$=0.113 (Superficial)	$\geq$1.68 million	$\geq$3.71 million
B) 1μm crushed rock, ε=0.4	k =5×10^{-16}	A$_p$=0.113	338,000	761,000
C) Impermeable plug δ =9.56 μm, τ=1	k$_{eff}$= 5×10^{-16}	A$_a$=1.82×10^{-5}	54	122

*D$_p$=0.6 m, ΔP=0.3 MPa, μ=10^{-3} Pa-s

The key conclusion from Table 3-1 is that when gap flows are compared to bulk porous flow, for an equal effective permeability (and thus volumetric flow rate) the extremely small flow area of an annular gap increases the velocity and significantly reduces the travel time from the disposal zone to the surface. This clearly demonstrates that small gaps and fractures could pose a threat

to deep borehole confinement assurance; however, a much more detailed analysis of these contrasting bulk and crack transport phenomena are presented in the following chapters.

3.2.2. Proposed plug materials

To prevent gaps from developing, a number of plug materials were investigated and proposed. The first major change is the addition of a cement with MgO additive which expands upon curing, thereby preventing gaps due to shrinkage[137]. Table 3-2 shows the expansive concrete formulation.

Table 3-2. Expansive concrete formulation[137]

Ingredient	w/o	Properties (density)	Average particle size (μm)
Portland cement	31	3.15	8
Fine sand	20	2.20	300
MgO (powder)	26	3.58	75
Water	23		
	100		

The second change is the use of crushed rock mixtures, which are more likely to remain malleable and capable of deforming to close gaps as they may form over time, compared to solidifying materials such as cements. Crushed host rock should be available from drill cuttings, maintains favorable reducing chemical conditions[138], and provides the plug with the demonstrated radionuclide sorption properties associated with the host granite[91]. Although a porous bed may have a higher bulk permeability than typical cements, it is likely to maintain that permeability with greater confidence because of its malleability. From the arguments outlined in Table 3-1, it is also apparent that the higher porosity of a bed proportionally reduces the transit velocity and time to the surface. As for the permeability, a modified form of a correlation for permeability vs. crushed granite particle size [139] from the literature is shown as Eq. (3-5) [137],

$$k = 7.7 \times 10^{-3}(d_{g,10})^{2.5}$$ (3-5)

Overall, the extensive review of data on sealing materials and experiments completed on the expansive cement[140] at MIT allow us to estimate bounds on the permeability that the deep borehole plug may have, as shown in Table 3-3.

Table 3-3. Summary of hydraulic data on proposed plug materials.

	Description	Permeability range	Tested conditions	Ref.
MgO based expansive cement	See Table 3-2	3×10^{-19} - $1.5\times10^{-17}\,\text{m}^2$	Up to 120 °C, pure water	[140]
Crushed granite (e.g., drill cuttings)	1 μm particle size, assuming 40% porosity	7.7×10^{-18} - $5\times10^{-16}\,\text{m}^2$	Based on flow path tortuosity, likely to be independent of temperature, salinity.	[141][139] see Eq. (3-5)
Clay/crushed rock mixtures	60/40 palygorskite* bentonite mixture	1.78×10^{-18} to 2×10^{-18}	0-10% (1.8 M) NaCl	[142]
	30/70 bentonite crushed rock mixture	10^{-19} to 10^{-18} m^2	Pure water	[143]
	*Sepiolite-soil mixtures (25/75)	$10^{-16}\,\text{m}^2$	Pure water	[144]

*Palygorskite and sepiolite are the same group of clays[145]

Overall, the data summarized in Table 3-3 suggest that 30/70 clay and crushed rock mixtures and expansive cements should readily achieve a permeability of $10^{-16}\,\text{m}^2$, with $10^{-18}\,\text{m}^2$ being a design goal that could be justified with further experiments that are more representative of deep borehole conditions. The updated design of the borehole plug [137] is shown in Figure 3-3.

Surface
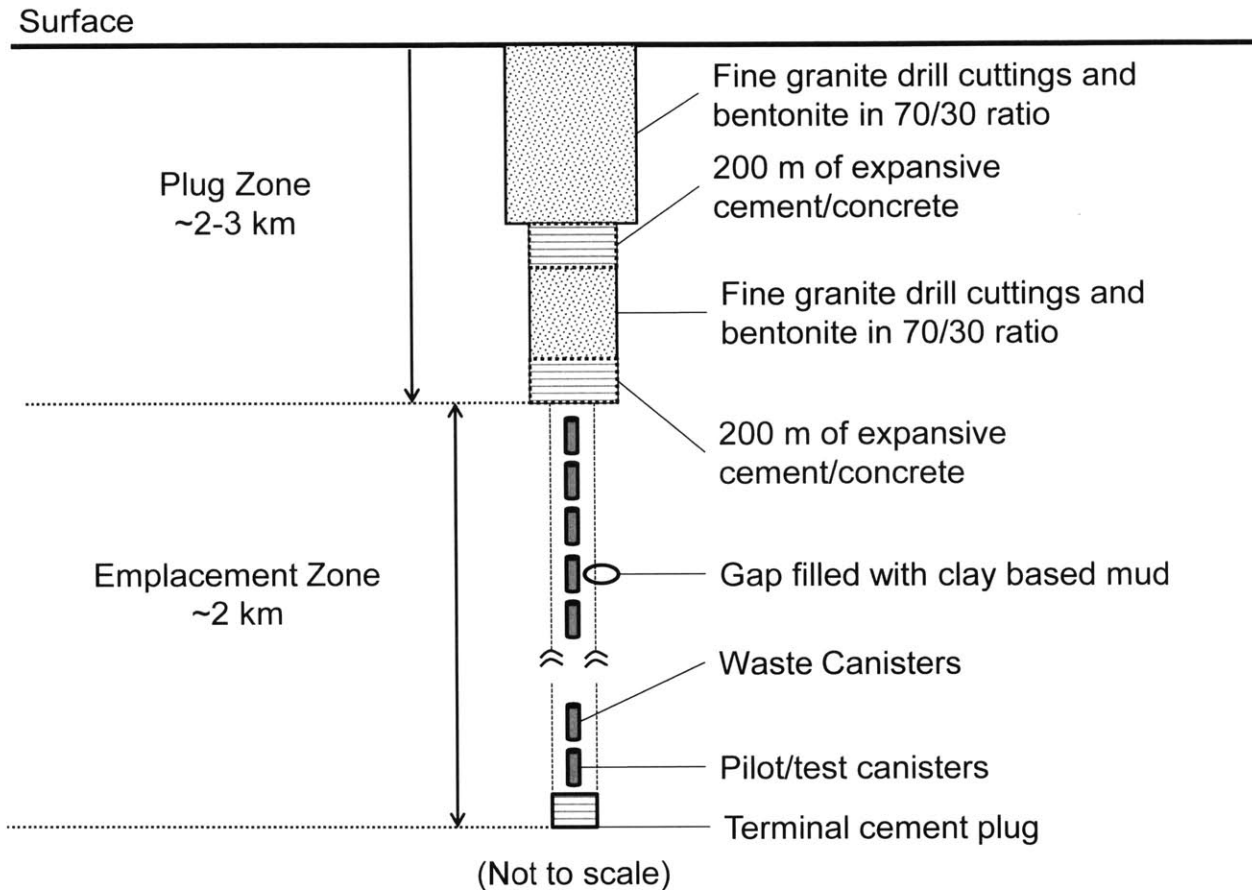
Figure 3-3. Updated borehole plug design (as of 2014) [137]

3.3. Canister Design

3.3.1. Introduction

In some repository concepts, canister design and longevity plays an integral role in the isolation and performance of the system. For example, in the Yucca Mountain reference design[29], titanium drip shields and steel alloys protecting each waste package are necessary components in the series of barriers designed to delay radionuclide release. In the SKB's current KBS-III design, canister integrity plays a similar and integral role to performance (primarily, a copper liner provides corrosion resistance). If advective conditions prevail and many of the canisters and buffer fail, dose limits are vastly exceeded [146]. As such, the required reliability of the

canister and buffer is high; for example, even under "pessimistic" advective flow conditions, only a few canisters (out of ~6000) are presumed to fail in the entire performance period [146].

Canister integrity analyses (particularly via corrosion resistance) can be controversial and complicated to experimentally justify, particularly on the time scales relevant to geologic disposal [29], [147], [148]. As a result, it could be difficult to translate expenditures on canister materials and corrosion resistance into verifiable or quantifiable radionuclide isolation benefits. As discussed in more detail in the following chapters, canister integrity is not assumed in the deep borehole safety case. Thus, with respect to the current DBD design philosophy, canister integrity is dictated by requirements to safely emplace canisters, and possibly maintain the ability to retrieve waste canisters (rather than radionuclide isolation). However, the precise definition of the legal (or social) requirement for "retrieveability" remains to be established and clarified for DBD. The main focus of this section is to update the deep borehole canister design using more accurate mechanical limits and to place these designs within the context of current drilling capabilities. Lastly, this section covers experiments that were conducted to evaluate the efficacy of the promising fill materials (sand, silicon carbide) to improve crushing resistance.

3.3.2. Canister geometry

Previous canister design efforts at MIT focused on mechanical integrity [17] with corrosion resistance being a secondary goal that was analyzed more generally [105], [106]. SNL's major canister design constraint is a hydrostatic crushing limit (57 MPa at 5 km) [149]. A key difference between the MIT and SNL reference design is that the MIT design conservatively assumes that the fuel rods will not be consolidated or rearranged into a more compact geometry. Fuel consolidation could be shown to be a favorable from a technical and economic viewpoint, but the logistical complexity (political, social, transportation, etc.) associated with intimately handling the fuel before final disposal could be limiting.

Both previous canister designs adhere to American Petroleum Institute (API) casing geometries, but neither analysis simultaneously accounts for the effects of hydrostatic pressure and crushing due to axial compression. Furthermore, they do not account for the increased fluid pressures or frictional forces that would result during the tripping in of the ~1000 m long drill string of waste canisters, an integral component of their emplacement schemes. This frictional load and a tensile load limit (created by connecting waste canisters) would be less of a constraint when using MIT's current, updated drop-in concept in which canisters are individually emplaced

into the borehole [150]. The drop-in concept also avoids possible limitations or weaknesses of the connections (threading) between canisters, which have their own set of design guidelines and limits. For example, certain buttress connections may be susceptible to leaking when temperatures exceed 200 °C [151].

Methods to account for the simultaneous effects of axial and hydrostatic crushing of oil well casings are available from the literature [152]. The equations necessary to predict the maximum hydrostatic pressure (or collapse pressure) due to either an elastic or plastic failure are summarized in Table 3-4. Material properties for the liner material are shown Table 3-9.

Table 3-4. Stress equations used to determine mechanical limits of deep borehole canisters.

Term	Equation	Description
M_{net}	$N_{can}(M_{can} - V_{can}(\rho))$	Net mass of N_{can}, with mass of M_{can} and volume V_{can} (accounting for buoyancy assuming fluid density of ρ)
$\sigma_{z,comp}$	$\dfrac{M_{net}g}{\pi Dt}$	M_{net} assumed to be supported by the shell of the bottom canister with diameter D and thickness t.
$\sigma_{z,hydr}$	$\dfrac{P_0(\pi D^2/4)}{\pi Dt} = \dfrac{(P_o)(D/t)}{4}$	Force balance on top of canister due to fluid pressure, with outer pressure (P_o) assumed to be hydrostatic.
$P_{c,e}$	$\dfrac{2E}{1-v^2}\dfrac{1}{D/t(D/t-1)^2}$	Elastic collapse pressure, for a material with Young's modulus (E) and Poisson ratio of (v) [152]
P_y	$\dfrac{2\sigma_y(D/t-1)}{(D/t)^2}$	Plastic yield pressure, with no axial stress [152]
$P_{c,p}$	$\left(\sqrt{1-\dfrac{3}{4}\left(\dfrac{\sigma_z}{\sigma_y}\right)^2} - \dfrac{1}{2}\left(\dfrac{\sigma_z}{\sigma_y}\right)\right)P_y$	Plastic collapse pressure with combined axial loading of σ_z, for a material with yield strength σ_y [152]

Table 3-5. Mechanical properties of P110 casing steel relevant to collapse pressure.

Variable	Description	Value	Reference
σ_y	Yield strength	760 MPa	[153]
E	Young's modulus	206 GPa	[152]
v	Poisson ratio	0.3	[152]

At low axial loadings, high yield strength materials and high D/t, the elastic collapse pressure $(P_{c,e})$ is constraining. At lower D/t and/or higher axial loadings and the critical plastic collapse pressure $(P_{c,p})$ reduces and becomes the limit[152]. The ID is used as the diameter in the equations shown in Table 3-4. There are two alternative geometric design constraints considered here:

1. Assume that the canister must use available API casing dimensions.

2. Assume that the OD is fixed by the API casing dimension and the ID is constrained by the diagonal width of the contained assembly (303 mm for PWR, 197 mm for BWR)

Lastly, we assume that at 1 km intervals (e.g., every 200 canisters) a packer, bridge material, or casing dimension change can be implemented to support the overlying canisters. Table 3-6 and Figure 3-4 shows a series of updated canister designs that meet the necessary crushing, hydrostatic, and geometric limitations.

Table 3-6. Summary of PWR and BWR canister design possibilities, subject to mechanical crushing limits and geometric constraints.

Can type	OD (mm) [inches]	ID (mm)	t (mm)	Casing Mass (kg/m)	Can Mass (kg)	$P_{c,e}$ (MPa)	$P_{c,p}$ (MPa)	Limit (depth)
PWR (standard casing)	339.72 [13-5/8]	313.6	13.06	107.15	1850 *	35.74	36.07	3600 m (Elastic)
PWR (max. thickness)	339.72 [13-5/8]	303	18.36	146	2010 *	114.58	54.22	5500 m (plastic)
BWR (standard casing)	219.08 [8-5/8]	198	10.16	53.34	1220 **	67.42	37.4	3700 m (plastic)
BWR (max. thickness)	244.4 [9-5/8]	197	23.73	131.6	1610 **	1027	102.9	10,000 m (plastic)

*assuming 5 m length, 77% packing fraction and solid density of 2650 kg/m³ for fill, 700 kg assembly
**assuming 5 m length, same density fill materials, 273 kg assembly

ID=0.303 to 0.3136 m

Fuel rods of a
17x17 single PWR
assembly:
L=4.06 m
L_{fuel}=3.58 m
Width=0.214 m
M_{HM}=512 kg
M= 700 kg

t=13.06 to
18.36 mm

(P110 steel)

OD=0.339 m
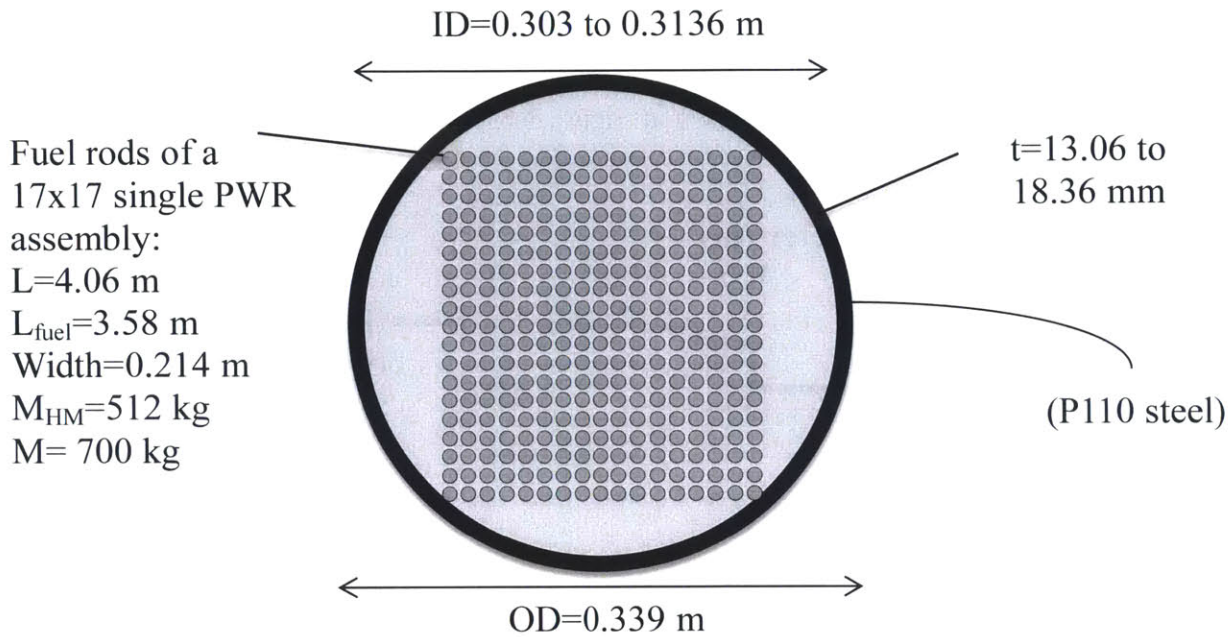
Figure 3-4. Reference deep borehole canister designs for a single PWR assembly. Assembly dimensions from [154].

Fuel rods of a 9x9
single BWR
assembly:
L=3.87 m
L_{fuel}=3.658 m
Width=0.139 m
M_{HM}=192 kg
M= 273 kg

ID=0.197 m

t=11.43 to 23.7 mm

(P110 steel)

OD=0.219-0.244 m
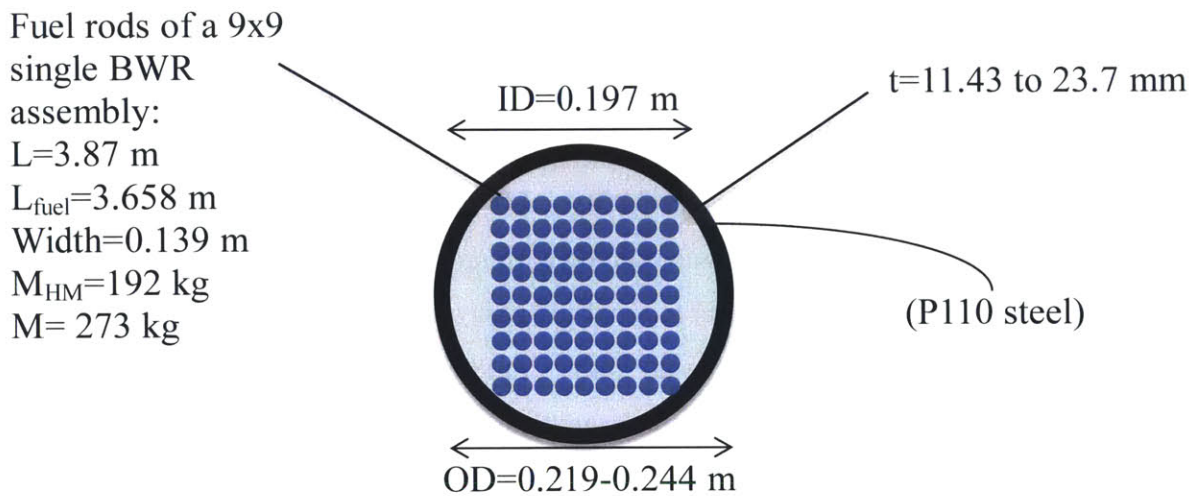
Figure 3-5. Reference deep borehole canister designs for a single BWR assembly. Assembly dimensions from [154].

The maximum depth at which a canister will be deployed will depend on available drilling technology (and a performance and cost optimization). As a reference, the casing and borehole diameter for a recent "generic" [151] deep borehole (for geothermal research) developed by the international deep drilling project (IDDP) is shown in Figure 3-6.
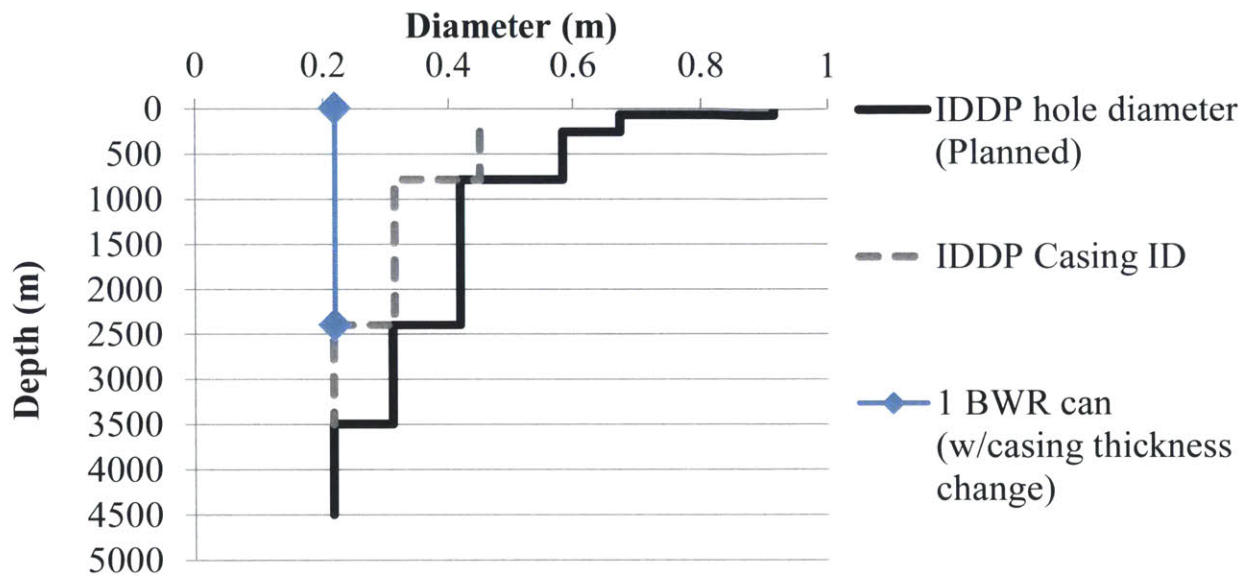
Figure 3-6. Drilling and casing program developed for the Iceland deep drilling project [151]. The diameter of a single BWR assembly canister (0.219 m) is shown for reference.

Note that this borehole was designed for considerably more difficult drilling conditions than expected for DBD (e.g, 300-500° C pore fluids containing corrosive H_2S). This necessitates higher strength and thickness casings (to sustain thermal stresses) as well as specialized high temperature cements. A key advancement in design is shown in Figure 3-6; specifically, the planned borehole diameter of 41.4 cm at 2400 km is larger than the KTB borehole (36 cm) [12] and previously drilled geothermal wells in Iceland (31.15 cm) diameter at the same depth. Specifically, this was enabled by the availability of a 300 ton (hook capacity) rig in Iceland[151]. Overall, the important conclusion is that the designed BWR assembly canisters (0.219 m) could be emplaced in 2.4 km deep boreholes achievable with current drilling technology, simply by modifying the liner thickness. If slightly larger modifications to the liner (e.g., change of borehole casing size) are deemed realistic and feasible, both PWR and BWR assemblies could be

disposed in the borehole to a depth of 2.4 km. Figure 3-7 shows the expanded range of possibilities with modifications to liner of the generic borehole.
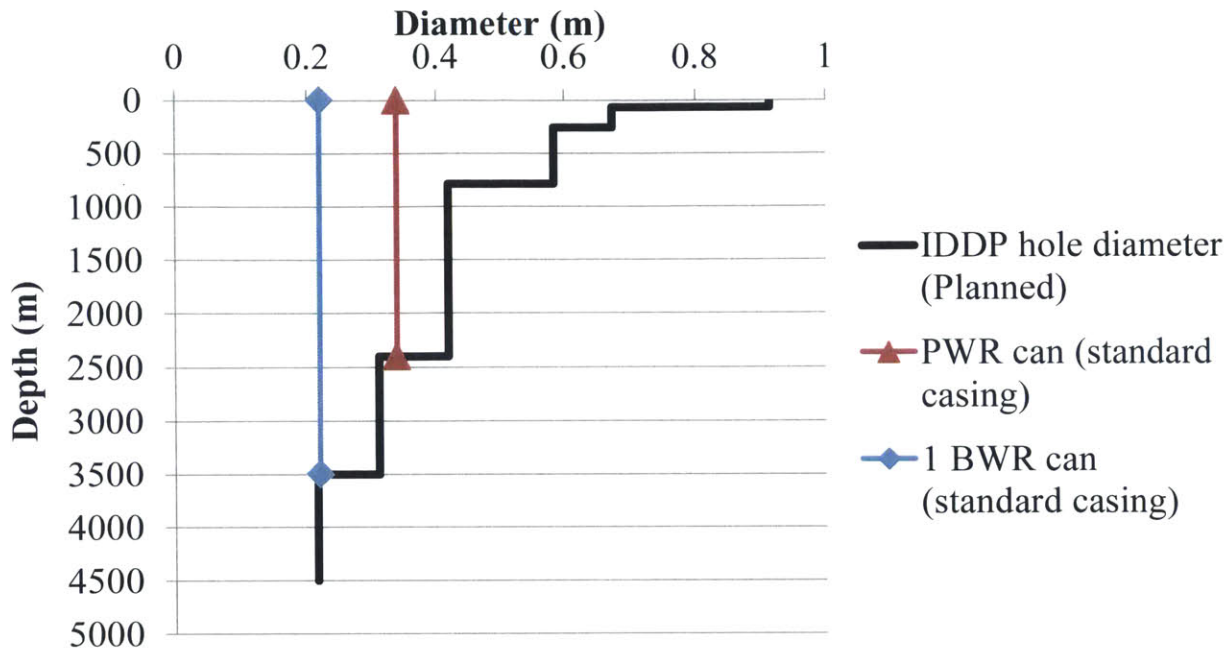
Figure 3-7. Drilling program developed for the Iceland deep drilling project [151]. Single BWR and PWR assembly canister diameters (0.219 m, 0.339 m) are shown for reference.

3.3.3. Canister fill materials

Canister fill materials have been proposed for use in DBD canisters as early as 1983 in the Woodward and Clyde system design [18]. Since then, SKB reviewed and proposed a number of criteria and metrics by which canister fill materials should be selected (although fill materials were never incorporated into the KBS-III design) [155]. More recently, Forsberg [156] proposed a novel fill material composed of depleted uranium dioxide pellets, which could also help maintain reducing repository conditions. In both of these cases, reduction of criticality seemed to be the primary evaluated benefit of reducing the void space in the canister. The most comprehensive review of fill materials and their use in spent nuclear fuel containers (SNF) was completed by Maheras et. al. in 2012 [157]. Again, since stresses during transportation are not as high as during emplacement, crush resistance was not a key criterion in the discussion. For the deep borehole concept, where hydrostatic stresses are very high (e.g., 40 MPa at 4 km) the primary goal of the filler material is high compressive strength [158] and thermal

conductivity[159]. These can be achieved by minimizing the initial void ratio (porosity) and by using high strength and conductivity materials.

Silicon carbide and sands have also been suggested as a filler material for deep borehole canisters[17], [160], and thus were considered as the reference materials to be crush tested in this work. As discussed in [161] porosity (voids) can be reduced in a number of ways: reordering of the particles to a more dense configuration (e.g., via vibratory compaction) and careful selection of particle size distribution. For a low porosity fill material, sands are convenient because of their low cost and wide availability of particle sizes. To achieve material uniformity and ensure repeatability, ASTM graded sands were selected as the primary fill material. ASTM –C778 and C-190 are commonly used in crush tests for concretes and have a high sphericity to improve packing efficiency. In addition they are chemically pure (~99.8% SiO_2, quartz) and have a corresponding high compressive strength. To achieve the smaller particle sizes, laboratory grade microcrystalline quartz silica was used. Given a set of particle sizes, the relations presented in [162] can be used to select mass ratios that result in very low porosities. The three constituent particles used in our laboratory tests are described in Table 3-7.

Table 3-7. Composition and properties of the ternary mixture used to fill canister.

Source	Particle Size Distribution	Effective Particle Size	Density (g/cc)	Mass % of Mixture
ASTM C-778 (20/30)	Predominantly between 20 and 30 standard sieves (650-800 μm)	671 μm (Calculated using [163])	2.65	49.4%
ASTM C-190 Sand (30/100)	Sieved in lab between 150-300 μm	190 μm (Calculated using [163])	2.65	33.7%
Alpha Aesar, Microcrystalline Quartz- Silicon (IV) Oxide	-	2 μm	2.65	16.81%

For the particle sizes and ratios given in Table 3-7, theoretically the packing fraction should be as high as 85%. Slight improvements could be gained by varying the three volume fractions and searching for a global optimum. The details of the as-purchased silicon carbide mixture are presented in Table 3-8.

Table 3-8. Details of the SiC grit used in the canister crushing tests

Source	Approximate particle size	Solid particle density
McMaster- Carr, abrasive grade, 100-120 grit	~0.11 mm	3.21 g/cc

3.3.4. Methods

3.3.4.A. Filling

During attempts to compact the sand bed using a vibratory process, significant segregation and agglomeration of microparticles was observed. Thus, an alternative method of loading the copper test cylinder- saturating the fill material (to avoid agglomeration), stirring, subsequently drying the mixture at 120° C- yielded satisfactory results. After sealing the top of the canister using cast Zamak-3 plugs (96% Zn,4% Al) and a copper tube sealant , the volume of the canister was measured within 0.3 ml using a graduated cylinder and displacement method (Archimedes method). The total internal fill volume was calculated by subtracting the volume of the canister and plugs (since the mass and density of all materials are known). The results of the filling and sealing process are shown in Table 3-9.

Table 3-9. Results of canister filling, using the ternary mixture described in Table 3-7.

Canister (Mass in grams)	Top and bottom plug (Mass in grams)	Fill Mass	Fill Volume	Packing Efficiency of Fill material
Copper (77.293)	Zamak-3 (83.7, 84.52)	89.72 g	43.69 cm^3	77.4% ± 0.5%

The lower packing efficiency (than theoretical) is likely due to entrapped bubbles during the stirring process and stable voids created after vaporization of water. In addition to the sand-only canister fill, a single particle, as-poured silicon carbide powder was investigated in an identically fabricated canister (copper tubing with Zamak-3 plugs).

3.3.4.A. Canister crushing

The canister was subjected to increasing pressures at increments of 100 psi (6.89 bar), up to 6000 psi (413 bar) over a 15 minute period using the apparatus described in detail by Wium [164] . The apparatus is shown in Figure 3-8.
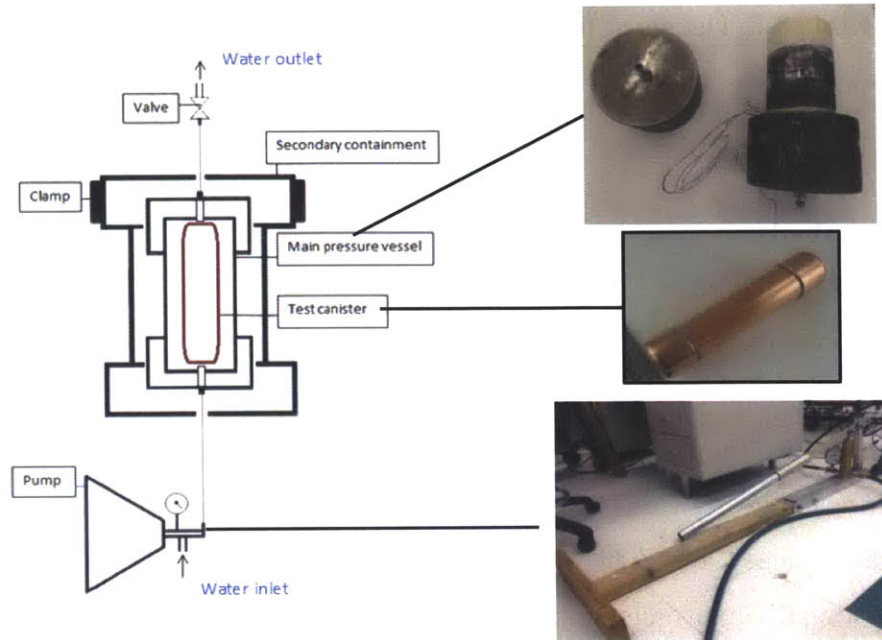
Figure 3-8. Diagram and photos of experimental setup for canister crushing.

The high pressure hydrostatic test pump is a Richard Dudgeon, Inc. Hydrostatic Test Pump Model 7J-55.1. The maximum working pressure is 6000 psig, with a piston diameter of 0.75 inches and displacement between 0.9-1.7 in^3, depending on which leverage point is chosen. At the maximum leverage, a 100 lb lever load achieves 3500 psi; therefore, to achieve 6000 psi, approximately 171 lbs of lever load applied at the end of the extended aluminum handle is required. The pressure vessel was constructed from a super thick wall steel pipe nipple with threaded ends. The ends were capped with high pressure pipe ends of Extreme-Pressure Forged Steel rated to 6000 psi, which were each threaded with ¼ inch NPT inlets threaded into the top and bottom caps to allow for connection to the pump.

3.3.5. Results of canister crushing

During pressurization of the sand filled and silicon carbide canisters, at two moments the pressure dropped sharply, but to a stable value, indicating that deformation occurred (but no fluid leaking was occurring). The canisters were held at the maximum pressure for an additional 25 minutes. The final volume and deformation of the canister is compared to the no-fill canister in Table 3-10 and Figure 3-9.

Table 3-10. Results of canister crushing (with sand fill) compared to silicon carbide fill

Canister fill	Initial internal volume	Initial packing efficiency	Initial porosity	Volume decrease	Final Porosity	Volume change	Change in void volume
SiC (~110 μm)	44.37 cm^3	47.6%	52.4%	3.44 cm^3	51.6%	7.74%	14.80%
Blended sand fill	43.69 cm^3	77.4%	22.6%	2.47 cm^3	17.96%	5.67%	25.21%
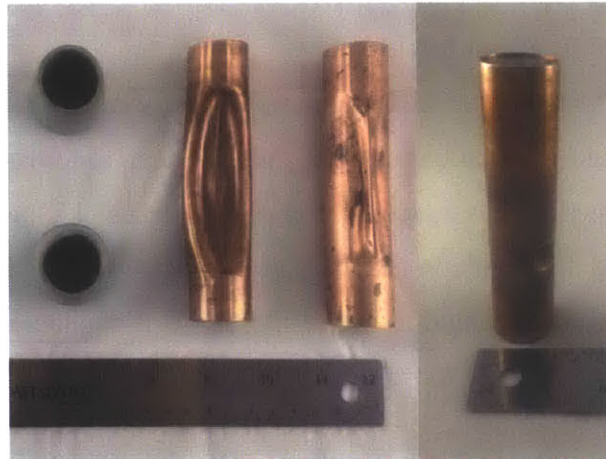
Figure 3-9. Final states of the empty (left), silicon carbide (middle) and blended sand (right) filled canister after being subjected to 6000 psi (41.3 MPa).

Note that mass of the filled canisters remained constant, indicating that water was not able to leak around the rubber plugs (shown on the left) used to seal each end of the canister in these experiments. The cast end plugs have slipped from their initial sealing point (presumably due to axial compression and porosity reduction of the sand bed).

Overall, the canister fill materials successfully prevented catastrophic crushing of the canister, as shown in Table 3-10 and Figure 3-9. Note that the empty copper tube (sealed in an identical method with zinc-aluminum and rubber plugs) breached at (16.5 MPa) 2400 psi with almost complete collapse of the internal void volume.

By the previous definition of canister failure (i.e., onset of plastic deformation and thus internal porosity reduction) fill materials provide measureable benefits if they sustain compressive stresses with very small porosity and volume changes. By this metric, the sand performed more favorably than the SiC mixture (5.76% volume change, vs. 7.74% volume change for SiC). However, the SiC appears to have compressed in a more uniform fashion,

compared to the sand, which appears to have had a void collapse (apparent from the hemispherical indentation).

Also note that many trials were completed before the final sealing method was developed (cast zinc/aluminum plugs glued into the ends of the canister, with rubber plugs surrounding the ends). Experiments were difficult to repeat due to the sensitivity to the quality of the seal, which raises a key point about the final canister design that needs to be addressed in future work. Although previous work has proposed that canisters be threaded and connected, it is likely that a welded seal will provide a more robust barrier.

In conclusion, using wet blended sand mixtures can provide an additional barrier to crushing under deep borehole hydrostatic pressures. Wet blended sand has a number of possible advantages that could address previous concerns with fill materials [157]:

1. The wet blended sand does not consolidate significantly with additional vibration, like dry blended sand (e.g., occurring during transportation or emplacement of the canister). The final material appears to be more similar to a dried cement, rather than a porous bed.

2. The wet blending could reduce welding issues associated with micron-sized particles being deposited on canister sealing surfaces.

3. The assembly is less likely to experience damaging vibrational acceleration and shocks under a wet filling process.

Ideally the fill material would be precompacted or cemented in some way to increase initial compressive strength. Ultimately, the selection of the fill material will be constrained by the feasibility and cost of the loading procedure. Thus, since it has not yet been demonstrated that a convenient wet fill (and sealing) procedure (or precompaction/cementing) can be devised for a 4 meter long PWR fuel assembly, the fallback option of using an approximately single particle size SiC sand is still recommended. This would provide a simpler loading method (no vibration, no small micron sized particles). Again, note that the steel canisters have been designed to withstand downhole hydrostatic pressures even if unsupported internally. In addition, the encapsulated fuel pins are internally supported over most of their length by their UO_2 fuel pellets.

3.3.6. Heat transfer of fill materials

The dry conductivity of quartz and silicon carbide beds are expected to be ~0.3 W/m-°K [17], [165]. For analyzing the temperature gradients in the canister, it is far more convenient to use a homogenized approach and model the canister as a radially symmetric cylinder. This is approach has been used previously[166] and is made possible using Selengut's relation[167] for two dimensional diffusion, written as Eq. (3-6),

$$k_{th,hom} = \frac{(1 + \gamma)k_f + (1 - \gamma)k_{th,b}}{(1 - \gamma)k_f + (1 + \gamma)k_{th,b}} k_{th,b} \qquad (3-6)$$

where $k_{th,b}$ is the porous bed conductivity (i.e., filler material), k_f is the effective thermal conductivity of the UO_2 fuel rods (1.86 W/m-°K[17], including a gap conductance factor of 31,000 W/m²-k), γ is the volume fraction of the UO_2 rods to total volume, calculated using Eq. (3-7),

$$\gamma = \frac{\frac{\pi}{4}d_{pin}^2}{P_{Pin}} \qquad (3-7)$$

where d_{pin} is the fuel pin diameter and P_{pin} is the pin pitch (spacing) of the assembly (9.5 and 12.6 mm for a PWR, respectively [166]) which leads to a value of 44.6%. With an effective thermal conductivity (and assuming that the heat production rate of the fuel is spread uniformly throughout the entire canister), the temperature difference between the centerline and surface may be calculated via direct solution to the radial heat conduction equation with heat generation, which gives Eq. (3-8),

$$\Delta T_{hom} = \frac{q'''R^2}{4k_{th,hom}} \qquad (3-8)$$

where R is the radius of the canister and q''' is the uniform volumetric heat production rate in the canister. Figure 3-10 shows the effect of increasing the porous fill conductivity on the PWR canister internal temperature difference at the time of emplacement (with uniform heat generation 2176 W/m³).
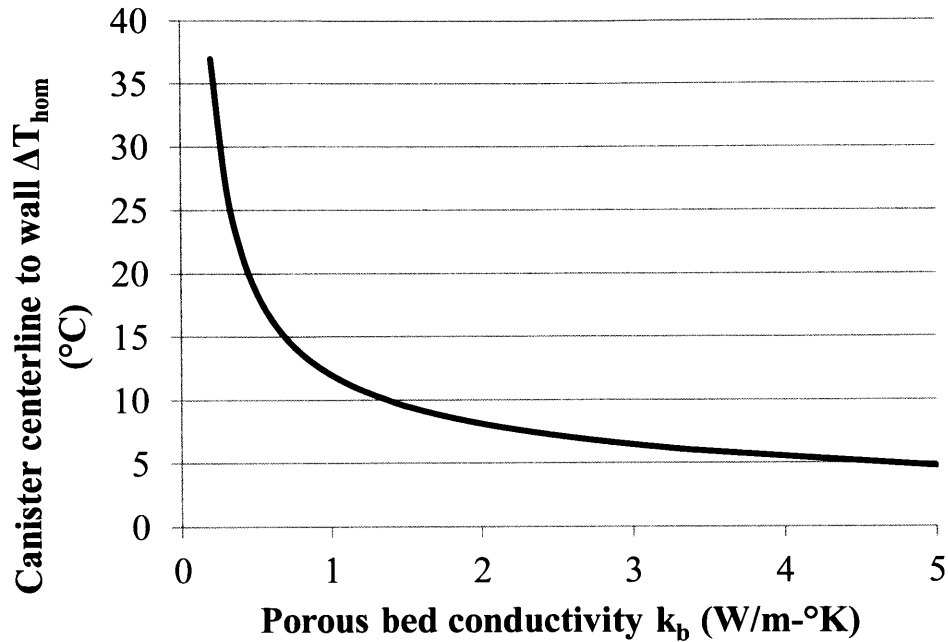
Figure 3-10. Canister centerline to wall temperature drop (ΔT_{hom}) vs. porous fill conductivity for a PWR canister with 2176 W/m^3 heat generation and diameter of 0.34 meters.

When a fill material with conductivity of 0.33 W/m-°K is emplaced in a PWR assembly this results in an effective homogenized (assembly filler) thermal conductivity of ~0.63 W/m-°K[17]. As seen in Figure 3-10 and confirmed in numerical models[98], this results in an acceptable (but relatively high) temperature difference between the centerline at canister surface of ~25°C, leading to peak centerline temperatures <150°C [98]. With higher heat generating wastes, even greater thermal conductivity materials may be necessary to meet temperature limits. Table 3-11 shows the relevant properties of a promising, low-cost, fill material that could be cast directly into the canister (filling all voids between the fuel rods and canister walls).

Table 3-11. Properties of Zamak-3 for filling high heat generating wastes, ASTM B86 [168].

Elements	Zn	Al	Mg	Cu
Composition	Remainder	3.7-4.3	0.02-0.06	0.1 (max)
Physical Properties				
Melting Point (°C)	381			
Thermal Conductivity (W/m-K)	113			
Density (kg/m^3)	6600			
Specific Heat (J/kg-K)	419			
Mechanical Properties				
Tensile Yield Strength (MPa)	221			
Compressive Yield Strength (MPa)	414			
Young's Modulus (GPa)	>85.5			
Cost	$1.32/kg, $0.60lb [169]			

With such a high thermal conductivity, the canister temperature difference would essentially be eliminated (less than 1°C, even for fuel generating 10x more heat than a PWR). However, future work would have to determine the feasibility of emplacing these materials at the elevated temperatures required (~400 °C), and confirm that shrinkage during solidification does not lead to gaps or excessive thermal stresses.

3.4. Gap Fill Material

The materials selected to fill the annulus between the canister and borehole wall determine heat and mass transfer within the disposal zone and have beneficial effects not previously considered in deep borehole assessments. There are a number of promising materials that can be used to significantly increase the thermal conductivity and heat transfer in the gap. In addition, gap fill materials can have beneficial chemical effects (e.g., maintain redox conditions) which would act as an additional barrier to the degradation of the canister and spent fuel. At the same time, material selection is restricted by cost and other (currently not well defined) constraints, such as feasibility of emplacement, retrievability, and structural limitations.

This section begins with a discussion of the applicable heat transfer mechanisms in the deep borehole gap. A number of metallic and ceramic candidates were proposed and experimentally tested in the form of suspensions and saturated mixtures. Finally, the benefits of high thermal conductivity materials in gaps is discussed on the basis of economic cost and benefit to waste management (decay cooling time).

3.4.1. Convection

3.4.1.A. Water

If the gap between the canister is filled only with water (e.g. after the drop-in concept has been used for emplacement) significant heat transfer could occur via convection (with upflow along the heated canister and downflow along the cooler borehole wall). Figure 3-11 presents a diagram of the variables pertinent to estimating the convection heat transfer coefficient in the borehole gap.

$$q'' = \frac{q'[W/(m)]}{\pi d_c[m]} = \frac{232}{\pi(0.4)} = 185\frac{W}{m^2}$$

$t_{g,c} = 0.02\ m$

q''

$(\rho, c_p, v, \beta, k)_{fluid}$

ΔT
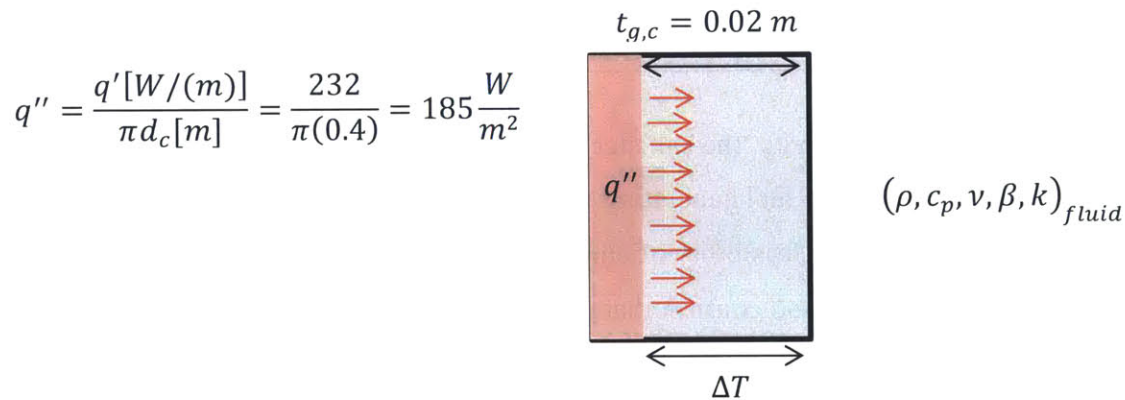
Figure 3-11. Parameters relevant to determining the magnitude of natural convection and temperature difference between a deep borehole canister (20 years aging, 50 MW-d/kg) and the granite borehole wall, assuming the gap is filled with water.

In a quasi-steady state (a reasonable assumption considering the slow rate of decay of decay heat), the heat flux is uniform and equal to the heat flux emitted by the canister (in this case conservatively assumed to be aged only 20 years). Thus, the primary variable to be determined is the temperature change across the gap, which is smaller if more convection occurs in the gap.

Natural convection between small planar gaps (adjacent to a heated wall with uniform heat flux) has been studied numerically and experimentally over a range of fluid properties by MacGregor [170] and Keyhani et al [171]. A planar gap is a close approximation of the borehole canister gap when the gap is small and the effects of curvature are assumed to be negligible. The Rayleigh number in this configuration is defined as Eq. (3-9),

$$Ra = \frac{\rho \beta c_p g(\Delta T) t_{g,c}^3}{v_k k_{th}} \tag{3-9}$$

The Nusselt number in this configuration is correlated to the Rayleigh number using Eq. (3-10) [170],

$$Nu = 0.42 \ (Ra)^{0.25}(Pr)^{0.012} \left(\frac{L_c}{t_{g,c}}\right) \tag{3-10}$$

where L_c (the height of the annulus) is assumed to be the length of a single canister (5 m). By the definition of the Nusselt number and law of convection, the temperature difference across the gap is calculated using Eq. (3-11),

$$\Delta T = \frac{q''}{h} = \frac{q''}{\left[\frac{(Nu)k_{th}}{t_{g,c}}\right]} \tag{3-11}$$

Since the Rayleigh number determines the temperature change (ΔT), which implicitly determines the Rayleigh number, an iterative technique must be used to solve for ΔT. For the sake of simplifying comparisons, heat transfer in a purely conductive annulus is determined by Eq. (3-12),

$$q' = \frac{2\pi k(\Delta T)}{\ln\left(\frac{OD}{ID}\right)} \tag{3-12}$$

Thus, given the heat flux, temperature change, and dimensions, the "effective" thermal conductivity of the annulus with convective heat transfer can be determined. Rearranging terms in Eq. (3-12) gives Eq.(3-13),

$$k_{eff,conv} = \frac{q'\ln\left(\frac{OD}{ID}\right)}{2\pi\Delta T} \tag{3-13}$$

Table 3-12 presents the results for average fluid water properties assuming a borehole wall temperature of 135 °C and hydrostatic pressure 500 bar (at 5 km), for gap widths of 1 to 10 cm.

Table 3-12. Iteratively solved temperature difference and effective thermal conductivity across a gap with convection, subject to a uniform heat flux of 185 W/m^2 at a diameter of 0.4 m.

Gap Width (m)	Nu	h (W/m^2-°K)	ΔT (°K)	OD (m)	$k_{eff,conv}$
0.01*	0.93(1)	66.29	2.79	0.42	*0.714
0.02	1.92	68.63	2.70	0.44	1.31
0.03	2.94	70.03	2.64	0.46	1.96
0.04	3.98	71.05	2.61	0.48	2.59
0.05	5.03	71.84	2.58	0.50	3.21
0.10	10.41	74.37	2.48	0.6	6.03

*only conduction occurs in this case since Nu≤1, so k_{eff}=k_{water}=0.714

Note that in this case (water), convection does not occur with very small gaps (<1 cm) and heat transfer occurs through conduction only. Convective heat transfer in water becomes a dominant heat removal mechanism as the gap size grows >3 cm. Larger gaps (>5 cm) are unlikely for economic and structural reasons. The gap will only be large enough to allow for smooth insertion of the canisters (2-3 cm in the current reference design).

This analysis assumes the water has no clay impurities (from the drilling process or host rocks), which would give the fluid non-newtonian properties (or at a minimum, increase the viscocity which would inhibit the onset of convection). It has been noted that forced convective heat transfer coefficients are overpredicted when fluids with clay (i.e., drilling muds) are assumed to be Newtonian[172]. The same would apply to the natural convection case, considering the effect of thixotropy which causes drilling muds to behave as solids at low stresses. No alternative methods of calculating natural convection heat transfer coefficients (accounting for thixotropy) are given in the paper, or could be found in a broader review of literature on drilling muds. In conclusion, a conservative approach assumes that thixotropy (which cannot be ruled out) inhibits the onset of natural convection, in which case heat transfer is purely conductive (with k ≈0.7 W/m-°K for drilling mud [172]).

In addition, a convective heat transfer regime would have undesirable consequences, such as increased rates of convective transport of oxygen and hence oxidation of metals [173] in the disposal zone. Vertical flow of waterborne radionuclides would also be enhanced. In general, convective transport depends on a greater number of variables and has a much higher sensitivity to geometry than conduction transfer. Thus, to limit corrosion, reduce uncertainty, and improve confidence of predictions, convective conditions in the gap are avoided in the design.

3.4.1.B. *Porous medium*

Even if the gap is filled with a porous medium (which significantly increases viscous resistance and tends to inhibit convection), it is still possible that convective heat transfer could occur. Natural convection in an annulus composed of a porous medium has been experimentally and numerically studied by Prasad [174]. Figure 3-12 shows the relevant parameters required to estimate convection in a porous gap, based on an idealized, quasi-steady state abstraction of the canister and borehole.

$$q'' = \frac{q'\,[W/(m)]}{\pi d_c\,[m]} = \frac{232}{\pi(0.4)} = 185\,\frac{W}{m^2}$$

$t_{g,c} = 0.02\ m$

$(k_{th}, k)_{porous\ medium}$

q''

$(\rho, c_p, \nu, \beta)_{fluid}$

T_w
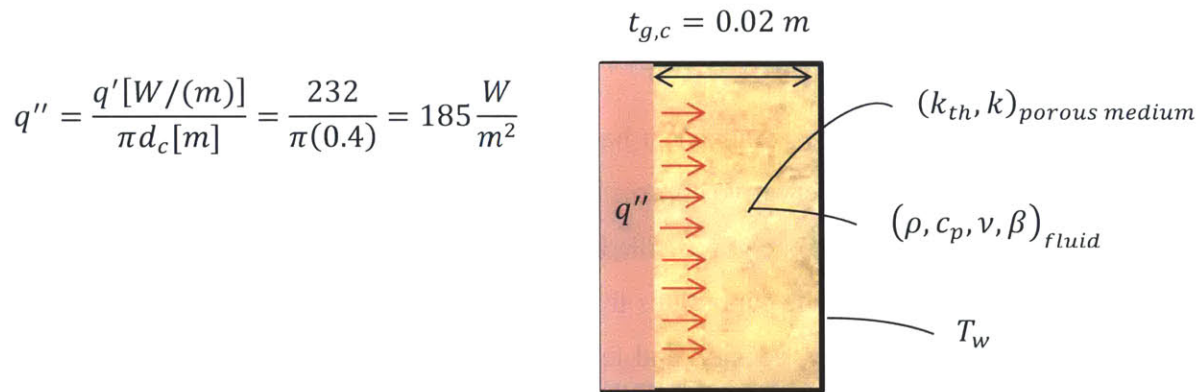
Figure 3-12. Parameters relevant to determining the magnitude of natural convection heat transfer between a deep borehole canister (20 years aging, 50 MW-d/kg) and the granite borehole wall, assuming the gap is filled with a saturated porous medium.

The outer wall temperature (T_w) can be determined independently by the analytical or numerical solution of the transient heat transfer problem in the far field rock [98]. For a wall with a constant heat flux, the heat flux based Rayleigh number with a porous medium is defined as Eq. (3-14) [174],

$$Ra_{por}^* = \frac{\rho c_p g \beta k q'' t_{g,c}^2}{\nu_k k_{th}^2} \tag{3-14}$$

For fluid water properties evaluated at 135 °C and 500 bar (at 5 km), quartz sand bed with a stagnant conductivity (k_{th}) of 2.5 W/m-K as measured and consistent with [165], and permeability (k) of 2.59×10^{-10} m^2 as evaluated by the Kozeny Carmen relation for an average particle size of 0.72 mm [165], the Rayleigh number in the porous gap can be evaluated,

$$Ra_{por}^* = \frac{(954)(4155)(9.8)(8.22 \times 10^{-4})(2.59 \; 10^{-10})(185)(0.02)^2}{(1.09 \times 10^{-6})(2.5)^2} = 0.089$$

This is less than the Rayleigh number for which correlations with the Nusselt number exist (and for which there is convective heat transfer). Since most other gap fill materials (bentonite, cement, metals etc.) would have a lower permeability and/or higher thermal conductivity than this sand bed, (resulting in lower Rayleigh numbers) it can be concluded that as long as there is a porous fill material in the gap heat transfer will occur purely by conduction.

3.4.2. Conduction

In the previous analyses on gap heat transfer, it has been shown that only accounting for conduction heat transfer is a conservative approach (in the case that the gap is filled with a liquid) and is accurate (in the case the gap is filled with a saturated porous medium). Thus, the following section discusses possible candidates for the gap filler, which are discussed on the basis of their thermal conductivity, density, and feasibility of implementation. From a theoretical point of view, the properties are relatively easy to optimize; however, implementation is likely to dominate the initial down selection of gap fill materials. Table 3-13 presents a summary of the relevant mechanical, thermal, chemical, and economic factors affecting a few possible gap filler materials.

Table 3-13. Mechanical, thermal, chemical properties and costs of iron, aluminum, silicon carbide and sand and graphite as gap filler candidates. Key favorable properties are shaded in green, unfavorable properties are denoted with an asterisk (*).

Material	Solid Density	Thermal Cond. (W/m-°K)	Chemical	Cost	Comments
Iron	*7.8 g/cc [175]	44.8 [176]	Reducing agent, effective for precipitating uranium[177] and other heavy metals	$0.60/kg [178] (Cheapest reactive metallic medium available)	Voluminous corrosion products, causes reductions in permeability and water flows [175].
Aluminum	2.7 g/cc [179]	204 [179]	Reducing agent, *more reactive than iron in water (galvanic series).	$2.2/kg Ref. [180], similar to iron per volume [181].	Sacrificial (protective) anode for steel in chloride environments where passive layer is not stable[182], [183].
Silicon carbide (powder)	3.21 g/cc	18-490 [184][185]	Inert, insoluble in water	*$4.85/kg Ref. [186]	Very high compressive strength [186]
Sand	2.65 g/cc [165]	*5.83-7.59 [165]	Inert, chemically compatible with host rock.	$0.04/kg [178]	
Graphite	2.15 g/cc [187]	161[187] 74-704[188]	Corrosive to metal with O_2	$1.3/kg (flake graphite)[189]	Acts as a lubricant
Sepiolite (clay power)	2.2-2.5 g/cc [144], [190]	Data not available	Adsorbs heavy metals, uranium [46], [47]	$0.01/kg[144] $0.45/kg[192]	Unlike bentonite: does not flocculate in saline water [193], stable to high temperatures[194].

In general, pure metals show promise for their high thermal conductivity and low cost. For example, aluminum powder is used as a high thermal conductivity filler material for thermal interface pastes (e.g., computer heat sinks) [195]. In the case of the cheapest metal (iron), high density increases forces on the canisters and the borehole. Silicon carbide is an interesting engineered (man-made) material with favorable mechanical and thermal properties, but has the highest cost of all materials considered.

Due to its high thermal conductivity[188] and low cost, natural graphite flake, has been evaluated for heat transfer enhancement in composites[196], phase change materials[197] and other applications. Other natural materials such as clays and sands are advantageous for their stability and compatibility with rock, but have low thermal conductivity. Sepiolite is favored (over bentonite for example) for its stability at high temperatures (up to 300 °C) and resistance to porewater salinity [194].

The thermal conductivity of the material depends on state of the material (dry, saturated, suspended in mud), which must be appropriate so that the material can be properly emplaced in the disposal zone. The most feasibly emplaced materials are those most similar to existing drilling fluids (e.g. drilling muds), which by design to allow solids (i.e., crushed rock) to be pumped and transported in a smooth and efficient manner. Highly compacted beds of particles (while desirable from the perspective of thermal conductivity and low permeability) would present greater difficulties (e.g., it might hinder canister emplacement, or be difficult to achieve after the canisters have been emplaced). Furthermore, materials such as silicon carbide and graphite exhibit large ranges in reported thermal conductivity (due to impurities, anisotropic effects in graphite); therefore, experimental data is necessary to support their use. To better investigate the effects of gap filler preparation and form on thermal conductivity and density, a series of experiments were conducted.

3.4.2.A.   *Experimental measurements of gap fill conductivity*

3.4.2.A.1.   Experimental method

The KD2 pro (Decagon devices) is a portable electronic thermal conductivity measurement device specifically designed for measuring the thermal conductivity of natural materials (soils) and concretes. It operates on the transient line source method, an accepted method for measuring thermal conductivity in liquids, soils, concretes and rocks. This method is fully described in the ASTM standard D5334-08 [198] and in the KD2 Pro manual. A very thin electrical heater transfers a given amount of heat into the medium–consequently, linear regression on the rate of decay of temperature of the probe yields the thermal conductivity of the medium. The 60mm length, 1.3mm diameter, (KS-1) needle probe was used in all experiments. The accuracy of the KS-1 probe is only rated for materials with conductivity up to 2 W/m-K, so the accuracy had to be confirmed with a reference material.

The physical characteristics and thermal conductivity of dry and saturated mixtures of C-190 (also sold as C-778), standardized ASTM sand[199] with specified particle size (600-850 μm) and chemical composition (quartz) have been previously described by Tarnawski et al. [165]. It is a convenient reference material which can be used to check the accuracy of the thermal conductivity measurement device.

Samples (with measured mass) were loaded into VWR centrifuge tubes to create a sufficient and consistent length (114 mm) and diameter (22.45 mm) of sample. It also permits the probe to be fully inserted into the sample, and reduces the amount of prepared material. The centrifuge tube internal volume of 55 ml ±0.5ml was measured by filling the tube with water and recording mass (and hence volume) of the water. A Mettler Toledo Pb3002 scale was used for all mass measurements, providing a precision of 0.01g (accuracy was checked with a standardized 100 g weight). The bulk density and solid fraction is calculated using the rule of mixtures because the mass and density of sand, water, and mixture are known from measurement and the literature. Table 3-14 presents a comparison of the measured thermal conductivity with the reference values from the literature[165].

Table 3-14. Summary of thermal conductivity measurements on a reference sand with known thermal conductivity.

Preparation	Bulk density (g/cc)	Solid fraction	Porosity	Measured thermal conductivity (W/m-K)	Reference thermal conductivity(W/m-K) [165]
Dry	1.66±0.2	0.63±0.07	0.37±0.07	0.176	0.275*
Wet	2.05±0.2	0.63±0.06	0.37±0.06	2.75±0.06	3.03*

*linearly interpolated between thermal conductivities reported for porosity of 0.36 and 0.4[165]

From Table 1, it is seen that within 10%, the KD2 Pro accurately measures the thermal conductivity of saturated porous materials. However, it is not accurate for dry granular materials (as noted in the manual for the device and indicated by the anomalously low measurement for dry thermal conductivity). This is due to the effects of contact resistance, which is reduced when the material is saturated with a wetting liquid (i.e., water). Thus, the dry thermal conductivity measurements can be seen as lower bound measurements.

3.4.2.A.1.   Results and discussion

Experiments were conducted on the basis of the candidates presented in Table 3-13, the ability of the instrument to measure water saturated samples, and goal to measure mixtures with a wide range of thermal conductivities. Additionally, the mixtures should be representative of what could possibly be emplaced in a deep borehole. To simulate a drilling mud with suspended solid, powders of SiC, Fe and Al, and flaked graphite, were suspended at various volume ratios (30%-40%). This volume fraction is the amount of fill material required to appreciably affect of thermal conductivity of a mixture[179]. Suspension of solids was achieved using 2% by (total

mass) mixture of sepiolite. Thus, materials with high densities contained higher concentrations of sepiolite in water (which aids in keeping denser material in suspension). The purchased form of powders are described in the first column of Table 3-15. Abrasive grade blasting media were chosen for their cost-effectiveness and level of standardization.

Table 3-15. Summary of thermal conductivity measurements on sepiolite clay, Fe, Al, and SiC. The ratio of thermal conductivity to bulk density is shaded in green.

Material	Particle Size	Property	Suspension (2% by mass sepiolite)	Saturated
Sepiolite powder (Sigma Aldrich, analytical grade, product of Spain)	(Not reported) but typically ~10µm	k_{th} (W/m-°K)	0.62	0.61
		ρ_{bulk} (g/cc)	1.01±0.1	1.08±0.1
		Solid Mass	2%±0.1%	25%*±0.1%
		k_{th}/ρ_{bulk}	0.62	0.61
SiC grit (McMaster- Carr, abrasive grade, 100-120 grit)	~0.11 mm	k_{th} (W/m-°K)	3.0	5.5
		ρ_{bulk} (g/cc)	1.85 ±0.05	2.11±0.02
		Solid volume	40% ±0.5%	50%±0.5%
		k_{th}/ρ_{bulk}	1.6	2.6
Steel grit (Ervin Industries Amasteel Martensitic steel,	0.18-0.30 mm (SAE G50 size)	k_{th} (W/m-°K)	1.9	3.5
		ρ_{bulk} (g/cc)	3.14 ±0.07	4.42±0.03
		Solid volume	30%±0.5%	50%±0.5%
		k_{th}/ρ_{bulk}	0.6	0.8
Natural flake graphite (Asbury carbons, industrial lubricant)	3-50µm (as reported by manufacturer)	k_{th} (W/m-°K)	4.8	Higher concentrations of graphite result in voids during experiment [187].
		ρ_{bulk} (g/cc)	1.37±0.1	
		Solid volume*	31.1%±0.1%	
		k_{th}/ρ_{bulk}	3.51	
Al (Alpha Chemicals, 99.5% purity)	30 µm	k_{th} (W/m-°K)	2.07	
		ρ_{bulk} (g/cc)	1.6±0.05	
		Solid volume	44%±0.5%	
		k_{th}/ρ_{bulk}	1.3	-
Al (Pyrochem source, 18 mesh flake)	1 mm ×0.1 mm square flakes	k_{th} (W/m-°K)	2.08	
		ρ_{bulk} (g/cc)	1.29±0.1	
		Solid volume	18.36%±0.5%	
		k_{th}/ρ_{bulk}	1.6	

*25% mass was the maximum loading of sepiolite with water that could still be inserted into the measurement tube. With suspensions, the bulk density of the mixture was measured by dividing by the mass of the material by the volume of the centrifuge tube.

The error in thermal conductivity measurement is dominated by the 10% systematic error of the probe, while error in density is determined by uncertainty of volume of the centrifugal tube. The saturated thermal conductivities (fifth column) and densities are what would be approached if the

suspension and solids settled over time. This is a phenomenon called "slumping" by the drilling industry, which can result in large variations in drilling mud density with depth [200]. Thus, the saturated thermal conductivities could be realistic (with time), but since they are higher than the suspended ones, it is not conservative to use them in a thermal analysis.

The measured thermal conductivity of the aluminum (micron sized) suspension is likely to be lower than actual because rapid generation of hydrogen caused voids and gaps to be formed in the material (decreasing thermal conductivity). For this reason, the conductivity was not measured for saturated aluminum, as it was concluded to be susceptible to the same error. Aluminum in flake exhibited a similar thermal conductivity of 2.08 W/m-°K at a lower vol%, but after one day also showed significant reactions with water (water was consumed).

On the basis of suspended thermal conductivities and density (highlighted rows in green), graphite is clearly the best choice. For comparison, artificial exfoliated graphite flake composites (~15μm) at 20 vol% with nylon (lower thermal conductivity than water) have thermal conductivities of more than 4 W/m-°K[196] Graphite powder (not flake form) suspended in water at a similar 32 vol% was measured by Jefferson to have a thermal conductivity of 1.1-2.1 W/m-°K. Thus, the very high thermal conductivity of flake graphite at low loading (31%), is reasonable and within the range found by other investigators

Another important criterion is cost. Total cost estimates for various gap sizes and each of the materials are summarized in Table 3-16.

Table 3-16. Estimated costs of using various mud suspended filler materials for a borehole diameter of 0.4 meters and length of 2000 meters. Candidates are presented in order of increasing thermal conductivity.

Material	Cost ($/kg)	Volumetric cost ($/m³ of solid)	1 cm gap (Total cost)	2 cm gap (Total cost)	3 cm gap (Total cost)
Sepiolite (2% mass, ~1% vol.)	*0.45[192]	990	$231	$475	$729
Fe (35 % vol.)	0.6 [178]	4680	$42,197	$86,452	$132,765
Al (44% vol.)	2.2 [180]	5940	$67,329	$137,943	$211,840
SiC (40% vol.)	4.5 [186]	15,569	$160,424	$328,674	$504,750
Graphite (31.1 vol%)	1.3 [189]	2,795	$22,392	$45,877	$70,454

*Upper bound estimate on cost for sepiolite. Cost estimates on other materials do not include cost of 2% by mass sepiolite required to suspend the material.

For the various fill materials considered, there is a three order of magnitude variation in cost, with silicon carbide (at 40 % vol.) costs approaching $300,000 for a single borehole. In comparison to the total to cost of the borehole (~$40 million), this may seem significant, so the additional benefit provided by having a low density, high thermal conductivity gap filler should be evaluated. The temperature drop across a conductive gap is evaluated using Eq. (3-15),

$$\Delta T_{gap} = \frac{q' \ln\left(\frac{D_o}{D_i}\right)}{2\pi k_{gap}} \tag{3-15}$$

Figure 3-13 shows how specific decay heat (W/MTHM) and ΔT_{gap} across the gap evolves with time for 60 MW-d/kg burnup[201], and a PWR assembly with 0.45 MTHM and length of 3.8 m.
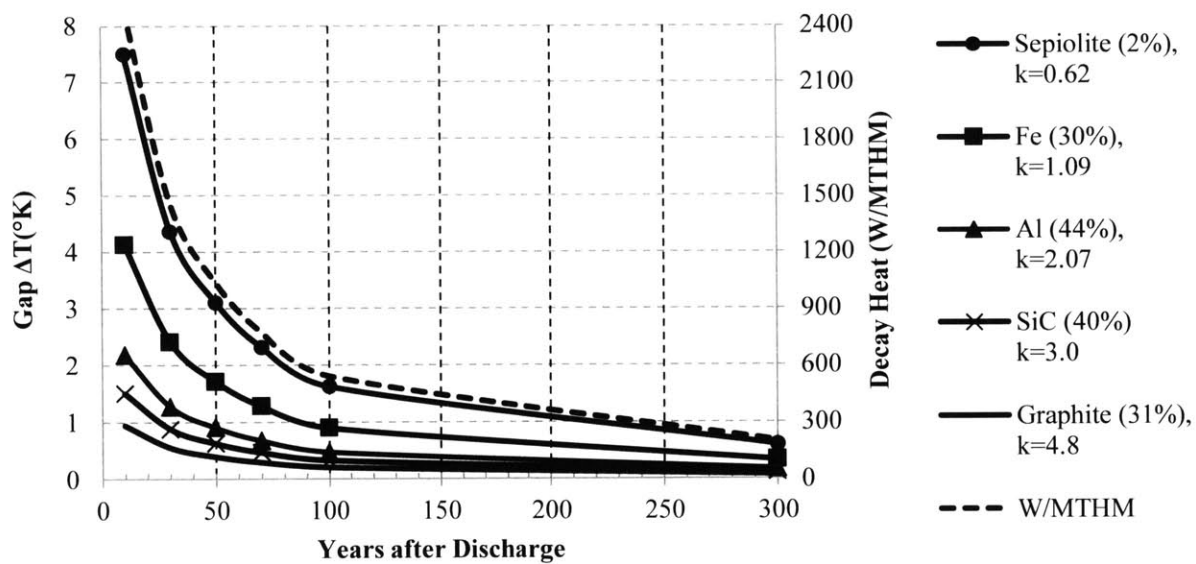
Figure 3-13. Decay heat and gap temperature difference (2 cm gap) vs. time after discharge for various gap fillers. Data is for a 60 MW-d/kgHM burnup [201] PWR assembly with 0.45 MTHM and active length of 3.8 m.

The high thermal conductivity of the graphite suspension reduces the temperature drop across of the gap to less than 1°K. Although 7°K may seem like a small increase, if borehole repository capacity is limited by decay heat and temperatures (on canisters, fuel, or cladding), then additional surface cooling time becomes necessary before waste can be disposed. If this is the limit, increases in thermal conductivity can be translated into reductions in cooling time, and thus

cost. An analytical expression for decay heat ($q'\sim t^{-0.75}$)[202] allows for a convenient comparison. Assume that the temperature difference is to be the equal in two cases:

1. A high thermal conductivity material (denoted with thermal conductivity k_H) is used with younger fuel, disposed at a minimum disposal time t_1 (10-30 yrs after discharge)

2. A lower thermal conductivity material (denoted with thermal conductivity k_L) is used with an older fuel, disposed at a later time t_2 after surface aging.

Since the temperature difference is proportional to the decay heat and inversely proportional to the gap thermal conductivity (apparent in Eq. (3-13)), we can relate the two cases using Eq. (3-16),

$$\Delta T_{gap_1 = \Delta T_{gap_2 =}} = \frac{t_2^{-0.75}}{k_L} = \frac{t_1^{-0.75}}{k_H} \tag{3-16}$$

Note that this is independent of the gap width. Solving for the surface cooling temperature period (t_2-t_1) that is avoided by the higher thermal conductivity gap filler, we obtain Eq. (3-17)

$$t_2 - t_1 = t_1 \left[\left(\frac{k_H}{k_L}\right)^{1.33} - 1 \right] \tag{3-17}$$

Table 3-17 presents a comparison of avoided cooling periods afforded by the various gap fill materials considered here.

Table 3-17. Avoided cooling period (t_2-t_1) in yrs for fill materials (compared to drilling mud).

Fill Material	k (W/m-°K)	k_H/k_L	(t_2-t_1) in years			
			t_1= 10 yr	t_1=20 yrs	t_1=30 yrs	t_1=50 yrs
Drilling mud (2% Sepiolite)*	0.62	1	0	0	0	0
Fe (35 % vol)	1.09	1.76	11	22	34	56
Al (44% vol)	2.07	3.34	40	79	119	199
SiC (40% vol)	3.0	4.84	71	143	214	357
Graphite (31.1% vol)	4.8	7.74	142	284	426	711

*similar to a stagnant water or solid concrete

Table 3-17 and Figure 3-13 both highlight the surprisingly large beneficial effect that small increases in thermal conductivity can have when implemented in zones that are limited by

temperature and decay heat production. It also raises the importance of improving the thermal conductivity of the canister fill material.

3.4.3. Summary

The de-facto gap fill material (drilling mud) is a cost-effective and feasible to employ material, satisfying the density constraints that would exist on the fluid in the borehole due to structural limits. However, its thermal conductivity is very low. If borehole temperatures are limited (canister, cladding, fuel) graphite represents the most promising material tested, with the highest thermal conductivity to density ratio. In addition, graphite's lubricating properties could greatly facilitate emplacement and retrieval of canisters (with the latter being an unproven and unresolved limitation with the deep borehole concept). The main limitation of graphite is the potential for accelerating galvanic corrosion (discussed more in Section 3.4.4) in the presence of oxygen. Silicon carbide's high strength causes it to behave in an opposite manner (abrasive vs. lubricant) but it also exhibits high thermal conductivity and is likely to have fewer chemical issues than graphite. Aluminum is cheaper and more abundant than silicon carbide and represents the second most promising fill candidate if the sacrificial protection offered by aluminum (for the iron canisters) is accounted for [182]. Resultant hydrogen production would reduce the corrosion rate of UO_2 [203] and consume water[204] which might be considered a benefit. Iron shot is the cheapest fill material and its geochemical effect of reducing concentrations of uranium are the most well tested of all the materials considered[177], [205], [206]. However, iron shot suspensions will likely exceed the density constraints even at the low concentrations necessary to increase the thermal conductivity of the gap (~same density as rock even at only 30% vol).

Solid materials inserted into the gap will likely make retrieval of the canisters more difficult in the long run (particularly ones that corrode) and this will also have to be taken into account. For high-heat generating wastes that are intended to be difficult to retrieve, silicon carbide and aluminum particles represent promising candidates due to abrasiveness and expansion during corrosion. Additional testing of these advanced materials would support the use of boreholes for very high-heat generating wastes (e.g., sodium fast reactors, cesium and strontium sources), which could be an additional niche application of boreholes.

3.4.4. Future work

3.4.4.A. Corrosion of graphite

In spite of the strong performance of graphite on the basis of thermal conductivity and density, it remains to be proven that it will be compatible with the waste canisters. Graphite is a noble material compared to most metals in sea water (even high alloy metals). Figure 1 shows the galvanic series for materials in seawater. When electrically connected to a material of greater activity, it is very likely to act as cathode and create a galvanic cell that accelerates corrosion of the less noble material. Table 3-18 shows the galvanic series for materials in seawater.

Table 3-18. Galvanic series for materials in seawater (modified from [183]).

	Platinum
↑Noble, passive (cathodic)	Gold
	Graphite
	Titanium
	Chromium stainless steel (13-30% Cr)
	Copper
	Nickel
	Tin
	Lead
	Chromium stainless steel (13% Cr)
	Steel, iron, Cast iron
Active, (anodic)↓	Aluminum
	Zinc
	Magnesium

The same phenomenon explains why aluminum and zinc can serve as sacrificial and protective anodes for steel. Loading of the disposal zone with graphite powder would be contrary to general recommendations for avoiding accelerated galvanic corrosion (of the metal canister):

1. Avoid putting materials of dissimilar activity in contact and with an electrolyte[183].

2. If dissimilar materials must be used in a system, the surface area of the cathode (more noble material) [207] should be small compared to the anode. The dissolution rate of the anode is proportional to the area of the cathode in galvanic cells[183], [208], [209].

The literature contains recommendations against using graphite for seals (e.g., gaskets, flanges) for metals in seawater environments[207]. Accelerated corrosion rates ~ 10× higher for alloy steels have been measured in systems where carbon fiber (with epoxy) reinforcement of metal

95

materials created a galvanic cell [210]. This could be avoided if titanium alloys (Ti-6Al-4V) are used, but corrosion will still increase with high temperatures [208] and the high cathode areas[211]. Another approach to enable use of graphite would be to prove that the disposal zone has an extremely low oxygen diffusion rate (which would cause galvanic corrosion rates to be proportionally smaller[211]).

3.4.4.B.   Solidifying materials

There are a number of promising gap fill materials that would solidify, thereby reducing access of water to the canister. From a hydraulic perspective, these materials are thus likely to be superior (i.e., less permeable) when compared to porous fill materials. However, they introduce greater uncertainty with respect to other factors. Table 3-19 presents a summary of some candidates that would serve as solidifying gap filler materials that should be investigated further (possibly with the high thermal conductivity additives evaluated here), particularly when retrievability requirements have been better defined.

Table 3-19. Emplacement, hydraulic, thermal, and chemical properties of MgO, sodium silicate and cement as gap filler candidates. Favorable properties are shaded in green, unfavorable properties are indicated by an *.

Material	Emplacement	Hydraulic	Thermal	Chemical
Magnesium oxide	*Has not been demonstrated in a borehole.	Low, hydration causes expansion.	Theoretically has a very high solid thermal conductivity [212]	Provides favorable reducing chemistry. *Soluble in water so geometry may change.
Sodium silicate	Setting time can be controlled, lower viscosity than cement. 177 °C temperature limit for gelation. [213]	Used to seal high permeability formations (seals host rock)[214]	Thermal conductivity can be improved with addition of particles, very low thermal contact resistance [215]	*Highly alkaline. *Gelation sensitive to site specific pore water chemistry, dissolved salts[213].
Cement	*Exothermic setting, maximum acceptable temperature during setting possibly exceeded with waste canisters.	Possible shrinkage [216]. Limited intrusion into host rock.	Thermal conductivity ranges 0.3-0.8 W/m-K. [217] Shrinkage may dominate thermal conductance.	

For all of these promising candidates, further experiments would be required to validate that emplacement is feasible and that there would be no harmful chemical interactions with the waste (with the exception of MgO).

3.5. Chapter Summary

This chapter presents improvements to the fundamental engineered components in the deep borehole concept, including the plug, canister, and fill materials. The newly proposed plug materials (a 30/70 clay and crushed rock mixture and MgO based expanding cement) readily achieve a permeability of 10^{-16} m^2, with 10^{-18} m^2 being a future design goal that could be justified with more detailed experiments at conditions characteristic of a deep boreholes. Canister design is updated to include the simultaneous effects of hydrostatic and axial crushing (not previously considered), and new canister dimensions are proposed for both PWR and BWR assemblies using standard oil well casings. More robust designs (suitable for depths ~5 km) are also presented, assuming that the canister can be custom fabricated to a desired thickness. The BWR

canister is smaller (0.219 m) and could be disposed in recently developed and generically designed deep boreholes (for the geothermal industry) at depths of 2.4 km with no additional technology development or changes. With casing dimension changes to the current, generic borehole design, the presented PWR and BWR canisters could be disposed to depths of 2.4 and 3.5 km (respectively).

Gap heat transfer mechanisms are reviewed and it is concluded that as long as there is a porous fill material in the gap, heat transfer will occur by conduction. Based on a series of experiments testing many candidates, a graphite based mud is proposed as the new reference design gap fill material. The mud has a thermal conductivity 5-7× greater than regular drilling mud (k~0.7 W/m-°K) and would reduce the peak temperature difference (at the time of emplacement) across the gap to < 1°C. Furthermore, it could provide lubrication benefits during emplacement. Canister fill materials of quartz sand and silicon carbide are experimentally shown to be effective at providing an additional barrier to crushing. Finally, the effect of fill material thermal conductivity is reviewed, and a high strength and high thermal conductivity zinc aluminum alloy is proposed for future DBD designs accommodating higher heat generating wastes.

4. Transport Model

4.1. Chapter Introduction

Accurately calculating the release rate and absorbed doses potentially resulting from geologically disposed radionuclides is inherently challenging due to the extremely long time scales and large number of physical phenomena involved. The large uncertainty associated with making predictions on geologic scales with interconnected physics and systems is commonly addressed with numerical and probabilistic methods: most recently these were used in the Yucca Mountain repository license application that was submitted to the NRC [218], [219]. This was achieved using Monte Carlo techniques, in which the (hundreds of) uncertain variables are each characterized by probability distributions, rather than deterministic values. Although sampling methods (such as Latin Hypercube) have been used to reduce the number simulations required for Waste Isolation Pilot Plant and Yucca Mountain performance assessments[220], it is still a very computationally and time intensive approach to understanding system performance. Furthermore, in light of the high complexity of these models, some have argued that alternative regulatory and performance assessment approaches would be more transparent [29] (e.g., setting performance criteria on individual parts of the system, rather than only using the final dose metric as the limit).

Analytical models are useful for building confidence and explaining the basis of more complex numerical models typically used for repository assessment. The reason for avoiding numerical models here is the benefit of succinctly expressing the solution to a highly complex calculation in the simplest possible form (without losing the fundamental characteristics or physical processes affecting the exact solution). Showing agreement between simple models (which are more easily explained to stakeholders) and complex models demonstrates a fuller understanding of the repository behavior and that the fundamental processes and parameters have been identified. The numerical and probabilistic approach may still be eventually necessary for evaluating and licensing deep borehole disposal; however, this thesis maintains focus on first developing and validating analytical models, which have the additional benefit of rapidly and clearly providing insights on the sensitivities of the system.

Without sustained vertical fluid flow to transport dissolved radionuclides to the surface, there is no credible mechanism for significant contamination of groundwater from a deep borehole

facility. This chapter begins with discussion of an analytically derived thermal-hydraulic model for vertical fluid flow in the repository and host rock. The energy and pressure balance model (derived in Appendix B) is tested and shown to give satisfactory (and conservative) agreement when compared to a fully coupled 3D numerical model over a wide range of conditions (such as decay heat production, domain size, and permeability).

The second portion of this chapter describes the solutions and parameters necessary to calculate the vertical transport rate of radionuclides and dose committed to an individual consuming them. Radionuclide transport begins with assumptions on canister radionuclide inventory, degradation rate and solubility, which together dictate the source concentrations of radionuclides in the disposal zone. Transport from the disposal zone to the surface occurs along an assumed preferential high permeability vertical flow path to the surface (for example, a permeable plug directly above the disposal), subject to the velocity determined by the thermal-hydraulic model. The 2D transport model accounts for advection, dispersion, radial diffusion, sorption, and radionuclide decay in both zones (the transport path and surrounding rock matrix). Radionuclide ingrowth is included by modifying the dose conversion factors for radionuclides with radioactive daughters. Finally, by combining the velocities obtained from Appendix B with the transport solution from Appendix A, the steady state (maximum) radionuclide concentrations at a specified vertical distance from the disposal zone are obtained. Radionuclide concentration and flow rate are then readily converted into estimates for absorbed dose rate to an individual assumed to be consuming the fluids from the preferential flow path.

4.2. Characteristic Scales of Transport

For each of the various transport phenomena (heat, molecular diffusion, pore pressures, etc.), the typical diffusivity (which can now be calculated from the material properties given in Chapter 2) represents a single, summarizing parameter that can be used to estimate the time scale on which each quantity is transported. Before going into the details of the transport model, it is critical to understand the representative time scales of each phenomenon so that simplifying assumptions and approximations can be made to reduce the complexity of this multi-physics, multi-scale, and multi-species problem of repository modeling.

The response time (1D analytical) approach outlined in the previous analysis (Eq. (2-4)), provides highly informative "characteristic" diffusion times for other transport phenomenon.

Table 4-1 presents a comparison of diffusivities and time scales of the key transport phenomena in deep boreholes.

Table 4-1. Characteristic times for the transport over 5 km for various physical phenomena involved in deep boreholes [85].

Phenomena	Value	Diffusivity (m^2/s)	Characteristic time (over 5 km)	Ref.
Hydraulic diffusion (Pore pressure response time)	D_{hydr}	10^{-3}- 10^{-2}	~1-10 years	
Thermal diffusion (heat flow)	$\dfrac{k_{th}}{\rho c_p}$	1.38×10^{-6} (calculated from reference properties)	574,000 years	[98]
Residence time of (stagnant brines)	-	-	80 million years	[65], [66],
Chemical/salinity diffusion (molecular flow)	D_m	$<3 \times 10^{-10}$ (measured from salinity profiles)	>2.64 billion years (~ Age of earth), beyond time horizon of concern for sole means of transport)	[15]
Mechanical strain rate of the crust (ductile deformation of crust)	10^{-18} to 10^{-19} s^{-1}	-	>>Age of earth	[86]

We see an 8 order of magnitude difference in the spatial diffusivity of the hydraulic, thermal and chemical phenomena. Generally speaking, the higher the diffusivity, the faster the quantity will reach a uniform (i.e., small gradient) distribution, and the more sensitive that particular physics will be to assumptions on the boundary conditions. In previous transient thermal models of deep boreholes [98], boundary distance (e.g., 200 m) and type (e.g., flux vs. temperature specification) significantly affected the thermal behavior in the long term. With the hydraulic diffusivity exceeding the thermal diffusivity, we expect the applied hydraulic boundary conditions (specifically, distance to boundary) to have an even greater impact on the hydraulic behavior of this system. A high hydraulic diffusivity is the basis of the simplified analytical model presented in Appendix A. As for chemical transport, even with the conservatively high diffusion coefficient selected, the characteristic time for diffusive transport is on the order of billions of years. Mechanical strain of the earth (e.g., movement of the crystalline basement) is also not a major concern.

4.2.1. Minimum significant velocity

In order to define a limit on convergence and determine if modeling errors are significant, the question of a "minimum" physical velocity must be considered. This estimate is also valuable to put the values of advection transport into perspective. Sleep and Zoback[87] give a simple expression for the characteristic Darcy velocity (created due to buoyancy) in a uniform geologic system,

$$v_D = \frac{kg\beta\rho\Delta T}{\mu} \tag{4-1}$$

where ΔT is the temperature difference between the water at a given depth and the surface, and k is the permeability. A 5 km depth with a 20 °C/km gradient corresponds to a temperature difference of 100°C. Evaluating the numbers,

$$v_D\left[\frac{m}{s}\right] = \frac{k(9.8)\left[\frac{m}{s^2}\right] * (6 \times 10^{-4})\left[\frac{1}{\circ K}\right](1000)\left[\frac{kg}{m^3}\right](100)[\circ K]}{(0.3 \times 10^{-3})\,[Pa - s]} \tag{4-2}$$

$$= k[m^2](1.96 \times 10^6)\left[\frac{1}{m - s}\right]$$

For permeability between 10^{-16} to 10^{-17} m^2, the characteristic vertical velocity is $\sim 10^{-10}$ to 10^{-11} m/s, or $\sim 6 \times 10^{-3}$ to 10^{-4} m/yr.

Another limit on the minimum resolvable or significant velocity could be based on the assumptions of a completely laterally uniform domain and topography. For example, in numerical models of the KTB borehole, lateral variations in heat generation and flow resulted (along with temporal variations in surface temperature) in lateral and slightly downward velocities on the order of 10^{-10} m/s ($\sim$0.3 cm/yr) in numerical models (see Figure 9 of [101]) within the upper 1500 meters of caprock. This translates to $\sim$0.3 cm/yr. To estimate the importance of this effect analytically, we assume a lateral variation of temperature of 5 °C over the lateral extent of the domain[87]. This results in a density difference of $\sim$3 kg/m^3 which results in a Darcy velocity,

$$v_D = \frac{kg\Delta\rho}{\mu} = \frac{k(9.8)\left[\frac{m}{s^2}\right](3)\left[\frac{kg}{m^3}\right]}{(0.3 \times 10^{-3})\,[Pa - s]} = k(9.8 \times 10^4) \approx k \times 10^5 \left[\frac{m}{s}\right]$$

102

Thus, for a permeability of 10^{-17} to 10^{-16} m^2, 10^{-11} to 10^{-12} m/s is could be an estimate for the lowest significant Darcy velocity (below which, modeling uncertainties related to topographic or other lateral variations are equivalent to numerical errors).

Another limiting velocity may be calculated from residence times that have been recorded (e.g., using I-129 dating methods) at sites. For a steady system, the residence time of a fluid with a advection velocity (v_a) traversing a distance of rock H is given by Eq. (4-3),

$$\tau_{res} = \frac{H}{v_a} \tag{4-3}$$

where the advection velocity is higher than the Darcy velocity by a factor of the porosity of the rock, as shown in Eq. (4-4),

$$v_a = \frac{v_D}{\phi} \tag{4-4}$$

Inserting Eq. (4-4) into Eq. (4-3) gives Eq. (4-5),

$$v_D = \frac{H\phi}{\tau_{res}} \tag{4-5}$$

Table 4-2 compares variations in velocities created by modeling uncertainties with stagnant velocities calculated from residence times at sites in Germany and Canada.

Table 4-2. Comparison of velocities and residence times, based on estimates of minimum velocities in the system and typical stagnant brine fluid systems. H= 5 km.

v_D (m/s)	ϕ	v_A (m/s)	τ_R (Residence time in yrs)	t/τ_R (# of pore volumes transported in 1 mY)
10^{-11}	1%	10^{-9}	158,700	6.3
10^{-12}	1%	10^{-10}	1.587 million	0.63
*1.59×10^{-14} to *1.59×10^{-13}	0.1% to 1%	1.59×10^{-12} to 1.59×10^{-11}	10 million (in KTB borehole [66])	0.1
*2 ×10^{-14}	1%	2 ×10^{-12}	80 million (in Canadian Shield mine [65])	0.013

* Calculated based on the residence time given in the reference, assuming a domain size of 5 km.

The number of pore volumes transported in 1 million years is another useful metric for the chemical inactivity or stability of the system, especially when discussing the possibility of certain chemical reactions that may be limited by supply of reactants (e.g., oxygen, other sources of free energy[87]). For example, chemical changes and degradation in cement typically happens after 5,000-10,000 pore volumes have passed through the cement [221]. Thus, under ideal bedrock conditions (with small existing velocities), the pore fluid residence time is very high, decreasing the rate of potentially deleterious (or difficult to model) chemical reactions.

Modeling uncertainties (variations in assumptions, model capabilities) may result in velocity variations as high as 10^{-12} m/s, but these could in principle be addressed with additional model refinement and details. Based on the residence time data (KTB and Canadian Shield), convective Darcy velocities that are on the order of 10^{-14} m/s and lower are effectively zero or "stagnant". For such a velocity and with a porosity of 1% (fourth row) a conservative tracer only travels 1.3% of the domain (65 meters) in 1 million years. In this case, the thermal output of the waste would not be a significant driving convective transport mechanism for radionuclides and diffusion is likely to be the dominant transport mechanism.

4.3. Thermally Driven Fluid Transport

Typically, the first step in evaluating the performance and limitations of deep geologic disposal is to calculate the spatial temperature response of the waste and surrounding rock. Many of the early repository design and evaluation efforts in the 70's and 80's focused on thermal loading and temperature distribution as a performance metric and limit on the capacity of the repository[202], [222], [223]. With the shelving of the Yucca Mountain repository, generic thermal modeling is still the initial basis for repository comparisons [224] and methods to reduce thermal loading of repositories are frequently considered (e.g., through burnup modification[225], transmutation[226], cooling periods, etc.) This is generally because:

1. Some reactions affecting waste barriers that are kinetically limited at low temperatures may become important at hot repository conditions [227].

2. High temperatures may lead to undesirable perturbations in the host rock and engineered barrier properties (i.e., near field thermo-mechanical criteria) [228].

3. Transport mechanisms such as expansion and buoyancy driven convection are inherently thermally driven (i.e., far field thermo-hydrologic criteria) [229].

Previous work at MIT focused on evaluating temperature increases in the borehole repository as a single physics problem [20], [98], [230]; more recently, the coupled thermal-hydraulic nature of the problem has been addressed, and it was proposed that large salinity gradients could play a role in preventing natural convection [108].

4.3.1. Onset of natural convection

From the preceding list of thermal limitations on repository design, a distinction between thermal expansion and buoyancy driven (sometimes referred to as natural circulation) flows must be established. While they both result from expansion of fluid (i.e., density changes), buoyancy driven flows are a much more complex (inherently instable, chaotic) and involve coupled (thermal-hydraulic-chemical) phenomena; in relative terms, fluid expansion can be modeled more simply as a volumetric injection process. Convection is further complicated by high sensitivity to boundary conditions and geometry, making it difficult to generalize. Despite this complexity, linear and homogenous approximations are frequently used to draw conclusions (e.g., infer bounds on material properties, history) about significantly heterogeneous and real systems. For example, the thresholds for natural convection are particularly important in the field of geosciences [67], [82], [87] where convection must be understood as a transport mechanism for minerals, fluids, and heat. At the most fundamental level, the conditions governing the onset of convection are demonstrated and exemplified in the classic Rayleigh-Benard cell, in which parallel plates are uniformly heated and cooled to a point at which fluid circulation begins. A slight modification of the Rayleigh-Benard cell involves a saturated porous medium (instead of a pure fluid). Figure 4-1 presents the parameters of an idealized (1D) porous convection system.
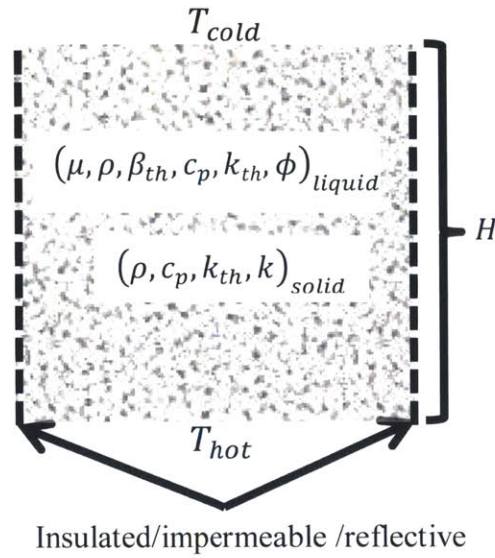
Figure 4-1. Diagram of an idealized, 1D permeable cell with horizontal, heated walls

The material properties (of the solid and liquid) relevant to convection are shown in Figure 4-1. By far, the parameter with the greatest variability and effect in this system is the permeability of the solid matrix, which governs the viscous forces that inhibit convection. Although a positive buoyancy driving force may exist in the system, a certain instability criterion must be met before the fluid circulates in a sustained manner. In order for convection to occur, the motion of the heated fluid (which is driven by buoyancy forces and inhibited by viscous and drag forces) must occur before redistribution of thermal energy within that fluid can occur via conduction.

If the buoyancy forces overcome the viscous forces, instabilities may form where lobes of hotter less dense fluid move upward, counterbalanced by cooler and more dense fluid moving downward (thereby transporting fluid, chemical species, thermal energy, etc.) The onset condition, as determined by a (linearized) stability analysis of the governing equations for fluid flow is expressed in terms of a dimensionless Rayleigh number[231]–[233] , defined in Eq.(4-6),

$$Ra_{c,p} = \frac{g(\Delta\rho_T)Hk_m}{\mu\alpha_{eff}} = \frac{g(\rho\beta_{th,w}\Delta T)Hk_m}{\mu\alpha_{eff}} > 14 \text{ to } 4\pi^2 \tag{4-6}$$

where $Ra_{c,p}$ is the critical porous Rayleigh number, the density change with temperature $\Delta\rho_T = \rho_{avg}\beta_{w,th}\Delta T$ can be linearized, $\beta_{th,w}$ is the thermal expansion coefficient of water ($\sim 7\times10^{-4}$

106

1/°C) (see Appendix B.3) , H is the height of the porous cell considered, ΔT is the temperature difference across the cell and k_m is the permeability of the porous matrix. The value of $Ra_{c,p}$ can change by about a factor of two, depending on the specific boundary conditions used (e.g., constant heat flux vs. temperature, impermeable vs. permeable boundaries). The effective (or special [231]) thermal diffusivity is defined in Eq.(4-7),

$$\alpha_{eff} = \frac{k_{th,2ph}}{\left(\rho c_p\right)_f} \qquad (4\text{-}7)$$

In essence, the Ra number may be viewed as the ratio of the driving force for fluid motion (gravitational buoyancy) to the forces opposing fluid motion (primarily, the viscous losses of fluid transport in a porous medium). Overall, k_m is the key parameter in determining (or inhibiting) the possibility of significant geothermal temperature disturbances caused by forced convection [114]. A key outcome of this analysis is that if the temperature gradient is not perturbed significantly from a purely conductive one, then fluid convection may be ruled out as a preexisting transport phenomenon. Thus, the presence of a geothermal conductive temperature gradient may be used as one indicator for the suitability and hydraulic properties of a deep borehole site. For the expected geothermal gradient magnitude (~15-25°C/km) and typical rock thermal properties, Rayleigh number analysis shows that a concordance of temperatures with a conductive gradient sets an upper bound on the host rock permeability to <10^{-14} m^2 [87].

While this analysis allows us to rule out the presence of existing convection at a deep borehole site, further analysis is required to conclude that the fluids will remain stagnant after the SNF and additional thermal energy is introduced to the system. As prior thermal modeling has shown[98], the deep borehole repository's unique geometry (aspect ratio and orientation) promotes heat conduction radially away from the disposal zone. This geometry maximizes the surface area to volume of the waste, so the thermal energy is spread across the largest mass of rock in the smallest period of time. The temperature peak therefore occurs very quickly (within 10 years of emplacement), far sooner than other repository designs. The combined effect is to significantly reduce the long term vertical temperature gradient, which is the driving force of concern. After heat has been distributed radially and uniformly (~3000 years) it begins to be conducted vertically to the surface. At this point, the temperature elevation in the rock surrounding the disposal zone is limited to 10-20° C above ambient temperature.

Using the 2D analytical method described previously, a simplified and conservative representation of the system can be developed and assessed. The boundary conditions and steady state assumption imply that the entire disposal zone (radially infinite) is held at a fixed temperature. In this homogenized approach, bounding (and extreme) values are used to compensate for the lack of spatial variation allowed by the analytical method. Thus 150°C, which corresponds to the maximum canister centerline temperature experienced for a brief (<10 year) period[98], is used as a conservative value for the disposal zone temperature. This temperature difference (65° C above the ambient temperature at 3 km) is ~3 times greater than a best estimate (long term and relatively radially uniform) value of 20°C obtained from[98]. Table 4-3 and Figure 4-2 show the conservative values used to assess whether natural convection would be possible in the porous media above the disposal zone.

Table 4-3. Conservative values used to assess the possibility of convection due to deep borehole disposal facility.

Variable	Value	Description
H (m)	3000	The maximum length of the plug and overburden to the surface is 3000 meters (assuming total maximum depth is 5 km, and a 2 km long disposal zone)
k_m (m^2)	1×10^{-16}	The permeability of host rock/plug zone between 100-500 m used in (Ref. [96]).
g (m/s^2)	9.8	-
$\rho_{c,f}$ (kg/m^3)	999.7	Density of water at the surface at temperature of 10°C
$\rho_{h,f}$ (kg/m^3)	927.43	Density of water at 150°C, the maximum canister centerline temperature for the 200 m borehole pitch case [98], assumed here to exist at the start of the disposal zone at 3 km and under hydrostatic pressure of 196 bar. Note that the ambient (initial) temperature at this depth assuming a 25 °C/km gradient and 10°C surface temperature is ~85°C.
μ_f (Pa-s)	3.56×10^{-4}	Water dynamic viscosity at average temperature (80°C).
$c_{p,f}$ (j/kg-°K)	4194	Water specific heat at average temperature (80°C).
$k_{th,f}$ (W/m-°K)	0.666	Water thermal conductivity at average temperature (80°C).
$k_{th,s}$ (W/m-°K)	3.0	Conductivity of the rock.
α_{eff} (m^2/s)	7.42×10^{-7}	Effective thermal diffusivity of the overlying rock.
Ra_p	4.02<14-39.5	The Ra_p is less than the critical value necessary for convection.

Cooled wall boundary
condition (Surface T=10°C)

Overlying rock
and plug
$k_m = 10^{-16}$ m^2
$k_{th} = 3.0$ W/(m-K)
$\alpha_{eff} = 5.11 \times 10^{-7}$

Equivalent 3D
domain extends
in each direction

Waste
emplacement
zone

Heated wall
boundary condition
(T=150°C)

- - - - Adiabatic, impermeable
boundary
(reflective)
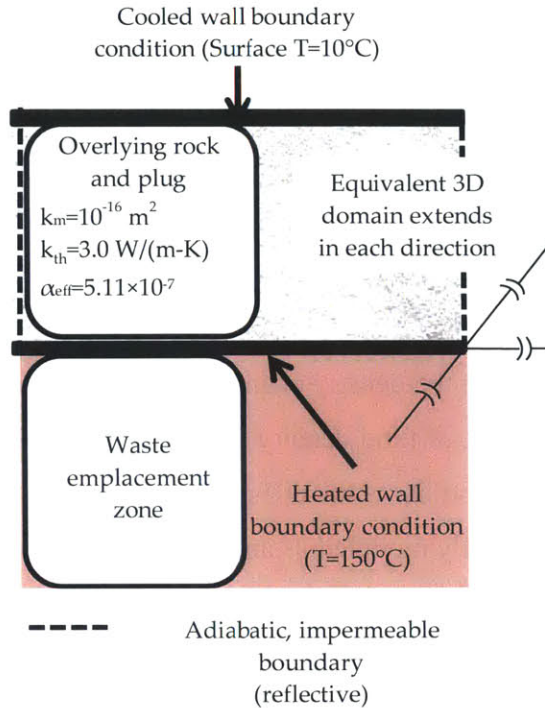
Figure 4-2. Diagram of the conservative conditions assumed in a deep borehole repository to assess the possibility of natural convection.

The results from Table 4-3 and Figure 4-2 suggest that even if the entire disposal zone remained at the peak canister centerline temperature for all time, natural convection would still not be initiated in the overlying rock. For the assumed temperatures, the critical overlying rock permeability (at which $Ra_p = 14$-39.5 and convection would be possible) is calculated to be 1.73-4.93×10^{-15} m^2. Thus, a suitable deep borehole site (without significant salinity that increases with depth) should have an overlying rock permeability lower than this range ($< 10^{-15}$ m^2)

4.3.2. Stratification due to salinity

If groundwater salinity and density increases with depth (as is indicated by saline groundwaters North American Craton and Fennoscandian Shield) the convection problem becomes coupled with chemistry (in addition to the thermal-hydraulic physics already involved). Densities at depths of 1-2 km are expected to be between 50-200 kg/m^3 greater than pure water, due to the effect of dissolved salts (see Figure 2-3). Downward increasing concentration tends to stabilize the system against the destabilizing effect of water thermal expansion. Convection in the presence of concentration gradients is referred to as thermohaline convection. To determine the

conditions for the onset of thermohaline convection, another characteristic parameter, the solute (salinity) Rayleigh number is needed. The solute Rayleigh number, analogous to the Rayleigh number, is defined as Eq. (4-8),

$$Ra_s = \frac{g\Delta\rho_s H k_m}{\mu D_m} = \frac{g\rho\beta_c(\Delta C)H k_m}{\mu D_m}$$

(4-8)

where Ra_s is the solute Rayleigh number, the density change with salinity $\Delta\rho_s = \rho_{avg}\ \beta_c\Delta C$ is sometimes linearized, β_c is the coefficient of fluid density change with salinity (m^3/kg), ΔC is the concentration difference across the cell and D_m is the diffusivity of solutes (ions). The density change (with respect to salinity) is typically modeled as an independent effect from temperatures and pressures[113], [114]. The conditions for oscillatory convection (where convective cells continually form and vanish) are more easily met than the conditions for stable convection[114]. The condition for oscillatory convection [114] is written as Eq. (4-9),

$$Ra_p > Ra_s\left(\frac{D_m}{\alpha_{th}}\right) + 4\pi^2\left(1 + \frac{D_m}{\alpha_{th}}\right)$$

(4-9)

Since the effective molecular diffusivity (10^{-13} to 10^{-9} m^2/s) in the rocks is so much smaller than the thermal diffusivity (10^{-6} to 10^{-7} m^2/s), the right-most term is negligible compared to 1. Thus Eq. (4-9) simplifies to Eq. (4-19),

$$Ra_p > Ra_s\left(\frac{D_m}{\alpha_{th}}\right) + 4\pi^2$$

(4-10)

Inserting Eq.(4-6) and Eq. (4-8) into Eq. (4-19) gives Eq. (4-11),

$$\frac{g\Delta\rho_T H k_m}{\mu\alpha_{th}} > \frac{g\Delta\rho_s H k_m}{\mu D_m}\left(\frac{D_m}{\alpha_{th}}\right) + 4\pi^2$$

(4-11)

Note that when the rock permeability is low and salinity differences are small or zero, the criterion reverts to the original criterion for convection- Eq.(4-6)- and the criterion is dominated by the $4\pi^2$ term. Grouping and cancelling terms,

$$\Delta\rho_T > \Delta\rho_s + 4\pi^2 \left(\frac{\mu\alpha_{th}}{gHk_m}\right) \tag{4-12}$$

When the rock permeability is large the criterion for convection becomes dominated by the salinity term, allowing for the simplification shown in Eq. (4-13),

$$\Delta\rho_T > \Delta\rho_s \tag{4-13}$$

Which is essentially the same criterion used by Driscoll et. al. [108] in previous analyses on salinity and density in deep boreholes. Intuitively, the criterion means that as long as the density increase due to salinity counterbalances the density decrease due to thermal expansion, the system will remain stagnant (not convective). In other words, a sufficiently large salinity gradient acts as a barrier to convection that is independent of the rock's thermal hydraulic properties. These results are clearly explained in Figure 4-3, which shows the Rayleigh number and critical Rayleigh numbers vs. the overlying rock permeability.
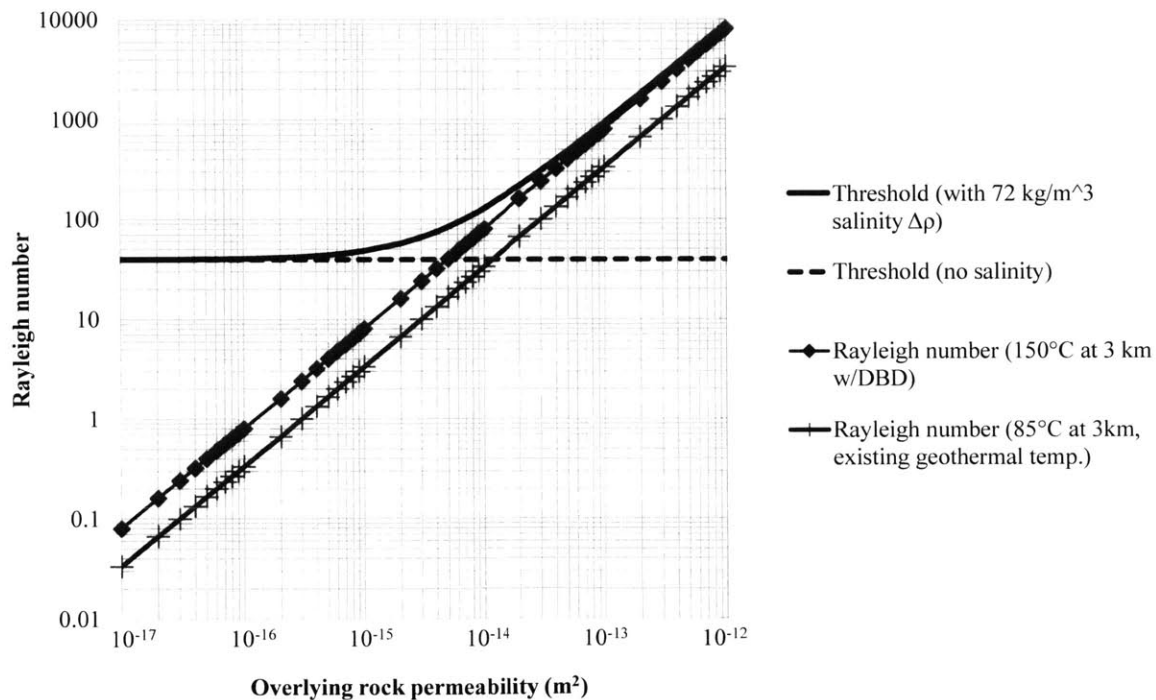
Figure 4-3. Rayleigh number (Ra$_p$, Eq.(4-6)), and critical Rayleigh numbers for oscillatory convection (Eq. (4-9),) vs. permeability (m^2) for a horizontal layer of thickness H = 3 km and temperature gradient of 46.6°K/km created by the disposal zone+geothermal gradient (diamond) and a temperature gradient of 25°K/km created by the geothermal gradient alone (cross).

The bottom line in Figure 4-3 shows the Raleigh number of the system (vs. permeability) before the DBD is implemented. The graph clearly shows that 10^{-14} m^2 would be an upper bound on the existing permeability of the system (otherwise, convection would already be apparent, and the site would not be acceptable). The net effect of introducing DBD is to increase the temperature gradient and shift the line upwards. Thus, there could be a special case where convection did not preexist, but the introduction of DBD pushes the system into a state where convection is possible (e.g., if $5\times10^{-15}<k_m<10^{-14}$ m^2). The previous recommendation of ensuring that host rock permeability is less than 10^{-15} m^2 would provide safety against this possibility. However, including the effect of salinity profoundly changes the threshold. Using the expected salinity and density gradients- see Eq. (2-17) and Eq. (2-18)- it can be shown that depths greater than 1200 meters provide a minimum salinity density difference >72 kg/m^3 necessary to offset the thermal expansion density decrease caused by DBD (represented by in Eq. (4-13)). The nature of this Raleigh number analysis assumes that the salinity varies linearly between the depths of 3 km and the surface. The criterion for convection (without salinity) is shown by the dotted line, while the criterion including a $\Delta\rho_s$=72 kg/m^3 is shown by the solid line. Thus, an overlying host rock with permeability >5×10^{-15} m^2 and zero salinity gradients would experience convection with DBD; however, if the salinity effect on the convection threshold is included, the requirements for convection are never met, regardless of the host rock permeability. Increasing permeability above the values shown in Figure 4-3 does not change the result because of the linear dependence of Ra and Ra$_s$, apparent in Eq. (4-11).

Overall, these results suggest that the (expected) downward increasing salinity and density (at depths >1000 m) would very effectively prevent convection from occurring, even in the presence of conservative vertical temperature gradients created by the DBD. Without salinity, an overlying rock permeability <10^{-15} m^2 is sufficient to prevent convection.

In addition to these theoretical considerations related to convection, disposal at sufficient depths to reach highly saline waters (>1000 meters) is preferable because the distinct contrast in composition and chemistry between fresh and saline groundwaters indicates that there cannot be very rapid infiltration of groundwater across the boundary between fresh and saline groundwaters. The residence times of such saline waters must be considerably longer than those of freshwaters, improving confidence that the site is appropriate for long term waste disposal.

4.3.3. Thermal expansion driven flow

Having ruled out convection as a significant transport mechanism in the overlying host rock, attention is focused on the transport phenomenon of thermal expansion. Appendix B presents the assumptions and derivation of a 1D analytical model for the thermal expansion rate and resulting vertical velocity in a deep borehole repository overlain by caprock with homogenous (Section B.3) and heterogeneous (Section B.4) hydraulic properties. The key conclusions that can be derived from this analytical model for fluid velocities are summarized below:

1. Total water flow, expansion, and vertical travel distance are driven by the cumulative heat production of the waste.

2. Vertical velocities in all regions are proportional to the decay heat production rate with time.

3. Flow is decoupled and independent of the spatial temperature distribution. Pressure is assumed to diffuse rapidly to the radial boundary, setting up a radially uniform pressure gradient that drives all introduced volume towards the surface.

4. The ratio of flow in either the plug or host rock is determined by the relative resistance that each path provides (analogous to electric resistors in parallel), where the resistance is proportional to $(kA)^{-1}$ (permeability$\times$area)$^{-1}$ of that path.

5. Because the area of the borehole plug is so small in comparison to the entire domain, it does not significantly affect the total hydraulic resistance and pressure increase (unless the permeability difference between the plug and rock is greater than 4 orders of magnitude).

The model developed in Appendix B greatly simplifies the calculation of vertical velocities as it decouples the spatial temperature distribution problem from the pressure distribution and flow problem. The justification for this decoupling is the large difference in the diffusivity of each physical phenomenon (pressure, temperature). To support this analytical model and provide the ability to model more complex geometries, a flexible numerical model called BVR (Borehole Virtual Reality) is currently being developed by Nazar Lubchenko at MIT. The starting point for this code was Idaho National Laboratories' Multiphysics Object Oriented Simulation Environment (MOOSE), which provided a finite element based solver capable of simultaneously treating the multiple physics that are desired in the BVR model (thermal, hydrologic, mechanical

and chemical). Specifically, the fracturing and liquid conservation (FALCON) and reactive transport (RAT) codes provided many useful existing and modularized "kernels"- mathematical constructs that translate and discretize the physical governing equations into systems of equations that may be solved across the entire domain.

Currently, BVR has been set up to solve thermal and hydraulic problems, while chemical and possibly mechanical physics are to be added in the future. With the complex thermal and hydraulic modeling capabilities of the BVR code, it is possible to validate a more convenient analytical model for fluid (and radionuclide) transport. In the following section, we present a detailed comparison of results obtained from the numerical method (BVR) and this analytical method.

4.4. Comparison of Numerical and Analytical Models

4.4.1. Homogenous case

The starting point for comparing the numerical model with the analytical model is the simplest possible case: a completely homogenous domain (entirely crystalline host rock) with the generic hydraulic and thermal properties summarized in Sections 2.3 and 2.4. As discussed previously, a rock permeability of 10^{-16} m^2 is an approximate upper limit for the host rock granite (if permeability was significantly higher than this, natural convection from the geothermal heat gradient would be apparent and the site would be avoided). 10^{-16} m^2 has also been deemed achievable for the plug as well, using clay/sand mixtures[137]. Thus, while the assumption of homogenous properties may seem overly simple, it should be achievable and realistic for an appropriate site (containing low permeability granite starting at the surface) and using the plug design discussed previously. The key parameter of the disposal zone (accounted for by the analytical model) is the volumetric heat generation rate and volume. The properties for the homogenous caprock and disposal zone are summarized in Table 4-4.

Table 4-4. Summary of rock and disposal zone properties assumed for first comparison of the analytical and numerical models.

Depth (m)	Lateral Extent	Region	Permeability (m^2)	ϕ*	Density (kg/m^3)	Thermal conductivity (W/m- °K)	Specific heat (J/kg-°K)
3000	200 m by 200 m square area surrounding a single borehole. Numerically, ¼ symmetry is used.	Crystalline rock matrix	1×10^{-16}	1%	2750	3.0	790
5000	0.17 m radius	Disposal zone	1×10^{-16}	1%	4405**	0.628**	499

*interconnected water filled effective porosity
**assumed in numerical model only, not used by the analytical model

A very important assumption in both models is that the lateral boundaries (drawn at a 100 m distance from the center of the borehole) are closed or reflective (both in the thermal and hydraulic senses). The bottom boundary at 10 km was also modeled as closed, which represents the fact that the rock becomes effectively impermeable with great depths (at the brittle to ductile transition)[84]. In the numerical model, the surface (i.e., ground) represents the only open boundary (or sink) in terms of hydraulic and thermal quantities (and is modeled with a constant pressure and temperature conditions). In other words, any volume or heat introduced into the system eventually must travel vertically and be removed at the surface. Thus, this case effectively represents a highly conservative scenario for thermal energy buildup and vertical water transport: an infinite square array of boreholes separated only by 200 meters, underlain by impermeable rock. The volumetric decay heat production of the disposal zone is based on the (conveniently integrated) analytical correlation previously used for deep borehole thermal modeling[98] and is shown in Appendix B (2176 W/m^3 at the time of disposal, assumed to take place after t$_c$=25 years of surface cooling). The numerical model incorporates some additional details (e.g., the borehole disposal zone thermal properties are explicitly modeled and a geothermal flux of 45 mW/m^2 is assumed at the bottom boundary). However, these should not affect the comparison with the analytical model, which is only concerned with the velocities in the upper caprock region (as long as convection is not naturally occurring due to this geothermal heat flux). The geothermal heat flux should not affect the thermal expansion rate or vertical

velocities because the energy is always steadily removed at the surface via conduction (and/or convection to the atmosphere), so there is no buildup of this thermal energy in the domain. In addition, the numerical model uses temperature and pressure dependent water properties throughout the domain, while the analytical model assumes a constant thermal expansion coefficient and does not account for compressibility effects. The analytical prediction of Darcy velocity in this "homogenous" case is written as Eq. (B-15),

$$v_D(t) = \frac{\dot{V}_{inj}(t)}{A_{DBD}} = \frac{\beta_{w,th}}{A_{DBD}} \left(\frac{\phi}{\rho c_p}\right)_m \dot{Q}(t) \tag{B-15}$$

where $\dot{V}_{inj}(t)$ is the volumetric injection rate (m^3/s) due to thermal expansion, $\beta_{w,th}$ is the average thermal expansion coefficient of water ($\sim 8.35 \times 10^{-4}$ °C^{-1}), A_{DBD} is the area of the (semi-closed) square deep borehole field (in this case, 200×200 m), and the subscript m denotes the properties of the host rock matrix. From this equation, it may already be noticed that the assumption of a small, closed domain has a profound effect on the calculated vertical velocities. On the other hand, the host rock permeability (assumed in the first row of Table 4-4) does not affect the velocity in this homogenous case. Physically, this occurs because the fluid injection is inherently assumed to be entirely accommodated by vertical flow, regardless of the resistance to flow. Figure 4-4 presents a comparison of the predicted velocities for the analytical and numerical models in this homogenous case.
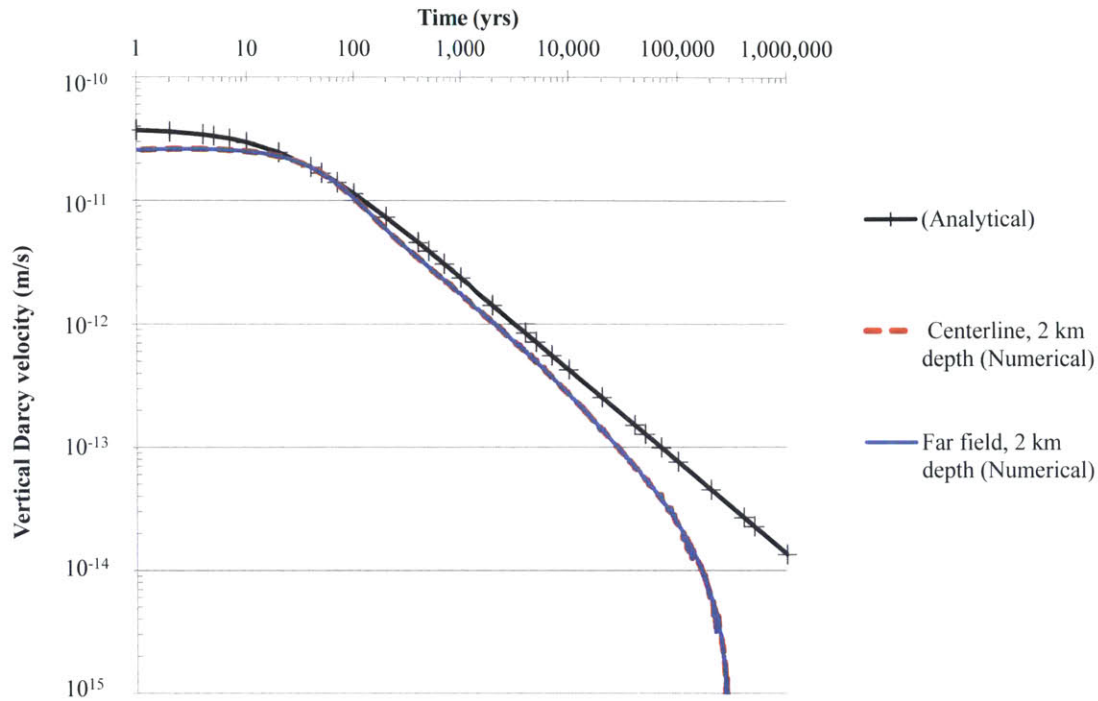
Figure 4-4. Comparison of vertical Darcy velocity vs. time for the analytical and numerical (BVR) models, assuming uniform host rock and plug properties in an infinite array of boreholes with 200 meter square spacing.

The vertical velocities fall according to the decay heat (at a rate of $t^{-0.75}$) which directly supports the analytical models' assumption of a thermal expansion mechanism and a decoupled spatial temperature pressure field (i.e., the pressure increase is only a function of the energy input, not the temperature distribution).

Note that the analytical model (indicated by the solid line with markers) predicts uniform vertical velocities throughout the entire caprock (0-3 km) (i.e., there is no theoretical difference between the centerline and far field velocities). This is consistent with the numerical results, depicted by the coincident dashed and solid lines representing the centerline and far field velocities, respectively. Not shown are the numerically predicted velocities at 1 km depth, which in this case are identical to the velocities at 2 km. The numerically predicted vertical velocity precisely at 3 km is slightly higher than reported here, due to very localized (<50 meters) convection effects on the edge of the canisters (top of the disposal zone). Other than this slight difference, the analytical model conservatively predicts the vertical velocity across all time periods. The early overprediction of velocities can be explained by fluid compression effects

117

(discussed in more detail in Appendix B.2), which is a result of the large pore pressure increase ($\sim 10^5$ Pa) caused by fluid expansion in the disposal zone. The rapid fall in numerical predictions after 100,000 years is likely due to the effect of heat removal at the surface over long time periods, which tends to reduce the fluid expansion and is conservatively neglected in the analytical model. At 300,000 years, the numerical velocities in the plug and matrix fall off rapidly and actually become negative. Negative velocities could be due to a reduction in the average water temperature from the peak value (compared to the earlier period), causing a shrinkage in volume.

The total vertical penetration distance derived in Appendix B.5 (which is the integral of the Darcy velocity shown above, divided by the porosity) characterizes the importance of advection transport in this system. At 1 million years, the analytically predicted total vertical penetration distance is only 169 meters, which is insignificant compared to the length of the caprock zone (2000-3000 meters). The numerically predicted maximum penetration distance of 44 m is significantly less than the analytical prediction, because the numerical model accounts for heat losses at the surface (and uses more realistic and less conservative equations for calculating fluid expansion). In other words, if 10^{-16} m^2 permeability could be achieved for all regions, radionuclides are not driven by advection beyond a distance of 170 m above the disposal zone at 1 million years.

4.4.2. Heterogeneous "base" case ($k_p = 10^{-15}$ m^2)

The heterogeneous case (hereafter referred to as "base case") addresses a reasonable concern that the (engineered) plug may be fractured and have a higher permeability than the preexisting host rock (assumed in this case to remain at a permeability of 10^{-16} m^2). This case inclusively treats the possibility that the host rock surrounding the plug zone may have significantly increased in permeability during excavation (also referred to as "excavation damaged zone"). The behavior and governing equations of the heterogeneous base case with a plug region of different permeability are derived in Appendix B.4. Although 10^{-16} m^2 is an achievable design goal using clay/sand mixtures[137] and solutions to seal/heal the disturbed rock [213], [234], this base case assumes that the plug/disturbed rock permeabilities are higher than the host rock by an order of magnitude (10^{-15}m^2). In addition, the plug zone is assumed to have a slightly larger radius (0.4 m) than the borehole (0.17 m), which is consistent with how deep boreholes are drilled

(generally narrower at greater depths). The total domain size is the same as before (200 × 200 m), which tends to maximize the pressure increase and thus vertical flow of water. The resulting pressure increase (caused by thermal expansion) is effectively the same as the previously discussed homogenous case because the plug area is so small that it does not affect the total hydraulic resistance to vertical flow from the disposal zone. Thus, since the vertical pressure gradient is the same, but the plug permeability is 10× higher, the Darcy velocity in the plug is expected to be 10× higher as well. This effect, along with a comparison with the numerical predictions, is clearly demonstrated in Figure 4-5.
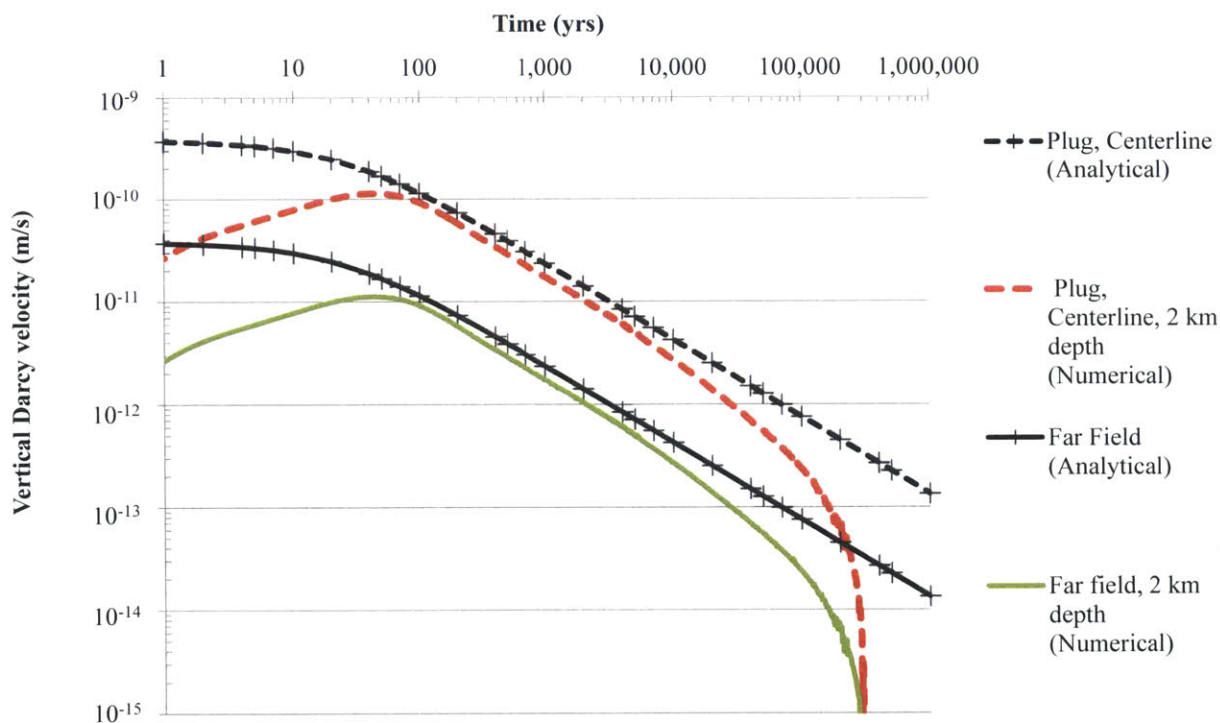
Figure 4-5. Comparison of vertical Darcy velocity vs. time for the analytical and numerical (BVR) models assuming heterogeneous host rock and plug properties ($k_p=10^{-15} m^2$) in an infinite array of boreholes with 200 meter square spacing.

Again, the velocities follow the decay heat profile, according to the relationship ($t^{-0.75}$). The numerical and analytical models behave as expected, with the plug (centerline) velocity exceeding the far field rock matrix velocity by a factor of 10. Thus, the vertical travel distance within the plug (assuming an equal porosity of 1%) is 10× further compared to the homogenous case and the surrounding matrix (1.69 km in the plug, vs. 169 meters). While this does represent a significant penetration distance into the caprock, it is still not enough to result in finite

radionuclide concentrations at the top of the plug, or enough to begin satisfying the analytical coupled advection and diffusion solutions discussed in Appendix A.

4.4.2.A.   Base case with rock compressibility

As discussed in detail in Appendix B.2, the compression of the rock and its pore fluids at elevated pressures significantly affects how the medium accommodates fluid injections (e.g., from thermal expansion of fluids or direct injection) . Particularly when pressure increases are large (>10^5 Pa), compressibility significantly affects the storage capacity and time dependence of flow within the rock. Reference pore compression parameters and models that relate pore compression to the diffusion of pressure are discussed in Section 2.3.1. For this variation on the previous base case, the effect of rock compressibility was added within BVR. A rock compressibility (c_r) of 4.62×10^{-12} Pa^{-1} previously shown and defined in Table 2-2 and Eq. (2-10),

$$D_{hydr} = \frac{k}{\mu(\phi\beta_f + c_r)}$$

(2-10)

was applied during the solution of the pressure diffusion equation (governed by the hydraulic diffusivity D_{hydr}) in all regions including the higher permeability plug. Thus, the fluid compression (β_f) is still calculated exactly at all points in space by BVR's internal fluid property routines, but now a separate rock compressibility term has been added in the pressure diffusion equation. Figure 4-6 shows a comparison of the analytical and two sets of predicted numerical velocities for the plug and host rock, where one set of the numerical velocity predictions accounts for compression.

120
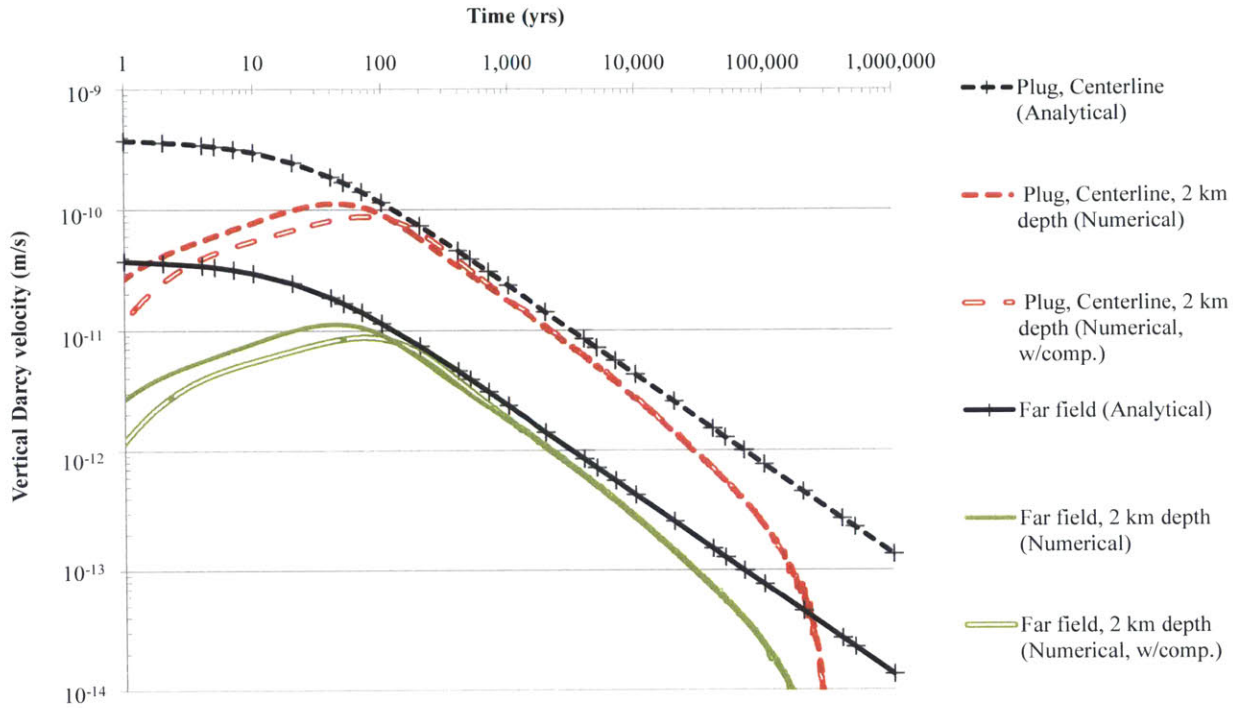
Figure 4-6. Comparison of vertical Darcy velocity vs. time for the analytical and numerical (BVR) models assuming heterogeneous host rock and plug properties ($k_p=10^{-15} m^2$) in an infinite array of boreholes with 200 meter square spacing, accounting for rock/pore compressibility effects (hollowed lines) in BVR.

As intuitively expected, the pore compressibility effects are only important at early time periods when the pore pressure increase is very large. Eventually, when the pressure decreases, there is no difference between the velocity predicted in both numerical models (with and without rock compression). In the very long term, pore compression does not affect the velocity (or even distance travelled by the fluid) because compression essentially provides a time delay to the flow of current (similar to the effect of a capacitor). This can be observed in the slight overshoot of numerical predicted velocities (between 100 to 1000 years) which compensates for the earlier period of lower velocities.

4.4.2.B. *Base case (with variation in decay heat production)*

Another realistic variation is based on total decay heat production which could be significantly less if the fuel has lower burnup than 57 MW-d/kg (previously assumed in correlations and numerical simulations). Since the cumulative decay heat production theoretically determines the total vertical travel distance of the radionuclides, it could serve as metric to compare different

121

disposal scenarios. The cumulative thermal energy produced out to 1 million years (and thus cumulative volume of water discharged in the disposal zone) approximately scales with the burnup of PWR fuel [225]. Halving the total decay heat therefore approximates the cumulative decay heat production of 30 MW-d/kg fuel that has been cooled for 25 years, which would be more characteristic of the current inventory of ~70,000 MTHM of SNF. Alternatively, doubling the decay heat that has been used here would approximate PWR fuel with a burnup of ~120 MW-d/kg. The cumulative decay heat could be significantly higher for other fuel types such as sodium fast reactor fuel, separated vitrified reprocessing wastes, or reconstituted fuel rods which can be loaded to increase the volumetric heat rate. Thus, we compare the analytical and numerical model's abilities to predict the variations in velocity in these decay heat variation cases. The results for the halved and doubled decay heat cases are shown in Figure 4-7 and Figure 4-8, respectively.
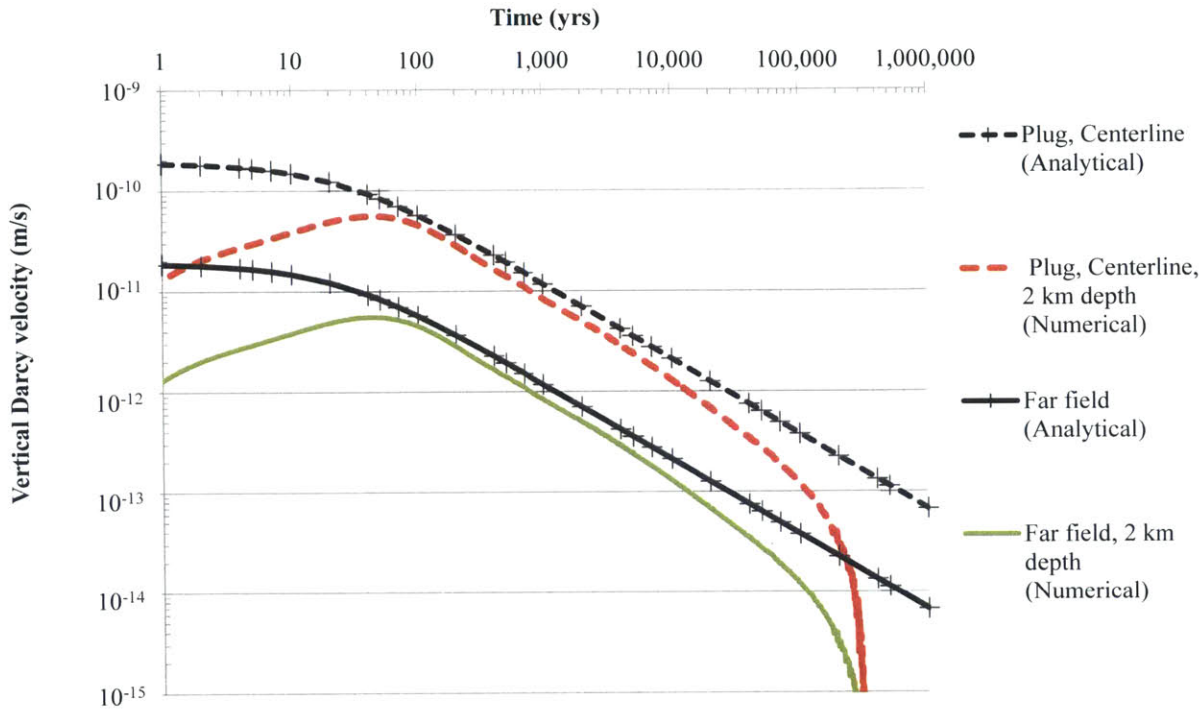
Figure 4-7. Comparison of vertical transport velocity vs. time for the analytical and numerical (BVR) models base heterogeneous case with decay heat reduced by 50%.
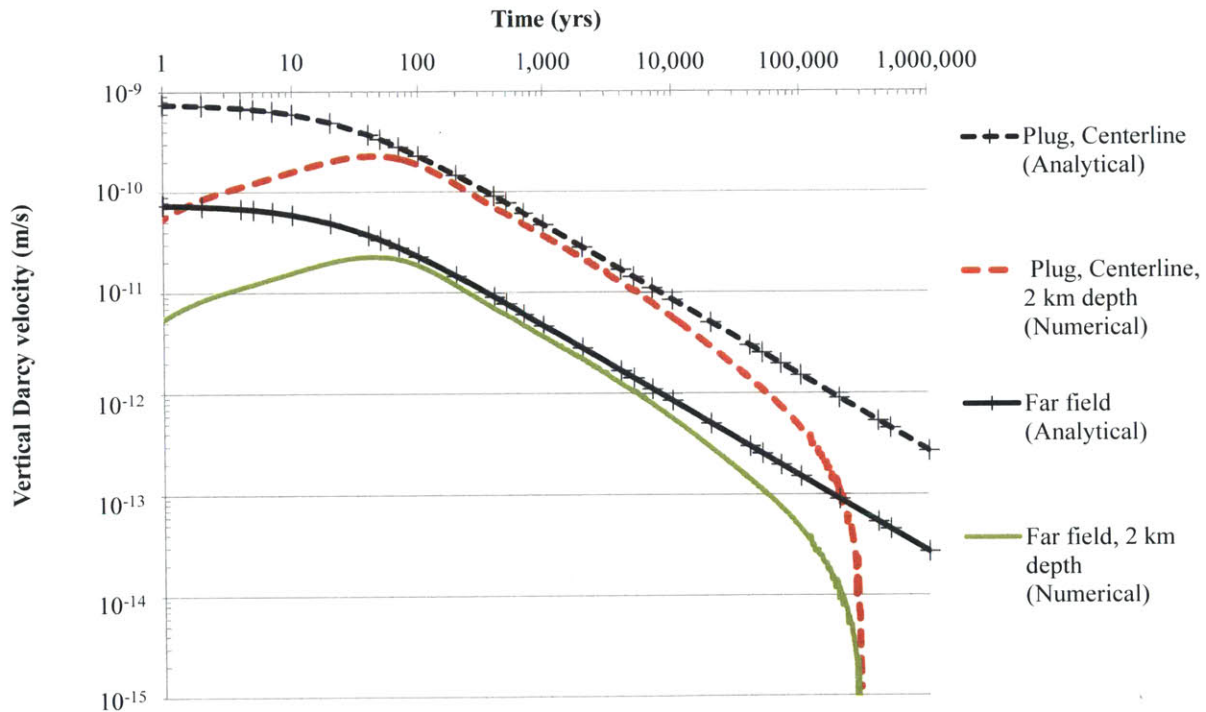
Figure 4-8. Comparison of vertical transport velocity vs. time for the analytical and numerical (BVR) models base heterogeneous case with decay heat increased by 200%

Again, there is good agreement between the two models over a 4× difference in decay heat. The penetration distance is proportional to the total decay heat produced, so the penetration distances would be half and double, respectively, compared to those previously computed for the base heterogeneous case. Note that in either of these cases, the cooling period has essentially no effect on the long term total cumulative heat production (see Eq. (B-9)), which is an interesting observation.

4.4.2.C.   Base case (with variation in boundary size)

The assumed borehole spacing is an obvious parameter that reduces velocities in the system (which may require the least cost to implement). The equations suggest that as borehole spacing (i.e., distance to the closed boundary) is increased, vertical velocities will decrease by a squared factor. The first variations shown here are a doubling and quadrupling of borehole spacings to 400 and 800 meters, which seems to be a reasonable but not excessively large increase in the space required for a disposal facility. Since the total area has increased by a factor of 4-16 (respectively), the system accommodates the same fluid expansion with 4-16× less vertical velocities and penetration distance (across the whole system, even in the high permeability zones). These results are demonstrated in Figure 4-9 and Figure 4-10, which again show good agreement between the analytical and numerical models.
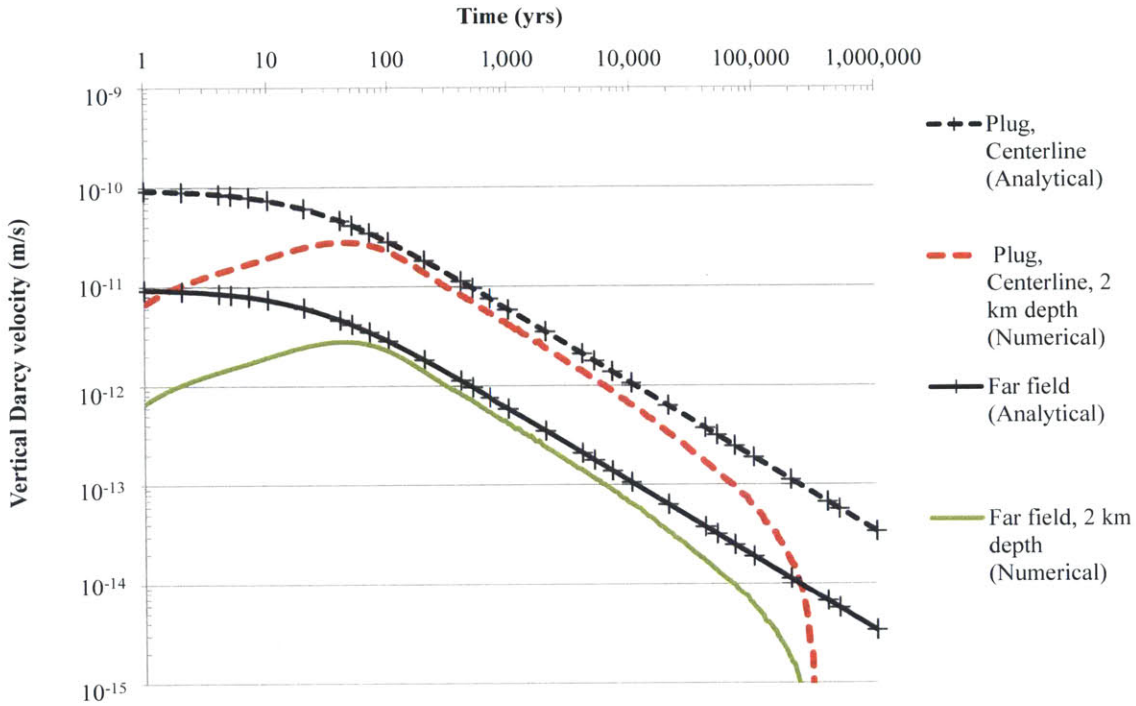
Figure 4-9. Comparison of vertical transport velocity vs. time for the analytical and numerical (BVR) models base heterogeneous case with borehole spacing of 400 meters.
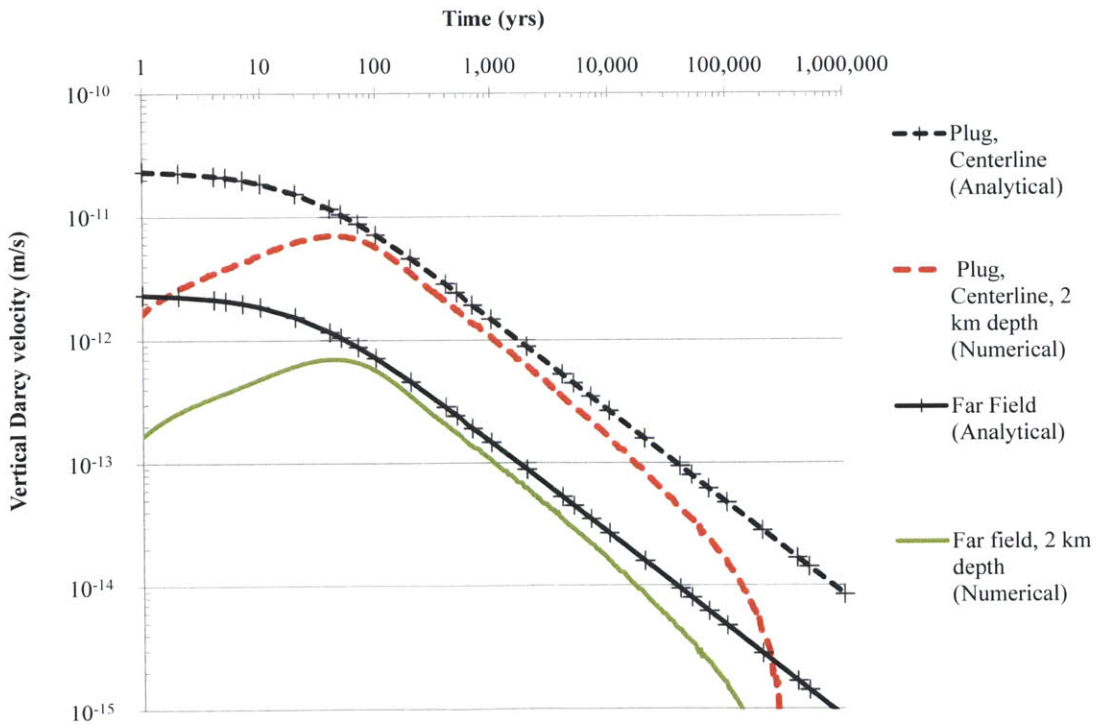
Figure 4-10. Comparison of vertical transport velocity vs. time for the analytical and numerical (BVR) models base heterogeneous case with borehole spacing of 800 meters.

In the furthest limit (where the boundary is drawn many kilometers from a borehole), the system begins to approximate a "single" isolated borehole, and the assumptions of the analytical model (e.g., radially uniform pressures) may not be completely valid. The results for borehole spacings of 1.5 km, 3.5 km, and 7 km are shown in Figure 4-11, Figure 4-12, Figure 4-13, respectively.
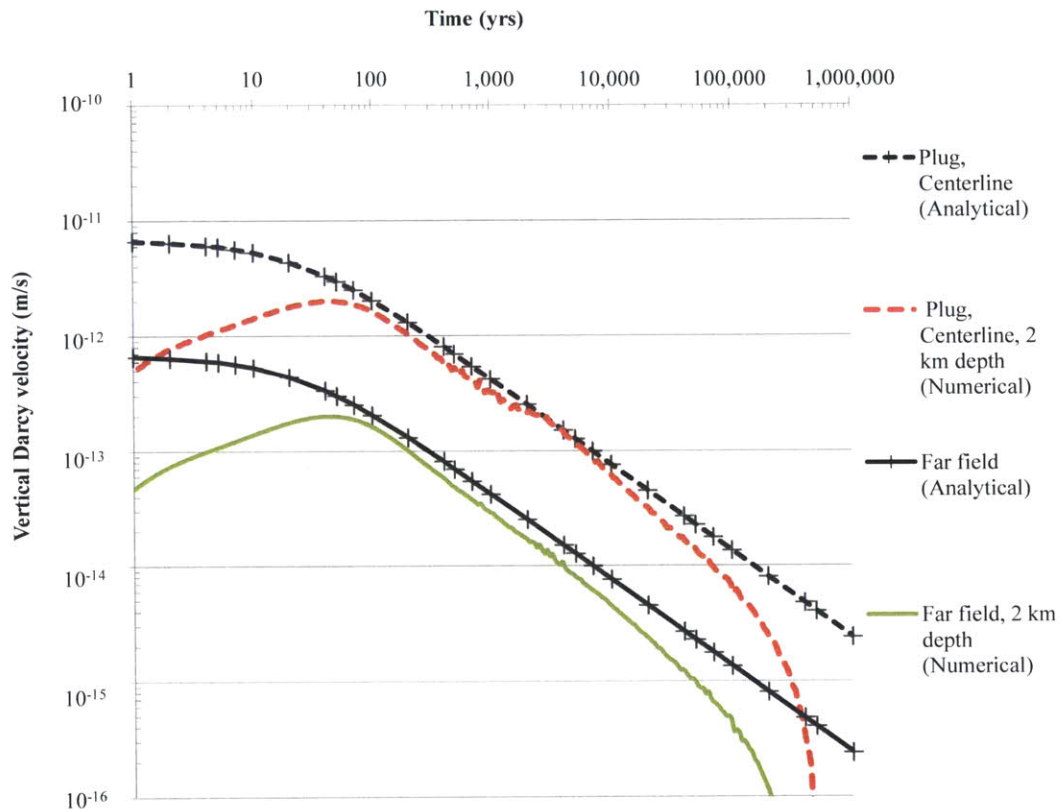
Figure 4-11. Comparison of vertical transport velocity vs. time for the analytical and numerical (BVR) models base heterogeneous case with borehole spacing of 1.5 km.
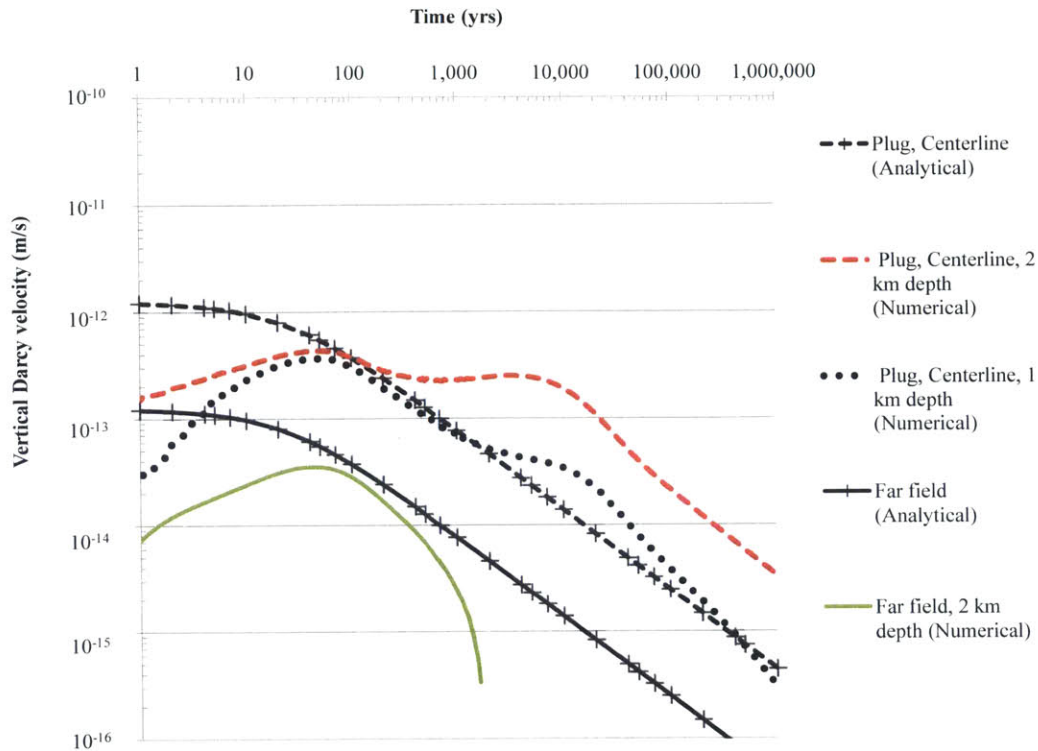
Figure 4-12. Comparison of vertical transport velocity vs. time for the analytical and numerical (BVR) models base heterogeneous case with borehole spacing of 3.5 km.
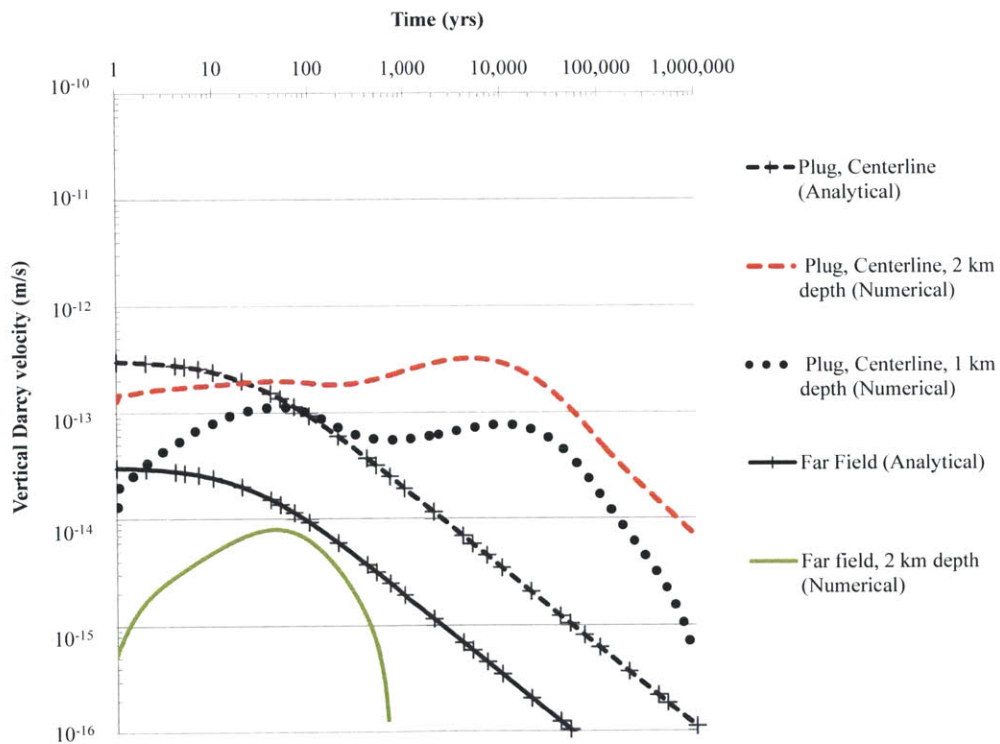
Figure 4-13. Comparison of vertical transport velocity vs. time for the analytical and numerical (BVR) models base heterogenous case with borehole spacing of 7000 meters.

The 1500 meter spacing case still demonstrates a reasonable agreement between the analytical and numerical models. However, as the spacing is increased to 3.5 km, the analytical model underestimates the velocities (particularly in the near field) because it assumes that the pressure perturbation spreads out over a much larger area than it actually does/can. Thus, the analytical model starts to become inaccurate at larger borehole spacings, where the assumption of radially uniform pressures begins to break down. However, in these cases where the analytical model is incorrect, the numerically predicted Darcy velocities are on the order of 10^{-12} m/s (corresponding to an advection velocity of 10^{-10} m/s), which according to Section 4.2.1 is effectively insignificant.

4.4.1. Very low permeability heterogeneous base case (k_p=10^{-17},k_m=10^{-18}) m^2

Although the effect of rock compressibility has already been discussed, it is instructive to analyze an extreme case with even lower rock permeability, which results in lower pressure diffusivity and greater overpressures, such that fluid compression has a more important impact on predicted velocities. The results from modeling the base case (again, where k_p/k_m=10) with very low rock permeability (k_m=10^{-18} m^2) are shown in Figure 4-14.
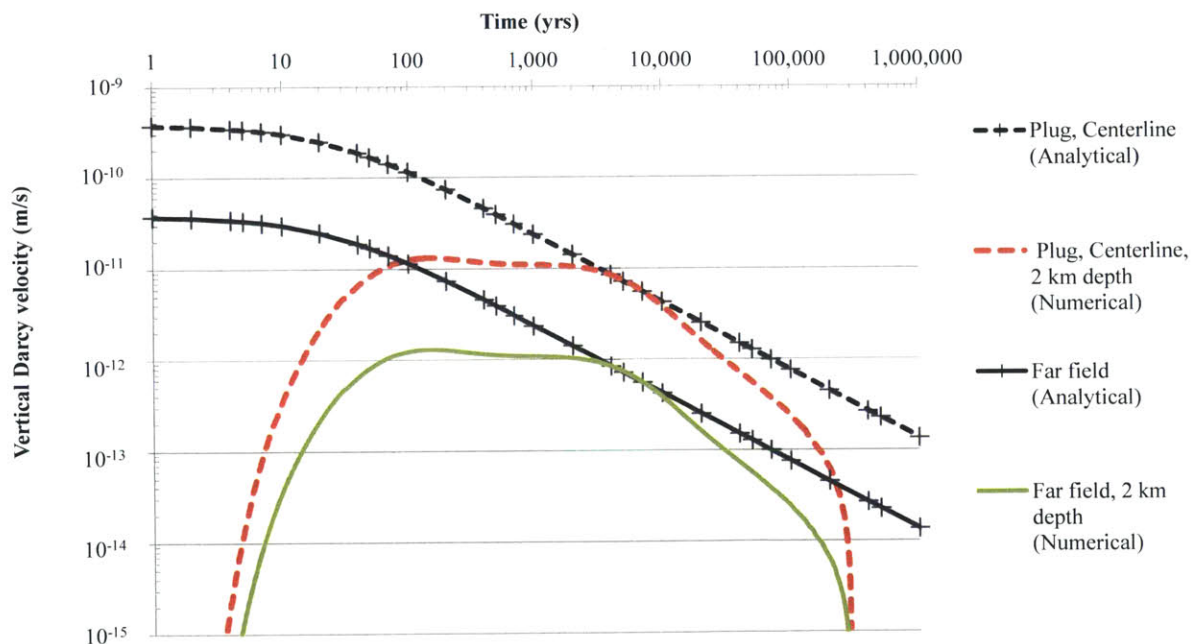
Figure 4-14. Comparison of vertical transport velocity vs. time for the analytical and numerical (BVR) models assuming very low plug and host rock permeability k_p= 10^{-17}m^2, k_m= 10^{-18}m^2 and infinite array of boreholes with 200 meter square spacing.

The analytical predictions for velocities are identical to the previously discussed heterogeneous base case (since k_p/k_m and all other variables are the same), but the system experiences much higher pressures to produce the same velocities. For example, using Eq. (B-22) from the lumped parameter resistance network analogy, the analytical model predicts an initial overpressure of 223×10^5 bar (required to drive the predicted vertical flow) which is clearly unrealistic. If the analytical model could account for compression, such high pressures would subsequently result in compression of fluid, a reduced injection volume and velocity, and thus a lower (and finally, a more realistic) overpressure. This explains why the initially predicted numerical velocities are close to zero (at early periods cumulative fluid injected= fluid stored in compression). In this case, pore fluid compression (effectively behaving as a capacitor in the hydraulic resistance network) significantly delays the transport of the (injected) fluid, and the numerical model only approaches the predictions of the analytical model at around 3000 years. In the larger context of radionuclide transport, accounting for the storage mechanism and delay due to pore fluid compression would improve performance of the repository (allowing a longer time for radionuclide decay, diffusion etc.). Thus, using the analytical model, (which neglects pore fluid compression) is a conservative approach. Accounting for this could be achieved by adding a capacitance term to the lumped parameter model, and integrating the resulting differential equation for ΔP to solve for the flow or current in the system.

4.4.2. Plug failure ($k_p = 10^{-14}\,m^2$)

A very high plug region permeability of $10^{-14}\,m^2$ can be modeled to even further demonstrate the flexibility of the analytical model and to show a severe failure mechanism. According to the equations derived in section Appendix B.4, the Darcy velocity in the plug (or centerline) will be $100\times$ higher than the far field. This is clearly shown in Figure 4-15, which compares the analytical and numerical Darcy velocities for the centerline (e.g., plug zone) and in the far field.
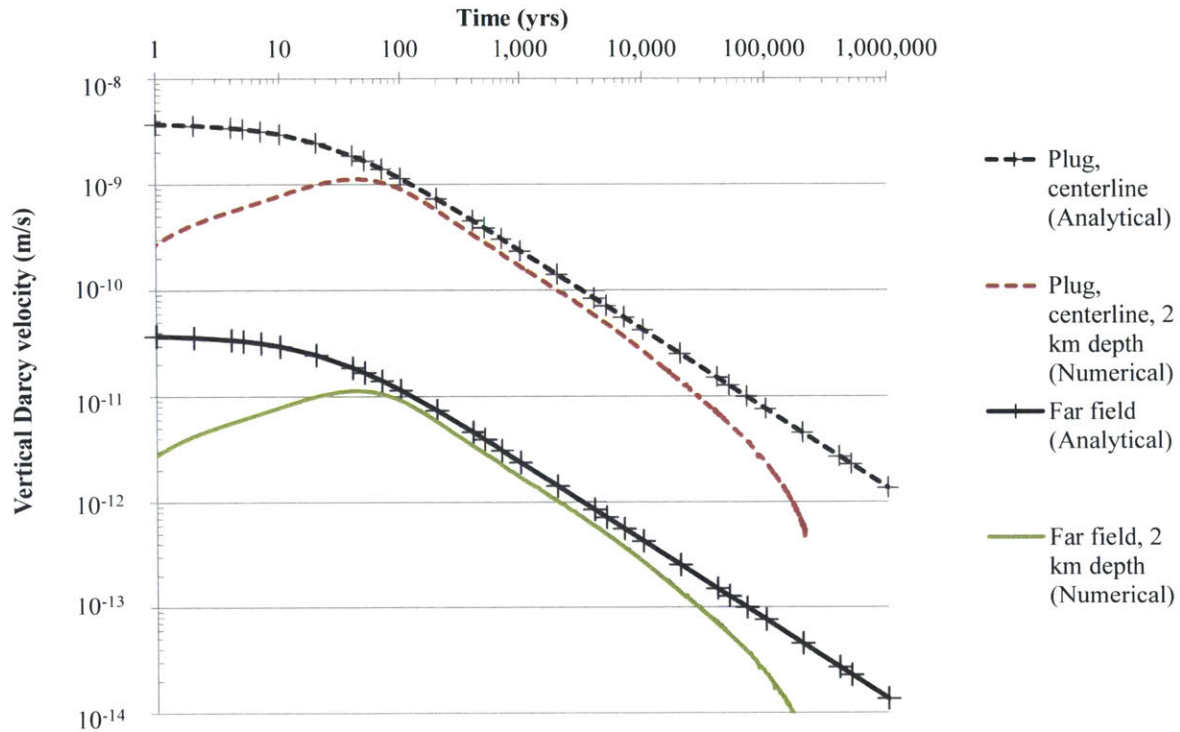
Figure 4-15. Comparison of vertical transport velocity vs. time for the analytical and numerical (BVR) models assuming high plug permeability ($k_p = 10^{-14} m^2$) compared to $k_m = 10^{-16} m^2$, with an infinite array of boreholes with 200 meter square spacing.

Despite the addition of a significant heterogeneity, the analytical model still captures the behavior of the system. Again, at early time periods the velocity is probably over-predicted by the analytical model due to the effect of fluid compression. For this particular case at 300,000 years the numerical solution becomes intractable (the time step became too small). The failed plug case (with $k_p = 10^{-14} m^2$) is the only case discussed so far that resulted in penetration of the

plug. The "breakthrough time" is shown graphically in Figure 4-16.
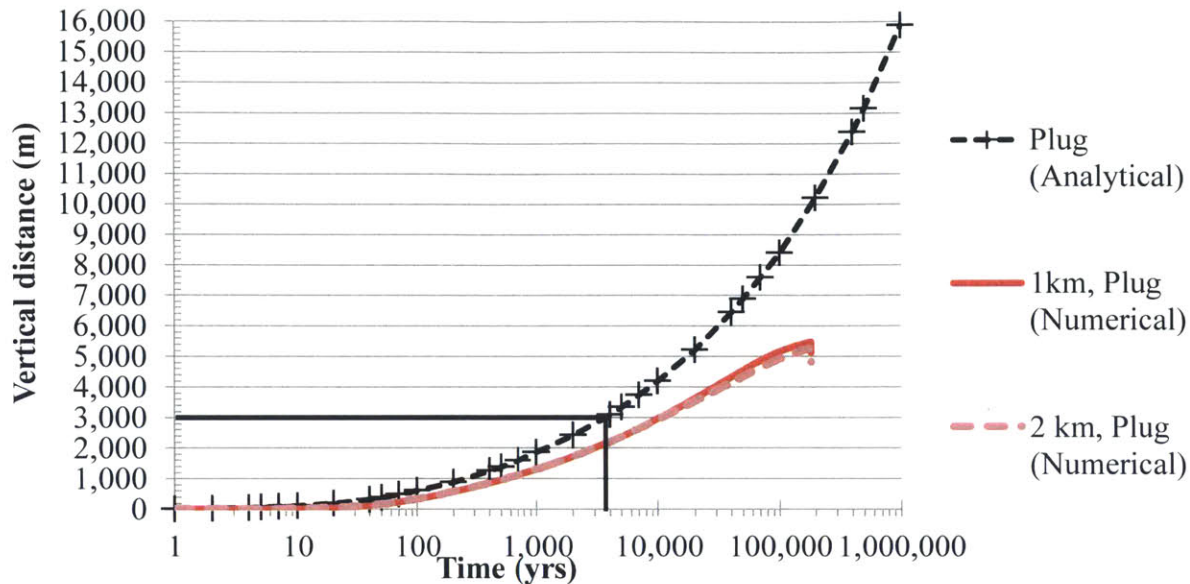
Figure 4-16. Comparison of the analytical and numerical predictions (BVR) for vertical distance in the failed plug ($k_p=10^{-14}m^2$). The breakthrough time (to reach an assumed 3000 m plug length/penetration distance) is shown.

Again, the conservative nature of the analytical solution is demonstrated in Figure 4-16, where the penetration distance exceeds the numerically calculated one by a factor of 2-4. Table 4-5 shows the corresponding velocities in the plug and matrix at the breakthrough time.

Table 4-5. Velocity and distance at the breakthrough time, for the failed plug case ($k_p=10^{-14}$ m^2) with a borehole spacing of 200 meters using the analytical model.

	Plug	Matrix
Breakthrough time, τ_b = 3692 years		
Porosity (ϕ)	0.01	0.01
Area (m^2)	1.13 m^2	3.9999×10^4 ($\sim200^2$)
Advection distance, $z_a(\tau_b)$	3000 meters	30 meters
Initial advection velocity, $v_a(0)$	3.81×10^{-7} m/s	3.81×10^{-9} m/s
Breakthrough advection velocity, $v_a(\tau_b)$	8.96×10^{-9} m/s	8.96×10^{-11} m/s
Flow rate (l/yr) at breakthrough	3.198	1131

The computed value of 3692 years (via Eq. (B-34)) is consistent with the graphic solution shown in Figure 4-16. Note that the plug porosity is conservatively assumed to be low here (1%), while the rock porosity is conservatively high (most crystalline rocks have porosity between 0.2% to 0.7%). Overall, both of these assumptions tend to maximize the advection velocity and penetration distance in the plug. Note that a doubling of either of these parameters would change

the time of penetration by a factor of 16, due to the fourth power dependence. Subsequently, this would reduce the velocity (at the time of breakthrough) by a factor of 8 (due to the ¾ power dependence of heat generation and velocity). Changing the host matrix porosity has no net effect on the penetration distance in the matrix.

For reference, such a high permeability would be characteristic of the simplest plug design consisting of a very fine bed of crushed sand particles with particle diameter ~5 microns (with no clay additive) and porosity of 0.4. Thus, since the porosity in this case would be higher than the host rock (~40%, vs. 1% for the host rock), the actual or advection velocity would only be 2.5× faster within that portion of the plug. At a constant permeability, a high plug porosity (hence high water storage inventory) is favorable to reducing the vertical penetration rate of radionuclides.

4.4.3. Comparison of total vertical distance for all cases

A compact way to compare all the cases shown thus far is to summarize the total vertical distance traveled in the centerline region (plug region). The results for the small borehole spacing (200 m) variations are shown in Table 4-6.

Table 4-6. Comparison of analytical and numerical predictions for total vertical distance travelled (in the plug/centerline and far field rock), for a 200 m square width domain.

Case Description	Total vertical distance at 1 million years (m) (Centerline/Far field)			Conservatism of vertical distance
	Integrated numerical velocity		Analytical prediction Eq. (B-29)	$\dfrac{\text{Analytical}}{\text{Numerical}}$
	2 km depth	1 km depth		
Homogenous $(k_p=k_m=10^{-16}m^2)$	(42.9/42.5)	(44.8/44.3)	(158.7/158.7)	3.5
Het. "base case" $(k_p=10^{-15}m^2)$	(544/54.4)	(561/56.1)	(1587/158.7)	2.82
Low permeability $(k_p,k_m)=$ $(10^{-17},10^{-18})$ m^2	(511.7/51.2)	(525.2/52.5)	(1587/158.7)	3.02
Base, w/rock compressibility	(549/54.9)	(566/56.6)	(1587/158.7)	2.8
Base, Low decay heat (50%)	(276/27.6)	(267/26.7)	(794, 79)	2.97
Base, High decay heat (200%)	(1113/111.3)	(1148/114.8)	(3175,317.5)	2.76
Failed plug $(k_p=10^{-14}$ m$^2)$	(5270/52.7)	(5475/54.7)	(15,870/158.7)	2.89

To obtain "maximum" penetration distance for the numerical results, negative velocities are assumed to be zero (typically velocities become negative at ~300,000 years) and the velocity is integrated numerically over the entire time period. In all of the cases shown in Table 4-6, the analytical model appears valid and behaves conservatively (typically over-predicting the distances traveled by a factor of 3). The numerical penetration distance follows the theoretical trends for various changes. For example, when decay heat is doubled, the penetration distance approximately doubles and when plug permeability is increased by a factor of 10 or 100 the penetration distance in that region increases by a factor of 10 or 100. As predicted, pore compressibility effects do not have a significant effect on the long term behavior and penetration distance of the system; however, at very low rock permeability fluid compression may serve to (beneficially) delay the vertical transport of fluid. Table 4-7 presents a summary of the penetration distances calculated by analytical and numerical means over a larger range of borehole spacing, for the base heterogeneous case.

Table 4-7. Comparison of analytical and numerical predictions for total vertical distance travelled along the centerline of the domain (within the plug zone) for variations in domain size, for the base heterogeneous case rock properties.

Square domain length	Total vertical distance (m) at 1 million years (centerline/far field)			Conservatism of vertical distance
	Integrated numerical velocity		Analytical prediction Eq. (B-29)	Analytical ⁄ Numerical
	At 1 km depth	At 2 km depth		
200 m	(544/54.4)	(561/56.1)	(1587/158.7)	2.8
400 m	(139.4/13.9)	(135.3,13.5)	(396.9,36.69)	2.9
800 m	(34.5/3.45/3.45)	(33.6/3.3/3.4)	(99.2/9.92)	2.9
1500 m*	(10.0/1.0/1.0)	(13.0/0.9/0.3)	(28.2/2.82)	2.1-2.8
3500 m*	(7.4/0.14/0.7)	(42.3/0.04/4.2)	(5.18,0.518)	0.122
7000 m*	(23.09/2.27/0.01)	(87.5/8.34/0.01)	(1.3, 0.13)	0.014

*Far field reported at radius of 10 m from the centerline and also at the far boundary because they are significantly different from each other for these cases with large spacing

The cases with smaller borehole spacing (<800 m) typically have similar velocities at depths of 1 km and 2 km (within 5%). The slight difference may be attributable to the effect of conduction and cooling from the surface. In addition, the velocity close to the borehole (10 meters) is identical to the velocity far from the borehole (at the boundary). However, when the spacing is increased beyond 1.5 km, there begins to be a clear radial dependence of the velocities (as indicated by the difference between vertical advection distance measured at 10 m and at the far field) which further confirms that the analytical model cannot be valid for such large borehole

spacings. In addition, significant differences develop between the vertical distances traveled in the plug measured at depths of 1 and 2 km. We thus conclude that the analytical model begins to break down and give non-conservative travel distances for the plug (relative to the numerical model) when the borehole spacing is increased beyond 1500 meters. However, in these cases the vertical travel distances are so low that they are considered insignificant (~80 meters in 1 million years). Overall, it appears that applying the analytical model with small borehole spacings (~200-400 meters) consistently provides the highest velocities and penetration distances and thus may be used as a conservative or bounding assumption when estimating the behavior of a deep borehole repository.

4.5. Canister Inventory, Failure, and Spent Fuel Degradation

4.5.1. Inventory and ingrowth of radionuclides

In Appendix A, it is shown that the concentration of a given radionuclide (i) (in a steady state, with constant vertical advection velocity) along a vertical plug or fracture is exponentially decaying in length (z) as given by Eq. (A-35),

$$\left(C(z) = C_0 e^{\lambda_z z} \right)_i \tag{A-35},$$

where $\lambda_{z,i}$ is a radionuclide specific parameter defined in Appendix A that must be negative, and includes the effects of advection, diffusion, dispersion, sorption, and radioactive decay in both the plug/fracture and surrounding matrix. Given a vertical velocity (which may be calculated based on the previous section and model) a first step is to determine the inventory of radionuclides in the disposed SNF and determine the source term concentration (C_0) of each radionuclide.

Radionuclide inventory for PWR fuel with 4.73% enrichment, burnup of 60 MW-d/kgHM, and aged for 30 years was obtained from [235]. Although more than 1500 isotopes are produced in the fission process, consideration must be limited to ones important to long term dose assessment. As a first cut, we limit consideration to those summarized in the IAEA Biosphere modelling and assessment (BIOMASS) research effort [236]. Table 4-8 presents this detailed radionuclide data, inventory half-life, and decay paths of each of these isotopes.

Table 4-8. Inventory, half-life of radionuclides (of those considered important to dose assessment in the IAEA BIOMASS[236]) and reported for 60 MW-d/kgHM PWR fuel cooled for 30 yrs[236].

Z	A	Element	Half Life (yrs)	Inventory (g/MTIHM)	Decay type and products, where (s):stable, (m):metastable.
6	14	C	5,710	0.454	β^- to N-14(s)
17	36	Cl	301,000	0.501	β^- to Ar-36 or EC to S-36, (s)
34	79	Se	65,000	10.5	β^- to Br-79 (s)
38	90	Sr	29.1	444	β^- to Y-90, β^- to Zr-90 (s)
40	93	Zr	1,530,000	1.47E+03	β^- to Nb-93 (m), Gamma to Nb-93 (s)
43	99	Tc	213,000	1.28E+03	β^- to Ru-99 (s)
46	107	Pd	6500,000	413	β^- to Ag-107 (s)
50	126	Sn	100,000	4.99E+01	β^- to Sb-126, β^- to Tl-126 (s)
53	129	I	15,700,000	313	β^- to Xe-129 (s)
55	135	Cs	2,300,000	772	β^- to Ba-135(s)
55	137	Cs	30.1	1.05E+03	β^- to Ba-137 (s)
88	226	Ra	1600	3.18E-06	α to Rn-222, α to Po-218...to Pb-206 (s)
90	229	Th	7900	6.37E-06	α to Ra-225, β^- to Ac-225...to Bi-209 (s)
90	230	Th	75,400	2.28E-02	**(α to Ra-226)**
90	232	Th	14,100,000,000	6.11E-03	α to Ra-228, β^- to Ac-228...to Pb-208 (s)
91	231	Pa	32,500	1.02E-03	α to Ac-227, β^- to Th-227... to Pb-207 (s)
92	233	U	159,000	1.40E-02	**(α to Th-229)**
92	234	U	245,000	306	**(α to Th-230)**
92	235	U	704,000,000	5.38E+03	α to Th-231, β^- to Pa-231... Pb-207 (s)
92	236	U	23,400,000	6.24E+03	**(α to Th-232)**
92	238	U	4,460,000,000	9.10E+05	α to Th-234, β^- to Pa-234...Pb-206 (s)
93	237	Np	2,140,000	1.24E+03	α to Pa-233
94	238	Pu	87.7	492	**(α to U-234, SF)**
94	239	Pu	24,100	7.42E+03	**(α to U-235, SF)**
94	240	Pu	6,540	4.09E+03	**(α to U-236, SF)**
94	241	Pu	14.4	377	**(β^- to Am-241)**
94	242	Pu	376,000	817	**(α to U-238, SF)**
95	241	Am	432	1.25E+03	**(α to Np-237)**
95	243	Am	7,370	271	α to Np-239
96	245	Cm	8,500	9.54	**(α to Pu-241)**

(Ingrowth into other radionuclides that are tracked)

Note that the table presents the subset of radionuclides which are both reported in the inventory given in[201] and for which dose conversion factors are reported in[236]. Thus there are some radionuclides (Sb-126, Pb-210, Ra-228, Ac-227, U-232) -all with half-lives less than 70 yrs- which are reported in the inventory [201] but are not considered in the IAEA's generic dose assessment, and are thus not explicitly modeled in this analysis. In addition there are radionuclides considered in the IAEA report, but not reported in the inventory given in [201] (e.g., Ni-59, Sm-151, Cm-246). In some assessments for repositories in fractured granite (i.e., SKB), Ni-59 has been reported to be an important radionuclide [237]; however, it is neglected in this thesis on the basis that it is neither included in the inventory [201] nor part of the current U.S. regulations on geologic disposal.

At this point, it is helpful to briefly discuss radiation protection standards developed by the U.S. Environmental Protection Agency (EPA) for permanent geologic disposal (specifically, Yucca Mountain) [238]. Originally established in 2001, the standard was set for 8 specific radionuclides: C-14, Tc-99, I-129, Ra-226, Ra-228, Np-237, Pu-239, and Am-241. Doses to a reasonably maximally exposed individual (RMEI) were limited to 15 mrem/yr (0.15 mSv/yr) for a 10,000 year compliance period. After concerns were raised that the 10,000 year compliance period was not long enough to characterize the peak doses resulting from the repository, in 2008 the EPA settled on a limit of 100 mrem/yr (1 mSv/yr) for the period between from 10,000 to 1 million years.

Radium isotopes are not significant in the initial inventory and are produced primarily from the decay of U-234, U-236, U-238, and Pu-238. Am-241 and Np-237 are present in significant quantities in discharged SNF and also grown from Pu-241.

Accounting for all the ingrowth chains of daughter products exactly would require a much more complex analytical solution to the equations in Appendix A (which only consider radioactive decay). The differential equations become coupled between many radionuclides, requiring numerical methods to solve for the steady state solutions. The exact transient numerical solution in space would also become much more complicated (perhaps even intractable for current numerical solvers). To explain how ingrowth (or chain growth) may be approximated by modifying dose conversion factors, it is beneficial to note the linearity of the radioactive decay equations. If there are two sources of a given radionuclide in a system, the spatial distribution resulting from each source may be superimposed (i.e., added) to obtain the

total concentration of the radionuclide in space. For a given daughter radionuclide, there are two or more sources- one established by its own advection/diffusion transport (described in Appendix A), and the others each determined independently by the daughter's parent(s). Regarding the latter (the ingrowth contribution of a daughter from a parent) the concentration (e.g., atoms/liter) of a parent (i) and daughter (ii) radionuclides (at a given point in space) are related by Eq. (4-14) and Eq. (4-15),

$$\frac{dC_i}{dt} = -\lambda_i C_i \tag{4-14}$$

$$\frac{dC_{ii}}{dt} = \lambda_i C_i - \lambda_{ii} C_{ii} \tag{4-15}$$

Evaluating Eq. (4-15) when,

$$\lambda_i C_i > \lambda_{ii} C_{ii} \tag{4-16}$$

$$and\ thus$$

$$\frac{dC_{ii}}{dt} > 0$$

the daughter concentration increases (with time). Since the "ingrown" daughter contribution initially starts out at zero, this condition will be met and the increase of C_{ii} will continue to occur until another equilibrium condition is met. In other words, when,

$$\lambda_{ii} C_{ii} > \lambda_i C_i$$

$$and\ thus \tag{4-17}$$

$$\frac{dC_{ii}}{dt} < 0$$

the daughter concentration would decrease (i.e., stop increasing). Thus, it is apparent that the steady state (or "secular") concentration of the daughter (when $dC_{ii}/dt=0$) gives the (conservative) maximum concentration of the ingrown daughter. The relative concentration at this steady state is given by Eq. (4-18),

$$C_{ii} = \frac{\lambda_i}{\lambda_{ii}} C_i \qquad (4\text{-}18)$$

If there is a subsequent decay from daughter (ii) to granddaughter (iii), the concentrations between (ii) and (iii) and (i) and (iii) will be related by an equation of the same form,

$$C_{iii} = \frac{\lambda_{ii}}{\lambda_{iii}} C_{ii} = \frac{\lambda_i}{\lambda_{iii}} C_i \qquad (4\text{-}19)$$

and so forth for further decays. A dose conversion factor (DCF) is multiplied to convert from an activity (decays/second) to an absorbed dose (Sv) for a given radionuclide, and thus has the units of (Sv/Bq). Given a concentration (C_i) of a radionuclide (e.g., atoms/liter), the dose received for each liter ingested is given by,

$$\frac{Dose_i}{liter} = DCF_i(\lambda_i C_i) \qquad (4\text{-}20)$$

Thus, the total dose contribution of a given parent radionuclide may be accounted for by summing the product of the DCF's and activities of the parent and all subsequent daughter(s), as shown in Eq. (4-21),

$$Total\left(\frac{Dose}{vol.}\right) = DCF_i(\lambda_i C_i) + DCF_{ii}(\lambda_{ii} C_{ii}) + DCF_{iii}(\lambda_{iii} C_{iii}) \qquad (4\text{-}21)$$

Inserting Eq. (4-18) and Eq. (4-19) into Eq. (4-21), we obtain Eq. (4-22),

$$Total\left(\frac{Dose}{liter}\right) = DCF_i(\lambda_i C_i) + DCF_{ii}(\lambda_{ii} \frac{\lambda_i}{\lambda_{ii}} C_i) + DCF_{iii}(\lambda_{iii} \frac{\lambda_i}{\lambda_{iii}} C_i) \qquad (4\text{-}22)$$

Cancelling terms,

138

$$Total\left(\frac{Dose}{liter}\right) = (DCF_i + DCF_{ii} + DCF_{iii})\lambda_i C_i \qquad \text{(4-23)}$$

Thus, to account for the effect of ingrowth, the DCFs of all daughter products are summed to obtain a conservative, ingrowth adjusted DCF for the parent radionuclide. Indeed, assumption of secular equilibrium has been proposed by other investigators as a means to simplify the ingrowth problem when requiring analytical solutions to radionuclide transport in the far field geosphere [237]. Table 4-9 and Table 4-10 show the calculation of the ingrowth-adjusted DCF's for all radionuclides listed in Table 4-8, based on the DCF's for individual radionuclides reported on the 2012 International Committee on Radiological Protection (ICRP) DCF's calculated for adult members of the public [239]. In this way, rather than associating the dose with Ra-226 for example, the dose is associated with each of the parents that may produce Ra-226. In other words, the dose and harm of a specific radionuclide includes the maximum harm (e.g., activity) that any of its ingrown daughter products could possibly have.

Table 4-9. Dose Conversion Factors for isotopes C-14 to Th-232, including all radioactive daughter products, calculated from individual DCFs reported in [239].

Z	A	Element	Parent DCF (Sv/Bq)	Radioactive Daughter(s)	Daughter DCFs (Sv/Bq)	Sum for Parent+Daughter(s) (Sv/Bq)
6	14	C	5.80E-10	-	-	5.80E-10
17	36	Cl	9.3E-10	-	-	9.3E-10
34	79	Se	2.9E-9	-	-	2.9E-9
38	90	Sr	3.07E-8	Y-90	2.7E-9	3.07E-8
40	93	Zr	1.1E-9	Nb-93 (m)	1.2E-10	1.22E-9
43	99	Tc	6.4E-10	-	-	6.4E-10
46	107	Pd	3.7E-11	-	-	3.7E-11
50	126	Sn	4.7E-9	Sb-126	2.4E-9	7.1E-9
53	129	I	1.1E-7	-	-	1.1E-7
55	135	Cs	2.0E-9	-	-	2.0E-9
55	137	Cs	1.3E-8	-	-	1.3E-8
88	226	Ra	2.8E-7	Rn-222	(not reported)	2.17E-6
				Po-218	(not reported)	
				Pb-214	1.4E-10	
				Bi-214	1.1E-10	
				Po-214	(not reported)	
				Pb-210	6.9E-7	
				Bi-210	1.3E-9	
				Po-210	1.2E-6	
90	229	Th	4.9E-7	Ra-225	9.9E-8	6.13E-7
				Ac-225	2.4E-8	
				Fr-221	(not reported)	
				At-217	(not reported)	
				Bi-213	2.0E-10	
				Po-213	(not reported)	
				Pb-209	5.7E-11	
90	230	Th	2.1E-7	**Ra-226**	2.17E-6	2.38E-6
90	232	Th	2.3E-7	Ra-228	6.9E-7	1.06E-6
				Ac-228	4.3E-10	
				Th-228	7.2E-8	
				Ra-224	6.5E-8	
				Rn-220	(not reported)	
				Po-216	(not reported)	
				Pb-212	6.0E-9	
				Bi-212	2.6E-10	
				Po-212	(not reported)	

Bolded daughter products represent those which have DCF's shown/calculated elsewhere in the table.

Table 4-10. Dose Conversion Factors for isotopes Pa-231 to Cm-245, including all radioactive daughter products, calculated from individual DCFs reported in [239].

Z	A	Element	Parent DCF (Sv/Bq)	Radioactive Daughter(s)	Daughter DCFs (Sv/Bq)	Sum for Parent+Daughter(s) (Sv/Bq)
91	231	Pa	7.1E-7	Ac-227	1.1E-6	1.92E-6
				Th-227	8.8E-9	
				Ra-223	1E-7	
				Rn-219	(not reported)	
				Po-215	not reported)	
				Pb-211	1.8E-10	
				Bi-211	(not reported)	
				Tl-207	(not reported)	
92	233	U	5.1E-8	**Th-229**	6.13E-7	6.64E-7
92	234	U	4.9E-08	**Th-230**	2.38E-6	2.43E-6
92	235	U	4.7E-8	Th-231	3.4E-10	1.97E-6
				Pa-231	1.92E-6	
92	236	U	4.7E-8	**Th-232**	1.06E-6	1.11E-6
92	238	U	4.5E-8	Th-234	3.4E-9	2.48E-6
				Pa-234	5.1E-10	
				U-234	2.43E-6	
93	237	Np	1.1E-7	Pa-233	8.7E-10	7.75E-7
				U-233	6.64E-7	
94	238	Pu	2.3E-07	**U-234**	2.43E-6	2.66E-6
94	239	Pu	2.5E-07	**U-235**	1.97E-6	2.22E-6
94	240	Pu	2.5E-07	**U-236**	1.11E-6	1.36E-6
94	241	Pu	4.8E-09	**Am-241**	9.75E-7	9.8E-7
94	242	Pu	2.4E-07	**U-238**	2.48E-6	2.72E-6
95	241	Am	2.0E-07	**Np-237**	7.75E-7	9.75E-7
95	243	Am	2.0E-07	Np-239		2.42E-6
				Pu-239	2.22E-6	
96	245	Cm	6.2E-11	**Pu-241**	9.8E-7	9.8E-7

Bolded daughter products represent those which have DCF's shown/calculated elsewhere in the table, or previously in Table 4-9.

4.5.2. Degradation rate

Given an inventory of radionuclides (present within a UO_2 matrix, cladded by zirconium, and sealed by a canister), the next step is to consider the degradation rate of the canister and waste form. In many repository designs, canister integrity plays an important (if not critical) role in delaying water contact and degradation of the fuel. Typical repository designs rely on (expensive) metals such as copper and titanium to provide the necessary corrosion resistance[240]; however, it is inherently difficult to project the integrity of man-made canisters on such long time scales (10,000 years). A period of canister integrity (~100 years) could be socially justifiable and necessary to satisfy retrieval requirements (and is likely to be technically achievable with more work and experiments). However, this thesis focuses on the geologic and passive barriers that deep boreholes provide. Thus, it is simplest and most conservative to assume that the canisters and cladding are breached instantaneously and that the fuel begins to degrade immediately. This sequence was also adopted by SNL in their 2009 DBD assessment [21].

The degradation rate of nuclear fuels is an area where scarce data on the relevant time scales exists to justify long term predictions. Release of fission products from spent fuel is a complex process involving restructuring of the porous UO_2 matrix at the edges of the pellet, cladding pressurization, and alpha induced self-diffusion to the pellet boundary[241]. The typical simplification is to assume that there is an instantly released fraction (IRF) of fission products when the fuel begins to degrade [227], [241]. After this point, the release of fission products and actinides is limited by the degradation rate of the UO_2 matrix (in the case of oxide fuels). Higher burnup fuels are shown to have a significantly larger IRF[227], partly due to the fact that a greater percentage of fission products are released into the cladding during the burnup of the fuel. This is demonstrated in Table 4-11, which compares the IRF predicted for 37 and 75 MW-d/kg burnup fuel.

Table 4-11. IRF (% of total inventory) for 37 and 75 MW-d/kg PWR fuel, where IRF includes all fission products in the gap, grain boundaries and rim region. Data from [241].

Radionuclide	37 MW-d/kg IRF	75 MW-d/kg IRF
Fission gases	2	18
^{14}C	10	10
^{36}Cl	5	26
^{79}Se	1	17
^{90}Sr	1	17
^{107}Pd	1	17
^{126}Sn	1	17
^{129}I	3	26
^{135}Cs	2	26
^{137}Cs	2	26

Experimental studies suggest that the degradation rate of the uranium matrix can be lowered by orders of magnitude in the presence of reducing conditions and hydrogen (e.g., created during the corrosion of the iron waste package)[203], [242]. Unfortunately there is currently little/no data to support a UO_2 matrix alteration model at the high temperatures, pressure, and salinities that are expected in a deep borehole repository.

In addition, some generic assessments further assume that the fuel degrades at a certain fractional rate, for example, between 10^{-8} to 10^{-6} per year for fuel at 25 °C [201] (adopted from SKB's initial performance assessment at the Forsmark and Laxemar sites[243]), but even these rates are presumably temperature dependent. If the fuel matrix degradation rates are so low (i.e., ~ 63% fuel has degraded at 1 million years for a 10^{-6} yr^{-1} degradation rate) it seems that the IRF will dominate the total dissolved radionuclide inventory for most of the performance period.

In light of the uncertainty involved in this type of modeling and estimation, for now it is assumed that the entire inventory of radionuclides is available for dissolution into the borehole repository gap.

4.6. Geochemical Transport Properties

Once radionuclides escape the UO_2 matrix, cladding and canister, geochemical conditions will determine their solubility and sorption behavior. A key benefit of deep crystalline bedrocks is that they provide reducing chemical conditions (as opposed to oxidizing conditions typically experienced near the surface and in rainwater)[227]. The redox potential measured in crystalline bedrock at Swedish sites (~500 m depth) is typically between-150 to -350 mV (with respect to

the standard hydrogen electrode), and pH varies between 7.0 to 8.1. Overall, these redox conditions decrease the maximum solubility of radionuclides by many orders of magnitude- perhaps most importantly for U, Np, Tc, and Pu, (which make up >97% of the inventory of radionuclides). For example, over this pH range, at a redox potential of ~ -200 mV, soluble U(VI) reduces to less soluble U(IV)[16], which ultimately causes precipitation of insoluble phases such as uraninite ($UO_{2+x}(s)$, where 0<x<0.25), coffinite ($USiO_4(s)$) or pitchblende (U_3O_8). The general trend of more negative redox potentials(from +500 mV at the surface to < -100 mV at greater depths), basic chemistry (from a pH 6.5-9.3 at the surface to 7.5-8.8 at greater depths), and low uranium concentrations at greater depths (600 m to 1000 m) are similarly exhibited in geochemical data from the Canadian Shield from the Whiteshell Research Area (WRA) [16]. Notably, the presence of carbonate (HCO_3^-) in pore fluids is highly correlated with higher dissolved concentrations of uranium at these sites[16], [244] because together they form highly stable carbonate complexes. However, these (deleterious) carbonate concentrations tend to decrease in deeper groundwaters as pH increases (causing calcite precipitation) or as calcium concentrations increase [16].

Granitic basement rocks also contain several Fe(II) minerals, such as pyrite, biotite or magnetite, which are responsible for an average FeO content (in Canadian Precambrian granite for example) of 2.75 wt.% [245] Previous studies have indicated that Fe(II) in all three minerals can reduce U(VI) to insoluble U(IV) [246]–[249], provided that HCO_3^- is not present and pH does not increase significantly above 8[249], [250]. These naturally (favorable) redox conditions might also be supplemented by engineered materials, such reduced iron[203], [227], silicates, or other chemicals capable of consuming CO_2 (e.g., MgO) and carbonates. Another interesting property of granitic basement rocks is their uranium concentration. For example, the uranium content in granitic basement rocks can vary from 0.5 to 44 ppm, and the natural iodine content of the pore fluids varies from 0.1 mg/l to as high as 18 mg/l [65],[80]. A comparison of the natural content to disposal zone content of these elements is shown in Table 4-12.

Table 4-12. Comparison of host rock and disposal zone iodine and uranium content, using data from various sites.

	Canadian Shield Lower Bound [65]	Stripa Mine (Scandinavian Shield[80]) ~1100 m depth	Canadian Shield Upper Bound[65]
Rock Type	Crystalline	Crystalline (Granite)	Crystalline Basement (Metabasalt)
Rock Porosity	0.01 (Assumed)	0.005 [80]	0.01(Assumed)
Uranium content	0.5 mg/kg [65]	44 mg/kg [80]	0.9 mg/kg [65]
Iodine concentration (mg/L of porefluid)	**0.1** [65]	**0.240**	**18** [65]
Borehole Cell Volume*, mass**	$200\times200\times1000(m^3)$ $=4\times10^{10}$ (liters), 1.1×10^{11} kg		
Borehole cell pore volume	4×10^8 (liters)	2×10^8 (liters)	4×10^8 (liters)
Iodine content in pores (kg)	40 kg	48 kg	7,200 kg
Uranium content in rock (MTHM)	**55 MTHM**	**4,840 MTHM**	**99 MTHM**
	Disposal zone		
Uranium content in disposal zone (400 PWR assemblies)**	200 MTHM		
I-129 Content in Disposal Zone***	~62 kg		
Dilution factor for I-129 (Ratio)	0.68	0.76	115
Dilution factor of uranium (Ratio)	0.275	24.2	0.495

*For 200 meter borehole spacing, 1 km long crystalline rock zone above the disposal zone
**Assuming 2750 kg/m^3 rock density
***313 g I-129/MTHM

The data suggests that the very high iodine and uranium content in the rock and pore fluid could create substantial dilution effects (especially when considering that the fluid that finally escapes from the disposal zone and reaches the surface will already have a very low concentration of radionuclides).

Table 4-13 presents a comparison of geochemical conditions obtained from various sites and depths as they pertain to radionuclide transport and solubility in deep boreholes.

Table 4-13. Summary of geochemical and pore fluid data obtained from basement rock sites [244]

	Canadian shield	**Finland**	**Sweden**	**Germany**
Age of rock	2.6 Gy (Lac du Bonnet batholith)	1.8 Gy (Palmottu site)	1.8 Gy (Forsmark)	300-400 My (KTB borehole [22]
Shallow rock interactions	Presence of tritium indicates interactions with meteoric water at depths <200 m[16], [244]	High tritium contents indicate dynamic flows, open water conducting fractures found at depths <150 m [244]	Upward flow of ~2.6 mm/yr at depth of 100 m, larger turnover of shallower waters. Less than 1% of upward water flux originates from 500 m depth[251]	Upper zone of circulating groundwater extends down to 650 m[22]
pH	6.5-9.3 at depths of 0-200 m 7.5-8.8 at depths >200 m		7.0 at depth of 500 meters	8.3-8.4 at depth of 4 km [22], [252]
Eh	+500 mV at surface, <-100 mV at greater depths	At depths >130m, reducing (-300 mV) with low uranium concentrations (<10 ppb), despite large amount of uranium in the rock	-143 mV	-150 mV [22] -440 mV [252] at depth of 4 km
Bicarbonate chemistry	Decrease from surface value of ~250 mg/l to < 10 mg/l as salinity increases	High uranium concentrations associated with oxidative HCO_3 groundwaters down to 130 m	Very low at 500 meters (1.8×10^{-3} mol/l)	45 mg/l at 4 km [22]
Glaciation	Glacial or post-glacial water was recharged into the bedrock, possibly 10^4 years ago into permeable fault zones ranging from 200-600 m [16], [244]	Glaciation events mobilized uranium under oxidizing conditions, leading to precipitation of U(VI) silicates at shallow depths. Surface rebound from ice age occurring at ~4-5 mm/yr [253]	Infiltration of meteoric water (during interglacial periods) generally lowers pH, raises carbonate concentrations and increases redox potential	

The trends from all crystalline bedrock sites (Canada, Finland, Sweden, Germany, Russia) are generalized as follows [244]:

- Deep saline waters and brines transitions occur in most inland locations below depths of 500 m. Saline waters found at these great depths have longer residence times and have had little interaction with meteoric waters. In the upper part of the bedrock, mixing of groundwaters is a process that continuously modifies composition; therefore, brines and highly saline water can only be expected in especially well-isolated geological formations [254].

-At greater depths, the pH begins to increase (above 7) and oxygen-consuming reactions and redox mineral controls tend to lower the Eh (<-200 mV).

-Carbonate concentrations also decrease with depth, preventing increases in uranium solubility.

-Hydrogen (which may be a by-product of mineral – water reactions) and appears to become the dominant gas in systems below 3 km.

More geochemical data is needed from North American boreholes drilled deeper than 1000 m into crystalline rock. Thus, until further site specific work is completed, it must be assumed that these generic conditions (similar across each site, typically in the range of 500-1000 meters) may be valid or obtainable within deeper crystalline rocks.

4.6.1. Concentration limit (solubility and inventory)

With geochemical conditions expected in the basement rocks established, it is possible to estimate solubility limits for the radionuclides contained in the spent nuclear fuel. Calculating the solubility of chemical species generally requires identifying the most thermodynamically stable form (and redox state) of the elemental compound while accounting for the chemical conditions (pH and Eh) and other species present (Fe, Cl, HCO_3^-) etc.). Solubility limits are typically estimated using a combination of experimental data and thermodynamic databases and chemistry codes such as PHREEQC [201], [255]. In some cases, the solubility data for chemically similar elements are used as proxies for other elements. Some radionuclides do not have solubility limits (e.g., iodine) or thermodynamic data at the relevant conditions do not exist to calculate solubility limits. Table 4-14 summarizes and compares solubility limits that have been calculated or assumed by various investigators at Sandia National Laboratories (SNL), MIT, and SKB (Forsmark site safety assessment) for granite or deep bedrock conditions.

Table 4-14. Solubility (mol/l) of radionuclides evaluated in granitic bedrock chemistries.

Z	A	Elem.	DBD, 100°C (SNL, 2011)[201]	Granite 25 °C (SNL, 2011) [256]	DBD (MIT, 2002) [105]	SKB, 2011 [146]	Max.
6	14	C	-	-	4.34E-10	-	-
17	36	Cl	4.20	-		-	-
34	79	Se	2.00E-05	4.0E-08		6.70E-09	**2.00E-05**
38	90	Sr	-	-		3.70E-03	-
40	93	Zr	1.00E-10	2.0E-08	1.29E-39	1.80E-08	**2.0E-08**
43	99	Tc	3.95E-07	3.0E-08	8.85E-16	3.80E-09	**3.95E-07**
46	107	Pd	4.00E-04	3.0E-06		3.90E-06	**4.00E-04**
50	126	Sn	7.15E-08	3.0E-08		9.00E-08	**9.00E-08**
53	129	I	-	-	9.86E-09	-	-
55	135	Cs	-	-	4.15E+01	-	-
55	137	Cs	-	-	4.15E+01	-	-
88	226	Ra	-	1.0E-06		9.10E-07	-
90	229	Th	6.90E-08	4.0E-07	3.67E-10	2.60E-09	**4.0E-07**
90	230	Th	6.87E-08	4.0E-07	3.67E-10	2.60E-09	**4.0E-07**
90	232	Th	6.81E-08	4.0E-07	3.67E-10	2.60E-09	**4.0E-07**
91	231	Pa	1.90E-06	1E-09		3.30E-07	**1.90E-06**
92	233	U	2.23E-12	4.0E-10	6.92E-14	9.50E-10	**9.50E-10**
92	234	U	2.22E-12	4.0E-10	6.92E-14	9.50E-10	**9.50E-10**
92	235	U	2.21E-12	4.0E-10	6.92E-14	9.50E-10	**9.50E-10**
92	236	U	2.20E-12	4.0E-10	6.92E-14	9.50E-10	**9.50E-10**
92	238	U	2.18E-12	4.0E-10	6.92E-14	9.50E-10	**9.50E-10**
93	237	Np	5.99E-06	1.00E-09	6.61E-47	1.00E-09	**5.99E-06**
94	238	Pu	3.79E-13	2.0E-07	7.41E-06	4.80E-06	**7.41E-06**
94	239	Pu	3.78E-13	2.0E-07	7.41E-06	4.80E-06	**7.41E-06**
94	240	Pu	3.76E-13	2.0E-07	7.41E-06	4.80E-06	**7.41E-06**
94	241	Pu	3.75E-13	2.0E-07	7.41E-06	4.80E-06	**7.41E-06**
94	242	Pu	3.73E-13	2.0E-07	7.41E-06	4.80E-06	**7.41E-06**
95	241	Am	4.40E-08	6.0E-06	7.41E-14	2.50E-06	**6.0E-06**
95	243	Am	4.36E-08	6.0E-06	7.41E-14	2.50E-06	**6.0E-06**
96	245	Cm	6.49E-09	6.0E-06	1.01E-19	2.60E-06	**6.0E-06**
			Max. of range reported				

Dashes (-) indicate solubility unlimited radionuclides, blank cells indicate no data reported
*solubility limit reported for the near field (close to repository)

The data in Table 4-14 demonstrate the large variability in solubility estimates for these radionuclides (evaluated over different temperatures). A notable example is the solubility for uranium, which varies over 4 orders of magnitude between investigators; of course, some level of uncertainty is warranted given the large effect that relatively small amounts of carbonate may have on uranium solubility as previously discussed. Rather than attempt to treat this uncertainty (due to either chemical modeling uncertainty or assumptions on temperature and conditions), we

develop conservative, bounding, and presumably generically applicable values by finding the maximum values across all values for solubility that are reported. These maximum values for solubility are shown bolded in the last column of Table 4-14. This maximum solubility is assumed to be valid across the entire model as the radionuclide travels from the disposal zone to the point of withdrawal. In reality, solubility may be higher under oxidizing conditions near to the surface, but since the radionuclide has travelled away from the source (e.g., disposal zone) and primarily through a granitic bedrock region with these prescribed solubilities, it will not be physically possible for the fluid to increase in radionuclide concentration to a new solubility limit.

For radionuclides without solubility limits, it is necessary to assume a representative volume into which the inventory dissolves and concentrates. The smaller the volume assumed, the higher the source concentration of the radionuclide. The minimum possible fluid volume (into which the radionuclides may concentrate) is assumed to be the annular gap between the canister and borehole wall (with a thickness of 3 cm surrounding a canister of 0.34 m diameter). Assuming that the gap is filled with a porous medium (30% porosity) further reduces the available fluid volume (and increases the concentration) of these radionuclides. For a 2000 meter disposal length, this totals to 20.9 m^3 of water available for concentrating the (solubility unlimited) radionuclides. The resulting concentration may be referred to as the inventory limited concentration. When defined in this way, the inventory limited concentration remains constant for various disposal zone lengths. In some cases, the radionuclide may have a solubility limit, but the initial inventory of the radionuclide may be so low that the solubility limit is not reached. Table 4-15 compares the solubility and inventory limits- the smaller of the two determines the maximum concentrations of the radionuclide in the disposal zone (C_o).

Table 4-15. Maximum source concentrations (C_0) of radionuclides in a 2000 m long borehole disposal zone containing 400 PWR assemblies (~200 MTHM), accounting for inventory and solubility limitations.

Z	A	Element	Inventory (grams)	Inventory limited concentration (mol/l)	Solubility limited concentration (mol/l)	Maximum source concentration (C_0) (mol/l)
6	14	C	9.080E+01	3.100E-04	-	3.100E-04
17	36	Cl	1.002E+02	1.330E-04	-	1.330E-04
34	79	Se	2.100E+03	1.270E-03	2.00E-05	2.00E-05
38	90	Sr	8.880E+04	4.716E-02	-	4.716E-02
40	93	Zr	2.940E+05	1.511E-01	2.0E-08	2.0E-08
43	99	Tc	2.560E+05	1.236E-01	3.95E-07	3.95E-07
46	107	Pd	8.260E+04	3.690E-02	4.00E-04	4.00E-04
50	126	Sn	9.980E+03	3.786E-03	9.00E-08	9.00E-08
53	129	I	6.260E+04	2.319E-02	-	2.319E-02
55	135	Cs	1.544E+05	5.466E-02	-	5.466E-02
55	137	Cs	2.100E+05	7.326E-02	-	7.326E-02
88	226	Ra	6.360E-04	1.345E-10	-	1.345E-10
90	229	Th	1.274E-03	2.659E-10	4.0E-07	2.659E-10
90	230	Th	4.560E+00	9.476E-07	4.0E-07	4.0E-07
90	232	Th	1.222E+00	2.517E-07	4.0E-07	2.517E-07
91	231	Pa	2.040E-01	4.221E-08	1.90E-06	4.221E-08
92	233	U	2.800E+00	5.744E-07	9.50E-10	9.50E-10
92	234	U	6.120E+04	1.250E-02	9.50E-10	9.50E-10
92	235	U	1.076E+06	2.188E-01	9.50E-10	9.50E-10
92	236	U	1.248E+06	2.527E-01	9.50E-10	9.50E-10
92	238	U	1.820E+08	3.655E+01	9.50E-10	9.50E-10
93	237	Np	2.480E+05	5.001E-02	5.99E-06	5.99E-06
94	238	Pu	9.840E+04	1.976E-02	7.41E-06	7.41E-06
94	239	Pu	1.484E+06	2.968E-01	7.41E-06	7.41E-06
94	240	Pu	8.180E+05	1.629E-01	7.41E-06	7.41E-06
94	241	Pu	7.540E+04	1.495E-02	7.41E-06	7.41E-06
94	242	Pu	1.634E+05	3.227E-02	7.41E-06	7.41E-06
95	241	Am	2.500E+05	4.958E-02	6.0E-06	6.0E-06
95	243	Am	5.420E+04	1.066E-02	6.0E-06	6.0E-06
96	245	Cm	1.908E+03	3.722E-04	6.0E-06	6.0E-06

*Solubility limited radionuclides are shaded in grey, others are inventory limited.

Uranium and higher actinides are all limited by solubility under these conditions. Radium, protactinium and most isotopes of thorium are not present in SNF in sufficient quantities initially to even reach their solubility limits- and thus accounting for their ingrowth is an important factor. Solubility unlimited fission products such as Cs, I, and Sr are present in high concentrations.

4.6.2. Sorption

The transport of many isotopes will be slowed by chemical or ion exchange reactions with minerals (in rocks, clays, etc.) present along the flow path of the radionuclides. Sorption coefficients- also referred to as distribution coefficients (K_d) - depend heavily on chemical conditions (salinity, pH, Eh, temperatures) and require extensive experimental investigations to develop. The equations describing linear equilibrium isotherm sorption are discussed more extensively in Appendix A, but an important outcome of the distribution coefficient is the retardation factor (R), given by Eq. (4-24),

$$R = 1 + K_d \frac{\rho}{\phi}$$

(4-24)

where ρ and ϕ are the density and porosity of the medium, respectively. The retardation coefficient R is ≥ 1 and is a factor which proportionally decreases both advection and diffusion transport velocities in a porous medium.

As with solubility, we proceed by reviewing many estimates that have been developed specifically for granitic bedrock chemical conditions and selecting bounding (minimum) values. Some elements which sorb by ion exchange (e.g., alkali and alkali earth metals such as Cs, Sr) are particularly sensitive to high salinities. The counter ions to chloride, mostly Na^+ and Ca^{2+}, act as competitors, and thus an increase in their concentration leads to reduced K_d values, possibly by one order of magnitude [257]. As such, we make a distinct preference for sorption coefficients that have been calculated or estimated for saline porewaters. Table 4-16 summarizes and compares saline sorption coefficient (K_d) values from various SNL and SKB reports.

Table 4-16. Sorption coefficients K_d (m^3/kg) of radionuclides evaluated for deep granite bedrock chemistries.

Z	A	Elem.	DBD, 100°C (SNL, 2011)[201]	Granite, (SNL, 2011) [256]	SKB, (Ohlsson, 1997) [91]	SKB (Carbol, 1997) [257]	SKB, 2011 [146]	Minimum
6	14	C	0	0	0.001	0	0	0
17	36	Cl	0	0	0	0	0	0
34	79	Se	2.00E-04	5.00E-04	0.001	2.00E-04	2.50E-05	2.50E-05
38	90	Sr	4.00E-04	5.00E-03	0.0002	1.00E-04	3.84E-08	3.84E-08
40	93	Zr	3.00E-03	2.00E-01	1	0.5	4.84E-03	3.00E-03
43	99	Tc	1.00E-08	5.00E-02	1	0.3	2.84E-03	1.00E-08
46	107	Pd	0.001	0.001	0.01	0.001	1.22E-03	1.00E-03
50	126	Sn	2.00E-03	0.001	0.001	0	4.51E-02	0
53	129	I	0	0	0	0	0	0
55	135	Cs	5.00E-03	0.05	0.05	0.01	3.46E-05	3.46E-05
55	137	Cs	5.00E-03	0.05	0.05	0.01	3.46E-05	3.46E-05
88	226	Ra	4.00E-04	2.00E-01	0.02	0.01	3.87E-05	3.87E-05
90	229	Th	3.00E-03	2.00E-01	5	1	2.84E-03	2.84E-03
90	230	Th	3.00E-03	2.00E-01	5	1	2.84E-03	2.84E-03
90	232	Th	3.00E-03	2.00E-01	5	1	2.84E-03	2.84E-03
91	231	Pa	1.00E-03	5.00E-02	1	0.5	6.76E-03	1.00E-03
92	233	U	4.00E-04	1.00E-01	5	1	2.84E-03	4.00E-04
92	234	U	4.00E-04	1.00E-01	5	1	2.84E-03	4.00E-04
92	235	U	4.00E-04	1.00E-01	5	1	2.84E-03	4.00E-04
92	236	U	4.00E-04	1.00E-01	5	1	2.84E-03	4.00E-04
92	238	U	4.00E-04	1.00E-01	5	1	2.84E-03	4.00E-04
93	237	Np	1.00E-03	2.00E-01	5	1	2.84E-03	1.00E-03
94	238	Pu	1.00E-03	5.00E-01	5	1	5.74E-04	5.74E-04
94	239	Pu	1.00E-03	5.00E-01	5	1	5.74E-04	5.74E-04
94	240	Pu	1.00E-03	5.00E-01	5	1	5.74E-04	5.74E-04
94	241	Pu	1.00E-03	5.00E-01	5	1	5.74E-04	5.74E-04
94	242	Pu	1.00E-03	5.00E-01	5	1	5.74E-04	5.74E-04
95	241	Am	5.00E-03	4.00E-02	3	1	5.74E-04	5.74E-04
95	243	Am	5.00E-03	4.00E-02	3	1	5.74E-04	5.74E-04
96	245	Cm	5.00E-03	4.00E-02	3	1	5.74E-04	5.74E-04
Comments			Values were from [21], [258] then reduced by 10× for salinity [201]	For dilute/ brackish groundw ater	Reported for high ionic strength fluid.	Lower bound of uncertainty interval (for saline water)	Lower bound of uncertain -ty interval.	

Note that sorption coefficients for plug materials (such as bentonite) are typically higher than granite[201], so it could be assumed that using the values for granite is a reasonable upper bound

approximation for the sorption coefficient of the plug materials. Obviously -for the plug material- the most conservative assumption is that $K_d=0$ for all radionuclides.

4.7. Biosphere Model

The biosphere model is the final component of repository performance assessments. Although many pathways are possible and may be accounted for within site specific biosphere models (e.g., ingestion of groundwater, consumption of contaminated foods, and inhalation), generic assessments sometimes simplify the analysis by limiting their scope to groundwater consumption[201] which is typically the major contributor to absorbed doses [259]. One frequently used assumption is the dilution rate- or the factor that accounts for the reduction in radionuclide concentration due to dilution within an aquifer before uptake by the future individual[21], [201]. In the IAEA BIOMASS ER1B case, a generic consumption rate of 1.2 m^3/yr (per person) and dilution rate of 10^4 m^3/yr are suggested based on a review of many studies and dilution factors. However, the report specifically notes that the dilution factor is not necessarily realistic and thus cannot be used to obtain absolute or accurate dose estimates (they may still have value for relative comparisons between repository designs). These factors are obviously highly site dependent; in general, groundwater resources of aquifers in crystalline rock depend on the recharge capability and climactic conditions, such as precipitation, temperature distributions and rock weathering and permeability. On a long term basis, the recharge rate in crystalline rock aquifers is approximately 2-5% of rainfall, but in some arid environments it may be less [260]. Thus, a detailed study of the hydrology of the ground-water table forms the basis for calculating the extent of dilution and uptake by an individual (in addition to assumptions on future patterns of diet, population density, etc.).

Again, to circumvent uncertainty, complexity, and variations in assumptions that may exist across model and sites, we choose to make a conservative and bounding assumption on uptake rate. Physically, the uptake to a maximally exposed individual will be limited by the transport rate (e.g., flux) of the contaminated fluid to the surface. The models presented in this thesis focus consideration to a highly conservative case where the vertical flux of fluid is dominated through a single highly permeable fracture (or the plug). The maximum advection velocity (as soon radionuclide concentrations become non-zero) is the velocity at the time of breakthrough $(v_{a,p}(\tau_b))$. Thus, the maximum possible flow rate to the receptor (when concentrations are non-

zero) is simply the product of the advection breakthrough velocity ($v_{a,p}(\tau_b)$), total area (A_p) and porosity (ϕ_p) of the plug (or fractured zone) in which the contaminated fluids are (relatively) rapidly flowing (compared to the surrounding host rock). The flow rate from the disposal zone is typically less than the average consumption rate (~1200 l/yr). When the receptor extracts and consumes more water than comes from the disposal zone, it must come from another source (water from recharge, rainfall, or that previously stored within the reservoir). In reality, these other sources of water could contain higher concentrations of some elements (iodine for example), that would create an isotopic dilution effect; this is neglected here. Overall, the result is that the total mass of radionuclides consumed (and thus committed dose) remains the same (regardless of assumptions on the consumption rate of fluid). In this case, there is no dilution effect assumed: all radionuclides flowing from the outlet of the plug (at the time of breakthrough) are consumed by a single individual. Figure 4-17 depicts the assumptions for uptake by a maximally exposed individual.
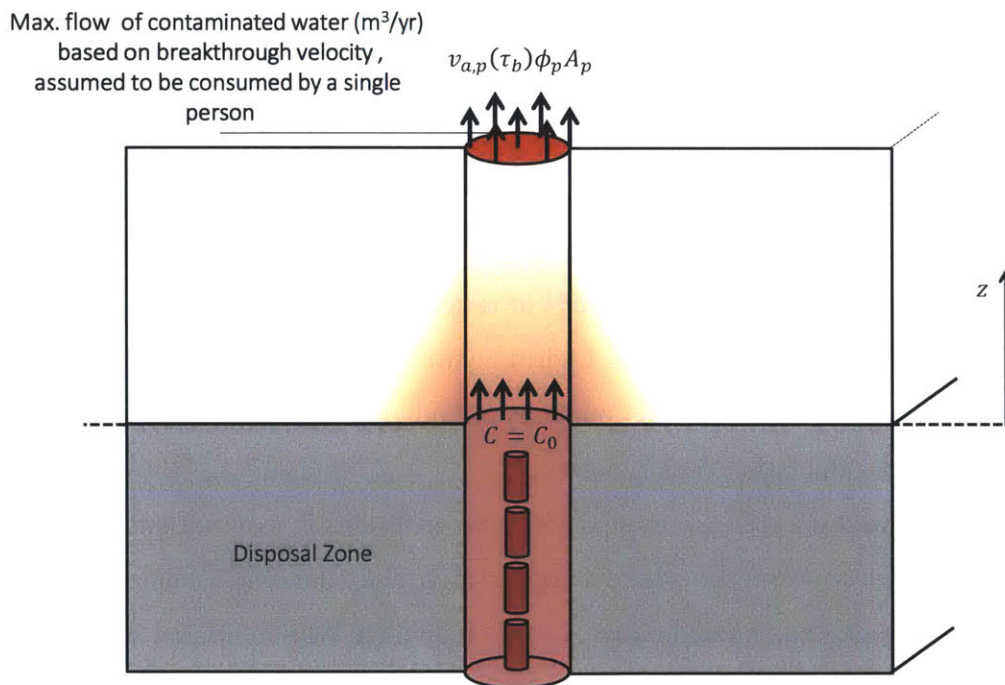
Figure 4-17. Diagram of maximum assumed uptake rate and thus dose.

4.8. Dose Calculation Method Overview

Ideally, the hydraulic barriers of the system (primarily, the plug's permeability and length) delay fluid transport across the plug for 10^6 years. In this case, system success may be confirmed using a relatively simple equation. The full solution for the breakthrough time (τ_b) is derived in Appendix B.5 as Eq. (B-34), and it is again shown due to its importance and variable sensitivity that it indicates,

$$\tau_b = \left(\left(\frac{\rho c_p}{\phi}\right)_m \frac{\phi_p L_p}{\beta_{w,th} V_{disp} 4.10 \times 10^{10}} \left[\frac{(kA)_p + (kA)_m}{k_p}\right] + (t_c)^{0.25}\right)^4 - t_c \qquad (B-34)$$

In the expected case where $(kA)_p \ll (kA)_m$ (i.e., the plug is more permeable than the host matrix, but not to the extent that it is the only path with flow), the expression approximately simplifies to Eq. (B-35),

$$\tau_b \sim \left(\left(\frac{\rho c_p kA}{\phi}\right)_m \left(\frac{L\phi}{k}\right)_p \frac{1}{\beta_{w,th} V_{disp} 4.095 \times 10^{10}} + (t_c)^{0.25}\right)^4 - t_c \qquad (B-35)$$

The left-most term represents thermal-hydraulic properties of the matrix (density, specific heat, permeability, area, porosity), the adjacent term represents the plug's hydraulic properties (length, porosity, permeability), while the other terms represent heat production by the fuel and fluid thermal expansion. If τ_b can be shown to exceed 10^6, it is not necessary to use a more complicated chemical advection transport model to conclude that the dose limits would be satisfied.

In a previously discussed "failed" case when the borehole area is small (~200 m) and the plug is fractured or failed ($k_p = 10^{-14}$ m^2) compared to the host rock ($k_m = 10^{-16}$ m^2), the total travel distance after 1 million years was shown to far exceed the length of the plug. In other words, at a certain point in time, the fluid breaks through the plug, and then there would be transport of water and chemicals from the disposal zone to the surface. However, the "breakthrough" time is simply the time at which the vertical advection distance exceeds the plug length and concentrations may become non-zero. Many other important phenomena occur simultaneously with vertical advection, such as diffusion into the surrounding rock, sorption, radioactive decay. An analytical model that accounts for all of these phenomena simultaneously is derived in

Appendix A. Reiterating the underlying components of the "steady-state" chemical transport model:

A. Vertical transport in the rock surrounding the failed plug (or disturbed zone) is assumed to be insignificant. This is apparent even in the 200 m borehole spacing "base" case, where the advection distance traveled after 1 million years is 160 meters. For greater borehole spacings, the vertical advection transport distance in the rock matrix is even smaller. Vertical diffusion from the disposal zone to the surface through the host rock is also insignificant as a transport mechanism, as discussed in [137] (concentrations are 1 billionth of their value in the disposal zone 450 meters above the disposal zone, at 1 million years, using a conservatively high diffusion coefficient of 2×10^{-9} m^2/s). As a result of the low transport rates in the surrounding rock, the surrounding host rock effectively serves as a diffusive sink for radionuclides in the plug (because its radionuclide concentrations are relatively low/zero compared to the plug).

B. The radial losses into the surrounding host rock are evaluated assuming a steady state condition (i.e., assuming the rock has become saturated, and diffusion in the host rock is equally balanced by radioactive decay). To be clear, a "steady state" (saturated) assumption for the host rock matrix concentration profile gives a lower bound on the radial diffusion loss rate from the plug into the host rock. Radial losses would be much higher than this during an initial period when sharper concentration gradients exist between the flow path and surrounding host rock [261]. The cylindrical geometry analyzed provides a slightly improved radial loss effect (compared to diffusion away from a planar crack). This argues for allowing radial diffusion from the plug (i.e., having no liner or a slotted/permeable borehole liner).

C. The steady state concentration profile is valid only after the solute has broken through the plug (this is given Eq. (A-41), or reached advection breakthrough.

By these considerations, the major bifurcation in the use and validity of the model depends on the breakthrough time (a simple to calculate thermal-hydraulic parameter). This is shown in Figure 4-18.

Calculate breakthrough time to travel L_p

$$\tau_b = \left(\left(\frac{\rho c_p}{\phi}\right)_m \frac{(\phi L)_p}{\beta_{w,th} V_{disp} 4.10 \times 10^{10}}\left[\frac{(kA)_p + (kA)_m}{k_p}\right] + (t_c)^{0.25}\right)^4 - t_c$$

If $\tau_b > (10^6$ yrs) $\longrightarrow$ **Advection is not significant**

otherwise,

If $\tau_b \leq 5$yrs   If $\tau_b > 5$ years

Use **steady** dose model, assume that $\tau_b = 5$ yrs

Use a **transient** (quasi-steady) dose model
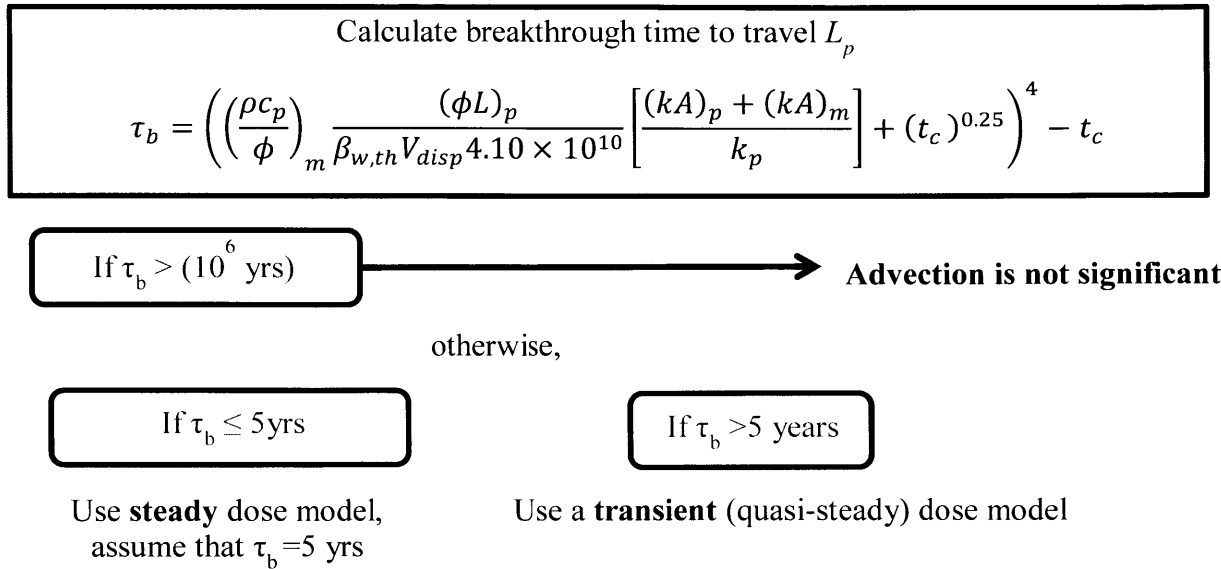
Figure 4-18. Test for plug advection breakthrough, determining whether the concentrations due to advection transport are zero, or which detailed chemical model is more appropriate.

In the case that breakthrough is rapid (e.g., <5 years) (left side of Figure 4-18) the steady state approximation for the velocity is actually accurate, because the velocity does not decrease significantly over the period that the fluid travels from the disposal zone to the surface. In this case, the inlet velocity (which determines the concentration profile along the entire plug) is equal to the outlet velocity (which determines the mass flow rate to the receptor). Thus, a single velocity determines both the chemical concentration profile and the dose delivered to the receptor, and the calculation for the concentration profile (of each radionuclide) may be completed relatively rapidly. With the initial/breakthrough vertical advection velocity, the axial concentration profile and mass flow rate of each radionuclide may be evaluated, respectively (incorporating the radionuclide specific properties such as source concentration limit C_0, granite matrix sorption coefficient $K_{d,m}$ etc.). Finally the maximum mass flow rate of each radionuclide may be converted into a dose rate to the maximally exposed individual (using the correct dose conversion factors), and the process may be repeated and summed for all radionuclides to calculate the maximum dose rate from the deep borehole facility. Figure 4-19 compactly summarizes the steady state dose calculation model. The chemical and thermal-hydraulic equations shown in the figure are fully derived in Appendix A and Appendix B, respectively.

Thermal-hydraulic

Evaluate breakthrough
velocity $v_{a,p}(\tau_b)$

$$v_{a,p}(\tau_b) = \dot{V}_{inj}(\tau_b) \left[\frac{k_p}{(kA)_p + (kA)_m} \right] \phi_p^{-1}$$

Chemical

Use velocity to determine steady state
axial concentration profile in
plug/fracture: $C_i(z)$

$$\lambda_{z,i} = \frac{v}{2D_{isp}} - \left(\left(\frac{v}{2D_{isp}} \right)^2 + \frac{\psi}{D_{isp}} \right)^{0.5}$$

$$C_i(z) = C_{0,i} e^{(\lambda_{z,i} z)}$$

Dose

Evaluate exit concentration (at $z=L_p$) and
breakthrough mass flow (Ψ) (atoms/yr)
of radionuclide to surface/receptor.

$$\Psi_i = \left(C(z = L_p) \right) A_p \phi_p v_{a,p}(\tau_b)$$

Multiply activity and ingrowth
adjusted dose conversion factors to
obtain dose (Θ)

$$\Theta_i \left(\frac{Sv}{yr} \right) = [\Psi \lambda (DCF)]_i$$

Repeat and sum for (i)
radionuclides with radionuclide
specific properties $(C_0, \psi, \lambda)_i$

Figure 4-19. Steady state model for radionuclide transport and dose rate resulting from transport through the plug or preferential vertical flow path.

The chemical model of Appendix A was derived for steady velocities and conditions. In the remaining time span considered ($5 < \tau_b < 10^6$ yrs), the problem is clearly unsteady with respect to a key parameter, velocity. In this case where the velocity decreases as the fluid traverses the distance of the plug (right side of Figure 4-18), there is no single velocity that may accurately be used to calculate both the concentration profile and the outlet flow rate. If the (lower) outlet velocity is used to calculate the concentration profile, the concentration profile along the fracture will be underestimated. If the (higher) inlet velocity is used to calculate the concentration profile, the predicted concentrations will be overly high and conservative. Although the numerical methods to integrate the governing equations in the plug are relatively straightforward (e.g., finite differencing), here we outline an analytical method that obtains equivalent answers using a fraction of the computational cost. The solution is to treat the transient problem by connecting a number of steady state solutions, in series and in time and space (this is applicable

because the axial transport is advection dominated, and the velocities are decreasing). Figure 4-20 shows a schematic of the "quasi-steady" approach to this problem; that is, the plug is split into portions (spatially and thus temporally), such that a steady state solution may be applied in each segment to calculate the maximum possible concentration experienced at any point along the plug, for all time. In this case, only three segments are shown for clarity, but an arbitrary number of segments can be used in this approach.
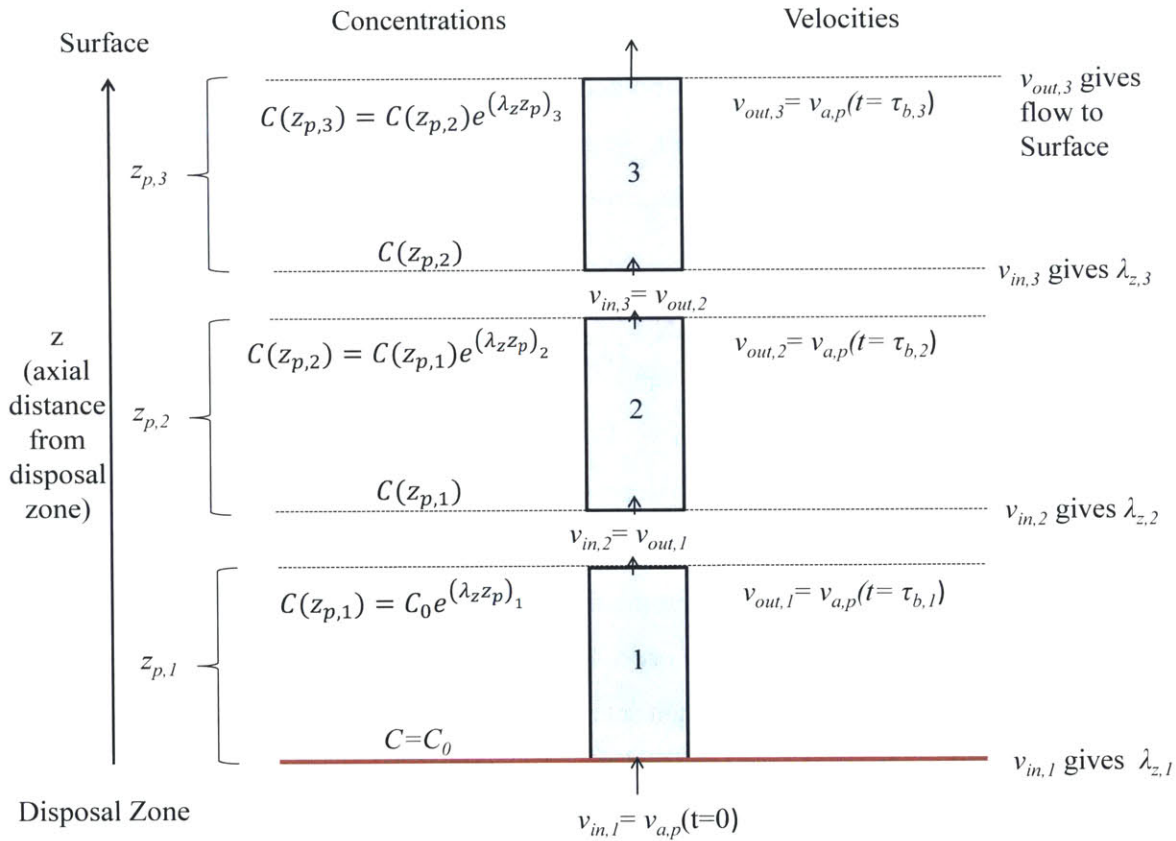
Figure 4-20. Schematic and equations describing the quasi-steady method to calculate outlet concentrations of a radionuclide.

Beginning at the disposal zone (z=0), the inlet concentration is given (by C_0) and the inlet velocity is also known (the initial velocity $v_{a,p}(t=0)$). Assuming the velocity remains constant during the period that the fluid completely traverses the first portion (1) of the plug, the steady state model may be applied to obtain the concentration profile (e.g., governed by $\lambda_{z,1}$); thus, the steady state or maximum outlet concentration ($C(z_{p,1})$) for the first plug portion may be determined. Intuitively, the outlet concentration of the first portion of the plug provides the inlet concentration to the second portion. By replacing L_p (the total plug length) by discretized axial

159

portions $(\delta z)_j$, the breakthrough time period for the jth plug portion $(\tau_{b,j})$ can be calculated using a modification of Eq. (B-34), which gives Eq. (4-25),

$$\tau_{b,j} = \left(\left(\frac{\rho c_p}{\phi} \right)_m \frac{(\phi z)_{p,j}}{\beta_{w,th} V_{disp} 4.10 \times 10^{10}} \left[\frac{(kA)_{p,j} + (kA)_m}{k_{p,j}} \right] + \left(t_{c,j} \right)^{0.25} \right)^4 - t_{c,j} \tag{4-25}$$

where $(\delta z, \phi, k, A)_{p,j}$ is the length, porosity, permeability, and areas of the jth plug portion, and all other properties are related to the host matrix and decay heat of the waste. For the first plug portion, the reference cooling period is simply t_c (e.g., 7.88×10^8 seconds which is 25 years). For all plug portions after the first one (i.e., $j>2$) the cooling period t_c is determined by the sum of the previous breakthrough periods,

$$t_{c,j} = t_c + \sum_{2}^{j-1} \tau_{b,j} \tag{4-26}$$

At the time when the fluid has broken through the first portion $(\tau_{b,1})$ and reaches the inlet of the second portion of the plug, velocity will have decreased (from the initial or inlet value for the first portion). Since the velocity is lower (slightly) in the second portion compared to the first portion, the decay constant of the concentration profile $(\lambda_{z,2})$ will be larger (i.e., greater attenuation of concentration) compared to the preceding portion of the plug $(\lambda_{z,1})$. The outlet concentration of the second portion $(C(z_{p,2})$ then serves as the initial or inlet concentration of the third portion, and so forth. The concentration at the outlet of the series may be related to the inlet, disposal zone concentration (C_0) by multiplying the concentration attenuation that occurs in each segment of the plug, as shown in Eq. (4-27),

$$C(z_{p,3}) = C_0 (\exp \lambda_{z,1} z_{p,1})(\exp \lambda_{z,2} z_{p,2})(\exp \lambda_{z,3} z_{p,3}) \tag{4-27}$$

which may be rewritten as Eq. (4-28),

$$C(z_{p,3}) = C_0 \exp(\lambda_{z,1} z_{p,1} + \lambda_{z,2} z_{p,2} + \lambda_{z,3} z_{p,3}) \tag{4-28}$$

For an arbitrary number of plug segments (j) it is apparent that the concentration at the outlet may be obtained by summing the products of the attenuation factors and plug lengths of each portion ($\lambda_{z,j}$, $z_{p,j}$), as shown in Eq. (4-29),

$$C(z_{p,j}) = C_0 \exp\left(\sum_1^j (\lambda_z z_p)_j\right) \tag{4-29}$$

As the number of segments (j) approaches infinity, the answer for the outlet concentration converges to a single value. Using these assumptions, the two analytical transport models described in the Appendix A and Appendix B (steady state advection/diffusion and thermal expansion) can be used together to obtain a conservative estimate for the radionuclide concentrations and release rate to the surface. The flow diagrams and approach is summarized in Figure 4-21.

Thermal-hydraulic
(Quasi-steady model)

$$\tau_{b,j} = \left(\left(\frac{\rho c_p}{\phi}\right)_m \frac{(\phi \delta z_p)_j}{\beta_{w,th} V_{disp} 4.10 \times 10^{10}} \left[\frac{(kA)_{p,j} + (kA)_m}{k_{p,j}}\right] + \left(t_{c,j}\right)^{0.25}\right)^4 - t_{c,j}$$

Evaluate breakthrough times and
outlet velocities $v_{a,p}(\tau_b)$ for each plug
portion (j) with length $z_{p,j}$.

$$v_{a,p}(\tau_b) = \dot{V}_{inj}(\tau_b)\left[\frac{k_p}{(kA)_p + (kA)_m}\right]\phi_p^{-1}$$

$v_{a,p}(\tau_{b,j})$

$v_{a,p}(\tau_{b,j-1})$

$v_{a,p}(\tau_{b,2})$

$v_{a,p}(\tau_{b,1})$

$v_{a,p}(t = 0)$
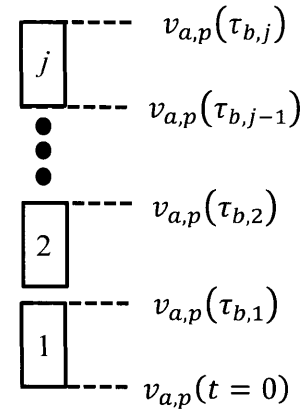
Chemical

Since velocities monotonically decrease,
assume inlet plug velocities determine
steady state axial concentration profiles in
each plug/fracture portion (j), calculate the
attenuation factor for each plug portion
(with length $z_{p,j}$).

$$\lambda_{z_{i,j}} = \frac{v_j^2}{2D_{isp,j}} - \sqrt{\frac{v_j^2}{2D_{isp,j}} + \psi_{i,j}}$$

$$C_i(z = L_p) = C_{0,i} \, exp\left(\sum_1^j \lambda_{z,i,j} z_{p,j}\right)$$

Dose

Evaluate exit concentration and breakthrough mass
flow rates (e.g. atoms/yr) of radionuclide to
surface/receptor.

$$\Psi_i = (C_i(z = L_p))A_p\phi_p v_{a,p}(\tau_{b,j})$$

Repeat and sum for (i)
radionuclides with
radionuclide specific
properties $(C_0, \psi, \lambda_z)_i$

Multiply activity by ingrowth adjusted
dose conversion factor to obtain dose (Θ)

$$\Theta_i(Sv/yr) = [\Psi\lambda(DCF)]_i$$

Figure 4-21. Schematic and equations describing the quasi-steady method to calculate maximum dose.

These equations and methods were implemented in MATLAB® in two ways to confirm the validity of the "quasi-steady" assumption. In one case, the axial transport Eq. (A-26),

$$\frac{dC}{dt} = -\frac{v(t)}{R_p}\frac{\partial C}{\partial z} + \frac{D_{isp}}{R_p}\frac{d^2C}{dz^2} - \left(\frac{2\phi_m D_m}{R_p\phi_p r_p}\right)\lambda_m K_{1/0}(\lambda_m r_p)C - \lambda C \tag{4-30}$$

is discretized in space (z) and the (1D) concentration profile in the fracture is integrated with time using the ode15s function using a second-order accurate "upwinded" differencing scheme

for the first order term (dC/dz), a second-order accurate central difference scheme for the d^2C/dz^2 term, and a time dependent advection velocity v(t) determined via Eq. (B-27). Note that the term with the quotient of Bessel functions represents diffusive losses into a surrounding host rock matrix assumed to be saturated (at steady state profile) with the given radionuclide. In the "quasi-steady" case, the concentration profile is calculated using the methods previously described in Figure 4-21. Representative results for the slowly decaying and non-sorbing (i.e., $R_p, R_m = 1$) I-129 with the failed "base case" thermal hydraulic parameters, are shown in Figure 4-22.
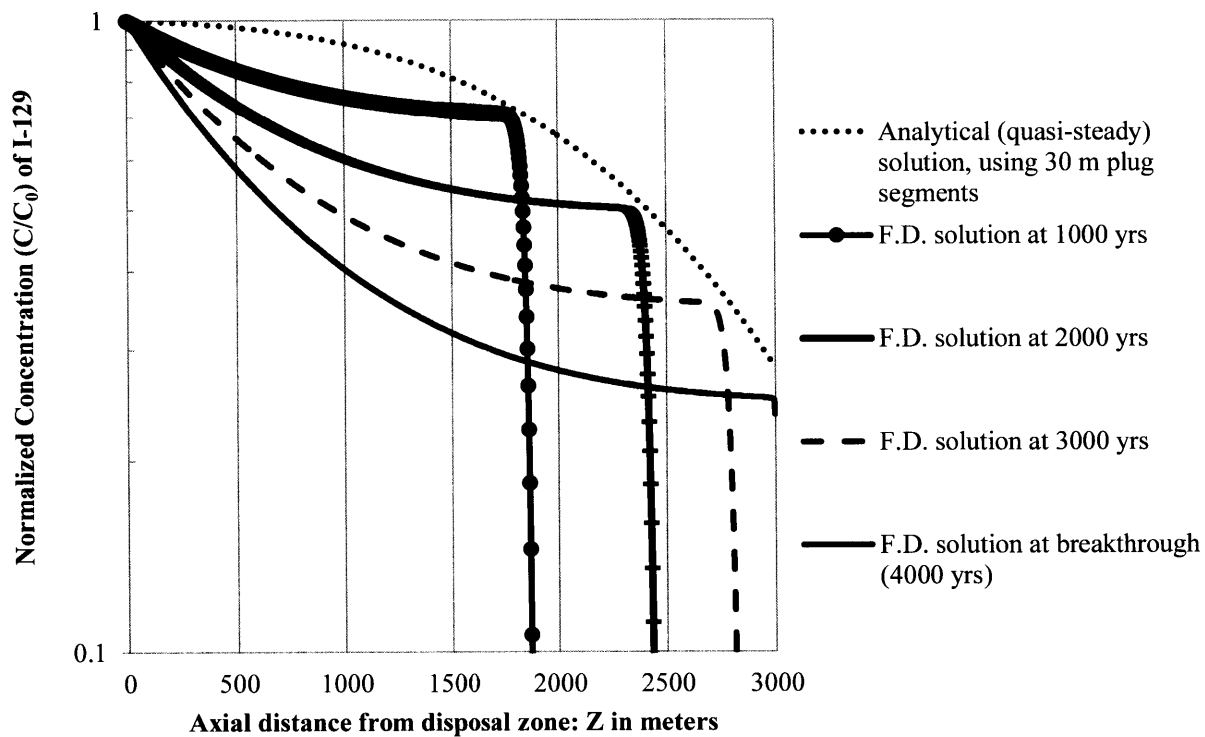
Figure 4-22. Semi-log comparison of exact numerical solution to quasi-steady analytical solution for the concentration profile in the matrix (for heterogeneous base case). Host rock apparent diffusion coefficient is $10^{-11} m^2/s$

The numerical results were obtained using 1000 segments with a discretization of 3 m, whereas the quasi-steady analytical solution only requires 100 segments (each with length of 30 m), and runs in a significantly faster time period due to the fact that no numerical integration is required. The analytical method is shown to correctly calculate the maximum concentrations in the

fracture, at any axial point. The numerical results display the expected "shockwave" behavior, whereby the concentrations in front of the traveling wave are zero prior to advection breakthrough.

4.9. Chapter Summary

This chapter presents an integrated analytic model for radionuclide transport from SNF disposed in a deep borehole. The chapter opens with a discussion of the fundamental thermal transport mechanisms of natural convection and expansion. A rock permeability of less than 10^{-15} m^2 is sufficient to rule out convection in the overlying host rock region (even when the temperature increases of the repository are accounted for). Furthermore, with the reference salinity and density gradient (~72 kg/m^3 at a depth of 1200 m), convection is inhibited, regardless of the overlying rock permeability. Under the expected borehole conditions, low rock permeability and groundwater salinity gradients effectively prevent convection. Ultimately, thermal expansion of water is concluded to be the most significant vertical transport phenomena.

The transport model has two main components- a thermal hydraulic model to calculate fluid velocities and a chemical/geosphere model to calculate the resulting concentrations within the flow path and surrounding host rock. Release is modeled along a preferential, high permeability flow path (e.g., the plug that overlies the disposal zone) with arbitrarily specified physical properties of diameter, permeability, porosity, diffusion coefficient, grain size. The surrounding host rock is assumed to have homogenous properties, with values informed by the discussion of basement rock properties in Chapter 2. The thermal-hydraulic model is based on thermal expansion effects created by the SNF decay heat and is shown to be conservative in calculating penetration distance (typically by a factor of two) compared to a more complex numerical model (BVR). The analytical model conservatively neglects the effects of pore fluid compression and heat loss to the surface- the former causing a time delay of transport and the latter resulting in less thermal expansion and velocities at long time periods. The chemical and geosphere transport model includes the effects of advection, longitudinal dispersion, diffusion, sorption, and radioactive decay. Decay chain ingrowth is treated by assuming that all daughter products exist in secular equilibrium with the parent, and modifying (increasing) the dose conversion factor of the parent radionuclide. A method of solving the transient problem (when vertical velocities in the plug decrease significantly with time) using a quasi-steady approach is

presented. The model does not require any numerical solvers, simulations, or integrations and results in convenient and closed-form expressions for the steady state dose rate resulting from each radionuclide. In cases where uncertainty is encountered (e.g., degradation of fuel, sorption coefficients, solubility) bounding values that tend to maximize the radionuclide concentrations are chosen.

The provided analytic model should be useful to future investigators and possibly regulators wishing to evaluate the compliance and accuracy of numerical calculations without necessarily penetrating all the details of the numerical modeling. In addition, as will be shown in greater detail in the following chapter, the analytic model is also useful for gaining insights into the sensitivity of the borehole facility performance to various engineered and geologic design choices and properties.

5. Integrated Performance and Economic Model

5.1. Introduction

The previous section introduced a versatile set of analytical models to calculate the rate of radionuclide release from a deep borehole repository, under a wide range of hydraulic and chemical assumptions and properties. The current section is devoted to utilizing this model over a range inputs to determine the sensitivity of the model to the design of the deep borehole repository. The primary goals are to:

1. Determine the effects of disposal depth, disposal zone length, and borehole spacing on both performance and cost.

2. Inform the development a list of site and engineered parameters that should be studied and verified in greater detail when preparing a safety assessment for a deep borehole facility.

The chapter begins by defining two basis failure conditions (modeling methods and assumptions) by which the reference design may be evaluated. For each of these design bases, the performance of the repository under various design changes can be evaluated. In the second portion of this chapter, an economic model for drilling, site characterization, and emplacement costs is outlined. The economic model incorporates a wide range and uncertainty in cost estimates, primarily because costs will be much higher for a first-of-kind DBD compared to an incremental project that has benefited from technology development. In the final section, the economic model is coupled with the performance model, and the deep borehole design is optimized for a range of economic conditions

5.1.1. Design basis failure conditions

Failure and transport of radionuclides in a repository occurs due to fractures which provide a preferential path for flow to the surface. Defining design basis failure scenarios thus depends on depicting fractures and "failed" or "damaged" (where structural damage and permeability increase may occur during excavation or drilling) rock regions. Some authors model fractures [237], [262] directly (using analytical models or hybrid analytical/numerical models), while others model "fracture zones" which have a higher effective permeability due to the assumed fracture network within the failed zone [96], [201], [263]. Typically, the latter is more

convenient for numerical codes which have difficulty refining small details (such as fractures) and incorporating regions with large differences in permeability or properties. In light of the uncertainty in modeling this process, this thesis will follow both approaches, where the failure is modeled by,

1. A large porous zone or region with elevated permeability compared to the host rock.
2. A (small) discrete cylindrical fracture.

5.1.1.A.   *Design Basis 1 (DB1): permeability increase in failed zones*

The first design basis approach has already been discussed in Chapter 4 (specifically, modeling the plug as a failed region). Considering that a potential drilling damaged host rock zone would be directly adjacent to the plug, it is assumed that they may both be treated as a single failed region with elevated permeability (similar to the approach of other DBD investigators [201]) Some previous assumptions and measurements of effective permeability in failed or damaged crystalline rock are summarized in Table 5-1.

Table 5-1. Assumed permeability (k_m) for modeling fractured or "damaged" crystalline rock.

Model/Data	"Disturbed Zone" k_m (m²)	Porosity (ϕ_m)	Damaged zone size	Undisturbed rock permeability	Disturbed Undisturbed Permeability ratio
Deep borehole disposal (SKB, 2011)[96]	5×10^{-16}	0.01	-0.8 m radius in the disturbed zone -50 m width for a penetrating fracture	10^{-18} m²	500
Bounding case, DBD seal [201]	10^{-12}	0.01	1 m² (seal)	10^{-16} m²	10^4
Emsley et al. (1997)[264] Excavation damaged zone (EDZ) at the ASPO rock laboratory, Sweden	$\sim 10^{-16}$	-	~ 50 cm into surrounding rock	10^{-18} m²	100
Autio et al. [265] (EDZ), bored deposition holes in Olkiluoto, Finland	5.16×10^{-21}	0.0034 (compared to 0.001 for undisturbed)	~ 3 cm into surrounding rock	2.96×10^{-19} m²	56 (average)
Souley et al., EDZ blasted and drilled TSX tunnel in Canada's URL [266] at 500 m depth	2×10^{-17}	-	50-70 cm	10^{-21} m²	2×10^4

In general, a permeability increase between 1-4 orders of magnitude has either been assumed or measured in boreholes or mines excavated in crystalline rock. Obviously, more work needs to be done to quantify this parameter and methods to "heal" the damaged zone (e.g., via sodium silicate injection) need to be better tested. In these future investigations, it will be important to distinguish between the damage caused by excavation method (e.g., blasting vs. drilling) and damage caused by stress redistribution. Blast damage (specifically in mined shafts) can account for up to 70% of the increased flow in a EDZ for a shallow excavated repository[267]. On the other hand, stress redistribution effects are likely to be more important for drilled, deep boreholes. The permeability increases in the EDZ that were measured (last three rows of Table

5-1) are also dependent on borehole size and in-situ stresses at the depth of the borehole. More work is needed to quantify the extent of the EDZ in a deep borehole, (particularly ones drilled at depths 1-3 km), along with the sensitivity to the drilling method and muds. The data from Autio suggests that the permeability increase due to excavation damage would also increase both porosity and diffusion coefficient of the damaged rock (which would have a beneficial effect in slowing vertical chemical transport).

As for plug failure, the expected plug properties have already been discussed in Section 3.2.2. Reiterating the findings summarized in Table 3-3, the plug materials should achieve a permeability of 10^{-16} m^2 (as an upper bound) with 10^{-18} m^2 being a design goal that could be justified with further work. Thus, with 10^{-17} m^2 being a lower bound on the bulk host rock permeability, a plug permeability increase of 100× appears reasonable as a design basis failure value. The "failed" zone is assumed to have a diameter of 1.2 meters (despite the fact that the borehole will have a significantly smaller diameter). Lastly, the porosity is assumed to remain at the reference, conservatively low value of 0.01.

5.1.1.B.   Design Basis 2 (DB2): fracture size

The second design basis requires additional derivations and assumptions so that a fracture can be captured by the previously derived thermal-hydraulic model. The classic (and idealized) fracture network is a set of perfectly repeating planar cracks within relatively impermeable rock. The half crack aperture (b) and uniform rock mass width or fracture spacing (w) may be related to the "effective" permeability of the rock mass by Eq. (5-1) [262],

$$k_{eff,planar} = \frac{(2b)^3}{12w} \tag{5-1}$$

Table 5-2 compares some previously assumed fracture network parameters that modelers have used for crystalline rock.

Table 5-2. Assumed fracture sizes and spacings for modeling fractured crystalline rock

Model	Fracture aperture (2b)	Fracture spacing (w)	Effective fractured continuum permeability Eq. (5-1)
SNL, Generic granite model[201]	10^{-5} - 10^{-4} m	25 m	3.33×10^{-18} to 3.33×10^{-14}
SKB, Analytical models [237], [268]	10^{-4} m	2 m	4.16×10^{-14} m^2
Shen et al. [262]	10^{-5} m	0.25 m	3.33×10^{-16} m^2
Bok et al. [269]	5×10^{-5} m (max.)	0.195 m (min.)	5.34×10^{-14} m^2 (max.)

Fracture apertures of 10-100μm appear to be a commonly assumed by previous modelers of crystalline rock. Injection tests completed at the KTB borehole [72] were used to calculate the hydraulic diffusivity of a major communicating fracture set between the pilot borehole and the main borehole. The equations used relate the hydraulic diffusivity to the average (planar) fracture width (2b), are shown as Eq. (5-2),

$$D_{hydr} = \frac{(2b)^2}{12\mu(\beta_w + \beta_r)}$$

(5-2)

where β_w is the fluid compressibility, and the rock fracture compressibility (β_r) was concluded to be 5×10^{-8} Pa^{-1}. Clearly this effect dominates over the fluid compressibility ~ 3.4×10^{-10} Pa^{-1}. Assuming a fluid viscosity of 3×10^{-4} Pa-s and using the measured hydraulic diffusivity of 0.15 m/s^2, the average fracture aperture via this method is ~5 μm (consistent with that stated in the paper of 5-7 μm). Based on an estimate of 15,400 fractures intersected (across a 3000 meter length between 3000-6000 m) results in an average fracture spacing of 0.195 meters. Finally, using Eq. (5-1) gives an effective (fractured) rock permeability of 5.33×10^{-17} m^2. Thus, experimental data on fracture apertures is roughly consistent with the modeling assumptions shown in Table 5-2.

From these data, we take 100 μm as a conservative, design basis value for fracture size (2b) in a failed rock region. However, it is unlikely that the failed region would exist as an idealized, completely continuous, straight, vertical, planar fracture from the receptor (at the surface) to the disposal zone (~over 1-3 km). True fractures will exhibit much more tortuosity (i.e., longer effective path lengths) and have changes in fracture aperture along the path. Longer paths increase the rock surface area with which the radionuclides are in contact, thus increasing

170

diffusive losses. Secondly, changes in fracture aperture (or effective permeability of the fracture) will cause radial inflows and outflows from the fracture (see Appendix B.8), thereby causing dilution of the contaminated stream. Thus, a realistic model of the fracture network will have much lower radionuclide concentrations than an ideal fracture model (for reasons that cannot be captured by the steady state analytical models developed in this thesis).

The solutions for concentration profiles developed in the Appendix A are for a cylindrical geometry, so for consistency, the fracture flow is treated in the same way. The effective permeability relations for flow within a cylindrical fracture are written as Eq. (B-50) (see derivation in Appendix B.9),

$$k_{eq,cyl} = \frac{(2b)^2}{32}$$

(B-50)

where b is the fracture radius, $k_{eq,cyl}$ is the equivalent permeability of the open ($\phi_p=1$), cylindrical fracture. Thus, a cylindrical fracture with diameter of 100 μm has an equivalent permeability of 3.125×10^{-10} m^2. This would be a crack that forms a cylindrical "pipe" through the plug as shown in Figure 5-1.
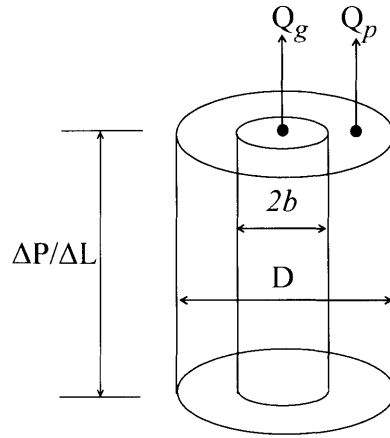
Figure 5-1. Description of fluid flow through a cylindrical gap with thickness b in a impermeable plug in a region with diameter (D)

The flow rate through the cylindrical gap (Q_g) with flow area πb^2 can be calculated using equivalent permeability of the cylinder (with area πb^2), and is shown in Eq. (5-3),

$$Q_g = \pi b^2 \left(\frac{(2b)^2}{32}\right)\left(\frac{1}{\mu}\right)\left(\frac{\Delta P}{\Delta L}\right)$$

(5-3)

The effective permeability ($k_{eff,g}$) of the cylindrical hole and surrounding (impermeable rock) system can be derived to be Eq.(5-4),

$$k_{eff,g} = \frac{b^4}{8r^2}$$

(5-4)

The effective permeability of the 50µm radius cylindrical gap in a plug of diameter 0.6 meters is thus 2.17×10^{-18} m^2.

5.1.1.C.   Other design basis parameters: D_m and k_m

A key insight from inspecting the analytical solutions in the Appendix (albeit counterintuitive) is that to obtain the most conservative design, the smallest matrix diffusion coefficient (D_m) and host rock permeability (k_m) must be assumed. This is because the lower the assumed diffusion coefficient, the lower the diffusive losses into the surrounding host matrix. Secondly, the lower the host rock permeability, the greater the overpressure created in the disposal zone, which leads to greater flows through the preferential flow paths (keeping the preferential flow path properties constant).

In Section 2.3, the variable and complex nature of the diffusion coefficient and host rock permeability was discussed. Over large distances and geologic time scales, both the host rock permeability and diffusion coefficient in crystalline rock are inferred to be higher compared to those measured at small scales (e.g., $D_m = 10^{-11}$ to 3×10^{-10} m^2/s for the UPH-3 borehole[15]). This elevated "kilometer" scale diffusion coefficient was also observed in more recent tracer tests in crystalline rock, which suggested that the matrix diffusion (D_m) coefficient was the same as the free or water diffusion (D_w) coefficient ($\sim 2 \times 10^{-9}$ m^2/s)[99], [270]. When measured on very small scales, the diffusion coefficient is typically many orders of magnitude lower than the free water diffusion coefficient. On the basis of these observations, 10^{-11} m^2/s appears to be a reasonable and conservative value for the (kilometer scale) design basis diffusion coefficient (D_m). With an assumed rock porosity of 0.01, the effective diffusion coefficient is 10^{-13} m^2/s. Note that this (very low) matrix diffusion coefficient actually improves the validity of two of the model's assumptions: purely diffusive transport from the disposal zone to the surface is not a credible transport mechanism; there is no simultaneous diffusive vertical transport in the host rock matrix.

As discussed in Section 2.3.1, 10^{-17} m^2 is expected to be a lower bound on the permeability of basement crystalline rocks (on the scale of ~km). A host rock permeability of 10^{-17} m^2 would be in between the previously used "base case" host rock permeability of 10^{-16} m^2 and the "very low" permeability of 10^{-18} m^2 evaluated in Section 4.4. For an even lower rock permeability ($k_m < 10^{-18}$ m^2) the effect of delayed hydraulic diffusion, larger pore pressure buildups, and fluid compression needs to be taken into account. The model proposed here (which assumes instantaneous equilibrations of profiles) is conservative and cannot capture these time delay effects. In any case, it is probably be beneficial to avoid sites where pore fluid compression behaves as a significant delay mechanism, as it implies that pore pressure becomes elevated significantly (increasing the risk of seismic events and fracturing).

All other thermal hydraulic parameters are based off the ones previously discussed in Chapter 2 and evaluated in Chapter 4.

5.2. Transport results for DB1 and DB2

5.2.1. Borehole spacing

Having fully outlined the thermal, hydraulic, chemical, and radionuclide inventory assumptions of a conservative (steady state) model, we continue our analysis of the failure scenarios to obtain insights into the system's sensitivities and behavior. The first design parameter that is investigated is the borehole spacing. SNL's reference design document suggests that boreholes may be spaced as closely as 50 meters, while the previous MIT design [108] used 200 meters as the reference borehole spacing. To date, there has not been a systematic evaluation of the effect of borehole spacing on repository performance (or cost, for that matter). Previous analysis of the temperature profiles in a borehole repository showed that increasing the borehole spacing from 200 to 400 meters (or reducing disposal zone length to 1000 meters from 2000 m) was required to eliminate a second peak in temperatures occurring between 1,000-10,000 years [98]. The analytical model shows that the pressure buildup and velocities would follow a similar trend: velocities decrease as the length of the disposal zone decreases and as the total facility area increases. This indicates that there is an important tradeoff to consider when increasing the borehole spacing beyond 200 meters (vs. increasing the disposal zone length). The borehole spacing is also a convenient place to begin parametric analysis because it allows for a wide

variation in the driving forces (e.g. pressure buildup), with a relatively small change in parameter.

As previously discussed, for the purposes of using the lumped parameter model for velocity, borehole spacing should be kept in the relatively narrow range of 200-800 meters to ensure that the predictions for vertical penetration distance remain valid (e.g., pressure is uniform in the disposal zone) and conservative when compared to the numerical predictions. A smaller spacing increases the vertical velocities by a squared factor. For this parametric study three key outputs are discussed:

1. Breakthrough time: a convenient metric of performance which may demonstrate the safety of the facility without relying on more complex modeling assumptions (e.g., chemical models).

2. The flow rate (at breakthrough): a convenient measure of the leakage rate of radionuclides to the receptor.

3. Maximum dose rate: the maximum dose rate is used to determine if the case satisfies the dose limits that could be imposed on a DBD facility (<15 mRem/yr).

Table 5-3 lists these three main outputs for the two design basis failure scenarios (DB1 and DB2), across a range of borehole spacings. Since DB1 typically exhibits breakthrough times >>10 yrs, a quasi-steady model (implemented in MATLAB®, using 1000 sequential plug segments) is required to obtain dose estimates. For the DB2 (fracture cases), the breakthrough times are <1 yr, and the (single segment) steady state dose model is appropriate. Comparing the 300 m borehole spacing cases (where the flow rates for DB1 and DB2 are close to being equal, but the fracture breakthrough time is much faster for DB2), it is apparent that the radionuclides must have experienced significant decreases in concentration during travel to the surface, despite the much shorter residence time in DB2. This can be explained by the fact that for small fractures, the surface area to volume ratio is increased, which increases the diffusive losses and lowers the concentrations in the fracture (compared to DB1, which has a larger diameter of 1.2 meters). In almost all cases, I-129 is the radionuclide that causes the maximum dose. Figure 5-2 presents the data from Table 5-3 in graphic form.

Table 5-3. Breakthrough time, flow rate, dose rate, and dominant radionuclides for borehole spacings of 200- 600 m, for DB1 and DB2.

Borehole spacing	Metric	DB1	DB2 (fracture)
200 m	Breakthrough time (yr)	3692	0.08
	Flow Rate at Breakthrough (l/yr)	3.198	0.296
	Dose Rate (mRem/yr)	2.116×10^5	0.219
	Contributing Isotopes	[I-129]	[Sr-90, I-129]
300 m	Breakthrough time (yr)	47,354	0.179
	Flow Rate at Breakthrough (l/yr)	0.2110	0.131
	Dose Rate (mRem/yr)	5.24×10^{-3}	7.84×10^{-10}
	Contributing Isotopes	[I-129]	[I-129]
400 m	Breakthrough time (yr)	358,943	0.320
	Flow Rate at Breakthrough (l/yr)	0.026	0.073
	Dose Rate (mRem/yr)	1.7836×10^{-29}	1.27×10^{-20}
	Contributing Isotopes	[I-129]	[I-129]
500 m	Breakthrough time (yr)	>1 mY	0.501
	Flow Rate at Breakthrough (l/yr)		0.047
	Dose Rate (mRem/yr)		2.323×10^{-34}
	Contributing Isotopes		[I-129]
600 m	Breakthrough time (yr)	>1 mY	0.723
	Flow Rate at Breakthrough (l/yr)		0.032
	Dose Rate (mRem/yr)		4.605×10^{-51}
	Contributing Isotopes		[I-129]
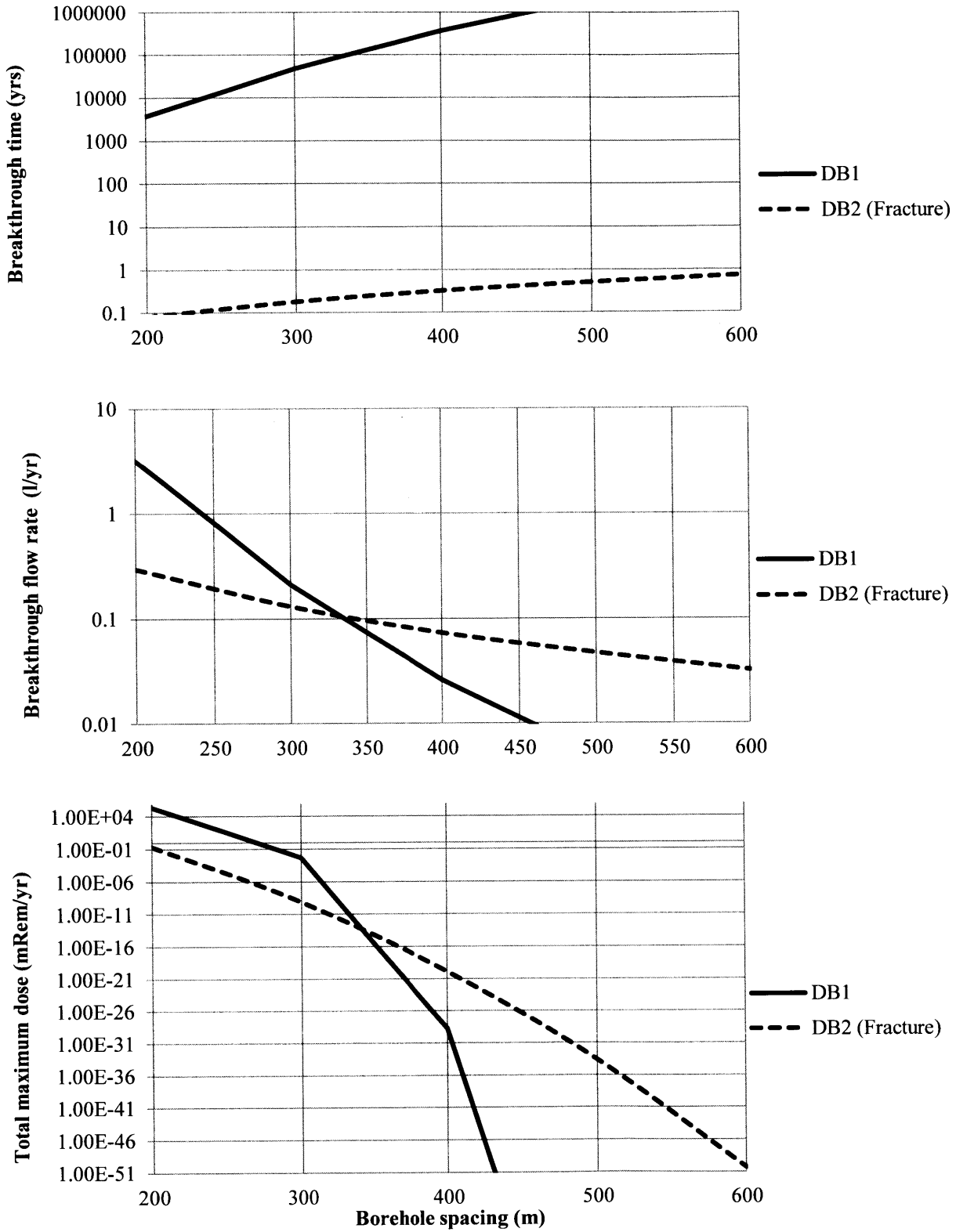
Figure 5-2. Breakthrough time, flowrate, and maximum dose (top, middle and bottom panels) vs. borehole spacing for DB1 and DB2.

Unless there are significant costs to increasing the area of the disposal facility, the results suggest that for this particular design (the 2 km disposal zone length), the 400 m spacing is more robust and preferred. When the spacing is increased to 450 meters or beyond, the design demonstrates a very large margin to failure, for both DB1 and DB2. In fact, at a 450 meter spacing the design could be said to be inherently safe with respect to DB1 (breakthrough time exceeds 10^6 yrs).

Borehole disposal depth or plug length is the another key design choice with regards to deep borehole disposal depths: previous models and designs have varied this parameter between 1 km [20] 2 km [108] and 3 [21] km depths. Again, to date there has been no parametric study on the importance of disposal depth for a deep borehole facility; the obvious answer is that disposal must be deep "enough" to ensure sufficient radionuclide retention. Obviously if sufficient performance can be demonstrated at shallower depths, cost reductions may be possible by combinations of:

   -reducing the depth of disposal

   -modifying the capacity (e.g., vary disposal zone length)

   -changing the borehole spacing and thus area of land that must be characterized

5.3. Economic models

The performance model described in the previous sections (where boundaries are assumed to be closed) demonstrates that there are performance tradeoffs between borehole depth, borehole capacity (length of disposal zone), and borehole spacing. To optimize the design through a cost benefit analysis, the costs of changing each parameter must be understood. The first two (depth, disposal zone length) depend on the drilling costs and emplacement costs, while the latter depends on the site characterization cost.

5.3.1. Site characterization costs (vs. area)

Experience and cost estimates from the Yucca Mountain project suggest that site characterization could cost up to $22M/km^2 (or $54/kgHM) [7], [27]–[29]. Another more systematic approach to estimating site characterization costs is based on the EPA's assessment of the costs of CO_2 sequestration, which includes site characterization, preparation, drilling, and monitoring [271]. Table 5-4 summarizes an itemized approach to estimating site characterization costs for a deep borehole repository of varying size.

Table 5-4. Site characterization and preparation costs (based on CO_2 sequestration estimates from 2008).[271]

Cost item	Estimate	**Fixed cost ($/site)	Marginal costs ($/km^2)
Site Characterization			
Maps of local geologic structure	60 hrs @ $106.31/hr $6379/site	$6,379/site	
3D seismic survey (faults/fractures) + Seismic history	60 hrs +$30,000/km^2 (upper bound est.)	$6,379/site	$30,000/km^2
Aerial survey of land use (0.5 m resolution)	$3000+ $400/mi^2 ($1,032/km^2)	$3,000	$1,032/km^2
Hydraulic properties/layers	24 hrs of geologists	$2,551/site	
Mechanical properties (stresses) using existing data	120 hrs of geologists	$12,757/site	
*Mechanical properties (new data)	$75/ft ($246/m) per well + $3000/core		$984,000+$74,000=$1.16M
Survey of drinking water	24 hrs	$2,551/site	
Survey of subsurface aquifers	60 hrs	$6,379/site	
Water rock chemistry, fluid geochemical analysis	240 hrs +$10,000 lab fees	$35,514/site	
Review well history, penetrations database	24 hrs	$2,551/site	
List of water wells	36 hrs	$3,827/site	
Geologic characterization report	240 hours	$25,514/site	
Total for Characterization		$107,000/site	$1.19M/km^2
Site Preparation			
Rights of way for surface use	$20,000/borehole		$20,000/borehole
Rights for subsurface use	$50/acre ($12,355/km^2)		$12,355/km^2
Land use, air/water emissions for drilling	$100,000/site +$20,000/mi^2 ($51,780/km^2)	$100,000/site	$51,780/ km^2
Total for Site Preparation		$100,000/site	$64,135/km^2 +$20,000/borehole
Total for Site Prep.+Char.		$227,000/site	$1.25M/km^2
Total, with 10× premium on fixed costs		**$2.27M/site**	**$1.25M/km^2+ $20,000/borehole**

*Assuming that one 4000 m test well is necessary to characterize 0.5 km^2 [70], and 1 core sample per 70 m are required [26]

Presumably, the costs of deep borehole disposal site characterization would be similar to those of CO_2 sequestration, as both require evaluating similar properties (mechanical, hydraulic, chemical) at similar depths (~3000 meters). However, we conservatively assume that the DBD site characterization fixed costs would be subject to a 10× premium (due to the fact that properties might have to be determined to a greater level of certainty, more money might have to be spent to purchase the rights for subsurface use for nuclear waste disposal, etc.). Another key assumption (not made in the CO_2 sequestration analysis) relates to a high density or number of test boreholes that might have to be drilled and cored to characterize a given area or site. In this case, we conservatively assume that one test borehole is required to characterize every 0.5 km^2, which is roughly consistent with the area of land that may be characterized by a seismic injection test for permeability and fractures[70]. It is also consistent with the observation from the KTB and UPH boreholes that multiple boreholes are required to qualify the extent, severity and continuity of fractures at a site[53], [72] (i.e., the disposal borehole alone is probably not sufficient to provide characterize the site). Secondly, we further assume that additional area surrounding the repository needs to be characterized. Figure 5-3 describes the total characterization area.

Additional area that must be characterized= $N_b P^2$

P: Borehole Spacing

Central area to be characterized=$N_b P^2$
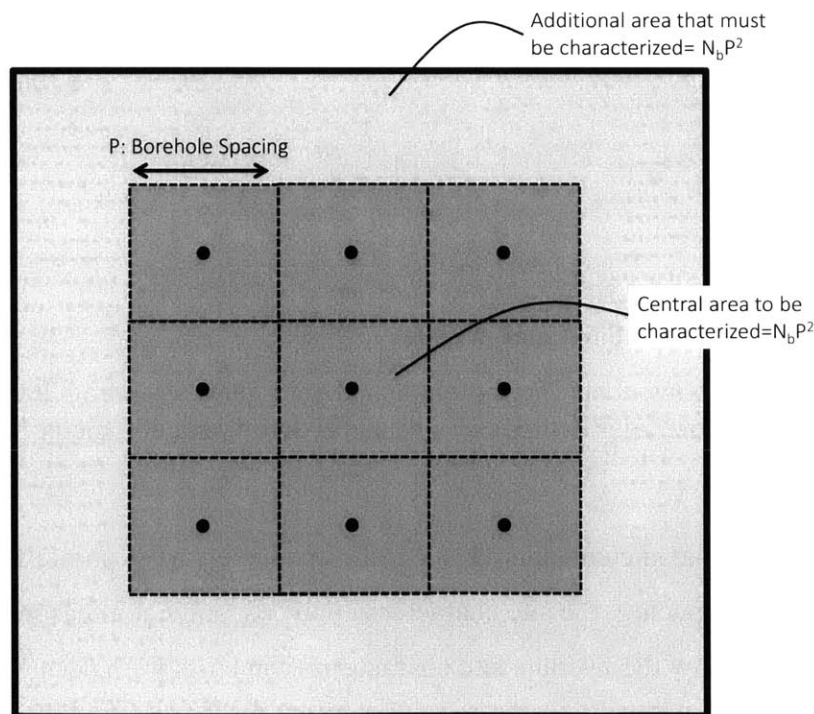
Figure 5-3. Diagram describing total borehole area to be characterized, where N_b is the number of boreholes at a site and P is the borehole pitch or spacing.

Overall, the assumed test borehole density and costs raise the marginal costs to $1.25M/km^2: significant when compared to fixed costs ($2.27M/site). The large marginal cost and large boundary area assumed tends to penalize designs with larger borehole spacings. Since there are some fixed (per site) costs, we expect the specific costs ($/kgHM) to decrease as the number of boreholes drilled at a single site increases. The minimum # of boreholes that would likely be drilled at a site is the number of boreholes required to dispose of 80 years of fuel from a 1 GW(e) PWR (~1600 MTHM), or 8 boreholes. For the minimum borehole spacing considered (200 meters), this corresponds to a total characterization area of 0.64 km^2 (~1 test borehole required). Figure 5-4 shows the site characterization costs vs. number of boreholes drilled at a site (and borehole spacings of 200, 400 and 600 meters).
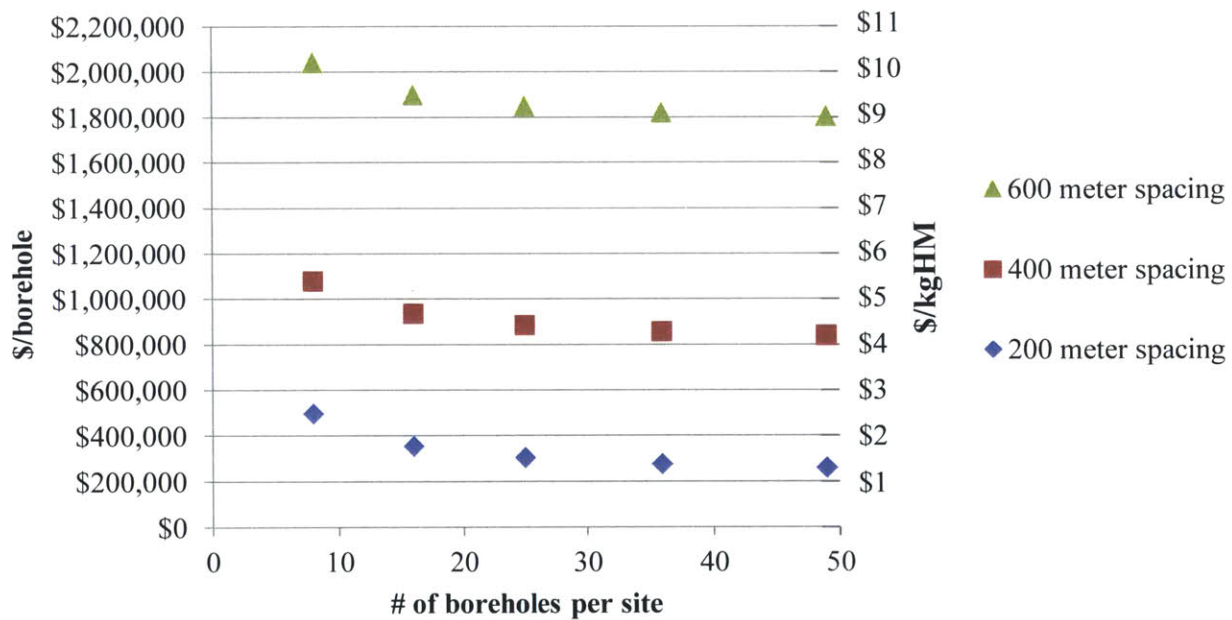
Figure 5-4. Site characterization costs (per borehole and per kgHM assuming 200 MTHM/borehole) vs. # of boreholes drilled per site, for 200, 400 and 600 meter borehole spacings.

Even for the smallest borehole site considered (8 boreholes, the left-most point of each curve), for the 400 meter borehole spacing, the site characterization cost stays at a reasonable $5.38 kgHM. This is still 10× below the average site characterization costs for Yucca Mountain, and less than 1.5% of the total collected waste fee of $400/kgHM. The right-most points (for 49 boreholes) shows the approximate behavior for a borehole site with an infinite number of

boreholes): marginal costs are so large in this analysis that the cost reduction with greater number of boreholes (>30) is not significant. Thus, for subsequent analyses, the marginal cost of $1.25 M/km^2 ($1.25/m^2) is used as the primary cost factor for site characterization.

5.3.2. Drilling costs (DC) (vs. depth)

Another major cost component is the drilling cost (DC), which has been estimated to vary exponentially with borehole depth [272]. Thus, drilling costs are fitted by an exponential curve, as described by Eq. (5-5),

$$DC(z) = DC_0(e^{\lambda_d z}) \tag{5-5}$$

where DC_0 is a fixed cost associated with starting the drilling operation (assumed to be $1M). With an estimate for the depth and cost of a borehole, the exponential factor (λ_d) may be calculated, and the drilling costs may be extrapolated to other depths.

The reported budget for the entire KTB scientific borehole project ($350M USD total cost in 1994 for both the KTB-HB to 9km and pilot KTB-VB to 4 km)[22] serves as a conservative, upper bound approximation on drilling costs. This is adjusted for inflation to $624M US 2013 [273]. As a middle bound, the "generic" IDDP borehole cost estimates (15.5M USD for a 4 km maximum depth borehole may be used). The estimated costs for the IDDP borehole are summarized in Table 5-5.

Table 5-5. Breakdown of estimated costs for the large diameter (type A) borehole from the IDDP feasibility study [274].

	Cost ($ 2002)	Rig Time (days)
Drilling	$7.55M	121
Coring	$5.94M	140
Logging	$0.641M	18
Total (w/ 10% contingency cost)	$15.5M	279

Adjusting the 2002 estimated IDDP drilling cost of $7.55M for inflation gives $9.55M [273]. For our low estimate, adjusting SNL's recent 2011 cost estimate[149] of $27M gives $27.9M. This is considered to be a lower bound, because the drilling costs were estimated for an "incremental" (in other words, Nth of a kind) borehole at a given site. Table 5-6 compares all

three drilling costs and the exponential factor which can be used to extrapolate costs to other depths.

Table 5-6. Comparison of drilling cost (DC) approximations, based off three deep drilling project costs or estimates.

Type of estimate	Source	Max useable depth ,diameter	Assumed fixed cost (DC$_0$)	$ Cost (Adj. 2013)	λ_d (1/km)	Projected cost	
						4 km	5 km
High (Scientific, first of a kind)	KTB-HB	6 km, 36 cm	$1M	$550M	1.051	$67.1M	$192M
Mid	IDDP	2.4 km, 41.4cm	$1M	$19.6M	0.94	$43.1M	$110M
Low (Incremental, nth of kind)	DBD (SNL)	5 km, 43 cm	$1M	$27.9M	0.666	$14.6M	$27.9M

Note that for calculating the exponential drilling constant (λ_d), the useable depth (third column of Table 5-6) is considered to be that which would be able to fit a PWR assembly with minor changes to the casing or borehole design. Figure 5-5 compares these three cost curves alongside other estimated and actual costs for deep boreholes. The actual points (depth, diameter) used to create the three curves are indicated by the circular dots.
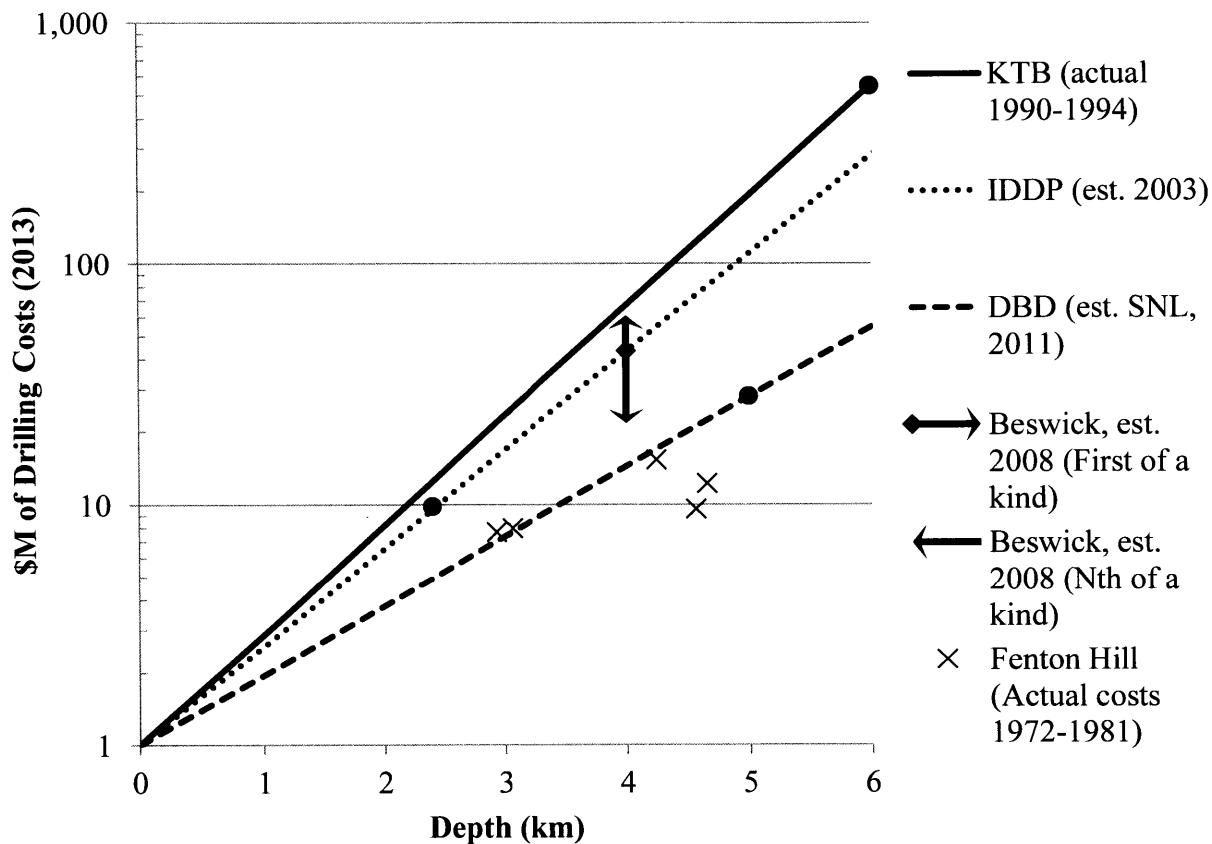
Figure 5-5. Comparison of drilling costs vs. depth based on various actual and estimated costs for deep boreholes. All costs are adjusted to 2013.

Actual drilling costs from the deep geothermal boreholes drilled at the Fenton Hill site [272] are also shown for reference (although the diameter of the boreholes was less than that required for DBD, so the costs are likely lower than would be expected). These data points are (literally) in line with the previous SNL DBD estimate being a "lower bound" for drilling costs.

The most recent drilling feasibility assessment completed by Beswick in 2008 estimated £25-35 million of drilling costs for a first-of-a-kind hole with diameter of 0.5 meters and depth of 4 km. Costs were estimated to decrease by 25-50% with subsequent holes and additional learning[275]. These results are shown by the bounded vertical arrows in Figure 5-5. Thus, the three curves developed thus far match Beswick's estimates, with the highest curve being representative of "first of kind" costs, and the lowest curve being representative of "Nth-of-a-kind" costs. By this comparison, the middle dotted curve (based off the IDDP data and in line with Beswick) clearly serves as a best-estimate for current or very near future costs.

5.3.3. Emplacement costs (EC)

The costs of loading, emplacing, and sealing are also addressed in this trade study because some of these could be significant and show strong dependencies on the disposal depth. Previous DBD studies by SKB in 1989 estimated emplacement and deployment costs to be roughly 30-40% of the total costs [19]. This is consistent with a more recent SNL estimate of $13M/borehole (out of $40M) for loading, canisters, sealing, and emplacement[149]. Divided among 400 canisters containing 1 PWR assembly (0.5 MTHM), corresponds to $65/kgHM of unit costs. Generally speaking, the canister material, loading, and transportation costs (i.e., almost all operational costs prior to disposal) scale linearly with each unit of SNF disposed (i.e., a "per unit" cost). However, since these unit costs are not strongly affected by the borehole spacing, plug length, or disposal zone length, the optimization problem and solution (with respect to these parameters) are not affected by assumptions on unit costs.

Based on previous work at MIT, the emplacement costs show great sensitivity to the average depth and speed at which canisters are lowered [276]. The average depth of disposal ($L_{d,avg}$) is $L_p+0.5L_d$. Assuming a drilling rig billing rate (B_r) of $4,852/hr[276] the average cost of emplacing a canister (EC) can be related to the speed, L_d, and L_p using Eq.(5-6),

$$EC = \frac{B_r}{v_e} 2L_{d,avg}$$ (5-6)

where a factor of two is included to account for the lowering and raising processes. The constants preceding $L_{d,avg}$ may be grouped into a proportionality term *(EC_l)* with units of $/(depth-canister) that relates the average depth of disposal to the per canister emplacement cost *(EC_c)*, as shown in Eq. (5-7),

$$EC_c \left(\frac{\$}{canister}\right) = EC_l L_{d,avg}$$ (5-7)

The total cost for loading a DBD facility is obtained by multiplying EC_c by the number of canisters loaded (i.e., the disposal zone length L_d divided by the canister length, L_{can}), resulting in Eq. (5-8),

$$EC(\$) = EC_l L_{d,avg} \left(\frac{L_d}{L_{can}}\right) = \frac{EC_l \left(L_p L_d + 0.5L_d^2\right)}{L_{can}}$$ (5-8)

184

The emplacement costs roughly increase with the square of the disposal zone length. Table 5-7 summarizes the lower and upper bound costs for emplacement, based off the previous emplacement study completed at MIT [276].

Table 5-7. Lower and upper bound estimates for emplacement speed and costs*.

	Description	Speed (v_e)	EC_1 $/(canister-km)	Cost to load 400 canisters at $L_{avg}=3$ km
Lower Bound	Drop-in method[276]	2.5 m/s (9000 m/hr) {27,432 ft/hr}	$539/(canister-km)	$647,933
Upper Bound	Lowering speed of drill string segments, used by SNL in an EGS drilling study[277]	0.08466 m/s (304 m/hr) {1000 ft/hr}	$15,919/(canister-km)	$19.103M

*B_r=$4852/hr [276]

The upper bound represents the costs of the least complex emplacement concept (lowering of individual canisters) which is assumed to be within current drilling capabilities. The lower bound represents achievable costs with foreseeable future development of the DBD concept (e.g., proof of the drop-in concept or if ~30 canisters can be proven to be linked together and emplaced as a single string). Overall, if these new concepts could be implemented, the loading and emplacement costs become practically insignificant compared to drilling costs [276].

Lastly, since the proposed borehole sealing materials are relatively inexpensive, natural materials (mostly crushed rock, drill cuttings, and clay) and cementing/emplacement of muds/clays are relatively routine processes in the drilling industry, it is assumed that the sealing costs do not significantly affect this cost optimization. This is in line with estimates from SNL, which suggest that the sealing operation will cost only ~$2M per borehole [240].

5.3.4. Summary of cost models

Table 5-8 summarizes the methods to calculate the total cost, including unit costs, drilling, characterization, and emplacement costs.

Table 5-8. Description and equations for the cost models used in the DBD design trade study.

Description		Equation	Variable definitions
Costs per unit kilogram of SNF disposed	Unit costs (UC)	$M_{tot} = L_d \rho_l$ $UC_{tot} = M_{tot}(UC)$	L_d: Disposal zone length (m) ρ_l: Linear density of SNF (100 kgHM/m) UC: <$65/kgHM
Drilling cost vs. total depth	Drilling costs (DC)	$DC = DC_0 e^{\lambda_d(L_d+L_p)}$	DC_0: Fixed cost ($10M) λ_d: Cost constant (1/m) L_p: Plug length (m)
Costs for characterizing an area of land	Site char. (SC)	$SC = C_a A$ $A = 2P^2$	C_a:Cost/area of site characterization ($/m^2) A: Area of single borehole P: Borehole spacing
Cost for emplacing all canisters	(EC)	$EC_l L_{d,avg} \left(\dfrac{L_d}{L_{can}} \right)$	EC_l: Per canister emplacement costs ($/(km-can)) L_{can}: Canister length (5 m) $L_{d,avg}$: $(L_p + 0.5\ L_d)$

For the parameters shown in Table 5-8, the drilling cost constant (λ_d), areal costs (C_a) and per canister emplacement costs (EC_l), vary greatly due to the previously discussed variations in methods, assumptions, and uncertainties. Table 5-9 summarizes the lower, middle and upper bound estimates for these parameters.

Table 5-9. Summary of lower bound, middle, and upper bound cost parameters.

Cost type	Lower Bound	Middle Estimate	Upper Bound
DC	λ_d= 0.666 km^{-1}	λ_d= 0.94 km^{-1}	λ_d=1.051 km^{-1}
SC	C_a=$1.25/m^2		C_a =$22/m^2
EC	EC_l=$539/(canister-km)		EC_l=$15,919/(canister-km)

Again, the upper bound represents the estimated costs for a first of a kind DBD project. The lower/middle estimates represent the costs for DBD with some additional technology development, or with learning that occurs through sequential DBD projects.

5.4. Optimization of Economics and Performance

With the assumptions for the both the economic and performance model presented, it is now possible to optimize DBD design. The goal is to minimize the total cost ($/kgHM), subject to a primary constraint that the repository meets the dose limits and other design space constraints.

The important design parameters are the borehole area (related to the spacing P), the disposal zone length (L_d), and the plug length (L_p). Again, note that since unit costs ($/kgHM) do not depend on L_d,L_p or P, they do not affect the optimization problem and may simply be added to the final objective function ($/kgHM) to obtain total, minimized disposal costs. Table 5-10 summarizes the calculation method, optimization goals, and constraints.

Table 5-10. Summary of optimization goals and design space constraints for DBD.

Variable	Calculation Method	Objective
Objective function : ($/kgHM)	$$\dfrac{DC + SC + EC}{M_{tot}}$$	Minimize.
Primary constraint: total maximum dose Θ (mRem/yr)	Transport model described in Chp. 4, using the design basis failure properties of DB1 or DB2.	<15 mRem/yr (if within 10,000 yrs) <100 mRem/yr (if after 10,000 yrs)
Constrained variables		
Total depth (L_{tot})	$L_{tot} = L_d + L_p$	$L_{tot} < 6\ km$ (assumed constraint on drilling feasibility)
Depth to disposal zone (L_p)	L_p	$L_p > L_{p,min} = 1200\ m$ (minimum depth to reach isolated porewaters with suitable chemistry, salinity gradients, rock properties inhibiting convection)
Borehole spacing (P)		50 m <P<800 m (50 is the minimum spacing considered by SNL[149], and 800 m is the maximum spacing at which the analytical model remains conservative.

The minimum depth to reach isolated porewaters with favorable chemistry, rock properties, and salinity gradients that inhibit convection is a site-dependent parameter. The best estimate for this parameter is obtained from the salinity curve developed in Section 2.5 and discussion of convection in Section 4.3, which together suggest that ideal (stagnant) chemical and hydraulic conditions are met at depths below 1200 m.

5.4.1. Optimized design (for minimum depth of 1200 m), without EC

A MATLAB® based multivariable constrained non-linear optimization algorithm called fmincon, was used to solve the optimization problem presented in Table 5-10. For the sake of

reducing the complexity and number of variables involved in this first set of optimizations, emplacement costs are neglected. The dose constraint is treated by a separate routine in MATLAB® that calculates the total dose (given L_p, L_d, and P) for a given design basis failure (DB1 or DB2). The costs are calculated by another routine implementing the equations shown in Table 5-8. Since both the objective function and constraints are completely analytical, the optimization routine is capable of evaluating many scenarios rapidly without excessive run times.

To check that the optimization routine was correctly calculating a global minimum, the problem was also solved by a traditional (brute force) method. The first step to reducing the size of the traditional search is to assume that the plug length (L_p) is reduced to its minimum length (1200 m). This cost minimization method would be (intuitively) expected: as two alternative means to meet a dose limit, the cost of increasing borehole spacing is less than the cost of increasing the plug length and total disposal depth (unless site characterization costs are very high, and drilling costs are very low, which is generally not expected). Thus, with L_p constrained to be its minimum value of 1200 m, for a given disposal zone length (L_d) and design basis failure (DB) pathway, the borehole spacing (required to meet the dose limit) can be calculated (via an iterative solution routine in MATLAB®). The results of this calculation for DB1 and DB2 are shown in Figure 5-6.
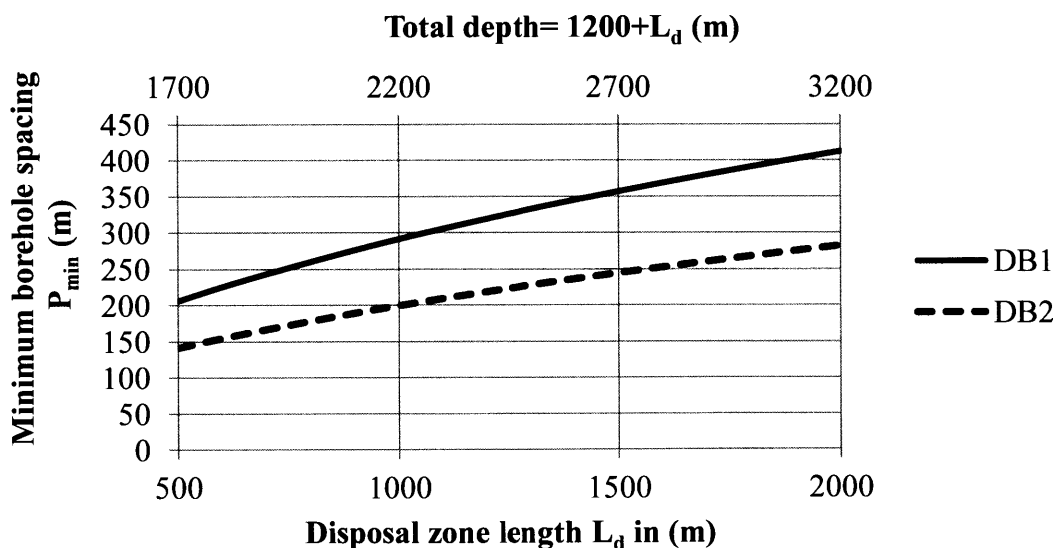
Figure 5-6. Minimum borehole spacing (required to meet dose limits) vs. disposal zone length for DB1 and DB2. Total depth is plotted on upper x axis is $L_p + L_d$ (plug length is held at 1200 m).

Intuitively, as the disposal length increases, the minimum borehole spacing must also increase (to limit the vertical velocity of fluids, and fundamentally, keep the breakthrough time constant). Maximum areal loading is a parameter that follows directly from examination of the breakthrough time (τ_b). An instructive, alternative way to plot the data in Figure 5-6 is to show the maximum areal loading (e.g., MTHM/km^2) allowed by the dose limit (for all the allowable combinations of L_d and P_{min}). The maximum areal loading (AL) can be directly calculated from the minimum borehole spacing (P_{min}) and the disposal zone length (L_d) via Eq. (5-9),

$$AL = \frac{L_d \rho_l}{P_{min}^2}$$

(5-9)

where the loading density (ρ_l) is 100 kgHM/m. Plotting the results in this way clearly shows that for a given design basis failure and disposal depth (L_d), the areal loading of SNF is a constant, limiting factor to the DBD design (regardless of the disposal length). The results of the maximum areal loading vs. disposal zone length are shown in Figure 5-7.
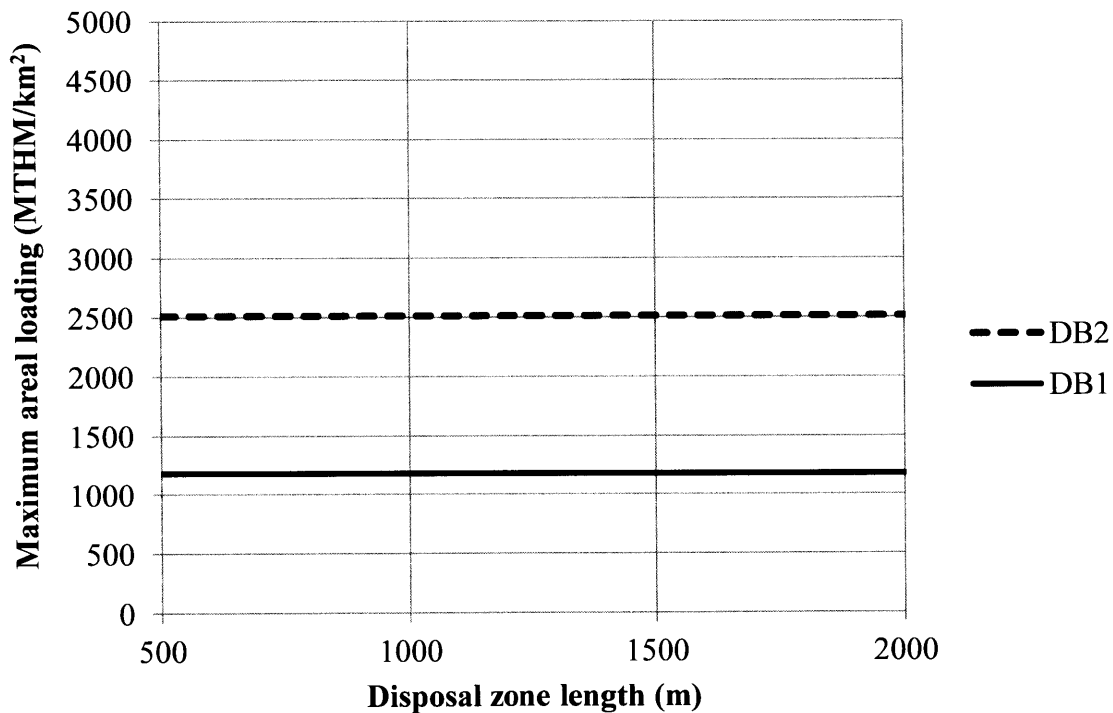
Figure 5-7. Maximum areal loading (constrained by dose limits) vs. disposal zone length for DB1 and DB2, for a minimum disposal zone depth (plug length L_p) of 1200 m.

DB1 (plug failure) clearly limits the design at 1178 MTHM/km^2. These results in Figure 5-6 further clarify the tradeoff between borehole spacing and disposal zone length. For the given plug length of 1200 m, the design space is now constrained to a single variable (e.g., now if disposal zone length is given, the minimum borehole spacing is also known/specified). Thus, the optimization problem is reduced to a single curve (disposal zone length vs. $/kgHM). In all cases (except for one), the optimization routine's global minimum matches the traditional (graphic/curve plotting) method exactly. The optimized designs for DB1 and DB2 obtained from the optimization routine (along with informative outputs such as breakthrough time) are summarized in Table 5-11 and Table 5-12.

Table 5-11. Optimized design assuming minimum disposal depth (L_p) is 1200 meters, for DB1 assumptions.

	Variable (unit)	Low DC	Med. DC	High DC
Low SC	τ_b (yrs)	18,555	18,555	18,555
	L_p (m)	1200	1200	1200
	L_d (m)	1501.0	1063.1	950.8
	L_{tot} (m)	**2701.0**	**2263.1**	**2150.8**
	P (m)	356.9	300.3	284.0
	SC ($/kgHM)	$2.12	$2.12	$2.12
	DC ($/kgHM)	$40.28	$79.05	$100.99
	SC+DC ($/kgHM)	**$42.40**	**$81.17**	**$103.11**
High SC	τ_b (yrs)	18,639	18,555	18,555
	L_p (m)	1250.4	1200	1200
	L_d (m)	1499.9	1062.5	950.4
	L_{tot} (m)	**2750.3**	**2262.5**	**2150.4**
	P (m)	349.7	300.2	283.9
	SC ($/kgHM)	$35.88	$37.33	$37.32
	DC ($/kgHM)	$41.66	$79.05	$100.99
	SC+DC ($/kgHM)	**$77.54**	**$116.38**	**$138.31**

*Maximum dose rate (Θ) =100 mRem/yr for all cases

Table 5-12. Optimized design assuming minimum disposal depth (L_p) is 1200 meters, for the DB2 (fracture failure) case

		Low DC	Med. DC	High DC
Low SC	L_d (m)	1501.1	1063.1	950.8
	L_{tot} (m)	**2701.1**	**2263.1**	**2150.8**
	P (m)	244.4	205.7	194.5
	SC ($/kgHM)	$0.99	$0.99	$0.99
	DC ($/kgHM)	$40.28	$79.05	$100.99
	SC+DC ($/kgHM)	**$41.28**	**$80.04**	**$101.99**
High SC	L_d (m)	1501.0	1063.2	950.8
	L_{tot} (m)	**2701.0**	**2263.2**	**2150.8**
	P (m)	244.4	205.7	194.5
	SC ($/kgHM)	$17.51	$17.51	$17.51
	DC ($/kgHM)	$40.28	$79.05	$100.99
	SC+DC ($/kgHM)	**$57.79**	**$96.56**	**$118.50**

* τ_b=0.063 yrs, Maximum dose (Θ)= 15 mRem/yr, and L_p=1200 m for all cases.

One matching example is shown in Figure 5-8, which compares the optimized costs for DB1 and DB2 using upper bound cost assumptions (high SC and high DC). The curves were developed by evaluating all allowable possibilities for L_d and P- according to the dose constraint- (while keeping L_p at the constant value of 1200 m). The tabulated data on the lower right sixth of Table 5-11 and Table 5-12 give the output of the optimization routine for this case, and are shown as the diamond and the cross in Figure 5-8.
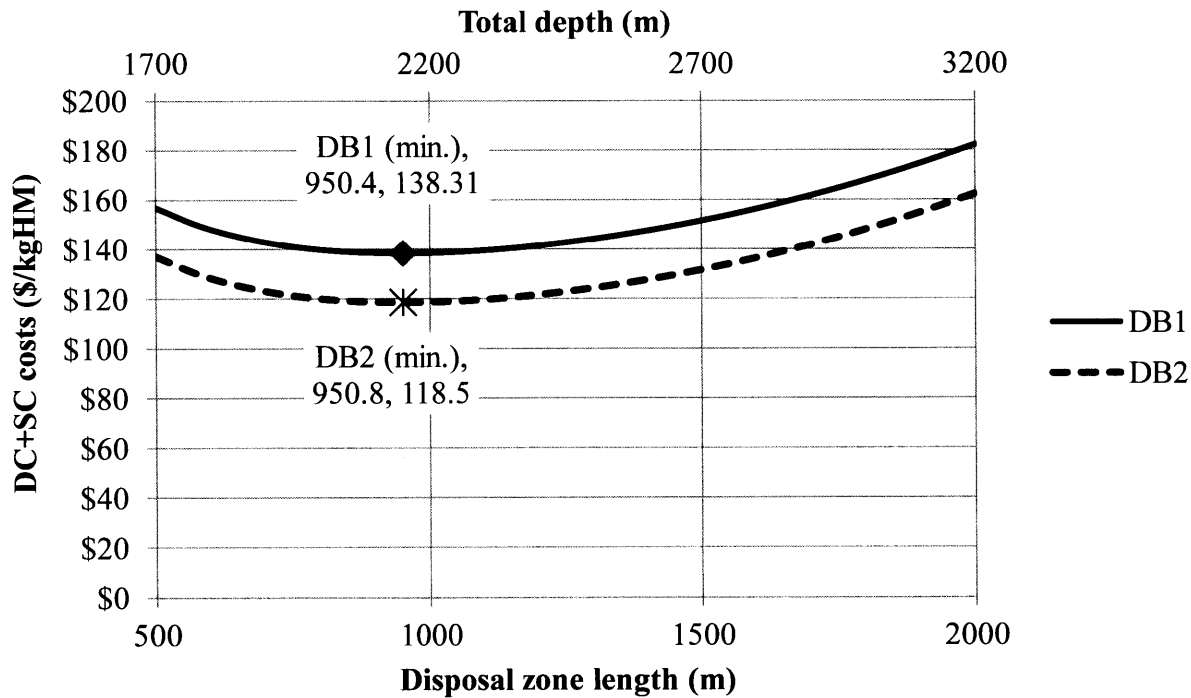
Figure 5-8. Optimized upper bound (high SC and high DC) costs and curve for DB1 and DB2.

The key finding from Figure 5-8 is that the optimized depth shows little sensitivity to the design basis failure assumed: for a given set of assumptions, the only major difference in design is borehole spacing, which is larger for DB1 compared to DB2 (283 m vs. 194 m, respectively). The resulting effect of higher site characterizations costs for DB1 (vs. DB2) results in a vertical shift of the cost curve (without changing the minimum with respect to L_d). For the low SC cases (shown in the first rows of Table 5-11 and Table 5-12) , the optimized designs are practically identical and the cost difference between DB1 and DB2 is insignificant, so the equivalent curves for DB1 and DB2 essentially lie on top of each other.

Note that in one particular case (High SC and Low DC) the MATLAB optimization converges to a solution that is different from the assumed design space; in this case, the optimal plug length is 1250 m, which is greater than the specified minimum value (1200 m). Thus, when drilling costs are very low and the site characterization costs are very high, the cost-tradeoff favors disposal at slightly greater depths (vs. increased borehole spacing). Overall, there are three main conclusions from this initial optimization study:

-For a given disposal depth (L_p) and design basis failure, the maximum areal loading (to meet the dose limit) is constant. The areal loading subsequently fixes the relation between the disposal zone length L_d and spacing P.

-Optimized designs show the greatest sensitivity to assumptions on the depth dependent drilling cost.

    -Higher drilling costs favor shorter disposal zones, which subsequently allows for closer borehole spacing.

    -Optimized designs are less sensitive to variations in site characterization costs (changed by a factor of 20×).

These results are also demonstrated in Figure 5-9, which compares the upper bound costs (high SC and high DC) to the lower bound costs (low SC and low DC), for the limiting design basis (DB1).
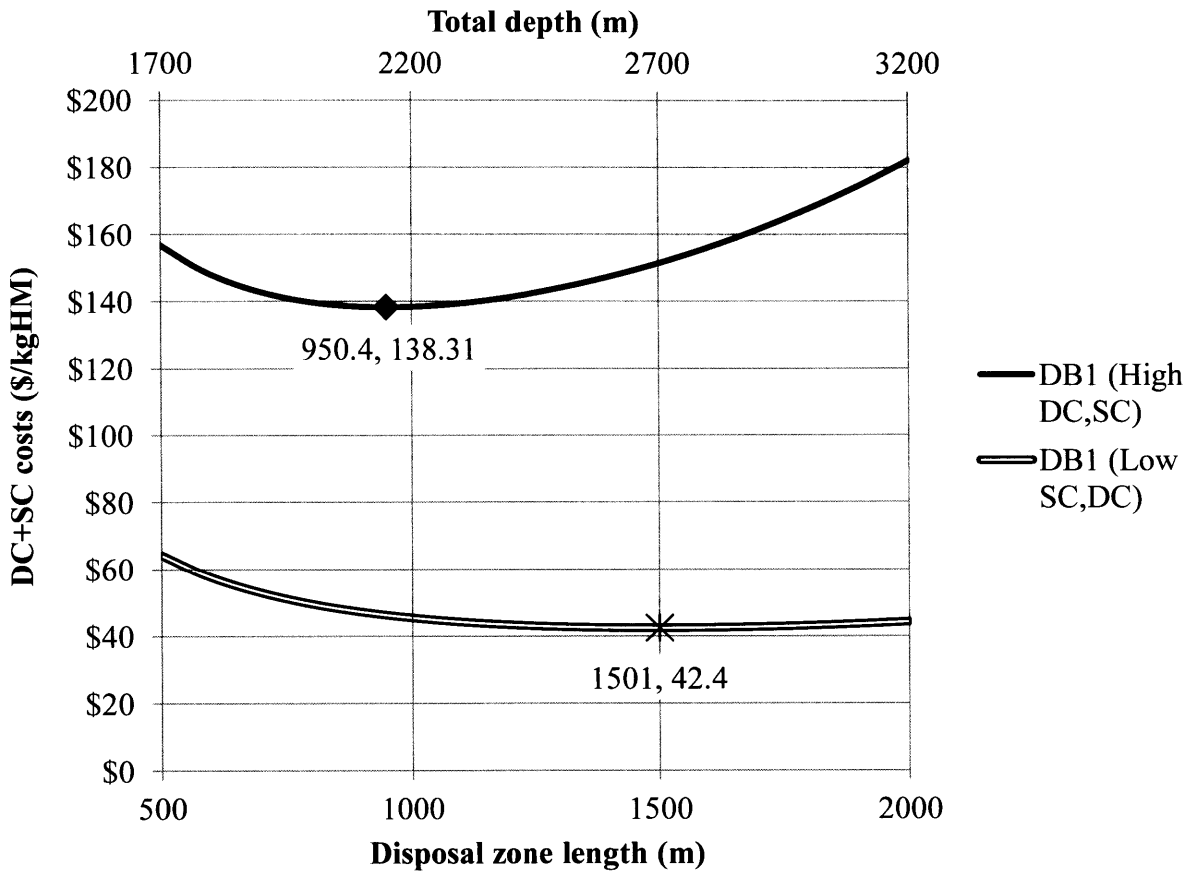
Figure 5-9. Optimized lower bound and upper bound costs for DB1.

These results show that as drilling costs increase with depth, the cost curve is shifted up and to the left (i.e., shorter disposal zone and higher costs) and the curve shows a more prominent minimum. Conversely, as drilling costs are reduced to the lower bound, the cost optimum shows a shallower minimum (meaning that a range of designs could be feasible and have similar costs).

5.4.2. Optimized design (for minimum depth of 1200 m), with EC

Thus far, emplacement costs have not been included. First, the results for the lower bound emplacement costs are shown in Figure 5-10. Since DB1 is the limiting design basis failure, attention is focused to that scenario.
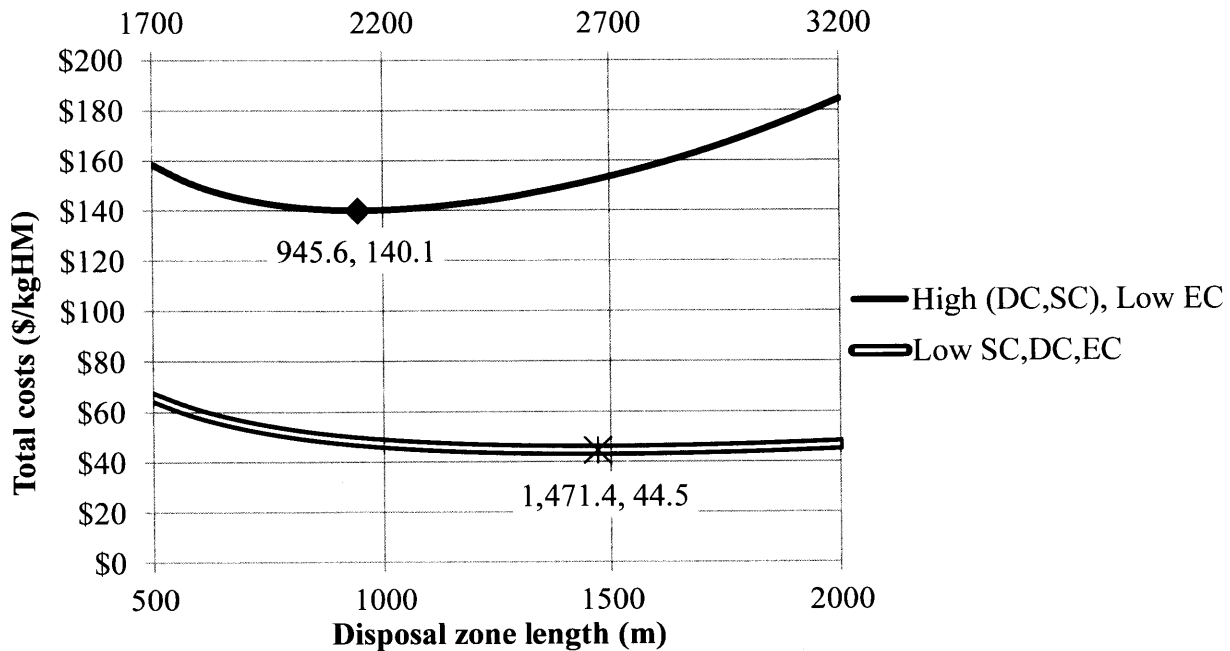
Figure 5-10. Optimized lower bound and upper bound total costs for DB1, with emplacement costs fixed at the lower bound.

As seen in Figure 5-10, the results with low EC are very similar to those that were just shown Figure 5-9 (with no EC). The slightly shorter disposal zone length and higher costs are expected (given that EC is a depth dependent cost). Generally, this confirms that when emplacement costs are low, the optimal design is not affected by them. Figure 5-11 shows the cost curves and optimized results for the lower and upper bound (SC,DC) costs, including the upper bound EC.

195
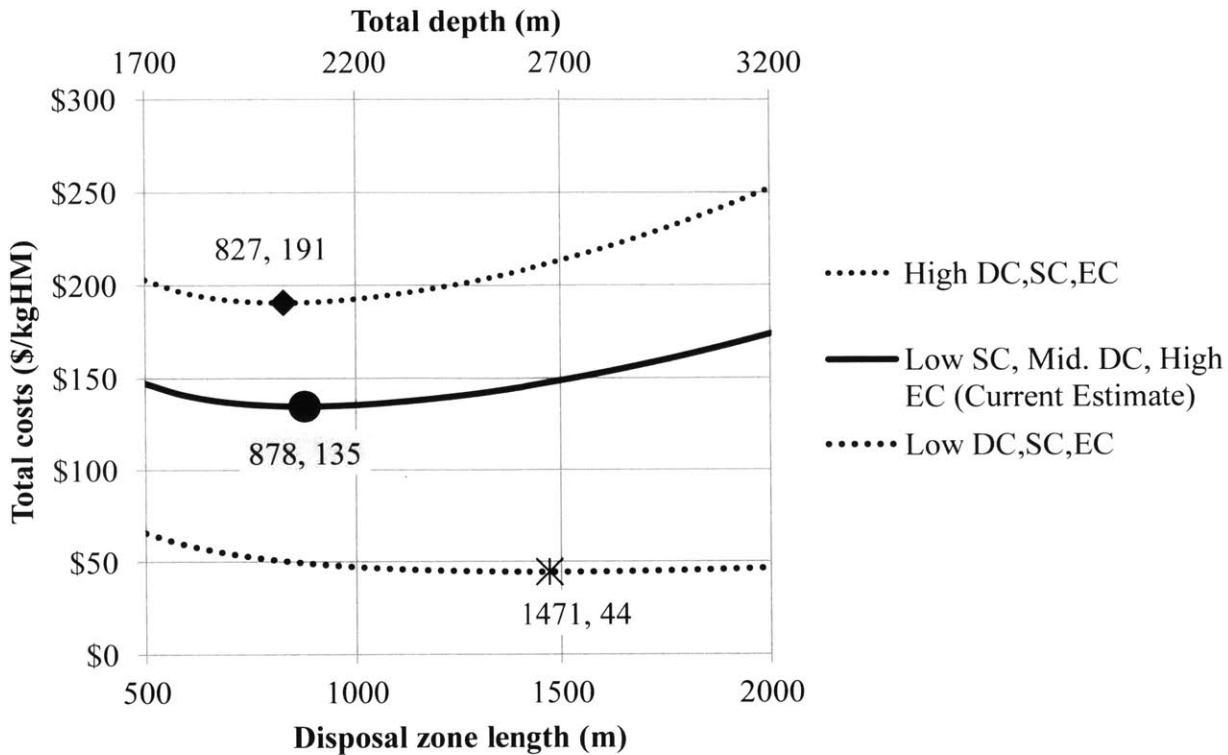
Figure 5-11. Optimized lower bound and upper bound (SC+DC) costs for DB1, with lower bound and upper bound EC.

The results in Figure 5-11 span the entire range of economic assumptions and uncertainty. The bottom cost curve is associated with the lowest drilling, site characterization, and emplacement costs: achievable in the future with additional drilling experience and pilot scale proof of the drop-in concept. The middle curve is the best estimate for what could be achieved with current technology (without the drop-in concept). The upper bound is the estimate for a first-of-a kind deep borehole.

Table 5-13. Summary of optimal designs for lower bound, best estimate and upper bound cost assumptions

	L_p (m)	Optimal L_d (m)	Optimal L_{tot} (m)	Optimal P (m)	Cost ($/kgHM)
Lower bound	1200	1471	2671	353.4	$44.49
Best estimate	1200	878.3	2078	272.9	$134.7
Upper bound	1200	827.41	2027	264.8	$190.6

Note that since the plug length (L_p) is fixed at 1200 m, the maximum areal loading is fixed at 1178 MTHM/km^2. This explains why as the disposal length is reduced, the borehole spacing is also reduced. Considering the extreme range in assumed costs (3-5× range in DC, 20× range in SC, 300× range in EC), the final optimal designs are constrained (by the DB1 case) to a relatively narrow range of optimal values:

L_p=1200 m

L_d= 878.3-1471 m

P= 264-353 m

5.4.3. Effect of variations in L_p

Thus far, the minimum L_p has been constrained to the best estimate value of 1200 m. For some, sites, this value may be shallower (e.g., those presenting low permeability crystalline rock at the surface), and for others, the value may be deeper. Thus, as a final exercise, we allow all variables (L_p,L_d and P) to vary. The first important parameter to determine is the maximum areal loading. As previously shown (when L_p was constrained to 1200 m) for a given disposal depth (L_p) and design basis failure, the maximum areal loading is a constant, which relates and constrains L_d and P. As the borehole disposal depth (L_p) is increased, the maximum areal loading is also shown to increase (as the host rock creates a longer barrier to the radionuclides). The results are demonstrated in Figure 5-12, which shows a linear relationship between the disposal zone length and the maximum areal loading.
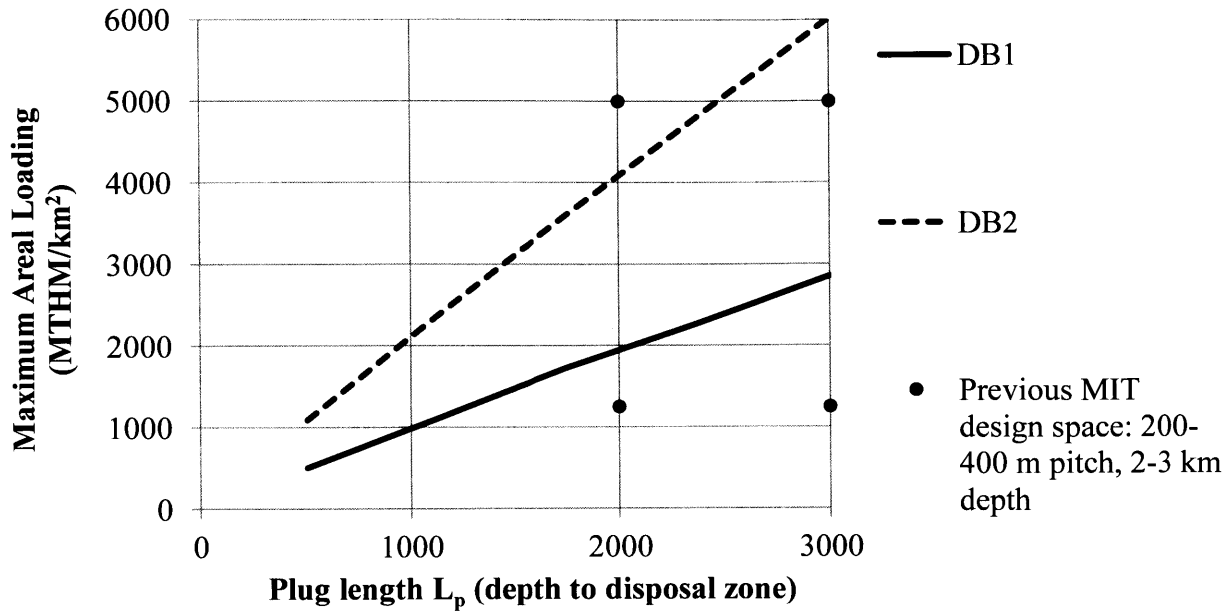
Figure 5-12. Maximum areal loading (MTHM/km^2) vs. plug length/disposal depth (L$_p$), for DB1 and DB2 with comparison to previous MIT and SNL reference designs.

Again, the results clearly show that DB1 is limiting, so focus is limited to this case. The maximum areal loading for DB1 can be described by a simple linear correlation shown in Eq. (5-10),

$$AL_{max,1}\left(\frac{kgHM}{m^2}\right) = \frac{L_d\rho_l}{P^2} = 0.9614 \times 10^{-3}\left(L_p\right) \tag{5-10}$$

Using this correlation, future multivariable optimizations and design can be completed analytically (without running the complex thermal or chemical transport models). For a given minimum disposal depth (L$_p$), the maximum areal loading (AL_{max}) gives a fixed relationship between disposal zone length and borehole spacing in Eq. (5-10). Then, the disposal length can be varied and the total costs may be calculated, and the minimum can be obtained via graphical solution. As a side note, considering that previous MIT designs were not based on a performance model, it is remarkable how closely the previously considered design space aligns with the currently developed design limits.

5.5. Chapter Summary

This chapter integrates all preceding components of the thesis by coupling the highly conservative radionuclide transport models, reference design assumptions, and a new economic model. First, two design basis failure modes are outlined; DB1 assumes a region with permeability elevated by 100× compared to the surrounding rock; DB2 assumes a cylindrical fracture with diameter of 100μm. In both cases, the failed zones are surrounded by host rock with permeability of 10^{-17} m^2 and diffusion coefficient of 10^{-11}m^2. The second component of this chapter is an economic model that accounts for depth dependent costs (drilling and emplacement) and site characterization costs which have not been simultaneously compared in previous DBD studies. Using the design basis failure assumptions, the design is optimized: cost/kgHM is minimized while the parameters of plug length, disposal zone length and borehole spacing are varied. The first set of optimizations revealed that the disposal depth (L_p) is typically reduced to its minimum value (specified and estimated to be 1200 meters, where stagnant fluids, appropriate chemical and hydraulic conditions are reached). This is significantly less than previous reference designs, which imply that 2-3 km disposal depths are required for sufficient containment of radionuclides. Minimizing the plug length to this value was always the optimal solution (except when drilling costs are at the lower bound and site characterization costs are at the upper bound of $22M/km^2). Throughout these optimizations, DB1 was shown to be the limiting design basis, always requiring larger borehole spacings compared to DB2 to achieve the dose limits. The final set of optimization focused on DB1, included all costs (DC,SC,EC), and covered their entire range. The best estimate for the currently achievable DBD costs are $134/kgHM, which is optimally achieved with an 878 m long disposal zone and 272 meter borehole spacing. This excludes other possible unit costs (such as transportation, canister materials, etc.) which do not affect the optimal design with respect to the varied parameters. A large fraction of the total cost is associated with emplacement of canisters (assumed to be lowered individually using current drilling rig technology). If drilling and emplacement costs can be decreased to their lower bound (e.g., with additional technology development) the optimal disposal zone length (L_d) displays a very shallow minimum at ~1500 m, and disposal costs could be reduced to $44.49/kgHM. This result clearly highlights the importance of proving the drop-in concept (or some other method) to reduce the time to emplace deep borehole canisters. Even with upper bound costs (characteristic of a first-of-kind scientific project) disposal would only

cost $191/kgHM, which is still significantly less than the $400/kgHM collected in the nuclear waste fund. Overall, the optimal designs are significantly shallower and shorter than other reference designs, which typically have disposal depths of 2-3 km, and disposal zone lengths of 2 km. Greater depths do provide an additional barrier and allow for greater maximum areal loading; thus, if site characterization costs increase, land becomes scarce (costly), or drilling becomes significantly cheaper, then deeper designs will be optimal. If the conservatism of the performance model was reduced (and appropriate pore fluid chemical conditions may be found at shallower depths), disposal depths and costs might possibly be even lower.

6. Summary, Conclusions, and Recommendations

6.1. Summary

Permanent disposal of nuclear waste represents both a formidable challenge and an opportunity. Although it has yet to be fully implemented in any country, geologic disposal of spent nuclear fuel promises to be a highly efficient, compact, scalable, and sustainable method to keep electricity clean and maintain equity to future generations. This work is devoted to demonstrating that nuclear waste can permanently and cost-effectively be disposed in deep boreholes that are available with current technological capabilities. To prove this, a new set of transparent, analytical, conservative, thermal, hydraulic, chemical, and mechanical parameters and models by which DBD designs may be evaluated was developed. For low permeability host rock where convection is not present or initiated by SNF, thermal expansion of water (which is directly proportional to integrated decay heat since emplacement) gives an upper bound on fluid travel distance and hence caprock penetration time. Therefore, for a given disposal depth (i.e., travel distance), thermal expansion transport creates a limitation on repository design via a simple parameter: areal loading (MTHM/km^2).

Previous borehole designs suggested disposing waste starting at depths 2-3 km, with a 2 km disposal zone reaching 4-5 km, and a borehole spacing of 200 m. However, there has never been a systematic or quantitative justification (e.g., in terms of dose and cost limitations) for these design choices. To solve this problem, an economic model (accounting for depth and area dependent costs) is coupled with the conservative performance model to optimize borehole design over a range of design basis failure scenarios and cost assumptions. Using the best

estimate for current costs, disposal beginning at a shallower depth of 1200 m (compensated by a shorter disposal zone length of ~900 m and larger spacing between boreholes of ~280 m) provides sufficient radionuclide containment and optimal total (drilling, emplacement, and site characterization) costs of $134/kgHM. The depth and diameter of the proposed design is within current drilling capabilities, and the cost is well within the total fee collected for nuclear waste disposal (~$400 kg/HM).

6.2. Conclusions

6.2.1. Engineered components

Significant changes and improvements in the understanding of the plug, canister, and the gap filling materials have been made. The proposed plug materials (MgO based cement, sepiolite/bentonite blends) should have a low permeability (10^{-16} to 10^{-18} m^2), comparable to previously suggested materials, but exhibit less susceptibility to the problems of shrinkage during curing and exposure to saline fluids, respectively. The canisters (both for PWR and narrower BWR assemblies) have been redesigned to account for the simultaneous effects of hydrostatic and crushing forces. The resulting canister diameters could be accommodated to depths of 2.4-3.5 km using commercially available (generically designed) boreholes, with only slight modifications to the liner design.

The proposed graphite based gap fill material has an experimentally measured thermal conductivity ~5-7× higher than the previously proposed reference material (drilling mud or water). The high thermal conductivity of the graphite suspension reduces the temperature drop across of the gap to less than 1°K. The use of a solid suspension would also help inhibit convection (and thus prevent fluid transport and canister degradation).

6.2.2. Thermal-hydraulic transport

Under ideal site conditions ($k_m < 10^{-16}$ m^2) and vertical temperature gradients created by the disposed fuel, analytical solutions for the onset of natural convection in porous media suggest that it will not be a significant vertical transport mechanism for radionuclides in the rock overlying the disposal zone. A strong increase of salinity and density with depth (measured at the UPH-3 borehole and other nearby sites in the Canadian shield) could provide an additional and redundant barrier to the onset of convection. Without existing pore overpressures or

convection occurring in the region between the host rock and the surface, thermal expansion is the only plausible transport mechanism. A compact analytical model for thermal expansion driven flow with (conservative) closed radial boundaries was developed to predict the vertical transport velocities vs. time. The analytical model proved to be conservative (overestimated travel distance by 3×) when compared to a detailed numerical model across a large range of borehole spacings (200-800 meters), host rock permeabilities (10^{-16} to 10^{-18}m^2), plug permeabilities (10^{-14} to 10^{-16} m^2), and heat production rates. The fluid velocity in the assumed high permeability region is determined by the ratio of its permeability to that of the surrounding rock (along with the total pressure buildup of the disposal zone, determined almost completely by the surrounding host rock). Thus, assuming a lower host rock permeability (10^{-17} m^2) tends to increase both the pressure buildup in the disposal zone and the vertical flow through the preferential pathway. The analytical thermal expansion model is advantageous because it also has the capability to calculate velocities in small (<100 μm) fracture flow paths (not implemented in previous DBD radionuclide assessments).

In the development of the thermal-hydraulic model, two previously undiscussed delay mechanisms were identified:

1. Fluid and rock compressibility becomes a significant delay mechanism as the host rock permeability falls below 10^{-18} m^2. However, it is probably undesirable to rely heavily on this delay mechanism, as it necessitates that fluid overpressures rise to very high levels (~10 MPa) at which the risk of rock fracturing becomes larger. In addition, the beneficial time delay effect of compression would have to be compared against the detrimental effect of higher pore pressures, which -all other things being equal- causes more rapid flow through the assumed preferential flow paths.

2. Variations in permeability along the flow path (or alternatively, changes in fracture aperture) causes significant inflow and/or outflow orthogonal to the path. These heterogeneities lead to advection losses into the host rock matrix (see Appendix B.8) and dilution of the travelling pulse of contaminants.

Both of these delay and dilution mechanisms were conservatively neglected in the thermal-hydraulic-chemical model. In general, the inclusion of greater heterogeneities (geometric or other) should increase travel times to the surface. For example, overlying regions with higher permeability and porosity will generally reduce pressure buildups and disperse flow away from

the straight, concentrated "channels" assumed thus far. Larger fracture tortuosity and directional changes would increase the total surface area of rock that the traveling radionuclides are exposed to, thereby increasing the losses due to diffusion in the rock matrix.

6.2.3. Radionuclide transport

A similar level of conservatism was applied during the development of a chemical transport model. The first major assumption is that the canister, cladding, and UO_2 are assumed to fail instantaneously (upon sealing of the borehole). All radionuclides are assumed to reach the higher of either a solubility limit or an inventory limited concentration (determined by the initial inventory of the radionuclide and volume of fluid within the borehole-canister gap). The solubility and sorption values were determined by reviewing the available data from SKB and SNL and choosing conservative upper and lower bound values (respectively). In the case that radionuclides do not decay rapidly, have an unlimited solubility, and do not sorb onto rock surfaces, the remaining loss mechanism is a slow diffusion process that occurs at a rate of 10^{-11} m^2/s (effectively, 10^{-13} m^2/s when the host rock's porosity of 0.01 is accounted for). The pathway from the disposal zone to the receptor is modeled as straight and cylindrical, and the transient behavior of the diffusion process into the surrounding host rock is conservatively approximated (by using the steady state or saturated concentration profile, which tends to minimize the diffusion loss rate).

With confidence in the conservative nature of the radionuclide transport model, to account for modeling uncertainty, the problem is further split into two possible design basis failure modes:

DB1: Flow dominated through a large (1.2 m diameter) permeable region (e.g., plug, host rock), assumed to be compromised and have 100× higher permeability compared to the surrounding rock.

DB2: Flow dominated through a single cylindrical fracture (with diameter of 0.1 mm) within host rock with permeability of 10^{-17} m^2, traversing directly to the surface and having no variations in aperture.

A conservative aspect of the relative (as opposed to absolute) nature of the DB1 permeability assumption is that the relative advection velocity through the preferential pathway is always

maintained to be 100× higher through the failed plug region than through the surrounding rock (for equal porosities). Thus, if in reality the surrounding host rock matrix permeability were to increase as the fluid travels vertically and approaches the surface, DB1 effectively assumes that the plug permeability also increases, so that the relative permeability and velocity always remains 100× higher (and there is no radial inflow/outflow from the plug to the matrix).

In the ideal situation, the thermal hydraulic properties of the site and SNF are chosen such that advection breakthrough time (the time required for fluid to travel from the disposal zone to the surface) does not occur on a 10^6 year time scale. In the case that fractures are assumed to exist continuously to the surface within a homogenous host rock, it is difficult to preclude breakthrough (i.e., rapid breakthrough occurs for fracture sizes >10μm, regardless of disposal depth). Despite very early breakthroughs, flow through small fractures were shown to be of less concern than flow through large permeable regions, for two reasons: the flow rate through a small fracture is significantly lower than through a large region and the diffusive losses occurring into the adjacent host rock matrix are much larger for very small fractures. Thus, it is found that when modeling fracture failures in deep boreholes it is particularly important to account for chemical diffusive losses that occur orthogonally to the fracture.

6.2.4. Economic model

The level of conservatism incorporated into the analytical model did not render it completely unrealistic, and the solutions still provided meaningful performance estimates and insights into the design of deep borehole facilities. The economic model compares the effects and benefits of various design changes, such as disposal depth, disposal zone length (i.e., capacity) and borehole spacing.

In this study, all potentially varying costs- including drilling, site characterization, and emplacement- were considered simultaneously. The cost estimates ranged from a lower bound (characteristic of Nth-of-a-kind projects that have already experienced technology development) to an upper bound (characteristic of an expensive, first of a kind scientific endeavor). The best estimates for costs are based on currently available technologies (e.g., sequential lowering of individual canisters, best current estimate for drilling cost vs. depth, and site characterization costs of $1.25 million/km^2). The optimum design and cost/kgHM for the various cost assumptions are summarized in Figure 6-1 and Table 6-1.
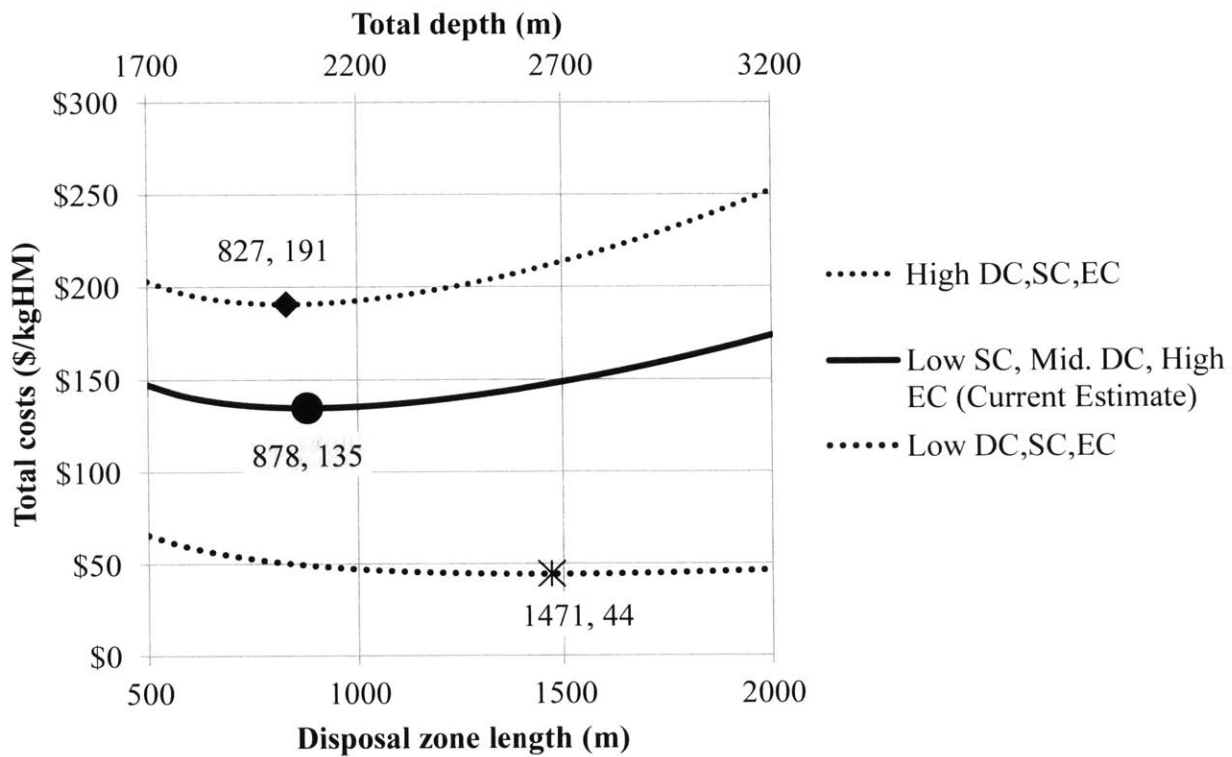
Figure 6-1. Optimized lower bound, best estimate, and upper bound costs for DB1.

Table 6-1. Summary of optimal designs for lower bound, best estimate and upper bound cost assumptions

	L_p (m)	Optimal L_d (m)	Optimal L_{tot} (m)	Optimal P (m)	Cost ($/kgHM)
Lower bound	1200	1471	2671	353.4	$44.49
Best estimate	1200	878.3	2078	272.9	$134.7
Upper bound	1200	827.41	2027	264.8	$190.6

The optimization finds that under a large range in cost assumptions, the minimum disposal depth of 1200 m (combined with a shorter disposal zone and larger borehole spacing) provides the lowest costs. For the DB1 designs at 1200 m depth, the areal loading (which relates the disposal zone length and the spacing) is constrained to 1178 MTHM/km^2. The previously considered disposal depths of 2-3 km would allow for proportionally higher areal loadings (~2000-3000 MTHM/km^2, respectively). However, site characterization costs are not estimated to be high enough to make such great disposal depths and high areal loadings the necessary or optimal design choice. The exponentially lower costs and complexity of drilling to depths of 2-3 km

(compared to 4 or 5 km) provides many other benefits that were not accounted for in the performance model and optimization:

-Reducing reliance on larger diameter (i.e., unproven) drilling capabilities at great depths.

-Reducing mechanical stresses and borehole breakouts decreases the extent and severity of drilling disturbed zones, lowers risk of deviated (off-vertical) boreholes and stuck canisters, etc.

-Reducing hydrostatic and crushing forces prolongs canister lifetime and greatly improves the feasibility of retrieving intact canisters.

-Reducing canister temperatures (considering the average geothermal gradient of ~25°C/km) provides a greater margin to meeting canister or cladding temperature limits.

In the future, there could be technological or political developments that qualitatively change the optimal design presented in this thesis, as summarized in Table 6-2.

Table 6-2. Summary of potential future developments and qualitative effect on optimal design.

Expected future development	Effect on optimal design	Effect on cost ($/kgHM)
Lower cost drilling (e.g., <$20M for 5 km borehole).	Optimal design will become insensitive to disposal zone depth or length (e.g., bottom curve of Figure 6-1). Emplacement costs determine optimum depth. Generally, a smaller borehole spacing (<300 m) will be favored.	Lower costs
Lower cost emplacement (e.g., drop-in concept).	Smaller borehole spacing and greater disposal zone length will be favored.	Lower costs
Conservative assumptions and approach in transport model are relaxed.	Maximum areal loading will increase, allowing for smaller borehole spacing and slightly longer disposal zone.	Lower costs
Site characterization cost decreases (e.g.,<$1.25/m^2, due to technology advancement, lower pilot borehole drilling costs).	No significant change from updated design, because site characterization costs are already low/insignificant in the optimization.	Slightly lower costs
Unexpected future development		
Site characterization cost increases (e.g., >$20/m^2 due to socio-political opposition/barriers)	Smaller borehole spacing and greater disposal depth.	Higher costs
Regulations on repository dose become more restrictive (e.g., <15 mRem/yr)	Maximum areal loading will decrease (higher borehole spacing).	Higher costs

In general, future technological advancement would tend to decrease the costs of all components simultaneously (drilling, emplacement, and site characterization), which will favor longer disposal zones, larger borehole spacing, and lower costs (the optimal plug length will likely remain at its minimum specified value, in this case 1200 m). With technology advancements, the optimum cost (vs. depth) will become relatively shallow. On the other hand, if depth-dependent costs drop drastically (second and third row of Table 6-2) while site characterization costs unexpectedly increase (second to last row of Table 6-2), the optimal disposal depth may increase from the minimum specified depth of 1200 m, and the optimal borehole spacing would decrease.

6.2.1. Summary of contributions

Based on these findings and optimizations, the updated borehole repository features are summarized in Table 6-3 and Figure 6-2.

Table 6-3. Updated borehole repository design features and motivation for choices.

Aspect	Choices, specification	Motivation
Host rock medium	Granitic bedrock $k_m < 10^{-16}$ $k_m \sim 10^{-17}\ m^2$ $\rho = 2750\ kg/m^3$ (high) $c_p = 790\ J/kg\text{-}°K$ (high) $\phi_m \sim 0.01$ in disposal zone, higher in caprock	-Low permeability to inhibit convection or topologic flows. k_m not much smaller than $10^{-18}\ m^2$, otherwise pore pressure buildups are high. -High density, high specific heat, and low porosity in disposal zone reduce fluid volume injection due to thermal expansion. -High porosity in caprock above disposal zone improves diffusive losses and reduces advection velocity.
Plug	$k_p < 10^{-16}\ m^2$ k_p/ϕ_p minimized Alternating layers of expansive cement, clay and crushed rock. $K_d > 1$ (for all radionuclides)	-Low permeability and high porosity increase transport time. -Independent, non-shrinking, layers of plug disrupt channeling, causes radial inflow/outflow, and statistically reduces the overall, effective permeability of the plug. -High sorption coefficients reduce transport in plug (not included in current analysis).
Gap filler material	Graphite drilling mud, $k_{th} > 4\ W/m\text{-}°K$	-High thermal conductivity reduces canister centerline temperatures. -Thixotropy and solid content inhibits convection. -Lubricity promotes emplacement/retrieval.
Host rock matrix apparent diffusion coefficient	$D_m > 10^{-11}\ m^2/s$	-Higher diffusion coefficients tend to disperse/dilute chemical species that flow rapidly in fractures.
Hole specification	~40-50 cm hole ID ~1.2 km caprock (plug length) ~1 km disposal zone length -Perforated/slotted liner (or if possible, removed liner)	-Accommodates intact PWR assemblies with sufficient canister thickness to avoid crushing, provides minimized drilling, emplacement, and site characterization costs. -Promotes radial outflow (prevents buildup of pressure in disposal zone) and horizontally disperses vertical leakage in plug zone.
Repository field	~300 m borehole spacing (areal loading of ~1100 MTHM/km^2) ~800 holes (28x28 array)	-Minimizes interactions between boreholes (thermal, hydraulic). -Contains ~80,000 MTHM, covering ~72 km^2
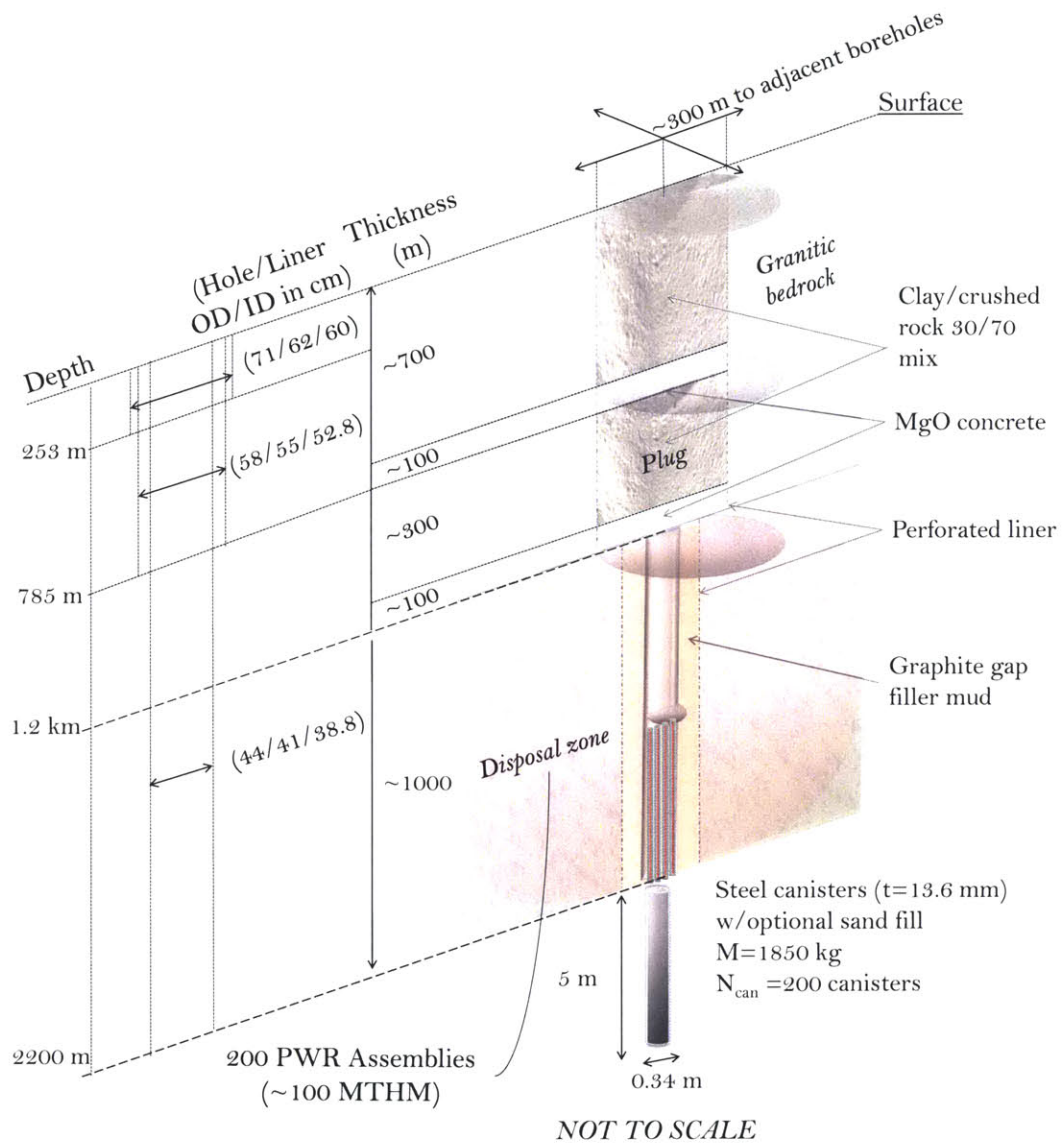
Figure 6-2. Schematic of updated borehole design features.

This thesis made contributions to each component of deep borehole modeling (inputs, fluid and radionuclide transport) and design, summarized in Table 6-4, Table 6-5, Table 6-6, and Table 6-7.

Table 6-4. Contributions to DBD reference modeling input parameters.

Physics	Previous DBD work/models	Novel aspect of this work
Chemical	Salinity profiles not based on realistic or site specific data.	Salinity profile based on site specific data from Canadian shield.
Hydraulic	No discussion of pore or rock compressibility.	Proposed generically applicable values for pore compression (Sec. 2.3.2.A) identified permeabilities where compressibility is significant (Appendix B.2).
Mechanical	No realistic mechanical stress or borehole failure analysis.	Developed stress profiles based on drilling data and conditions for borehole breakout [127].
All	No site specific data summarized or incorporated in performance models.	Compiled the most detailed thermal-hydraulic-mechanical-chemical description of a site at the UPH-3 borehole, suitable for DBD (Sec. 2.6.1).

Table 6-5. Contributions to DBD fluid transport modeling methods.

Physics	Previous DBD work/models	Novel aspect of this work
Chemical	Salinity has been discussed and modeled [108], [128].	Salinity, permeability and depth necessary to inhibit convection are analyzed analytically, based on real data (Sec. 4.3).
Thermal-hydraulic	Computationally expensive numerical models required to calculate vertical velocities in response to SNF [96] [124].	Derived a rapid, analytical model to calculate velocity based on thermal expansion due to waste (Appendix B).
Hydraulic/mechanical	Limited analysis of maximum pore pressures in DBD [21].	Analyzed margins to rock failure (Sec.2.7) based on site specific rock stresses.

Table 6-6. Contributions to DBD radionuclide transport modeling methods.

Physics	Previous DBD work/models	Novel aspect of this work
Chemical	Diffusive losses along a fracture flow path not modeled.	Derivation accounting for radial diffusion in the cylindrical geometry of interest (Appendix A).
Chemical/hydraulic	Analysis of radionuclide transport in small (micron sized) planar fractures[20].	DB2 (Sec. 5.1.1.B) models radionuclide transport in a 100 μm cylindrical fracture.
Hydraulic	Assume a constant velocity for a fixed period [21], after which there is zero velocity.	Velocities that drive radionuclide transport are based on an integrated thermal-hydraulic model.

Table 6-7. Contributions to DBD design.

Previous DBD work	Novel aspect of this work
Generic materials (e.g., cement, concrete, bentonite) for plug and gap fill (e.g., clay mud).	Developed specific composition and experimental estimates for cement mixtures (MgO based), salinity-resistant clay/crushed rock mixtures, [137] and graphite based gap filler materials (Sec. 3.4). Identified sensitivity of repository performance (e.g., escape velocity) to improvements in plug materials.
Neglect simultaneous axial and hydrostatic crushing of canisters.	Canister design accounts for both, and a sand fill was tested to provide an additional barrier.
Do not include site characterization costs[149]	First detailed and itemized cost assessment for site characterization (Sec. 5.3.1).
Make generous assumptions on canister emplacement capabilities[149] (e.g., linking of 40 canisters).	Accounts for uncertainty and difference in depth dependent cost that can occur if canisters must be emplaced with current technology (e.g., individually). (Sec. 5.3.3).
Designs do not include justifications for borehole spacing, borehole depth, or capacity.	First work to identify design tradeoffs between spacing, depth, and capacity. First to incorporate a full radionuclide transport model with economic model to obtain optimal design and justification for all design parameters (Sec. 5.4).

6.3. Recommended future work

6.3.1. Conservative assumptions

Additional safety margin for the updated design (which could be provided by either increasing the disposal depth, increasing borehole spacing, or decreasing capacity) has not been included, because it is expected that a large safety margin will be created when many conservatisms are removed from the modeling methodology, such as those summarized in Table 6-8.

Table 6-8. Conservative assumptions that could be relaxed via additional modeling efforts to provide additional margin in the design.

Model component	Conservative assumption
Fuel properties	-PWR SNF is assumed to be cooled for only 25 years, with 55 MW-d/kg burnup. This is a significantly higher burnup (thus decay heat, fission product content) compared to average assemblies in the current inventory of SNF (~35 MW-d/kg).
Radionuclides	**-Instantaneous breach of all canisters, cladding, and dissolution of all radionuclides.** -Solubility unlimited radionuclides are assumed to concentrate into a very small gap (~3 cm surrounding the canister). Advection in the disposal zone that would disperse/dilute these concentrations is neglected. -Lower bound sorption coefficients were selected for the host matrix, zero sorption in the plug or fracture.
Fluid transport	**-Radial inflows/outflow of the fracture/plug neglected.** -Heterogeneous rock/plug layers that interrupt (e.g., lower permeability) or disperse (e.g. higher porosity) flows and pressure buildups are neglected. -Failed zone assumed to have very low porosity (0.01), which tends to accelerate the flow through the region.
Radionuclide transport	**-Transient diffusion into the host rock is neglected**; in other words, the host rock surrounding the fracture or plug exists with a steady state (saturated) concentration profile. -Tortuosity of the fracture or flow path is neglected. -Host rock diffusion coefficient (10^{-11} m^2/s) and porosity (0.01) are low.
Biosphere/uptake assumptions	**-The receptor ingests all radionuclides exiting the flow path.** Generically, dilution in an aquifer and well provides a dilution rate of 10,000 m^3/yr [236]. Since breakthrough flows are typically <10 l/yr, in this analysis we have forgone a dilution (dose rate reduction) factor of 10^6. -Isotopic dilution (e.g. with I^{129} with stable forms of I in rain or porewater) is neglected

The most important conservative assumptions are shown bolded.

6.3.2. Transport model improvements

Instead of assuming that the host rock surrounding the fracture exists at its steady (saturated) state, conservatism should be reduced with a numerical transient solution for diffusion away from the fracture. Since this is a very slow process, the phenomenon occurs within a very small radius surrounding the plug or fracture; therefore, a high resolution (small grid size) may be required to reduce errors from discretization. A numerical transport model would also be better suited to account for the radial inflows and outflows (advection) that occur as the radionuclides

traverse the failed path to the surface, and the simultaneous axial (z direction) diffusion of radionuclides in the host rock.

Using a numerical model, the heterogeneity of the model should be increased. The site specific stratigraphy, thermal, hydraulic, and chemical properties summarized from UPH-3 borehole data should be incorporated into a numerical model that realistically captures the effects of varying rock layers and salinity. In particular, the conditions that inhibit convection should be confirmed with numerical models (this thesis has only used analytical models for convection). The (potentially beneficial) effects of alternating layers of low permeability sealing units (such as the Eau Claire shale unit in the UPH-3 borehole) and high porosity Mt. Simon sandstones (which may create a large dilution effect) should be evaluated. A more descriptive and numerical model of the water flows in the upper part of the system (0-200 m) could also be used to inform a more realistic dilution and biosphere model. For example, isotopic dilution of iodine could be an important mechanism, considering the iodine found in crystalline rock pore waters.

Other potential additions to the transport model are listed below:

-Canister, cladding, and UO_2 deterioration models are needed to estimate the time delay between canister disposal and assumed dissolution of radionuclides. A waste-form lifetime of only 50-100 years would greatly reduce the doses estimated here (considering that velocities are greatest during this period). Thus, a degradation model would be useful to quantify the benefits of expenditures on canister robustness.

-More accurate (less conservative) radionuclide solubility and sorption data should be incorporated into the model. In addition, each of the major uncertain parameters (diffusion coefficient, permeability) could be evaluated probabilistically. The initial probabilistic analysis on permeability(Appendix B.7) and heterogeneous numerical modeling (Appendix B.8) suggest that when the flow pathway consists of heterogeneous segments with permeability governed by independent probability distributions, flows are either significantly reduced or diluted (compared to the current homogenous and deterministic approach where flow is in effect, channeled to the surface).

- Include lateral variations in heat generation or topological details that could result in horizontal and slightly upward velocities in the system.

-Include the possible effects of gas transport (e.g., buildup of fission product pressures in cladding). It will be important to comprehensively survey and account for the possibility and effects of all other chemical and radiolysis reactions that produce gases.

Laboratory or pilot borehole scale tests validating the analytical and numerical thermal expansion model (which primarily considers expansion of the fluid) would further improve confidence in this transport model.

6.3.3. Further design optimizations

With more detailed numerical transport models, fewer conservative assumptions and improved site specific data, it is possible that minimum borehole disposal depth might be reduced even further from the value suggested here (1200 m). In addition, the current inventory of SNF is older, lower burnup, and less heat generating than assumed here (25 year cooled 60 MW-d/kgHM). Thus, the optimization could be repeated and disposal costs could be even more attractive when analyzed for current stocks of SNF. In addition to making DBD possible with current technology, a significantly shallower disposal zone (and possibly larger diameter borehole) enables new canister designs. A sizeable portion (~35%) of the current U.S. SNF inventory consists of smaller BWR assemblies, which provide a (less technically difficult) starting point for proving the DBD concept. Future work should evaluate optimal configurations of PWR and BWR (multiple or single assembly) canisters to fit within current drilling capabilities at 2 to 3 km (~0.75 to 0.5 m hole diameters, respectively) [275]. For example, at these shallower depths, a slightly larger 3 BWR assembly canister (with minimum inner diameter of 0.358 m) could be accommodated, and might further improve the economics of disposal (due to the higher loading of ~115 kgHM/m).

6.3.4. Seismicity

Future design efforts must be aware of and continue avoiding, pore-pressure-induced seismicity and rock fracturing. Although this thesis has shown that there are sites (e.g., UPH-3) where the pore overpressures expected from DBD could be sustained (e.g., 4 MPa at 1 km) and basement rock permeability is $\sim 10^{-17}$ m^2, more geomechanical models and borehole scale experiments need to be conducted to quantify the effects of fluid injection into even lower permeability host rocks, where even higher pore pressures could affect rock properties and seismicity.

6.3.5. Research objectives for a pilot borehole project

In addition to measuring the properties discussed in Chapter 2 and Section 5.3.1, a number of tests should be conducted at a pilot or test borehole to further improve understanding and confidence of confinement in deep boreholes. The following is an outline of particularly important objectives (along with references that provide details on the methods to obtain such data).

1. **Host Rock**
   a. Fluid injection tests
      i. Measure changes in permeability due to fluid injection (similar to tests conducted at the KTB and Soultz boreholes)[23], [76]
      ii. Conduct separate fluid injections at elevated temperatures to evaluate combined effect of thermal expansion and stress (from elevated pore fluid pressure).
   b. Simulated heater tests
      i. Determine effects of thermal expansion on rock stress and spallation [278].
   c. Tracer injection tests
      i. Characterize major fracture pathways[72] and measure ion diffusion coefficients [64] [54].
   d. Measure sorption coefficients (K_d) of drill cuttings for important radionuclides (I^{129}, U)
   e. Comparison of core samples across depth and multiple boreholes to determine lateral extent and uniformity of rock layers.
2. **Downhole water**
   a. Detailed depth-dependent description of relevant corrosion inducing parameters (pH, Eh, oxygen content, carbonate concentrations).
   b. Parallel laboratory tests to evaluate solubility of radionuclides at simulated temperature, salinities of downhole water.
3. **Engineered materials**
   a. Test various plug and canister emplacement methods (e.g., [279]), including the drop-in concept or canister interconnection.
   b. Canister
      i. Test various canister sealing methods under crushing and hydrostatic stresses (e.g., conventional threads, welding, friction stir welding, etc.)
      ii. Test retrieval methods for stuck or emplaced canisters (e.g., overcoring).
   c. Long term, high temperature, pressure and salinity tests on plug and gap filling materials:
      i. Sepiolite-palygorskite and bentonite mixtures
      ii. MgO based cements
      iii. Graphite suspensions

6.4. Closing remarks

Current feasibility evaluations of deep boreholes suggest that due to limited drilling experience in crystalline rocks (at 4-5 km depth and diameters proposed for intact PWR assemblies), substantial and expensive technological development will be required for DBD to become a feasible and cost-effective solution for SNF disposal[275]. The perceived limitation on DBD is based on borehole designs that were not optimized (with respect to performance and costs). In the past, fundamental design parameters (such as borehole disposal depth) were presented without full justifications; essentially, prior work suggested that waste be disposed as deep as technologically possible. Although maximum depth intuitively maximizes radionuclide confinement, it substantially raises the difficulty of implementation and costs. Furthermore, borehole disposal length (i.e., capacity) and borehole spacing were never simultaneously evaluated as design parameters. The lack of optimization is understandable; prior to the completion of this thesis, there were no integrated performance and economic models that could be used to systematically compare deep borehole designs. Existing thermal-hydraulic and performance (dose) models are available [21] and may be used to evaluate DBD generically[201], but they are not conducive to the vast and rapid variation of the design space required for DBD optimization (e.g., either because they make overly generic assumptions or because they require slow and complex 3D numerical codes). Even if they could be improved to be more flexible, less generic, and coupled to an economic model, previous transport models were missing fundamental physics that preclude their use in making design decisions (e.g., lacked the ability to model transport in fractures both hydraulically and chemically, and account for mechanical limits due to pore pressure increases).

This thesis began by treating the apparent knowledge gaps in deep borehole performance modeling and evaluation. Without taking previous work or models at face value, the thesis systematically reevaluated all assumptions involved in deep borehole design and performance. Thermal-hydraulic, chemical, and dose models were developed with a strict adherence to analytical methods (combined with conservative assumptions) to facilitate rapid variation of borehole designs. The analytical models are coupled within a single framework and allow the system sensitivity and behavior to be explained from first principles. The overall finding of this thesis is that safe and economically competitive boreholes are achievable with currently available technologies, such as generically designed geothermal boreholes, expensive emplacement

216

methods (e.g., lowering one-at-a-time), and site characterization costs of $1.25M/km^2. Using this flexible optimization framework, even if first-of-a-kind (i.e., extremely high) costs for drilling, emplacement, and site characterization ($22M/km^2) are assumed, borehole design can be optimized to meet dose requirements and still provide reasonable costs (<$200 kg/HM). No reasons have been identified to suggest that a demonstration borehole project will not fully confirm these conclusions. With respect to overall performance, the most important parameters to measure correctly (at the pilot borehole and future sites) are the permeability (as established via fractures within blocks of host rock) and diffusion coefficients of ions into the host rock. In the future, the analytical models proposed here might be insufficient (or overly conservative) when accounting for the large spatial heterogeneity of these properties at real sites, and thus may be supplanted by more detailed numerical models.

Overall, the analytical modeling treats important deficiencies in the prior art and provides a useful quality assurance check on future numerical modelling of radionuclide releases. Second, it demonstrates that potential doses are controlled by relatively simple processes (e.g., thermal expansion, diffusive losses) that are straightforward to understand and model. Lastly and most importantly the performance model provides conservative estimates, which provide a strong foundation for the economic model's conclusions that the borehole reference design can be made most cost-effective by using a shallower disposal depth (~1200 m), shorter disposal zone (~900 meters), and larger borehole spacing (~280 m) than previously considered.

Nomenclature

Symbol	Description	Units
A	Area	m^2
A_p	Plug area	m^2
A_{DBD}	Area of land for a single borehole	m^2
AL	Areal loading of spent nuclear fuel	$MTHM/km^2$
α	Effective stress coefficient	-
α_{eff}	Effective thermal diffusivity (porous medium)	m^2/s
α_{th}	Thermal diffusivity	m^2/s
α_d	Dispersivity of the plug	m
$\alpha_{d,m}$	Dispersivity of the matrix	m
b	Fracture size	m
B_r	Drilling rig billing rate	$/hr
β_g	Grain (solid) compressibility	Pa^{-1}
β_d	Drained (dry) matrix frame compressibility	Pa^{-1}
β_u	Undrained rock compressibility	Pa^{-1}
$\beta, \beta_{w,th}$	Volumetric thermal expansion coefficient, for water	$°K/°K$
β_w	Compressibility of water	Pa^{-1}
β_r	Rock compressibility	Pa^{-1}
c_r	Effective rock compressibility	Pa^{-1}
c_p	Specific heat	$J/kg-°K$
c'	Vertical compressibility	Pa^{-1}
C	Concentration in the (porous) plug or fracture	kg/m^3
C_a	Site characterization cost per area	$/m^2
C_m	Concentration in the host matrix	kg/m^3
C_0	Initial (source) concentration in the disposal zone	kg/m^3
$d_{g,10}$	Grain diameter for which 10% of particles are smaller	m
D_{pin}	Fuel pin diameter	m
D_{eff}	Effective chemical diffusion coefficient	m^2/s
D_p	Diffusion coefficient in the plug (apparent)	m^2/s
D_m	Diffusion coefficient in the matrix (apparent)	m^2/s
$D_{isp,}$	Dispersion coefficient in the plug	m^2/s
$D_{isp,m}$	Dispersion coefficient in the plug	m^2/s
D_{hydr}	Hydraulic diffusivity of pore pressure	m^2/s
D_w	Diffusion coefficient of ions in water	m^2/s
DC	Drilling cost	$
DCF	Dose conversion factor	Sv/Bq
δ	Crack width	m
ΔC	Concentration difference	kg/m^3
ΔP	Pressure increase (above initial or hydrostatic)	Pa
ΔT	Temperature difference	$°K$
ΔT_{gap}	Gap temperature difference	$°K$
ΔT_{hom}	Homogenized temperature difference	$°K$
$\Delta \rho$	Density difference	kg/m^3

$\Delta\rho_s$	Density difference due to solute concentrations	kg/m^3
$\Delta\rho_T$	Density difference due to temperature	kg/m^3
E	Young's modulus	Pa
EC	Emplacement cost	$
EC$_c$	Average per canister emplacement cost	$/can
EC$_l$	Average per canister emplacement cost per average disposal depth	$/can-km
F$_c$	Frictional failure criteria	-
g	Gravitational acceleration	m/s^2
G	Elastic shear modulus	Pa
γ	Volume fraction of solid (UO$_2$ pin) to total	-
H	Distance, height	m
I	Fluid current	m^3/s
k	Permeability	m^2
k$_H$	High thermal conductivity material	W/m-°K
k$_L$	Low thermal conductivity material	W/m-°K
k$_{th,b}$	Porous bed thermal conductivity	W/m-°K
k$_{eff,a}$	Effective permeability of the annulus	m^2
k$_{eff,conv}$	Effective conductivity of convection heat transfer	W/m-°K
k$_{eq}$	Equivalent fracture permeability	m^2
k$_{gap}$	Gap thermal conductivity	W/m-°K
k$_m$	Permeability of the porous (rock) matrix	m^2
k$_{th}$	Thermal conductivity	W/m-°K
k$_{th,hom}$	Homogenized thermal conductivity	W/m-°K
K$_d$	Distribution (sorption) coefficient	m^3/kg
K$_f$	Distribution (sorption) coefficient of the fracture	m
K$_m$	Distribution (sorption) coefficient of the matrix	m^3/kg
L,l	Length	m
L$_c$	Canister length	m
L$_d$,L$_{disp}$	Disposal zone length	m,km
L$_{d,avg}$	Average disposal depth of canisters	km
L$_p$	Plug length	m
L$_{tot}$	Total borehole length or depth	m
λ	Radioactive decay constant	s^{-1}
λ_d	Exponential drilling cost constant	km^{-1}
λ_p	Characteristic diffusive and sorptive decay length of the plug	m^{-1}
λ_m	Characteristic diffusive and sorptive decay length of the plug	m^{-1}
λ_z	Axial decay constant for concentration in the plug	m^{-1}
M$_{can}$	Mass of canister	kg
M$_{tot}$	Total mass disposed in the deep borehole	kgHM
μ	Dynamic viscosity	Pa-s
N$_{can}$	Number of canisters	#
Nu	Nusselt number	-
ν	Poisson ratio	-

Symbol	Description	Units
ν_p	Dry (drained) Poisson ratio	-
ν_k	Kinematic viscosity	m^2/s
P	Pressure	Pa
$P_{c,e}$	Elastic collapse pressure	Pa
$P_{c,p}$	Plastic collapse pressure	Pa
P_p	Pore (fluid) pressure	Pa
P_{pin}	Pin pitch (spacing)	m
P_{hydr}	Hydrostatic pressure	Pa
P_o	Outer or external pressure	Pa
P_y	Plastic yield pressure	Pa
Pr	Prandtl number	-
ϕ_p	Porosity of the plug	-
ϕ_m	Porosity of the matrix	-
Φ	Dispersive flux	$kg/(m^2\text{-}s)$
ψ	Concentration decay constant (sorption, diffusion, decay)	1/s
Ψ_i	Radionuclide flow rate to receptor	atoms/yr
r_p	Radius of the plug	m
R	Retardation factor	-
Ra	Rayleigh number	-
$Ra_{c,p}$	Critical Porous Rayleigh number	-
Ra_p	Porous medium Rayleigh number	-
Ra	Solute Rayleigh number	-
$Ra*_{por}$	Heat flux based, porous media Rayleigh number	-
R_p	Retardation factor of the plug	-
R_p	Plug flow (hydraulic) resistance	$Pa/(m^3\text{-}s)$
R_m	Retardation factor of the matrix	-
R_m	Matrix flow (hydraulic) resistance	$Pa/(m^3/s)$
R_{tot}	Total flow resistance	$Pa/(m^3/s)$
ρ	Density	kg/m^3
ρ_l	Heavy metal loading linear density	kgHM/m
ρ_{ref}	Reference density	kg/m^3
S	Solute sorbed per unit mass of solid in the porous matrix	-
S_h	Minimum horizontal stress	Pa
S_H	Maximum horizontal stress	Pa
S_{min}	Minimum stress	Pa
S_{max}	Maximum stress	Pa
S_v	Vertical stress	Pa
SC	Site characterization costs	Pa
σ_z	Axial stress	Pa
$\sigma_{z,comp}$	Compressive axial stress	Pa
$\sigma_{z,hydr}$	Axial stress due to hydrostatic pressure	Pa
σ_y	Yield strength	Pa
t	Time, thickness	s,m
t_c	Canister surface cooling period	s,yrs

$t_{g,c}$	Canister to borehole wall gap thickness	m
T_w	Wall temperature	°C
τ_B, τ_b	Breakthrough time	yrs
$\tau_r, \tau_{r,SKB}$	Tortuosity of the rock, (subscript implies SKB definition)	-
τ_{res}	Pore fluid residence time	yrs
τ_{or}	Tortuosity of the flow path	-
Θ	Dose rate	Sv/yr, mRem/yr
v	Mean pore velocity	m/s
v_a	Advection velocity	m/s
v_a	Plug advection velocity	m/s
v_D	Plug Darcy velocity	m/s
v_e	Emplacement velocity	m/s
v	Mean pore velocity	m/s
V_P	P-wave velocity	m/s
V_S	S-wave velocity	m/s
V_w	Volume of water	m^3
V_{disp}, V_{can}	Disposal zone volume, ,total volume of waste canisters	m^3
V_m	Host rock matrix volume	m^3
V_{pore}	Pore volume	m^3
V	Fluid injection	m^3
$\dot{V}_{inj}$	Fluid injection rate	m^3/s
q_r	Diffusive radial flux term	$kg/(m^2\text{-}s)$
q'	Linear heat generation rate	W/m
q''	Surface heat flux	W/m^2
q'''	Volumetric heat generation rate	W/m^3
$\dot{Q}$	Heat generation rate	Watts
Q	Heat generation (cumulative)	Joules
Q_a	Volumetric flow rate in the annulus	m^3/s
Q_p	Volumetric flow rate in the bulk porous plug	m^3/s
$(z_p)_j, \delta z_j$	Discretized plug segment length (for the jth segment)	m
z,Z	Depth, vertical distance	km

Acronym	
ASTM	American Society for Testing and Materials
BRC	Blue Ribbon Commission
BVR	Borehole Virtual Reality
DBD	Deep borehole disposal
DB	Design basis failure scenario (1 or 2)
DOE	Department of Energy
EGS	Enhanced geothermal system
EPA	Environmental Protection Agency
FCP	Fracture closure pressure
NRC	Nuclear Regulatory Commission

SBRC	Seismicity based reservoir characterization
SKB	Svensk Kärnbränslehantering Aktiebolag
SNF	Spent nuclear fuel
SNL	Sandia National Laboratories

Subscripts	
f	Fluid
i	Index for parent radionuclide
ii	Index for (daughter) radionuclide
iii	Index for (granddaughter) radionuclide
j	Index for the jth discretized, axial plug segment
l	Liquid
m	Host rock matrix
p	Plug (or failed rock region)
s	Solid

Prefixes	
m,M	million

References

[1] "Monthly Energy Review- October 2014," U.S. Energy Information Administration, Electric Power Annual DOE/EIA 0035, Oct. 2014.

[2] J. Wagner, J. Peterson, D. Mueller, J. Gehin, A. Worall, T. Taiwo, M. Nutt, M. Williamson, M. Todosow, W. Halsey, R. Omberg, P. Swift, and J. Carter, "Categorization of Used Nuclear Fuel Inventory in Support of a Comprehensive National Nuclear Fuel Cycle Strategy," Oak Ridge National Laboratory, Oak Ridge, TN, ORNL/TM-2012/308, Dec. 2012.

[3] D. A. Barnes, D. H. Bacon, and S. R. Kelley, "Geological sequestration of carbon dioxide in the Cambrian Mount Simon Sandstone: Regional storage capacity, site characterization, and large-scale injection feasibility, Michigan Basin," *Environmental Geosciences*, vol. 16, no. 3, pp. 163–183, 2009.

[4] P. H. Stauffer, H. S. Viswanathan, R. J. Pawar, and G. D. Guthrie, "A System Model for Geologic Sequestration of Carbon Dioxide," *Environ. Sci. Technol.*, vol. 43, no. 3, pp. 565–570, 2008.

[5] J. T. Birkholzer and Q. Zhou, "Basin-scale hydrogeologic impacts of CO2 storage: Capacity and regulatory implications," *International Journal of Greenhouse Gas Control*, vol. 3, no. 6, pp. 745–756, 2009.

[6] M. D. Zoback and S. M. Gorelick, "Earthquake triggering and large-scale geologic storage of carbon dioxide," *Proceedings of the National Academy of Sciences*, vol. 109, no. 26, pp. 10164–10168, 2012.

[7] P. Peterson, "Will the United States need a second geologic repository?," *BRIDGE-WASHINGTON-NATIONAL ACADEMY OF ENGINEERING-*, vol. 33, no. 3, pp. 26–32, 2003.

[8] E. Fridman, E. Shwageraus, and A. Galperin, "Implementation of multi-group cross-section methodology in BGCore MC-depletion code," in *Proc. of PHYSOR '08*, Kursaal Conference Center, Interlaken Switzerland, 2008.

[9] "Final Supplemental Environmental Impact Statement for a Geological Repository for the Disposal of Spent Nuclear Fuel and High-Level Radioactive Waste at Yucca Mountain, Nye County, Nevada," U.S. Department of Energy Office of Civilian Radioactive Waste Management, DOE/EIS-0250F-S1, 2008.

[10] L. Hamilton, B. Scowcroft, M. Ayers, V. Bailey, A. Carnesale, P. Domenici, S. Eisenhower, C. Hagel, J. Lash, A. Macfarlane, R. Meserve, E. Moniz, P. F. Peterson, J. Rowe, and P. Sharp, "Final Report to the Secretary of Energy," Blue Ribbon Commission on America's Nuclear Future, Washington D.C, Jan. 2012.

[11] A. Bala, "Sub-Seabed Burial of Nuclear Waste: If the Disposal Method Could Succeed Technically, Could It Also Succeed Legally?," *Boston College Environmental Affairs Law Review*, vol. 41, no. 2, p. 455, 2014.

[12] K. Bram, "The KTB Borehole: Germany's Superdeep Telescope into the Earth's Crust," *Oilfield Review*, vol. 7, no. 1, Feb. 1995.

[13] P. Möller, S. Weise, E. Althaus, W. Bach, H. Behr, R. Borchardt, K. Bräuer, J. Drescher, J. Erzinger, and E. Faber, "Paleofluids and Recent Fluids in the Upper Continental Crust: Results from the German Continental Deep Drilling Program (KTB)," *Journal of Geophysical Research: Solid Earth (1978–2012)*, vol. 102, no. B8, pp. 18233–18254, 1997.

[14] J. Smellie and A. Conterra, "Recent Geoscientific Information Relating to Deep Crustal Studies," SKB, R-04-09, 2004.

[15] R. A. Couture and M. G. Seitz, "Movement of fossil pore fluids in granite basement, Illinois," *Geology*, vol. 14, no. 10, pp. 831–834, 1986.

[16] M. Gascoyne, "Hydrogeochemistry, groundwater ages and sources of salts in a granitic batholith on the Canadian Shield, southeastern Manitoba," *Applied geochemistry*, vol. 19, no. 4, pp. 519–560, 2004.

[17] C. Hoag, "Canister Design for Deep Borehole Disposal of Nuclear Waste," S.B Thesis, MIT Department of Nuclear Science and Engineering, 2006.

[18] Woodward Clyde Consultants, "Very Deep Hole Systems Engineering Studies," Battelle Memorial Institute, prepared for ONWI BMI/ONWI-226, Dec. 1983.

[19] C. Juhlin and H. Sandstedt, "Storage of Nuclear Waste in Very Deep Boreholes: Feasibility Study and Assessment of Economic Potential. Part I Geological Considerations. Part II Overall Facilities Plan and Cost Analysis," SKB, Stockholm, Sweden, TR-89-39, 1989.

[20] W.-S. Kuo, "Evaluation of deep drillholes for high level nuclear waste disposal," Master of Science, Nuclear Engineer Thesis, MIT Department of Nuclear Engineering, 1991.

[21] P. V. Brady, B. W. Arnold, G. A. Freeze, P. N. Swift, S. J. Bauer, J. L. Kanney, R. P. Rechard, and Joshua S Stein, "Deep borehole disposal of high-level radioactive waste," *Sandia Report SAND2009-4401, Sandia National Laboratories, Albuquerque, New Mexico*, 2009.

[22] R. Emmermann and J. Lauterjung, "The German continental deep drilling program KTB: overview and major results," *Journal of Geophysical Research: Solid Earth (1978–2012)*, vol. 102, no. B8, pp. 18179–18201, 1997.

[23] K. F. Evans, "Permeability creation and damage due to massive fluid injections into granite at 3.5 km at Soultz: 2. Critical stress and fracture strength," *Journal of geophysical research*, vol. 110, no. B4, pp. B04204-1, 2005.

[24] C. A. Barton, M. D. Zoback, and K. L. Burns, "In-situ stress orientation and magnitude at the Fenton Geothermal Site, New Mexico, determined from wellbore breakouts," *Geophysical Research Letters*, vol. 15, no. 5, pp. 467–470, 1988.

[25] Q. Zhou, J. T. Birkholzer, E. Mehnert, Y. Lin, and K. Zhang, "Modeling basin and plume scale processes of CO2 storage for full scale deployment," *Ground Water*, vol. 48, no. 4, pp. 494–514, 2010.

[26] M. Coates, B. Haimson, W. Hinze, and W. Van Schmus, "Introduction to the Illinois deep hole project," *Journal of Geophysical Research: Solid Earth (1978–2012)*, vol. 88, no. B9, pp. 7267–7275, 1983.

[27] "Yucca Mountain: The Most Studied Real Estate on the Planet," U.S. Senate Committee on Environment and Public Works, Report to the Chairman, James Inhofe, Mar. 2006.

[28] M. Chu and R. Dyer, "Licensing, Design, and Construction of the Yucca Mountain Repository," *BRIDGE-WASHINGTON-NATIONAL ACADEMY OF ENGINEERING-*, vol. 33, no. 3, pp. 18–25, 2003.

[29] A. Macfarlane and R. C. Ewing, *Uncertainty underground: Yucca Mountain and the nation's high-level nuclear waste*. MIT Press, 2006.

[30] L. McGinnis and C. P. Ervin, "Earthquakes and block tectonics in the Illinois Basin," *Geology*, vol. 2, no. 10, pp. 517–519, 1974.

[31] A. Griscom and R. C. Jachens, "Tectonic history of the north portion of the San Andreas fault system, California, inferred from gravity and magnetic anomalies," *Journal of Geophysical Research: Solid Earth (1978–2012)*, vol. 94, no. B3, pp. 3089–3099, 1989.

[32] R. W. Simpson, R. C. Jachens, R. J. Blakely, and R. W. Saltus, "A new isostatic residual gravity map of the conterminous United States with a discussion on the significance of isostatic residual anomalies," *J. Geophys. Res.*, vol. 91, no. B8, pp. 8348–8372, Jul. 1986.

[33] U.S. Geological Survey, "Gravity anomaly map of the conterminous United States," *Mineral Resources On-line Spatial Data*, 14-May-2013. [Online]. Available: http://mrdata.usgs.gov/geophysics/gravity.html. [Accessed: 06-Jun-2014].

[34] J. L. Slate, M. E. Berry, P. D. Rowley, C. J. Fridrich, K. S. Morgan, J. B. Workman, O. D. Young, G. L. Dixon, V. S. Williams, and E. H. McKee, "Digital geologic map of the Nevada Test Site and vicinity, Nye, Lincoln, and Clark Counties, Nevada, and Inyo County, California," Geological Survey, Las Vegas, NV (US), 2000.

[35] E. B. Kisvarsanyi, "The Precambrian tectonic framework of Missouri as interpreted from the magnetic anomaly map," *Contrib. to Precambrian Geol*, no. 14 Part B, p. 19, 1984.

[36] H. E. Leetaru and J. H. McBride, "Reservoir uncertainty, Precambrian topography, and carbon sequestration in the Mt. Simon Sandstone, Illinois Basin," *Environmental Geosciences*, vol. 16, no. 4, pp. 235–243, 2009.

[37] J. Oliver, M. Dobrin, S. Kaufman, R. Meyer, and R. Phinney, "Continuous seismic reflection profiling of the deep basement, Hardeman County, Texas," *Geological Society of America Bulletin*, vol. 87, no. 11, pp. 1537–1546, 1976.

[38] H.-J. Kümpel, "Poroelasticity: parameters reviewed," *Geophysical Journal International*, vol. 105, no. 3, pp. 783–799, 1991.

[39] N. L. Bangs, G. K. Westbrook, J. W. Ladd, and P. Buhl, "Seismic velocities from the Barbados Ridge complex: Indicators of high pore fluid pressures in an accretionary complex," *Journal of Geophysical Research: Solid Earth (1978–2012)*, vol. 95, no. B6, pp. 8767–8782, 1990.

[40] R. J. O'Connell and B. Budiansky, "Seismic velocities in dry and saturated cracked solids," *Journal of Geophysical Research*, vol. 79, no. 35, pp. 5412–5426, 1974.

[41] B. W.F., "Permeability of crystalline and argillaceous rocks," *International Journal of Rock Mechanics and Mining Sciences & Geomechanics Abstracts*, vol. 17, no. 5, pp. 241–251, Oct. 1980.

[42] C. Clauser, "Permeability of crystalline rocks," *Eos Trans. AGU*, vol. 73, no. 21, pp. 233–238, May 1992.

[43] S. P. Neuman, "Universal scaling of hydraulic conductivities and dispersivities in geologic media," *Water resources research*, vol. 26, no. 8, pp. 1749–1758, 1990.

[44] S. P. Neuman, "Generalized scaling of permeabilities: Validation and effect of support scale," *Geophysical research letters*, vol. 21, no. 5, pp. 349–352, 1994.

[45] Q. Zhou, H.-H. Liu, F. J. Molz, Y. Zhang, and G. S. Bodvarsson, "Field-scale effective matrix diffusion coefficient for fractured rock: Results from literature survey," *Journal of contaminant hydrology*, vol. 93, no. 1, pp. 161–187, 2007.

[46] H. Liu, G. Bodvarsson, and G. Zhang, "Scale dependency of the effective matrix diffusion coefficient," *Vadose Zone Journal*, vol. 3, no. 1, pp. 312–315, 2004.

[47] B. J. Coyle and M. D. Zoback, "In situ permeability and fluid pressure measurements at~ 2 km depth in the Cajon Pass research well," *Geophysical Research Letters*, vol. 15, no. 9, pp. 1029–1032, 1988.

[48] C. A. Morrow and D. A. Lockner, "Permeability and porosity of the Illinois UPH 3 drillhole granite and a comparison with other deep drillhole rocks," *J. Geophys. Res.*, vol. 102, no. B2, pp. 3067–3075, Feb. 1997.

[49] C. Morrow and J. Byerlee, "Permeability of core samples from Cajon Pass scientific drill hole: Results from 2100 to 3500 m depth," *Journal of Geophysical Research: Solid Earth (1978–2012)*, vol. 97, no. B4, pp. 5145–5151, 1992.

[50] E. Huenges, J. Erzinger, J. Kück, B. Engeser, and W. Kessels, "The permeable crust: Geohydraulic properties down to 9101 m depth," *Journal of Geophysical Research: Solid Earth (1978–2012)*, vol. 102, no. B8, pp. 18255–18265, 1997.

[51] H. C. Heard, "Thermal expansion and inferred permeability of climax quartz monzonite to 300°C and 27.6 MPa," *International Journal of Rock Mechanics and Mining Sciences & Geomechanics Abstracts*, vol. 17, no. 5, pp. 289–296, Oct. 1980.

[52] L. T. Silver, E. W. James, and B. W. Chappell, "Petrological and geochemical investigations at the Cajon Pass deep drillhole," *Geophysical Research Letters*, vol. 15, no. 9, pp. 961–964, 1988.

[53] B. C. Haimson and T. W. Doe, "State of stress, permeability, and fractures in the Precambrian granite of northern Illinois," *Journal of Geophysical Research: Solid Earth (1978–2012)*, vol. 88, no. B9, pp. 7355–7371, 1983.

[54] P. Vilks, J. Cramer, M. Jensen, N. Miller, H. Miller, and F. Stanchell, "In situ diffusion experiment in granite: phase I," *Journal of contaminant hydrology*, vol. 61, no. 1, pp. 191–202, 2003.

[55] S. R. Carlson and H. Wang, "Microcrack porosity and in situ stress in Illinois borehole UPH 3," *Journal of Geophysical Research: Solid Earth (1978–2012)*, vol. 91, no. B10, pp. 10421–10428, 1986.

[56] C. Lu, C. Liu, T. Chen, J. Wang, X. Wang, R. Su, J. Sun, R. Yang, and X. Zhang, "Determination of the effective diffusion coefficient for 125I-in Beishan granite," *Radiochimica Acta*, vol. 96, no. 2, pp. 111–117, 2008.

[57] H. Johansson, J. Byegård, G. Skarnemark, and M. Skålberg, "Matrix diffusion of some alkali-and alkaline earth-metals in granitic rock," presented at the MRS Proceedings, 1996, vol. 465, p. 871.

[58] C. Chang and B. Haimson, "True triaxial strength and deformability of the German Continental Deep Drilling Program (KTB) deep hole amphibolite," *Journal of Geophysical Research: Solid Earth (1978–2012)*, vol. 105, no. B8, pp. 18999–19013, 2000.

[59] C. Galle, "Neutron porosity logging and core porosity measurements in the Beauvoir granite, Massif Central Range, France," *Journal of applied geophysics*, vol. 32, no. 2, pp. 125–137, 1994.

[60] J. J. Daniels, G. R. Olhoeft, and J. H. Scott, "Interpretation of core and well log physical property data from drill hole UPH-3, Stephenson County, Illinois," *J. Geophys. Res.*, vol. 88, no. B9, pp. 7346–7354, Sep. 1983.

[61] N. Marsic and B. Grundfelt, "Review of geoscientific data of relevance to disposal of spent nuclear fuel in deep boreholes in crystalline rock," SKB P-13-12, Svensk Kärnbränslehantering AB, 2013.

[62] P. A. Pezard and S. M. Luthi, "Borehole electrical images in the basement of the Cajon Pass Scientific Drillhole, California; Fracture identification and tectonic implications," *Geophys. Res. Lett.*, vol. 15, no. 9, pp. 1017–1020, Aug. 1988.

[63] Y. K. Kharaka, G. Ambats, W. C. Evans, and A. F. White, "Geochemistry of water at Cajon Pass, California: preliminary results," *Geophysical Research Letters*, vol. 15, no. 9, pp. 1037–1040, 1988.

[64] L. Birgersson and I. Neretnieks, "Diffusion in the matrix of granitic rock: Field test in the Stripa Mine," *Water Resources Research*, vol. 26, no. 11, pp. 2833–2842, 1990.

[65] D. J. Bottomley, R. Renaud, T. Kotzer, and I. D. Clark, "Iodine-129 constraints on residence times of deep marine brines in the Canadian Shield," *Geology*, vol. 30, no. 7, pp. 587–590, 2002.

[66] U. Fehn and G. Snyder, "Residence Times and Source Ages of Deep Crustal Fluids: interpretation of 129 I and 36 Cl results from the KTB VB drill site, Germany," *Geofluids*, vol. 5, no. 1, pp. 42–51, 2005.

[67] C. Williams and T. Narisimhan, "Hydrogeologic constraints on heat flow along the San Andreas fault," *Earth and Planetary Science Letters*, vol. 92, pp. 131–143, 1989.

[68] T. Kohl and L. Rybach, "Thermal and hydraulic aspects of the KTB drill site," *Geophysical Journal International*, vol. 124, no. 3, pp. 756–772, 1996.

[69] I. T. Kukkonen and C. Clauser, "Simulation of heat transfer at the Kola deep-hole site: implications for advection, heat refraction and palaeoclimatic effects," *Geophysical Journal International*, vol. 116, no. 2, pp. 409–420, 1994.

[70] S. A. Shapiro, E. Rothert, V. Rath, and J. Rindschwentner, "Characterization of fluid transport properties of reservoirs using induced microseismicity," *Geophysics*, vol. 67, no. 1, pp. 212–220, 2002.

[71] S. A. Shapiro, E. Huenges, and G. Borm, "Estimating the crust permeability from fluid-injection-induced seismic emission at the KTB site," *Geophysical Journal International*, vol. 131, no. 2, pp. F15–F18, 1997.

[72] W. Kessels and J. Kück, "Hydraulic communication in crystalline rock between the two boreholes of the continental deep drilling project in Germany," *International Journal of Rock Mechanics and Mining Sciences & Geomechanics Abstracts*, vol. 32, no. 1, pp. 37–47, Jan. 1995.

[73] S. A. Shapiro, P. Audigane, and J.-J. Royer, "Large-scale in situ permeability tensor of rocks from induced microseismicity," *Geophysical Journal International*, vol. 137, no. 1, pp. 207–213, 1999.

[74] V. C. Li, "Estimation of in-situ hydraulic diffusivity of rock masses," *pure and applied geophysics*, vol. 122, no. 2–4, pp. 545–559, 1984.

[75] M. D. Zoback and S. Hickman, "In situ study of the physical mechanisms controlling induced seismicity at Monticello Reservoir, South Carolina," *Journal of Geophysical Research: Solid Earth (1978–2012)*, vol. 87, no. B8, pp. 6959–6974, 1982.

[76] S. Shapiro, J. Kummerow, C. Dinske, G. Asch, E. Rothert, J. Erzinger, H. Kümpel, and R. Kind, "Fluid induced seismicity guided by a continental fault: Injection experiment of 2004/2005 at the German Deep Drilling Site (KTB)," *Geophysical research letters*, vol. 33, no. 1, 2006.

[77] B. J. Kowallis and H. F. Wang, "Microcrack study of granitic cores from Illinois deep borehole UPH 3," *Journal of Geophysical Research: Solid Earth (1978–2012)*, vol. 88, no. B9, pp. 7373–7380, 1983.

[78] Y. Eckstein, P. Dahl, and C. J. Vitaliano, "Petrographic and physical factors controlling thermal conductivity of granitic rocks in Illinois deep holes UPH 1, 2, AND 3," *Journal of Geophysical Research: Solid Earth (1978–2012)*, vol. 88, no. B9, pp. 7381–7385, 1983.

[79] P. G. Cook and A. L. Herczeg, *Environmental tracers in subsurface hydrology*. New York, NY: Springer Science and Business Media, LLC, 2000.

[80] J. . Fabryka-Martin, S. . Davis, D. Elmore, and P. . Kubik, "In situ production and migration of 129I in the Stripa granite, Sweden," *Geochimica et Cosmochimica Acta*, vol. 53, no. 8, pp. 1817–1823, Aug. 1989.

[81] J. Lippmann-Pipke, B. Sherwood Lollar, S. Niedermann, N. A. Stroncik, R. Naumann, E. van Heerden, and T. C. Onstott, "Neon identifies two billion year old fluid component in Kaapvaal Craton," *Chemical Geology*, vol. 283, no. 3, pp. 287–296, 2011.

[82] J. Bear, *Dynamics of fluids in porous media*. Courier Dover Publications, 2013.

[83] C. Manning and S. Ingebritsen, "Permeability of the continental crust: Implications of geothermal data and metamorphic systems," *Reviews of Geophysics*, vol. 37, no. 1, pp. 127–150, 1999.

[84] I. Stober and K. Bucher, "Hydraulic Properties of the Crystalline Basement," *Hydrogeol J*, vol. 15, no. 2, pp. 213–224, Mar. 2007.

[85] J. Townend and M. D. Zoback, "How faulting keeps the crust strong," *Geology*, vol. 28, no. 5, pp. 399–402, 2000.

[86] M. D. Zoback and J. Townend, "Implications of hydrostatic pore pressures and high crustal strength for the deformation of intraplate lithosphere," *Tectonophysics*, vol. 336, no. 1, pp. 19–30, 2001.

[87] N. H. Sleep and M. D. Zoback, "Did earthquakes keep the early crust habitable?," *Astrobiology*, vol. 7, no. 6, pp. 1023–1032, 2007.

[88] Q. Zhou, J. T. Birkholzer, C.-F. Tsang, and J. Rutqvist, "A method for quick assessment of CO_2 storage capacity in closed and semi-closed saline formations," *International Journal of Greenhouse Gas Control*, vol. 2, no. 4, pp. 626–639, 2008.

[89] I. Neretnieks, "Diffusion in the rock matrix: An important factor in radionuclide retardation?," *Journal of Geophysical Research: Solid Earth (1978–2012)*, vol. 85, no. B8, pp. 4379–4397, 1980.

[90] T. B. Boving and P. Grathwohl, "Tracer diffusion coefficients in sedimentary rocks: correlation to porosity and hydraulic conductivity," *Journal of Contaminant Hydrology*, vol. 53, no. 1, pp. 85–100, 2001.

[91] Y. Ohlsson and I. Neretniks, "Diffusion data in granite. Recommended values," SKB, Stockholm, Sweden, Technical Report TR-97-20, 1997.

[92] Y. Nakashima, "Diffusion of H2O and I− in expandable mica and montmorillonite gels: contribution of bound H2O," *Clays and Clay Minerals*, vol. 50, no. 1, pp. 1–10, 2002.

[93] R. Mills, "Self-diffusion in normal and heavy water in the range 1-45. deg.," *The Journal of Physical Chemistry*, vol. 77, no. 5, pp. 685–688, 1973.

[94] N. Cadelli, G. Cottone, S. Orlowski, G. Bertozzi, F. Girardi, and A. Saltelli, *Performance Assessment of Geological Isolation Systems for Radioactive Waste*. Brussels-Luxembourg: Commission of the European Communities, 1988.

[95] J. Rutqvist, D. Barr, J. T. Birkholzer, K. Fujisaki, O. Kolditz, Q.-S. Liu, T. Fujita, W. Wang, and C.-Y. Zhang, "A comparative simulation study of coupled THM processes and their effect on fractured rock permeability around nuclear waste repositories," *Environmental geology*, vol. 57, no. 6, pp. 1347–1360, 2009.

[96] N. Marsic, B. Grundfelt, M. Wiborgh, and K. Konsult, "Very Deep Hole Concept: Thermal Effects on Groundwater Flow," SKB, Stockholm, Sweden, R-06-59, Sep. 2006.

[97] H. Waber and J. Smellie, "Characterisation of pore water in crystalline rocks," *Applied Geochemistry*, vol. 23, no. 7, pp. 1834–1861, 2008.

[98] E. A. Bates, J. Buongiorno, E. Baglietto, and M. J. Driscoll, "Transient Thermal Modeling of a Deep Borehole Repository," in *Transactions of the American Nuclear Society, vol. 106*, Chicago, IL, 2012, vol. 106, p. 254.

[99] M. W. Becker and A. M. Shapiro, "Tracer transport in fractured crystalline rock: Evidence of nondiffusive breakthrough tailing," *Water Resources Research*, vol. 36, no. 7, pp. 1677–1686, 2000.

[100] D. Arcos, F. Grandia, and C. Domènech, "Geochemical evolution of the near field of a KBS-3 repository," SKB, TR-06-16, 2006.

[101] C. Clauser, P. Giese, E. Huenges, T. Kohl, H. Lehmann, L. Rybach, J. Šafanda, H. Wilhelm, K. Windloff, and G. Zoth, "The thermal regime of the crystalline continental crust: implications from the KTB," *Journal of Geophysical Research: Solid Earth (1978–2012)*, vol. 102, no. B8, pp. 18417–18441, 1997.

[102] A. Gens, A. Garcia-Molina, S. Olivella, E. Alonso, and F. Huertas, "Analysis of a Full Scale In Situ Test Simulating Repository Conditions," *International Journal for Numerical and Analytical Methods in Geomechanics*, vol. 22, pp. 515–548, 1998.

[103] C. Jaupart and J. Mareschal, "Heat flow and thermal structure of the lithosphere," *Treatise on Geophysics*, vol. 6, pp. 217–251, 2007.

[104] P. B. Slack, "Variance of terrestrial heat flow between the North American craton and the Canadian shield," *Geological Society of America Bulletin*, vol. 85, no. 4, pp. 519–522, 1974.

[105] V. K. Anderson, "An evaluation of the feasibility of disposal of nuclear waste in very deep boreholes," Master of Science Thesis, MIT Department of Nuclear Engineering, 2004.

[106] F. E. Dozier, "Feasibility of very deep borehole disposal of US nuclear defense wastes," S.M. Thesis, MIT Department of Nuclear Science and Engineering, 2011.

[107] E. A. Bates, M. J. Driscoll, R. K. Lester, and B. W. Arnold, "Can deep boreholes solve America's nuclear waste problem?," *Energy Policy*, vol. 72, pp. 186–189, Sep. 2014.

[108] M. J. Driscoll, R. Lester, K. Jensen, B. Arnold, P. Swift, and P. Brady, "Technology and Policy Aspects of Deep Borehole Nuclear Waste Disposal," *Nuclear Technology*, vol. 180, no. 1, pp. 111–121, 2012.

[109] T. Hagdu and B. Arnold, "Thermal-Hydrologic Modeling of a Deep Borehole Disposal System," in *Proceedings of the 14th International High-level Radioactive Waste Conference*, Albuquerque, NM, 2013.

[110] W. DeMaio and E. Bates, "Salinity and Density in Deep Boreholes," *MURJ MIT*, vol. 26, no. Fall, pp. 42–48, 2013.

[111] S. Frape, P. Fritz, and R. McNutt, "Water-rock interaction and chemistry of groundwaters from the Canadian Shield," *Geochimica et Cosmochimica Acta*, vol. 48, no. 8, pp. 1617–1627, 1984.

[112] P. Fritz and K. Frape, "Comments on the 18O and 2H, and Chemical Composition of Saline Groundwaters on the Canadian Shield," in *Isotope Studies of Hydrologic Processes*, Northern Illinois University Press, 1982.

[113] C. T. Simmons, T. R. Fenstemaker, and J. M. Sharp Jr., "Variable-density groundwater flow and solute transport in heterogeneous porous media: approaches, resolutions and future challenges," *Journal of Contaminant Hydrology*, vol. 52, no. 1–4, pp. 245–275, Nov. 2001.

[114] I. T. Kukkonen, "Thermal aspects of groundwater circulation in bedrock and its effect on crustal geothermal modelling in Finland, the central Fennoscandian Shield," *Tectonophysics*, vol. 244, no. 1, pp. 119–136, 1995.

[115] F. J. Millero, C.-T. Chen, A. Bradshaw, and K. Schleicher, "A new high pressure equation of state for seawater," *Deep Sea Research Part A. Oceanographic Research Papers*, vol. 27, no. 3, pp. 255–264, 1980.

[116] L. Biewick, "U.S Oil and Gas Historical Activity through 2005/2006," United States Geological Survey.

[117] M. D. Zoback, L. T. Silver, T. Henyey, and W. Thatcher, "The Cajon Pass scientific drilling experiment: Overview of phase 1," *Geophysical Research Letters*, vol. 15, no. 9, pp. 933–936, 1988.

[118] C. Morrow and J. Byerlee, "Permeability of rock samples from Cajon Pass, California," *Geophysical Research Letters*, vol. 15, no. 9, pp. 1033–1036, 1988.

[119] A. H. Lachenbruch and J. H. Sass, "The stress heat-flow paradox and thermal results from Cajon Pass," *Geophys. Res. Lett.*, vol. 15, no. 9, pp. 981–984, Aug. 1988.

[120] A. W. Laughlin, "Fenton Hill granodiorite-an 80-km (50-mi) right-lateral offset of the Sandia pluton?," *TC*, pp. 55–59, 1991.

[121] K. . Mickus and M. . Baker, "Program to correct anomalous subsurface temperature gradients resulting from surface temperature variations," *Computers & Geosciences*, vol. 17, no. 7, pp. 995–1008, 1991.

[122] B. J. Kowallis, H. F. Wang, and B.-A. Jang, "Healed microcrack orientations in granite from Illinois borehole UPH-3 and their relationship to the rock's stress history," *Tectonophysics*, vol. 135, no. 4, pp. 297–306, 1987.

[123] R. A. Couture, M. G. Seitz, and M. J. Steindler, "Sampling of brine in cores of Precambrian granite from northern Illinois," *J. Geophys. Res.*, vol. 88, no. B9, pp. 7331–7334, Sep. 1983.

[124] A. P. Visocky, M. G. Sherrill, and K. Cartwright, "Geology, hydrology, and water quality of the Cambrian and Ordovician systems in northern Illinois," Illinois State Water Survey and the Illinois State Geological Survey, 1985.

[125] F. Brigaud and G. Vasseur, "Mineralogy, porosity and fluid control on thermal conductivity of sedimentary rocks," *Geophysical Journal International*, vol. 98, no. 3, pp. 525–542, 1989.

[126] A. Lenardic and L. Moresi, "Some thoughts on the stability of cratonic lithosphere: Effects of buoyancy and viscosity," *Journal of Geophysical Research: Solid Earth (1978–2012)*, vol. 104, no. B6, pp. 12747–12758, 1999.

[127] E. Bates, J. Buongiorno, E. Baglietto, and M. J. Driscoll, "Mechanical Stresses Affecting Deep Borehole Disposal of High Level Waste," in *Proceedings of the 22nd ICONE*, Prague, Czech Republic, 2014, vol. ICONE22–31259.

[128] B. Arnold, T. Hagdu, D. Clayton, and C. Herrick, "Thermal-hydrologic-chemical-mechanical Modeling of Deep Borehole Disposal," in *Proceedings of the 13th International High-level Radioactive Waste Conference*, Albuquerque, NM, 2011.

[129] B. W. Arnold, D. Clayton, C. Herrick, and T. Hadgu, "Thermal-Mechanical Modeling of Deep Borehole Disposal of High-Level Radioactive Waste," presented at the AGU Fall Meeting Abstracts, 2010, vol. 1, p. 1086.

[130] T. Ito and M. D. Zoback, "Fracture permeability and in situ stress to 7 km depth in the KTB scientific drillhole," *Geophysical research letters*, vol. 27, no. 7, pp. 1045–1048, 2000.

[131] I. Song and B. C. Haimson, "Polyaxial strength criteria and their use in estimating in situ stress magnitudes from borehole breakout dimensions," *International Journal of Rock Mechanics and Mining Sciences*, vol. 34, no. 3, pp. 116–e1, 1997.

[132] C. D. Martin, P. K. Kaiser, and R. Christiansson, "Stress, instability and design of underground excavations," *International Journal of Rock Mechanics and Mining Sciences*, vol. 40, no. 7–8, pp. 1027–1047, Oct. 2003.

[133] M. Brudy, M. D. Zoback, K. Fuchs, F. Rummel, and J. Baumgärtner, "Estimation of the complete stress tensor to 8 km depth in the KTB scientific drill holes: Implications for crustal strength," *J. Geophys. Res.*, vol. 102, no. B8, pp. 18453–18475, Aug. 1997.

[134] M. Zoback, C. Barton, M. Brudy, D. Castillo, T. Finkbeiner, B. Grollimund, D. Moos, P. Peska, C. Ward, and D. Wiprut, "Determination of stress orientation and magnitude in deep wells," *International Journal of Rock Mechanics and Mining Sciences*, vol. 40, no. 7, pp. 1049–1076, 2003.

[135] "Determination of Maximum Injection Pressure for Class I Wells," U.S. Environmental Protection Agency, Region 5-Underground Injection Control Section Regional Guidance #7, 1994.

[136] Y. Zhang, M. Person, J. Rupp, K. Ellett, M. A. Celia, C. W. Gable, B. Bowen, J. Evans, K. Bandilla, and P. Mozley, "Hydrogeologic controls on induced seismicity in crystalline basement rocks due to fluid injection into basal reservoirs," *Groundwater*, vol. 51, no. 4, pp. 525–538, 2013.

[137] E. A. Bates, A. Salazar, M. J. Driscoll, E. Baglietto, and J. Buongiorno, "Plug Design for Deep Borehole Disposal of High-Level Nuclear Waste," *Nuclear Technology*, vol. 188, no. 3, pp. 280–291, Dec. 2014.

[138] M. Barral Silva, B. Silva Hermo, E. García-Rodeja, and N. Vázquez Freire, "Reutilization of granite powder as an amendment and fertilizer for acid soils," *Chemosphere*, vol. 61, no. 7, pp. 993–1002, 2005.

[139] J. Côté, M. Fillion, and J. Konrad, "Estimating Hydraulic and Thermal Conductivities of Crushed Granite Using Porosity and Equivalent Particle Size," *J. Geotech. Geoenviron. Eng.*, vol. 137, no. 9, pp. 834–842, Jan. 2011.

[140] A. Salazar, "Effect of Temperature on Permeability of Cement Sealant for Deep Borehole Repositories," in *Proceedings of the ANS 2013 Student Conference- Massachusetts Institute of Technology*, Boston, Massachusetts, 2013.

[141] W. McCabe, J. Smith, and P. Harriot, *Unit Operations of Chemical Engineering*, 6th ed. McGraw Hill, 2001.

[142] J. Frankovská, S. Andrejkovičová, and I. Janotka, "Effect of NaCl on hydraulic properties of bentonite and bentonite–palygorskite mixture," *Geosynthetics International*, vol. 17, no. 4, pp. 250–259, 2010.

[143] H. Komine, "Theoretical equations on hydraulic conductivities of bentonite-based buffer and backfill for underground disposal of radioactive wastes," *Journal of geotechnical and geoenvironmental engineering*, vol. 134, no. 4, pp. 497–508, 2008.

[144] Y. Guney, B. Cetin, A. H. Aydilek, B. F. Tanyu, and S. Koparal, "Utilization of sepiolite materials as a bottom liner material in solid waste landfills," *Waste Management*, vol. 34, no. 1, pp. 112–124, Jan. 2014.

[145] E. Galan, "Properties and applications of palygorskite-sepiolite clays," *Clay Minerals*, vol. 31, no. 4, pp. 443–454, 1996.

[146] SKB, "Long-Term Safety for the Final Repository of Spent Nuclear Fuel at Forsmark, Main Report of the SR-Site Project," SKB, Stockholm, Sweden, TR-11-01, 2011.

[147] R. C. Ewing, "Less Geology in the Geological Disposal of Nuclear Waste," *Science*, vol. 286, no. 5439, pp. 415–417, Oct. 1999.

[148] L. J. Carter and T. H. Pigford, "Proof of safety at yucca mountain," *Science(Washington)*, vol. 310, no. 5747, pp. 447–448, 2005.

[149] B. W. Arnold, P. V. Brady, S. J. Bauer, C. Herrick, S. Pye, and J. Finger, "Reference Design and Operations for Deep Borehole Disposal of High-Level Radioactive Waste," Sandia National Laboratories, Albuquerque, NM, SAND2011-6749, 2011.

[150] E. Bates, M. Driscoll, and J. Buongiorno, "A Drop-in Concept for Deep Borehole Canister Emplacement," Proceedings of the International High Level Waste Conference. Albuquerque, NM, 2011.

[151] S. Thórhallsson, B. Pálsson, S. Hólmgeirsson, K. Ingason, M. Matthíasson, H. Bóasson, and H. Sverrisson, "Well design for the Iceland Deep Drilling Project (IDDP)," *Geothermics*, vol. 49, pp. 16–22, 2014.

[152] T. Tamano, Y. Inoue, H. Mimura, and S. Yanagimoto, "Examination of commercial casing collapse strength under axial loading," *Journal of Energy Resources Technology*, vol. 104, no. 4, pp. 343–348, 1982.

[153] A. Spec, "5CT," *Specification for casing and tubing*, vol. 7, pp. 606–613, 2001.

[154] N. Todreas and M. Kazimi, *Nuclear Systems Volume 1: Thermal Hydraulic Fundamentals*, Second Edition. CRC Press, 2011.

[155] V. Oversby and L. Werme, "Canister Filling Materials-Design Requirements and Evaluation of Candidate Materials," presented at the MRS Proceedings, 1994, vol. 353.

[156] C. W. Forsberg, "Effect of depleted-uranium dioxide particulate fill on spent-nuclear-fuel waste packages," *Nuclear technology*, vol. 131, no. 3, pp. 337–353, 2000.

[157] S. Maheras, R. Best, S. Ross, E. Lahti, and D. Richmond, "A Preliminary Evaluation of Using Fill Materials to Stabilize Used Nuclear Fuel During Storage and Transportation," PNNL, PNNL, PNNL-21664, 2012.

[158] R. Salgado, P. Bandini, and A. Karim, "Shear Strength and Stiffness of Silty Sand," *J. Geotech. Geoenviron. Eng.*, vol. 126, no. 5, pp. 451–462, May 2000.

[159] E. Tsotsas and H. Martin, "Thermal Conductivity of Packed Beds: A Review," *Chem. Eng. Process.*, vol. 22, pp. 19–37, 1987.

[160] J. Gibbs, "Feasibility of Lateral Emplacement in Very Deep Borehole Disposal of High Level Nuclear Waste," Naval Engineer and Nuclear Engineer Thesis, MIT, 2010.

[161] J. Ayer and F. Soppet, "Vibratory compaction: I, compaction of spherical shapes," *Journal of the American ceramic society*, vol. 48, no. 4, pp. 180–183, 1965.

[162] A. Yu and N. Standish, "Porosity calculations of multi-component mixtures of spherical particles," *Powder Technology*, vol. 52, no. 3, pp. 233–241, 1987.

[163] W. D. Carrier, "Goodbye, Hazen; Hello, Kozeny-Carman," *Journal of Geotechnical and Geoenvironmental Engineering*, vol. 129, no. 11, pp. 1054–1056, Nov. 2003.

[164] E. Wium, "Canister Crushing Resistance for Deep Borehole Disposal of Nuclear Waste," MIT, Undergraduate Research Opportunity Project Final Report, Aug. 2013.

[165] V. R. Tarnawski, T. Momose, and W. H. Leong, "Thermal Conductivity of Standard Sands II. Saturated Conditions," *Int J Thermophys*, vol. 32, no. 5, pp. 984–1005, May 2011.

[166] P. Hejzlar, N. E. Todreas, and M. J. Driscoll, "Passive decay heat removal in advanced LWR concepts," *Nuclear engineering and design*, vol. 139, no. 1, pp. 59–81, 1993.

[167] D. S. Selengut, "Diffusion coefficients for heterogeneous systems," in *Trans. Am. Nucl. Soc.*, 1961, vol. 4, No. 2.

[168] "ASTM Standard B86, Standard Specification for Zinc and Zinc-Aluminum (ZA) Alloy Foundry and Die Castings," ASTM International, B86-13, 2013.

[169] K. Keller, "Low cost, high performance, high volume heatsinks," presented at the Electronics Manufacturing Technology Symposium, 1998. IEMT-Europe 1998. Twenty-Second IEEE/CPMT International, 1998, pp. 113–118.

[170] R. MacGregor and A. Emery, "Free convection through vertical plane layers—moderate and high Prandtl number fluids," *Journal of Heat Transfer*, vol. 91, no. 3, pp. 391–401, 1969.

[171] M. Keyhani, F. Kulacki, and R. Christensen, "Free convection in a vertical annulus with constant heat flux on the inner wall," *Journal of heat transfer*, vol. 105, no. 3, pp. 454–459, 1983.

[172] E. Santoyo, A. García, G. Espinosa, S. Santoyo-Gutiérrez, and E. González-Partida, "Convective heat-transfer coefficients of non-Newtonian geothermaldrilling fluids," *Journal of geochemical exploration*, vol. 78, pp. 249–255, 2003.

[173] R. Gundersen and K. Nisancioglu, "Cathodic protection of aluminum in seawater," *Corrosion*, vol. 46, no. 4, pp. 279–285, 1990.

[174] V. Prasad, F. A. Kulacki, and A. V. Kulkarni, "Free convection in a vertical, porous annulus with constant heat flux on the inner wall—experimental results," *International Journal of Heat and Mass Transfer*, vol. 29, no. 5, pp. 713–723, May 1986.

[175] C. Noubactep and S. Caré, "Dimensioning metallic iron beds for efficient contaminant removal," *Chemical Engineering Journal*, vol. 163, no. 3, pp. 454–460, Oct. 2010.

[176] J. Helsing and G. Grimvall, "Thermal conductivity of cast iron: Models and analysis of experiments," *Journal of applied physics*, vol. 70, no. 3, pp. 1198–1206, 1991.

[177] S. J. Morrison, D. R. Metzler, and C. E. Carpenter, "Uranium Precipitation in a Permeable Reactive Barrier by Progressive Irreversible Dissolution of Zerovalent Iron," *Environ. Sci. Technol.*, vol. 35, no. 2, pp. 385–390, Nov. 2000.

[178] S. Lahiri, C. Levenstein, D. I. Nelson, and B. J. Rosenberg, "The cost effectiveness of occupational health interventions: prevention of silicosis," *American journal of industrial medicine*, vol. 48, no. 6, pp. 503–514, 2005.

[179] I. Tavman, "Thermal and mechanical properties of aluminum powder-filled high-density polyethylene composites," *Journal of Applied Polymer Science*, vol. 62, no. 12, pp. 2161–2167, 1996.

[180] M. Ashraf Imam and F. H. S. Froes, "Low cost titanium and developing applications," *JOM*, vol. 62, no. 5, pp. 17–20, May 2010.

[181] W. C. Chard, C. E. Cooke Jr, and W. A. Hedden, "Hydraulic fracturing method using sintered bauxite propping agent," Jan. 1978.

[182] Y. Li, "Corrosion behaviour of hot dip zinc and zinc-aluminium coatings on steel in seawater," *Bulletin of Materials Science*, vol. 24, no. 4, pp. 355–360, 2001.

[183] X. Zhang, "Galvanic corrosion," *Uhlig's Corrosion Handbook*, vol. 51, p. 123, 2011.

[184] L. L. Snead, T. Nozawa, Y. Katoh, T.-S. Byun, S. Kondo, and D. A. Petti, "Handbook of SiC properties for fuel performance modeling," *Journal of nuclear materials*, vol. 371, no. 1, pp. 329–377, 2007.

[185] G. Pensl, F. Ciobanu, T. Frank, M. Krieger, S. Reshanov, F. Schmid, and M. Weidner, "SiC material properties," *International journal of high speed electronics and systems*, vol. 15, no. 04, pp. 705–745, 2005.

[186] I. A. Ibrahim, F. A. Mohamed, and E. J. Lavernia, "Particulate reinforced metal matrix composites — a review," *J Mater Sci*, vol. 26, no. 5, pp. 1137–1156, Jan. 1991.

[187] T. B. Jefferson, O. W. Witzell, and W. L. Sibbitt, "Thermal Conductivity of Graphite—Silicone Oil and Graphite-Water Suspensions," *Ind. Eng. Chem.*, vol. 50, no. 10, pp. 1589–1592, Oct. 1958.

[188] Z. Liu, Q. Guo, J. Shi, G. Zhai, and L. Liu, "Graphite blocks with high thermal conductivity derived from natural graphite flake," *Carbon*, vol. 46, no. 3, pp. 414–421, Mar. 2008.

[189] "Mineral Commodity Summaries- Graphite (Natural)," United States Geological Survey, Feb. 2014.

[190] J. Post, "Sepiolite deposits of the Las Vegas, Nevada area," *Clays and Clay Minerals*, vol. 26, no. 1, pp. 58–64, 1978.

[191] R. Donat, "The removal of uranium (VI) from aqueous solutions onto natural sepiolite," *The Journal of Chemical Thermodynamics*, vol. 41, no. 7, pp. 829–835, Jul. 2009.

[192] D. L. Gallup, "Treatment of geothermal waters for production of industrial, agricultural or drinking water," *Geothermics*, vol. 36, no. 5, pp. 473–483, Oct. 2007.

[193] G. Altun and U. Serpen, "Investigating Improved Rheological and Fluid Loss Performance of Sepiolite Muds under Elevated Temperatures," in *Proceedings of the World Geothermal Congress*, Antalya, Turkey, 2005, pp. 2440–2452.

[194] N. Guven, D. Panfil, and L. Carney, "Evaluation of saponite and saponite/sepiolite fluids for geothermal drilling," Sandia National Labs., Albuquerque, NM (USA); Texas Tech Univ., Lubbock, TX (USA). Dept. of Geosciences, SAND88-7115, 1991.

[195] S. Narumanchi, M. Mihalic, K. Kelly, and G. Eesley, "Thermal interface materials for power electronics applications," presented at the Thermal and Thermomechanical Phenomena in Electronic Systems, 2008. ITHERM 2008. 11th Intersociety Conference on, 2008, pp. 395–404.

[196] H. Fukushima, L. Drzal, B. Rook, and M. Rich, "Thermal conductivity of exfoliated graphite nanocomposites," *Journal of thermal analysis and calorimetry*, vol. 85, no. 1, pp. 235–238, 2006.

[197] S. Pincemin, R. Olives, X. Py, and M. Christ, "Highly conductive composites made of phase change materials and graphite for thermal storage," *Solar Energy Materials and Solar Cells*, vol. 92, no. 6, pp. 603–613, Jun. 2008.

[198] "Standard Test Method for Determination of Thermal Conductivity of Soil and Soft Rock by Thermal Needle Probe Procedure," ASTM Standard D5334-08.

[199] "Standard Specification for Standard Sand," ASTM Standard C778-13.

[200] K. Adamson, G. Birch, E. Gao, S. Hand, C. Macdonald, D. Mack, and A. Quadri, "High-pressure, high-temperature well construction," *Oilfield Review*, vol. 5, no. 2/3, pp. 15–32, 1993.

[201] D. Clayton, G. Freeze, T. Hadgu, E. Hardin, J. Lee, J. Prouty, R. Rogers, W. Nutt, J. Birkholzer, and H. Liu, "Generic Disposal System Modeling—Fiscal Year 2011 Progress Report," *Fuel Cycle Research and Development, Used Fuel Disposition, USDOE (SAND2011-5828P)*, 2011.

[202] C. Malbrain, R. Lester, and J. Deutch, "Analytical Approximations for the Long Term Decay Behavior of Spent Fuel and High Level Waste," *Nuclear Technology*, vol. 57, pp. 292–305, 1982.

[203] P. Carbol, P. Fors, T. Gouder, and K. Spahiu, "Hydrogen suppresses UO2 corrosion," *Geochimica et Cosmochimica Acta*, vol. 73, pp. 4366–4375, 2009.

[204] M. Telander and R. Westerman, "Hydrogen Generation by Metal Corrosion in Simulated Waste Isolation Pilot Plant Environments."

[205] A. D. Henderson and A. H. Demond, "Long-term performance of zero-valent iron permeable reactive barriers: a critical review," *Environmental Engineering Science*, vol. 24, no. 4, pp. 401–423, 2007.

[206] D. Phillips, T. V. Nooten, L. Bastiaens, M. Russell, K. Dickson, S. Plant, J. Ahad, T. Newton, T. Elliot, and R. Kalin, "Ten year performance evaluation of a field-scale zero-valent iron permeable reactive barrier installed to remediate trichloroethene contaminated groundwater," *Environmental science & technology*, vol. 44, no. 10, pp. 3861–3869, 2010.

[207] R. Francis, "Galvanic Corrosion of High Alloy Stainless Steels in Sea Water," *British Corrosion Journal*, vol. 29, no. 1, pp. 53–57, Jan. 1994.

[208] F. Bellucci, "Galvanic corrosion between nonmetallic composites and metals: I effect of metal and of temperature," *Corrosion*, vol. 47, no. 10, pp. 808–819, 1991.

[209] M. Pryor and D. Keir, "Galvanic Corrosion I. Current Flow and Polarization Characteristics of the Aluminum-Steel and Zinc-Steel Couples in Sodium Chloride Solution," *Journal of The Electrochemical Society*, vol. 104, no. 5, pp. 269–275, 1957.

[210] M. Tavakkolizadeh and H. Saadatmanesh, "Galvanic corrosion of carbon and steel in aggressive environments," *Journal of Composites for construction*, vol. 5, no. 3, pp. 200–210, 2001.

[211] F. Mansfeld and J. Kenkel, "Galvanic corrosion of Al alloys—III. The effect of area ratio," *Corrosion Science*, vol. 15, no. 4, pp. 239–250, 1975.

[212] R. Krupiczka, "Analysis of thermal conductivity in granular materials," *Int. Chem. Eng*, vol. 7, no. 1, pp. 122–144, 1967.

[213] J. K. Borchardt, "In-situ gelation of silicates in drilling, well completion and oil production," *Colloids and surfaces*, vol. 63, no. 1, pp. 189–199, 1992.

[214] U. Tare and B. Fersheed Mody, "Stabilizing boreholes while drilling reactive shale formations with silicate-base drilling fluids," *Drilling Contractor*, no. May/June, pp. 42–44, 2000.

[215] Y. Xu, X. Luo, and D. Chung, "Sodium silicate based thermal interface material for high thermal contact conductance," *Journal of Electronic Packaging*, vol. 122, no. 2, pp. 128–131, 2000.

[216] R. Palley, *Concrete: A Seven-Thousand-Year History*. Quantuck Lane Press/Norton, 2010.

[217] E. Santoyo, A. García, J. Morales, E. Contreras, and G. Espinosa-Paredes, "Effective thermal conductivity of Mexican geothermal cementing systems in the temperature range from 28 C to 200 C," *Applied thermal engineering*, vol. 21, no. 17, pp. 1799–1812, 2001.

[218] U. DOE, "Yucca Mountain repository license application," DOE/RW-0573, Rev 0, 2008.

[219] C. W. Hansen, J. T. Birkholzer, J. Blink, C. Bryan, Y. Chen, M. Gross, E. Hardin, J. Houseworth, R. Howard, and R. Jarek, "Overview of total system model used for the 2008 performance assessment for the proposed high-level radioactive waste repository at Yucca Mountain, Nevada," *Reliability Engineering & System Safety*, vol. 122, pp. 249–266, 2014.

[220] J. C. Helton and F. J. Davis, "Latin hypercube sampling and the propagation of uncertainty in analyses of complex systems," *Reliability Engineering & System Safety*, vol. 81, no. 1, pp. 23–69, Jul. 2003.

[221] U. Berner, "Evolution of pore water chemistry during degradation of cement in a radioactive waste repository environment," *Waste Management*, vol. 12, no. 2, pp. 201–219, 1992.

[222] J. S. Wang, D. C. Mangold, and C. F. Tsang, "Thermal Impact of Waste Emplacement and Surface Cooling Associated wth Geologic Disposal of High-Level Nuclear Waste," *Environmental Gel. Water Sci.*, vol. 11, no. 2, pp. 183–239, 1988.

[223] J. Wang, D. Mangold, and C. Tsang, "Long-term thermomechanical and thermohydrological factors controlling the optimal design of a nuclear waste repository," presented at the MRS Proceedings, 1982, vol. 15, p. 531.

[224] E. Hardin, J. Blink, H. Greenberg, M. Sutton, M. Fratoni, J. Carter, M. Dupont, and R. Howard, "Generic Repository Design Concepts and Thermal Analysis (FY11)," Sandia National Laboratory, SAND2011-6202, Aug. 2011.

[225] Z. Xu, "Design strategies for optimizing high burnup fuel in pressurized water reactors," Doctoral Thesis, MIT Department of Nuclear Science and Engineering, 2003.

[226] R. A. Wigeland, T. H. Bauer, T. H. Fanning, and E. E. Morris, "Separations and transmutation criteria to improve utilization of a geologic repository," *Nuclear Technology*, vol. 154, no. 1, pp. 95–106, 2006.

[227] P. Carbol, D. H. Wegen, T. Wiss, and P. Fors, "5.16 - Spent Fuel as Waste Material," in *Comprehensive Nuclear Materials*, Editor-in-Chief: Rudy J.M. Konings, Ed. Oxford: Elsevier, 2012, pp. 389–420.

[228] J. . Hudson, O. Stephansson, J. Andersson, C.-F. Tsang, and L. Jing, "Coupled T–H–M issues relating to radioactive waste repository design and performance," *International Journal of Rock Mechanics and Mining Sciences*, vol. 38, no. 1, pp. 143–161, Jan. 2001.

[229] J. S. Y. Wang, C. F. Tsang, N. G. W. Cook, and P. A. Witherspoon, "A study of regional temperature and thermohydrologic effects of an underground repository for nuclear wastes in hard rock," *J. Geophys. Res.*, vol. 86, no. B5, pp. 3759–3770, May 1981.

[230] F. Dozier, M. Driscoll, and J. Buongiorno, "Host Rock Temperature around a Borehole Containing HLW," in *Transactions of the American Nuclear Society*, Washington D.C, 2011, vol. 105, No.1, pp. 229–231.

[231] Y. Katto and T. Masuoka, "Criterion for the onset of convective flow in a fluid in a porous medium," *International Journal of Heat and Mass Transfer*, vol. 10, no. 3, pp. 297–309, Mar. 1967.

[232] H.-J. G. Diersch and O. Kolditz, "Variable-density flow and transport in porous media: approaches and challenges," *Advances in Water Resources*, vol. 25, no. 8–12, pp. 899–944, Aug. 2002.

[233] K.-K. Tan, T. Sam, and H. Jamludin, "The Onset of Transient Convection in Bottom Heated Porous Media," *International Journal of Heat and Mass Transfer*, vol. 46, pp. 2857–2873, 2003.

[234] J. Funehag and G. Gustafson, "Design of grouting with silica sol in hard rock – New design criteria tested in the field, Part II," *Tunnelling and Underground Space Technology*, vol. 23, no. 1, pp. 9–17, Jan. 2008.

[235] J. Carter, A. Luptak, J. Gastelum, C. Stockman, and A. Miller, "Fuel cycle potential waste inventory for disposition," Department of Energy, Fuel Cycle Research and Development FCR&D-USED-2010-000031 Rev 5, 2012.

[236] "'Reference Biospheres' for solid radioactive waste disposal," Waste Safety Section, International Atomic Energy Agency, Vienna, Austria, Report of BIOMASS Theme 1 IAEA-BIOMASS-6, Jul. 2003.

[237] A. Hedin, "Integrated analytic radionuclide transport model for a spent nuclear fuel repository in saturated fractured rock," Nuclear Technology, vol. 138, no. 2, pp. 179–205, 2002.

[238] U.S. Environmental Protection Agency, Public health and environmental radiation protection standards for Yucca Mountain, NV; Final Rule. 2001.

[239] K. Eckerman, J. Harrison, H.-G. Menzel, and C. H. Clement, "ICRP Publication 119: Compendium of Dose Coefficients based on ICRP Publication 60. ICRP Publication 119. Ann. ICRP 41 (Suppl.)," Annals of the ICRP, 2012.

[240] D. Bennett and R. Gens, "Overview of European concepts for high-level waste and spent fuel disposal with special reference waste container corrosion," Journal of Nuclear Materials, vol. 379, no. 1, pp. 1–8, 2008.

[241] L. Johnson, C. Ferry, C. Poinssot, and P. Lovera, "Spent fuel radionuclide source-term model for assessing spent fuel performance in geological disposal. Part I: Assessment of the instant release fraction," Journal of Nuclear Materials, vol. 346, no. 1, pp. 56–65, 2005.

[242] S. Röllin, K. Spahiu, and U.-B. Eklund, "Determination of dissolution rates of spent fuel in carbonate solutions under different redox conditions with a flow-through experiment," Journal of Nuclear Materials, vol. 297, no. 3, pp. 231–243, Sep. 2001.

[243] "Long-term Safety for KBS-3 Repositories at Forsmark and Laxemar—A First Evaluation, Main Report of the SR-Can Project," SKB, Stockholm, Sweden, TR-06-09, 2006.

[244] S. Frape, A. Blyth, R. Blomqvist, R. McNutt, and M. Gascoyne, "Deep fluids in the continents: II. Crystalline rocks," Treatise on geochemistry, vol. 5, pp. 541–580, 2003.

[245] D. Shaw, G. Reilly, J. Muysson, G. Pattenden, and F. Campbell, "An estimate of the chemical composition of the Canadian Precambrian Shield," Canadian Journal of Earth Sciences, vol. 4, no. 5, pp. 829–853, 1967.

[246] P. Wersin, M. F. Hochella Jr, P. Persson, G. Redden, J. O. Leckie, and D. W. Harris, "Interaction between aqueous uranium (VI) and sulfide minerals: spectroscopic evidence for sorption and reduction," Geochimica et Cosmochimica Acta, vol. 58, no. 13, pp. 2829–2843, 1994.

[247] E. S. Ilton, A. Haiduc, C. O. Moses, S. M. Heald, D. C. Elbert, and D. R. Veblen, "Heterogeneous reduction of uranyl by micas: Crystal chemical and solution controls," Geochimica et Cosmochimica Acta, vol. 68, no. 11, pp. 2417–2435, 2004.

[248] T. B. Scott, G. C. Allen, P. J. Heard, and M. G. Randell, "Reduction of U(VI) to U(IV) on the surface of magnetite," Geochimica et Cosmochimica Acta, vol. 69, no. 24, pp. 5639–5646, Dec. 2005.

[249] S. Regenspurg, D. Schild, T. Schäfer, F. Huber, and M. E. Malmström, "Removal of uranium (VI) from the aqueous phase by iron (II) minerals in presence of bicarbonate," Applied Geochemistry, vol. 24, no. 9, pp. 1617–1625, 2009.

[250] E. Liger, L. Charlet, and P. Van Cappellen, "Surface catalysis of uranium (VI) reduction by iron (II)," Geochimica et Cosmochimica Acta, vol. 63, no. 19, pp. 2939–2955, 1999.

[251] A. Hedin, J. Crawford, C. Greis, M. Lindgren, and S. Painter, "Radionuclide transport report for the safety assessment SR-Site," Svensk Kärnbränslehantering AB (SKB), Technical Report TR-10-50, Dec. 2010.

[252] P. Fritz, M. Lodemann, S. Weise, M. Wolf, H. Behr, B. Hansen, E. Horn, C. Reutel, J. Topp, and A. Pekdeger, "Saline fluids in the KTB pilot borehole," *Scientific Drilling*, vol. 2, pp. 231–243, 1991.

[253] M. Ekman, "A consistent map of the postglacial uplift of Fennoscandia," *Terra Nova*, vol. 8, no. 2, pp. 158–165, Mar. 1996.

[254] R. Blomqvist, *Hydrogeochemistry of deep groundwaters in the central part of the Fennoscandian Shield*. Geological Survey of Finland, 1999.

[255] D. L. Parkhurst and C. Appelo, "User's guide to PHREEQC (Version 2): A computer program for speciation, batch-reaction, one-dimensional transport, and inverse geochemical calculations," *U.S. Geological Survey*, 1999.

[256] P. Mariner, J. Lee, E. Hardin, F. Hansen, G. Freeze, A. Lord, B. Goldstein, and R. Price, "Granite Disposal of U.S. High-Level Radioactive Waste," Sandia National Laboratory, SAND2011-6203, Aug. 2011.

[257] P. Carbol and I. Engkvist, "Compilation of radionuclide sorption coefficients for performance assessment," SKB, R-97-13, 1997.

[258] I. McKinley and A. Scholits, "A comparison of radionuclide sorption databases used in recent performance assessments," *Journal of contaminant hydrology*, vol. 13, no. 1, pp. 347–363, 1993.

[259] G. Olyslaegers, T. Zeevaert, P. Pinedo, I. Simon, G. Pröhl, R. Kowe, Q. Chen, S. Mobbs, U. Bergström, and B. Hallberg, "A comparative radiological assessment of five European biosphere systems in the context of potential contamination of well water from the hypothetical disposal of radioactive waste," *Journal of Radiological Protection*, vol. 25, no. 4, p. 375, 2005.

[260] G. Gustafson and J. Krásný, "Crystalline rock aquifers: their occurrence, use and importance," *Applied Hydrogeology*, vol. 2, no. 2, pp. 64–75, 1994.

[261] D. Tang, E. Frind, and E. A. Sudicky, "Contaminant transport in fractured porous media: Analytical solution for a single fracture," *Water Resources Research*, vol. 17, no. 3, pp. 555–564, 1981.

[262] B. Shen, O. Stephansson, M. Rinne, K. Amemiya, R. Yamashi, S. Toguri, and H. Asano, "FRACOD Modeling of Rock Fracturing and Permeability Change in Excavation-Damaged Zones," *Int. J. Geomech.*, vol. 11, no. 4, pp. 302–313, Apr. 2010.

[263] J. Rutqvist, Y.-S. Wu, C.-F. Tsang, and G. Bodvarsson, "A modeling approach for analysis of coupled multiphase fluid flow, heat transfer, and deformation in fractured porous rock," *International Journal of Rock Mechanics and Mining Sciences*, vol. 39, no. 4, pp. 429–442, 2002.

[264] S. Emsley, O. Olsson, L. Stenberg, H. Alheid, and S. Falls, *ZEDEX: a study of damage and disturbance from tunnel excavation by blasting and tunnel boring*. Svensk Kärnbränslehantering AB/Swedish Nuclear Fuel and Waste Management Company, 1997.

[265] J. Autio, M. Siitari-Kauppi, J. Timonen, K. Hartikainen, and J. Hartikainen, "Determination of the porosity, permeability and diffusivity of rock in the excavation-disturbed zone around full-scale deposition holes using the 14C-PMMA and He-gas methods," *Journal of contaminant hydrology*, vol. 35, no. 1, pp. 19–29, 1998.

[266] M. Souley, F. Homand, S. Pepa, and D. Hoxha, "Damage-induced permeability changes in granite: a case example at the URL in Canada," *International Journal of Rock Mechanics and Mining Sciences*, vol. 38, no. 2, pp. 297–310, Feb. 2001.

[267] P. C. Kelsall, J. B. Case, and C. R. Chabannes, "Evaluation of excavation-induced changes in rock permeability," *International Journal of Rock Mechanics and Mining Sciences & Geomechanics Abstracts*, vol. 21, no. 3, pp. 123–135, Jun. 1984.

[268] M. Lindgren and F. Lindström, "SR 97-Radionuclide transport calculations," Swedish Nuclear Fuel and Waste Management Co., Stockholm (Sweden), Technical Report TR-99-23, 1999.

[269] K.-B. Min, J. Rutqvist, C.-F. Tsang, and L. Jing, "Stress-dependent permeability of fractured rock masses: a numerical study," *International Journal of Rock Mechanics and Mining Sciences*, vol. 41, no. 7, pp. 1191–1210, 2004.

[270] A. M. Shapiro, "Effective matrix diffusion in kilometer-scale transport in fractured crystalline rock," *Water Resources Research*, vol. 37, no. 3, pp. 507–522, 2001.

[271] "Geologic CO2 Sequestration Technology and Cost Analysis," U.S. Environmental Protection Agency, Office of Water, Technical Support Document EPA 816-B-08-009, Jun. 2008.

[272] C. Augustine, J. Tester, and B. Anderson, "A Comparison of Geothermal with Oil and Gas Well Drilling Costs," Proceedings of the Thirty First Workshop on Geothermal Reservoir Engineering. Stanford, CA, 2006.

[273] "Consumer Price Index- All Urban Consumers," U.S. Department of Labor, Bureau of Labor Statistics, Databases, Tables and Calculators by Subject, 2014.

[274] S. Thorhallsson, M. Matthiasson, T. Gislason, K. Ingason, and B. Palsson, "Iceland Deep Drilling Project (IDDP): The challenge of drilling and coring into 350-500 C hot geothermal systems and down to 5 km," presented at the International Geothermal Conference, Reykjavik, 2003, pp. 15–22.

[275] J. Beswick, "Status of Technology for Deep Borehole Disposal," *EPS International Contract No NP*, vol. 1185, 2008.

[276] E. A. Bates, "A drop-in-concept for deep borehole canister emplacement," Master of Science Thesis, Massachusetts Institute of Technology, 2011.

[277] Y. Polsky and L., et al Capuano, "Enhanced Geothermal Systems (EGS) Well Construction Technology Evaluation Report," Sandia National Laboratory, SAND2008-7866, Dec. 2008.

[278] J. C. Andersson, C. D. Martin, and H. Stille, "The Äspö Pillar Stability Experiment: Part II—Rock mass response to coupled excavation-induced and thermal-induced stresses," *International Journal of Rock Mechanics and Mining Sciences*, vol. 46, no. 5, pp. 879–895, 2009.

[279] R. Pusch and G. Ramqvist, "Borehole sealing, preparative steps, design and function of plugs–basic concept," *SKB Int. Progr. Rep. IPR-04-57*, 2004.

[280] A. Cihan and J. S. Tyner, "2D radial analytical solutions for solute transport in a dual-porosity medium," *Water Resources Research*, vol. 47, no. 4, 2011.

[281] M. Huysmans and A. Dassargues, "Review of the use of Péclet numbers to determine the relative importance of advection and diffusion in low permeability environments," *Hydrogeology Journal*, vol. 13, no. 5–6, pp. 895–904, 2005.

[282] M. Genuchten, D. Tang, and R. Guennelon, "Some exact solutions for solute transport through soils containing large cylindrical macropores," *Water Resources Research*, vol. 20, no. 3, pp. 335–346, 1984.

[283] E. Sudicky and E. Frind, "Contaminant transport in fractured porous media: Analytical solutions for a system of parallel fractures," *Water Resources Research*, vol. 18, no. 6, pp. 1634–1642, 1982.

[284] G. Grisak and J. Pickens, "An analytical solution for solute transport through fractured media with matrix diffusion," *Journal of Hydrology*, vol. 52, no. 1, pp. 47–57, 1981.

[285] M. M. Rahman, R. Liedl, and P. Grathwohl, "Sorption kinetics during macropore transport of organic contaminants in soils: Laboratory experiments and analytical modeling," *Water resources research*, vol. 40, no. 1, 2004.

[286] R. Wallach and J.-Y. Parlange, "Modeling transport in a single crack by the dual-porosity concept with a boundary layer at the interface," *Journal of contaminant hydrology*, vol. 34, no. 1, pp. 121–138, 1998.

[287] R. A. Freeze and J. Cherry, *Groundwater*. Englewood Cliffs, NJ: Prentice-Hall, 1979.

[288] T. Perkins and O. Johnston, "A review of diffusion and dispersion in porous media," *Society of Petroleum Engineers Journal*, vol. 3, no. 01, pp. 70–84, 1963.

[289] M. Abramowitz and I. A. Stegun, *Handbook of mathematical functions: with formulas, graphs, and mathematical tables*. Courier Dover Publications, 1972.

[290] W. Wagner and A. Pruss, "The IAPWS formulation 1995 for the thermodynamic properties of ordinary water substance for general and scientific use.," *Journal of Physical and Chemical Reference Data*, vol. 31, no. 2, pp. 387–535.

[291] K. Fuenkajorn and J. J. Daemen, "Cement borehole plug performance in welded tuff," presented at the The 32nd US Symposium on Rock Mechanics (USRMS), 1991.

[292] W. Cho, J. Lee, and K. Chun, "The temperature effects on hydraulic conductivity of compacted bentonite," *Applied clay science*, vol. 14, no. 1, pp. 47–58, 1999.

[293] H. Komine, "Predicting hydraulic conductivity of sand–bentonite mixture backfill before and after swelling deformation for underground disposal of radioactive wastes," *Engineering Geology*, vol. 114, no. 3–4, pp. 123–134, Aug. 2010.

[294] P. V. Sivapullaiah, A. Sridharan, and V. K. Stalin, "Hydraulic conductivity of bentonite-sand mixtures," *Can. Geotech. J.*, vol. 37, no. 2, pp. 406–413, 2000.

[295] T. Hadgu, B. Arnold, J. Lee, G. Freeze, P. Vaughn, P. Swift, and C. Sallaberry, "Sensitivity Analysis of Seals Permeability and Performance Assessment of Deep Borehole Disposal of Radioactive Waste.," Sandia National Laboratories (SNL-NM), Albuquerque, NM (United States), SAND2012-1118C, 2012.

Appendix A. Derivation of Steady State Analytical Solution for Radionuclide Concentration in a Permeable Plug Surrounded by Homogenous Rock

A.1 Introduction

An analytical solution to radionuclide transport from the disposal zone to the surface is useful because the simultaneous solution of advection (hyperbolic) and diffusion (parabolic) equations can be challenging to numerical codes[280], [281]. Frequently, modelers will use the dimensionless Péclet number (which characterizes advective/diffusive transport rates) to determine which transport phenomenon is dominant and on this basis neglect one of the transport mechanisms [281]. However, there are limitations to this approach, and there appear to be many suggestions for the Péclet number definition and which criteria to apply[281]. More importantly, there are highly plausible scenarios where advective transport will dominate in one region, while diffusive transport dominates in the other (e.g., flow in fractured zones). In these cases, it is clearly unrealistic to rule out one transport mechanism or the other completely, and a coupled approach is required. The primary purpose of this section is to outline an analytical solution which allows for the treatment of advection and diffusion simultaneously (albeit in different regions). A secondary goal of this section is to clearly outline (from first principles) the conditions under which advection may be neglected, specifically in the context of nuclear waste disposal.

Currently, the Finite Element Hybrid Method (FEHM) transport code used by Sandia National Laboratories (SNL) [281] only solves for advection transport. Diffusive transport (molecular) is treated separately in GoldSim (using models not yet described). As of this time, radionuclide diffusion has not yet been incorporated into the MIT's BVR tool either. Analytical solutions are highly useful for scoping and sensitivity studies, and for validating numerical capabilities when they become available. To the extent that the level of conservatism incorporated into the analytical model does not render it completely unrealistic, the solution provides meaningful performance estimates that can be used to improve the design of deep borehole facilities.

Neretnieks [89] was the among the first to detail how accounting for diffusion can reduce contaminant transport rate along fractures, the primary conduits for radionuclide transport typically considered in crystalline rock (and thus deep boreholes). Tang and others [261]

continued on that work and presented a number of analytical solutions[282]–[284] to the advection and diffusion equation to further demonstrate this effect. We begin by summarizing and discussing the validity of the simplifying assumptions used by Tang et. al. [261] in Table A-1.

Table A-1. Simplifying assumptions and transport mechanisms included in Tang et. al. [261]

	Fracture	**Surrounding Porous Matrix**	**Simplifications**
Size	Width<<Length	(Infinite, concentration of radionuclides $\rightarrow$ 0 at outer extent)	Mass transport in fracture is represented along the fracture in one dimension (i.e., axial).
Mixing	Transverse diffusion and dispersion within the fracture assures complete mixing across the width of fracture.		
Permeability	Not specified, equations are not coupled with Darcy's law- velocity is an input parameter.	Very low, such that transport is primarily diffusive.	The direction of the mass flux in the porous matrix is perpendicular to the fracture axis (i.e., radial)
Transport	Transport along fracture>> Transport within matrix		
Sorption	$R = 1 + \frac{K_f}{b}$, where R is the fracture retardation factor, K_f is distribution coefficient.	$R_m = 1 + \frac{K_m \rho_m}{\phi_m}$, where R is the matrix retardation factor, K_m, ρ_m, ϕ_m are the distribution coefficient, density, and porosity of the matrix.	Governed by a linear equilibrium isotherm.
Radioactive decay	Included		

The key simplification is that transport along the fracture is primarily vertical (due to advection and dispersion) while transverse (radial) diffusion occurs into a low permeability (stagnant) matrix. In addition, sorption is treated in a linear fashion (the amount sorbed is proportional to the concentration of solute). This allows the partial differential equations for transport, sorption and decay to be simplified to two ordinary differential equations coupled by a continuity boundary condition at the interface. Other more recent investigators have continued using similar assumptions in models and experiments[280], [285], [286]. The approximations regarding advection transport summarized in Table A-1 are realistic in the case that the plug has significantly lower permeability than the surrounding host rock and when hydraulic boundaries are assumed to be closed (i.e., reflective pressure boundaries are drawn close to the borehole,

which effectively simulates an infinite array of closely spaced boreholes). In this case, the fluid expansion created by decay heat is accommodated by flow through the least resistance path (e.g., in the low permeability plug and fracture if present). The fluid pressure increases to a sufficiently high value necessary to induce flow through that path and remove the excess volume. This is plausibly the most conservative case which maximizes the vertical velocities through failed zones that could carry radionuclides from the disposal zone to the shallow subsurface.

Tang and others' [261],[283] models of very small, planar, fractures cannot easily be represented in numerical solvers (which are required to calculate the velocity). Thus, rather than model a micron sized fracture (a water filled gap), it is sometimes preferable to evaluate a fault or failed plug (e.g., region with low permeability). In addition, for the borehole plug it seems more appropriate to use a radially symmetric cylindrical geometry instead of a planar one (a simplification others have made [280], [282], [285]). These previous investigators neglected the effect of dispersion in their equations and thus we complete a full derivation here that includes all effects, in cylindrical coordinates. In this case, the governing equations for the central zone are different from any previously found equations, but all of the assumptions and simplifications in Table A-1 remain. Figure A-1 presents the 2D axisymmetric representation of the plug and matrix system.
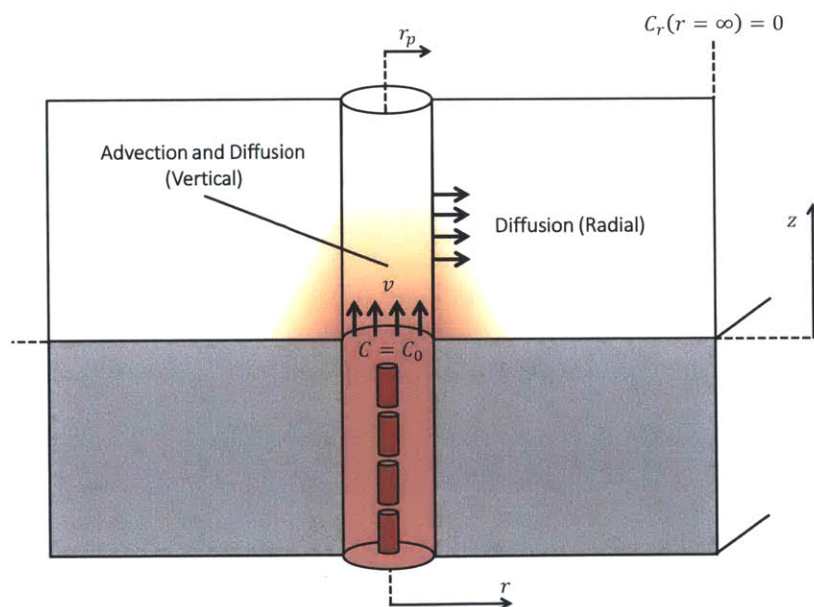
Figure A-1. Geometric representation of the plug-matrix system. Color gradients approximately indicate the expected steady-state concentration (C) gradient in this system.

A.2 Vertical advective and dispersive transport in the plug

The differential equation for concentrations in the plug can be obtained by a mass balance on the contaminant in the plug, drawn around a control volume with length dZ, radius dr, and with a spatial concentration difference of dC. To account for sorption, we adopt a linear equilibrium isotherm model [261], [287], in which the mass of solute sorbed per unit mass of solid in the porous matrix (S) can be related to the concentration using Eq. (A-1), and Eq. (A-2),

$$S = \frac{ds}{dc}C = K_D C \tag{A-1}$$

$$\frac{dS}{dt} = K_D \frac{dC}{dt} \tag{A-2}$$

where K_D is the frequently used "distribution coefficient" of the solid material in the plug, and is by definition the mass of solute adsorbed per unit volume of solid, divided by the concentration of solute with units of $(kg/m^3)^{-1}$. The transport equation in the plug, using discrete quantities of Δz, ΔC, ΔS, Δt, (having already integrated some quantities over r for the sake of brevity) is shown in Eq.(A-3),

$$\Delta C \left(\phi_p \pi r_p^2 \Delta z \right) \text{ [Accumulation in pore fluid volume]} =$$

$$-v\phi_p \left(\pi r_p^2 \right) \Delta C \Delta t \text{ } [Net \text{ axial advective transport]}$$

$$-\left(\pi r_p^2 \right) \left(\Phi(z + \Delta z) - \Phi(z) \right) \Delta t \text{ } [Net \text{ axial dispersive transport]}$$

$$-2\pi r_p \Delta z q_r \text{ } \Delta t [\text{Radial flux } (q_r) \text{ to adjacent matrix }]$$

$$-\lambda C \left(\phi_p \pi r_p^2 \Delta z \right) \Delta t [\text{Radioactive decay of solute in pore water]}$$

$$-\frac{\rho_p}{\phi_p} \Delta S \left(\phi_p \pi r_p^2 \Delta z \right) [\text{Sorption]}$$

$$-\lambda \left(\frac{S\rho_p}{\phi_p} \right) \left(\phi_p \pi r_p^2 \Delta z \right) \Delta t [\text{Radioactive decay of sorbed solute]}$$

(A-3)

where r_p is the radius of the plug, v is the mean advective velocity of the pore fluid (not the Darcy velocity), λ is the is the decay constant of the dissolved radionuclide, and Φ is the dispersive flux defined in Eq. (A-4) in a form similar to Fick's law of diffusion,

$$\Phi = -\phi_p D_{isp} \frac{dC}{dz} \tag{A-4}$$

where the hydrodynamic dispersion coefficient is expressed as [82], [261]

$$D_{isp} = \alpha_{disp} v + D_p \tag{A-5}$$

where D_p is the diffusion coefficient in the plug, and α_{disp} is the dispersivity. For a porous matrix composed of particles, the dispersion coefficient can be approximated Eq. (A-6) [89], [288],

$$\alpha_{disp} \sim 1.8 d_{cp} \tag{A-6}$$

where d_{cp} is a characteristic particle diameter. Dividing all terms by Δz, ΔC, Δt, $\phi_p, \pi r_p^2$, taking the limit as each discrete quantity goes to zero, and substituting Eq. (A-1), and Eq. (A-2), we obtain a differential form of the advection-dispersion equation,

$$\frac{dC}{dt} = -v\frac{dC}{dz} + D_{isp}\frac{d^2C}{dz^2} - \frac{2q_r}{\phi_p r_p} - \lambda C\left(1 + K_p\frac{\rho_p}{\phi_p}\right) - K_p\frac{\rho_p}{\phi_p}\frac{dC}{dt} \tag{A-7}$$

Collecting terms,

$$\frac{dC}{dt}\left(1 + K_p\frac{\rho_p}{\phi_p}\right) = -v\frac{dC}{dz} + D_{isp}\frac{d^2C}{dz^2} - \frac{2q_r}{\phi_p r_p} - \lambda C\left(1 + K_p\frac{\rho_p}{\phi_p}\right) \tag{A-8}$$

Substituting the definition for the retardation coefficient of the plug (R_p),

$$R_p = 1 + K_p\frac{\rho_p}{\phi_p} \tag{A-9}$$

we obtain the final equation for transport in the plug, shown in Eq. (A-10),

$$\frac{dC}{dt} = -\frac{v}{R_p}\frac{\partial C}{\partial z} + \frac{D_{isp}}{R_p}\frac{d^2C}{dz^2} - \frac{2q_r}{R_p\phi_p r_p} - \lambda C \qquad \text{(A-10)}$$

The radial diffusive flux (q_r) into the adjacent matrix containing concentration C_m (which is by assumption, a function of radius) is defined by Fick's first law in Eq. (A-11),

$$q_r = -\phi_m D_m \frac{dC_m}{dr}\bigg|_{r=r_p} \qquad \text{(A-11)}$$

where D_m is the diffusion coefficient in the matrix, and C_m is the concentration in the matrix. Note that if dispersion and radioactive decay are neglected, the problem reverts to the one presented in Cihan and Tyner and Eq. (A-10) matches Equation 1 of [280].

A.3 Radial diffusion in the rock matrix

To obtain the gradient that determines this flux term, we use the governing equations for transport in the matrix. This can be derived in an analogous manner and is similar to the equations for the plug. However, transport in the matrix does not include advection (a realistic assumption considering that the velocities due to thermal expansion in the caprock are small), and diffusion is assumed to occur only in the radial direction. Thus we have Eq. (A-12),

$$\frac{\partial C_m}{\partial t} = \frac{D_m}{R_m}\nabla^2 C_m - \lambda C_m = \frac{D_m}{R_m}\left(\frac{1}{r}\right)\frac{d}{dr}\left(r\frac{dC_m}{dr}\right) - \lambda C_m \qquad \text{(A-12)}$$

where R_m is the retardation factor of the matrix (i.e., granite). This assumes that the surrounding matrix is uniform in properties with space and neglects axial diffusion in the z direction. The gradient at the interface is obtainable by differentiating the solution of Eq. (A-12). While the problem is of course transient in nature, Tang et. al. [261] show that the steady state solution gives a convenient, conservative, and upper limit for the penetration distance and concentration of the solute. With a steady state problem, we obtain a second order ODE that can be solved rapidly, assuming the following boundary and initial conditions,

$$C_m(r_p, z, t) = C(z, t) \tag{A-13}$$

$$C_m(\infty, z, t) = 0 \tag{A-14}$$

$$C_m(r, z, 0) = 0 \tag{A-15}$$

$$C(0, t) = C_0 \tag{A-16}$$

Equation (A-13) represents the continuity of concentration at the boundary between the plug and matrix. Substituting the steady state condition we obtain Eq. (A-17),

$$\frac{D_m}{R_m} \left(\frac{1}{r}\right) \frac{d}{dr} \left(r \frac{dC_m}{dr}\right) - \lambda C_m = 0 \tag{A-17}$$

Define a decay length constant of the matrix (λ_m) given by Eq. (A-18),

$$\lambda_m = \left(\frac{\lambda R_m}{D_m}\right)^{0.5} \tag{A-18}$$

which is a decay length scale (m^{-1}) that encompasses sorption, diffusion and decay losses in the matrix. Substituting this into an expanded form (i.e., using the chain rule) of Eq. (A-17),

$$r \frac{d^2 C_m}{dr} + \frac{dC_m}{dr} - \lambda_m^2 C_m r = 0 \tag{A-19}$$

This is Bessel's modified equation of order zero[289], which has the general solution that is a linear combination of the modified Bessel equations of the first kind of zero order (i.e., I_0) and the second kind of zero order (i.e., K_0), as shown in Eq. (A-20),

$$C_m = A I_0(\lambda_m r) + B K_0(\lambda_m r) \tag{A-20}$$

Where A and B are arbitrary constants determined using the boundary conditions (B.C). To satisfy the B.C. of Eq. (A-14), the first constant (A) must be zero because I_0 diverges as r increases. The second constant (B) may be determined using the interface condition of Eq. (A-13),

$$C_m(r = r_p) = C = B K_0(\lambda_m r_p) \tag{A-21}$$

Therefore, the final solution (for the matrix region where $r > r_p$) is written as Eq. (A-22),

$$C_m(r, z) = C(z) \frac{K_0(\lambda_m r)}{K_0(\lambda_m r_p)} \qquad (A\text{-}22)$$

Evaluating the derivative with respect to r (using properties of the modified Bessel functions) gives Eq. (A-23),

$$\frac{dC_m}{dr} = C(z) \frac{-\lambda_m K_1(\lambda_m r)}{K_0(\lambda_m r_p)} \qquad (A\text{-}23)$$

where K_1 is the modified Bessel function of the first order. Evaluating the derivative at the interface with the plug (r_p), gives Eq. (A-24),

$$\left. \frac{dC_m}{dr} \right|_{r=r_p} = -\lambda_m \frac{K_1(\lambda_m r_p)}{K_0(\lambda_m r_p)} C(z) \qquad (A\text{-}24)$$

A number of analytical approximations could be used for the modified Bessel function quotient; however, none are accurate over the extremely large range of λ_m and r_p that exist for various radionuclides, diffusion coefficients and fracture sizes. For compactness, we define a function which is the quotient of the first divided by the zeroth order modified Bessel functions of the second kind,

$$K_{1/0}(\lambda_m r_p) = \frac{K_1(\lambda_m r_p)}{K_0(\lambda_m r_p)} \qquad (A\text{-}25)$$

Inserting flux at the interface determined using Eq. (A-21) into Eq. (A-10), we obtain Eq. (A-26), the time dependent transport equation for the concentration in the fracture (again, assuming that the surrounding rock is at a saturated, steady state),

$$\frac{dC}{dt} = -\frac{v}{R_p} \frac{\partial C}{\partial z} + \frac{D_{isp}}{R_p} \frac{d^2 C}{dz^2} - \left(\frac{2\phi_m D_m}{R_p \phi_p r_p} \right) \lambda_m K_{1/0}(\lambda_m r_p) C - \lambda C \qquad (A\text{-}26)$$

Solving for the steady state solution of C by setting the $dC/dt=0$ gives Eq. (A-27),

$$0 = \frac{dC}{dt} = -\frac{v}{R_p}\frac{\partial C}{\partial z} + \frac{D_{isp}}{R_p}\frac{d^2C}{dz^2} - \left(\frac{2\phi_m D_m}{R_p \phi_p r_p}\right)\lambda_m K_{1/0}(\lambda_m r_p)C - \lambda C \tag{A-27}$$

Multiplying through by R_p yields a term that may be called λ_p, shown in (A-28),

$$\lambda_p = \lambda R_p \tag{A-28}$$

which is a more compact, radionuclide specific decay time scale describing the effects of sorption and radioactive decay in the plug. Inserting this and grouping terms,

$$0 = \frac{dC}{dt} = D_{isp}\frac{d^2C}{dz^2} - v\frac{\partial C}{\partial z} - \left(\frac{2\phi_m D_m \lambda_m}{\phi_p r_p} K_{1/0}(\lambda_m r_p) + \lambda_p\right)C \tag{A-29}$$

$$0 = \frac{d^2C}{dz^2} - \frac{v}{D_{isp}}\frac{dC}{dz} - \frac{\psi}{D_{isp}}C \tag{A-30}$$

where ψ is defined as,

$$\psi = \frac{2\phi_m D_m \lambda_m}{\phi_p r_p} K_{1/0}(\lambda_m r_p) + \lambda_p \tag{A-31}$$

Guessing a steady state solution of the form $C(z) = Ae^{-\lambda_z z} + Be^{\lambda_z z}$, we obtain an equation that can be solved as a quadratic equation,

$$0 = \left(\lambda_z^2 - \frac{v}{D_{isp}}\lambda_z - \frac{\psi}{D_{isp}}\right)C \tag{A-32}$$

$$\lambda_z = \frac{v}{2D_{isp}} \pm \sqrt{\left(\frac{v}{2D_{isp}}\right)^2 + \frac{\psi}{D_{isp}}} \tag{A-33}$$

To obtain a finite solution as z tends to infinity, we select the only root that may be negative,

$$\lambda_z = \frac{v}{2D_{isp}} - \sqrt{\left(\frac{v}{2D_{isp}}\right)^2 + \frac{\psi}{D_{isp}}} \tag{A-34}$$

Applying the boundary condition of Eq. (A-16) (the constant concentration of radionuclides in the disposal zone), we obtain the final solution for the radionuclide concentration along the plug as shown in Eq. (A-35),

$$C(z) = C_0 e^{\left(\frac{v}{2D_{isp}} - \left(\left(\frac{v}{2D_{isp}}\right)^2 + \frac{\psi}{D_{isp}}\right)^{0.5}\right)z} = C_0 e^{\lambda_z z} \tag{A-35}$$

With the axial concentration profile along the plug, we also have the two dimensional distribution for radionuclide concentration in the surrounding rock matrix, shown as Eq. (A-36),

$$C_m(r,z) = C_0 \left(e^{\lambda_z z}\right) \frac{K_0(\lambda_m r)}{K_0(\lambda_m r_p)} \tag{A-36}$$

Note that Eq. (A-35) is very similar to the steady state solution presented as Tang et. al. Eq. (50) on pg. 561 [261]; however, note that there is an error because the solution's units are incorrect (the velocity must be divided by a diffusivity (or dispersion coefficient) with units of (m^2/s) so that the argument of the exponent remains unitless. For comparison and clarity, the correct expression for Tang et. al's Eq. (50), the steady state concentration for flow within a planar fracture, should be written as Eq. (A-37),

$$C(z) = C_0 e^{\left(\frac{v}{2D_{isp}} - \left(\left(\frac{v}{2D_{isp}}\right)^2 + \frac{\psi_p}{D_{isp}}\right)^{0.5}\right)z} = C_0 e^{\lambda_{z,p} z} \tag{A-37}$$

where all other variables are identical to the solution in in Eq. (A-35) except for ψ_p and $\lambda_{z,p}$ which corresponds to a "planar" (as opposed to cylindrical) case. The major difference in the definition of ψ occurs primarily due to shape effects resulting from the cylindrical geometry and the use of a water filled fracture (e.g., porosity =1) rather than a permeable fault/plug (which alters the dispersion coefficient (D_{isp}). For the planar geometry, ψ_p is defined as Eq. (A-38),

$$\psi_p = \lambda + \frac{\phi_m (D_m \lambda)^{0.5}}{b} \tag{A-38}$$

where b is the size of the planar fracture (and all other parameters are the same as before).

The cylindrical geometry and modified Bessel functions introduce a $\sim 1/\sqrt{r}$ dependence to the matrix concentration as the concentration is evaluated further away from the plug.

The term λ_z is a single term that allows for quick comparison of the importance of all of the phenomena that it encompasses (advection, dispersion, diffusion, sorption, radioactive decay, rock porosities, plug geometry) along the axis of the plug. As with any exponential solution, we may calculate the "halving distance" with the simple equation,

$$C(z) = \frac{0.693}{\lambda_z} \qquad \text{(A-39)}$$

Thus, we see that maximizing ψ (and thus λ_z) is beneficial to reducing the penetration distance of the radionuclides, which we write in its entirety here as Eq. (A-40),

$$\psi = \frac{2\phi_m (\lambda R_m D_m)^{0.5}}{\phi_p r_p} K_{1/0}\left(\left(\frac{\lambda R_m}{D_m}\right)^{0.5} r_p\right) + \lambda R_p \qquad \text{(A-40)}$$

A.4 Advection time delay (breakthrough time) to reach transient or steady state solutions

Although the steady state solution may provide the most conservative estimate for the travel distance of radionuclides, it is important to estimate the time scale on which this solution begins to be valid. At a minimum, a conservative tracer must traverse the relevant distance (e.g., length of the plug) before any measurable concentrations would be apparent at the surface. Thus, the concentration of radionuclides at the surface is zero until a traversing (breakthrough) time has passed, given by the advection time delay[137], or breakthrough time, given in Eq. (A-41),

$$\tau_B = \frac{LR_i}{v_a} \qquad \text{(A-41)}$$

Where R_i is the retardation factor of the particular radionuclide and medium being considered (minimum value of 1). In theory the length scale will be dependent on the distance to the nearest aquifer. For example, in the case of the UPH-3 borehole the Mt. Simon saline aquifer is located at a depth of 600 meters. Thus, the granite between this aquifer and the disposal zone effectively provides the time delay and traversing distance for the radionuclides. For a target isolation time

of 1 million years, and traversing distances of 500, 1000, 1500 and 2000 m, the vertical velocity is shown in Table A-2.

Table A-2. Maximum velocity allowed to achieve 1mY advection time delay with no sorption (R=1)

Traversing distance (m)	Maximum advection velocity (m/s)
500	2.2×10^{-11}
1000	4.39×10^{-11}
1500	6.59×10^{-11}
2000	8.78×10^{-11}

Appendix B. Lumped Parameter Model of Advection Transport Rates in DBD

B.1. Introduction

In order for the equation from Appendix A to be used, the velocity that results from thermal effects created by the waste must be evaluated. At first impression, this appears to be a complicated coupled heat and mass transport problem. However, by examining the boundary conditions and understanding the relative time scales of transport for each, it is possible to create a simple model that can be treated entirely analytically.

"Quick" methods for evaluating the response of geologic formations to fluid injections (e.g., CO_2 sequestration) have been developed [88] and we start by referencing aspects of their approach. The basic principle is that the thermal addition created by the waste causes a fluid expansion that must be accommodated through either storage (through compression) or leakage. Zhou and Birkholzer identify three primary methods by which a deep geologic system accommodates volume injection (or in our case, fluid expansion),

1. Within the pore volume of the disposal zone (through pressurization and compression of the fluid and rock).
2. Within the pore volume of the cap-rock seals (also through pressurization).
3. Through fluid flow into the overlying and underlying formations.

A useful first step to understanding these mechanisms is to consider the various possible boundary conditions of the system, as shown in Figure B-1.
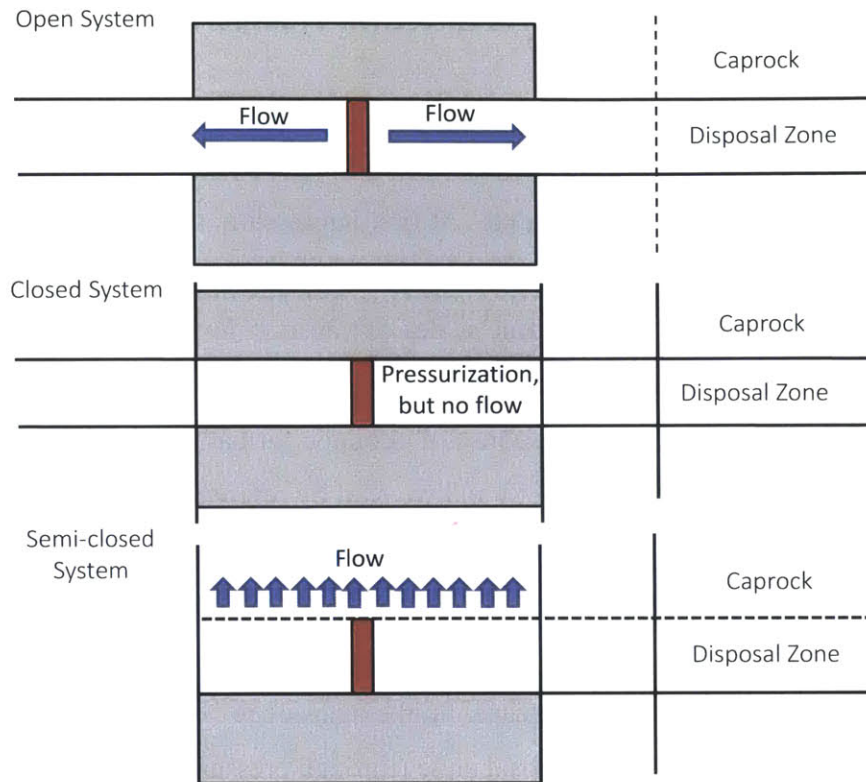
Figure B-1. Schematic comparison of open, closed, and semi-open systems experiencing fluid injection.

As is apparent in Figure B-1, the top two systems intuitively provide the lowest vertical velocities and superior confinement of fluids from the biosphere. In an open system (where the disposal zone has a large radial extent to any closed boundary) and the fluid is free to expand in radial directions, the pressurization will be much smaller compared to a closed system, and the vertical fluid transport will be small. In a closed system, the fluid expansion can only be accommodated by an increase in pressure in the disposal zone (resulting in compression and thus density reduction)[88]. Lastly, the semi-closed system appears to be the most conservative, with all or most fluid expansion being accommodated by vertical flow towards the surface.

B.2. Pore compressibility as a storage mechanism

The pressure increase with time ($\Delta P(t)$) in a completely closed system (where all fluid injection must be compensated by compression) can be modeled with Eq. (B-1)[88],

$$V_{inj}(t) = V_{pore}(\beta_w + \beta_r)\Delta P(t) \qquad\qquad (B\text{-}1)$$

where V_{inj} is the volume of fluid injected (via thermal expansion or actual injection), V_{pore} is the volume of pressurized pore space, and β_w and β_p are the water and pore compressibility. Note that the pore volume is assumed to be entirely interconnected and filled with transportable liquid (we neglect the presence of occluded pore fluids). Closed systems in porous rocks only accommodate fluid expansion to the point at which the pressure increase becomes unsustainable (e.g., due to geomechanical effects). If Townend and Zoback's previously discussed observations on the critical state of stress in basement rocks are correct [85], the critical pressure is relatively small (on the order of ~1 bar). Thus, we use Eq. (B-1) to estimate the maximum pore volume that is made available due to compression effects (mechanism 1) in a closed system,

$$V_{inj,max} = V_{pore}(\beta_w + \beta_r)\Delta P \qquad\qquad (B\text{-}2)$$

where the total pore volume of the disposal zone and overlying plug zone (V_{pore})

$$V_{pore} = A_{DBD}(L_d + 0.5L_p)(\phi_m) \qquad\qquad (B\text{-}3)$$

where A_{DBD} is the total area of a borehole disposal facility in a closed system (e.g., 200 × 200 m for a square borehole spacing of 200 meters), L_p is the plug length (~3000 meters), and L_d is the length of the disposal zone (e.g., 2000 meters). Assuming the water and granite pore compressibility from [25], the maximum acceptable pressure increase of 1 bar= 10^5 Pa, and a granite matrix porosity of 0.01, we evaluate the total pore volume made available due to pressure increase and compression of fluid,

$$V_{inj,max} = (200m)^2(3500m)(0.01)[(3.4 + 7.42) \times 10^{-10}Pa^{-1}](10^5 Pa) \qquad (B\text{-}4)$$
$$= 151.48\ m^3$$

Compared to the total volume of fluid injected via thermal expansion on a long time scale (>10,000 yrs) (quantified in the following section), this is not a significant volume of fluid that can be accommodated via compression effects. In addition, in a realistic formation (where the

system is not closed), the pore pressure increase cannot be sustained for very long (<100 yrs) as fluid eventually leaks and flows to relieve the pressure. This is consistent with the general observations made in CO_2 sequestration simulations, as shown in Figure B-2.
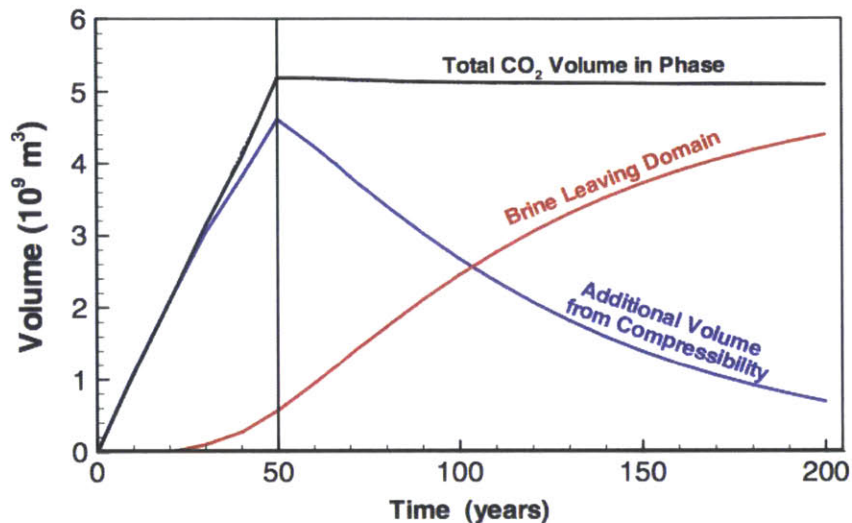
Figure B-2. Relative importance of various pore volume effects for CO_2 injection into deep brine formations. [5]

The vast difference in available pore volume shown in Figure B-2 for the CO_2 case ($\sim 10^9$ m^3) vs. borehole disposal (10^2 m^3) results from:

1. The assumption that that CO_2 sites have extremely large radial boundaries (~ 100 km), as opposed to (0.2) km for boreholes assumed in this case. The relatively small borehole spacing is chosen on the basis of conservatism (but borehole spacing smaller than 200 m is ruled out because it results in a second peak in temperature [98]).

2. The assumption that the sandstone formation may sustain pore overpressures up to 6×10^6 Pa, as opposed to 10^5 Pa typically stated for granitic rock.

3. Higher porosity of geologic formation 0.15 vs. 0.01 for Precambrian basement rock.

Unless significantly larger (or lower permeability) domains are assumed for deep borehole disposal, pore compressibility may be (conservatively) ruled out as a significant storage mechanism for fluid expansion in deep borehole disposal. Even if larger domains are assumed, the pore compression effect is short lived compared to the time scales important to geologic

disposal. Eventually, all of the fluid expansion will be accommodated by leakage and flow- pore compression only serves to delay the transport of fluid.

B.3. Evaluation of leakage rate due to thermal expansion in a semi-closed system with spatially uniform properties

Based on the results of the previous section we focus our model on the semi-closed system: the most conservative case in which all fluid volume increases are (instantaneously) accommodated by leakage. For a given volume of leakage that must be accommodated, the vertical flux and velocity is maximized by assuming a radially (laterally) limited and closed domain surrounding a single borehole. We begin here by summarizing the simplifying and conservative assumptions necessary for this model:

A. An infinite array of boreholes is effectively modeled by having a radially small domain with reflective, mirror, or closed boundaries at the edge surfaces (at which the orthogonal heat and mass flux and temperature and pressure derivatives with respect to r are all zero).

B. The homogenous borehole field has an area A_{DBD} determined by the specified borehole spacing (e.g., conservatively, a 200 m spacing resulting in a total area of $(200 \text{ m})^2$. The length is determined by the length of the heated disposal zone (L_{disp}).

C. Due to the high hydraulic diffusivity (~0.1 m^2/s) of the host rock and small radial distance to the boundary (where $dP/dr=0$), the radial pressure gradients are assumed to be uniform and close to zero. For a boundary at 200 meters, this assumption requires less than 0.1 years to be valid. As a result, we primarily consider the axial (z) variation in pressure and thus flow.

D. The disposal zone rock matrix has an interconnected porosity of ϕ_m, all of which is fluid filled. Pore compressibility effects are negligible on long time scales and porosity change is not accounted for in response to pressure increases.

E. All thermal energy released by the nuclear waste is absorbed (i.e., conducted) into a homogenous, insulated body of surrounding host rock with saturated density and heat capacity $(\rho c_p)_m$, previously described to be 2750 kg/m^3 and 790 J/kg-K, respectively. In reality, the actual energy absorbed by the rock is less than this (there will be small energy

losses to the surface after a long time period during which the thermal pulse travels vertically).

F. The native porewater has a volumetric thermal expansion coefficient $\beta_{w,th}$ ($1/\rho\,(\partial\rho/\partial T)$).

G. Thermomechanical effects in the rock are neglected and thermal expansion of the rock is assumed to have no effect on porosity.

H. The above parameters are assumed to be constant over the relevant range of pressure and temperature conditions.

We begin the derivation of this model by implementing an analytical correlation for the decay heat produced by the fuel, which is the same as has been used for MIT BVR runs and other thermal models[98],

$$q'''(t) = 2176\left(\frac{t_c}{t_c + t}\right)^{0.75} \tag{B-5}$$

where t_c is a cooling period (25 years), t is time after emplacement in years, and 2176 is the volumetric heat generation rate (W/m^3) of the used fuel having a burnup of 60 MWd/kg at t=0. Note the expression must be modified as follows, to allow for evaluation of cooling periods other than 25 years,

$$q'''(t) = 2176\left(\frac{25}{t_c + t}\right)^{0.75} \tag{B-6}$$

For other burnups, the decay heat approximately scales by $B_d/60$. Evaluating the total heat generation rate of the disposal zone,

$$\dot{Q}(t)[W] = V_{disp}(q'''(t)) = \pi r^2 L_{disp} 2176\left(\frac{25}{t_c + t}\right)^{0.75} \tag{B-7}$$

The temperature rise of a given volume of rock matrix (V_m) subject to a heat input rate of $\dot{Q}(t)$ is given by Eq. (B-8),

$$\Delta T(t) = \frac{\int_0^t \dot{Q}(t)\, dt}{\left(\rho c_p\right)_m V_m} \tag{B-8}$$

where the integrated or cumulative decay heat (the total thermal energy produced) $Q(t)$ can be evaluated using Eq. (B-11),

$$Q(t) = \int_0^t \dot{Q}(t)\, dt = V_{disp}(2176)(7.89 \times 10^8)^{0.75} \int_0^t \left(\frac{1}{t_c + t}\right)^{0.75} dt$$

$$= V_{disp}4.095 \times 10^{10}[(t + t_c)^{0.25} - (t_c)^{0.25}] \tag{B-9}$$

where t is now in seconds, rather than years. Note that the cooling period has a relatively weak influence on the total decay heat produced. As the time horizon for performance is increased to 1 million years, the cooling period has a smaller and smaller effect on the total heat produced. Using the definition of the coefficient of thermal expansion, the density change of the water can be calculated using Eq. (B-10),

$$-\Delta \rho = \Delta T \beta_{w,th}\rho_{ref} = \Delta T \left(\frac{1}{\rho_{ref}}\frac{\partial \rho}{\partial T}\right)\rho_{ref} \tag{B-10}$$

The density change is related to the volume change of the water by taking the derivative of the definition of density ($\rho = M/V$),

$$\frac{\partial \rho}{\partial V} = -\frac{M}{V_w}\left(\frac{1}{V_w}\right) = -\frac{\rho_{ref}}{V_w} \tag{B-11}$$

The volume change of the water is then calculated from the temperature change of the rock (and thus water) using Eq. (B-12),

$$\Delta V_w = \Delta \rho \frac{\partial V}{\partial \rho} = \frac{\Delta T \beta_{w,th}\rho_{ref}}{\frac{\rho_{ref}}{V_w}} = \Delta T \beta_{w,th}V_f \tag{B-12}$$

Inserting (B-8) into Eq. (B-12) and the definition of rock porosity ($V_f = \phi_m V_m$), we obtain the total water volume expansion (injection) as a function of time, as shown in Eq. (B-13),

$$V_{inj}(t) = \frac{\int_0^t \dot{Q}(t)\, dt}{\left(\rho c_p\right)_m V_m}\beta_{w,th}V_f = \frac{\int_0^t \dot{Q}(t)\, dt}{\left(\rho c_p\right)_m V_m}\beta_{w,th}(V_m\phi_m) = \left(\frac{\phi}{\rho c_p}\right)_m \beta_{w,th}Q(t) \tag{B-13}$$

Thus we see that the total fluid injection is independent of the spatial distribution of temperature increases for the rock. Equation (B-13) gives the cumulative volume injected (created by thermal expansion) with time. The rate of injection is obtained by differentiating Eq. (B-13) with respect to time,

$$\dot{V}_{inj}(t) = \left(\frac{\phi}{\rho c_p}\right)_m \beta_{w,th} \dot{Q}(t) \tag{B-14}$$

Since the pressure gradient is assumed to be uniform with radius, if the overlying rock is assumed to have radially uniform properties (specifically permeability) the vertical flux will also be radially uniform. In this simple case, the vertical Darcy flux is easily obtained from Eq. (B-14) which gives Eq. (B-15),

$$v_D(t) = \frac{\dot{V}_{inj}(t)}{A_{DBD}} = \frac{\beta_{w,th}}{A_{DBD}}\left(\frac{\phi}{\rho c_p}\right)_m \dot{Q}(t) \tag{B-15}$$

The actual or advection velocity is obtained by dividing the Darcy velocity (Eq. (B-15)) by porosity, as in Eq. (B-16),

$$v_a(t) = \frac{v_D}{A_{DBD}} = \frac{\beta_{w,th}}{A_{DBD}(\rho c_p)_m} \dot{Q}(t) \tag{B-16}$$

The advection velocity shown Equation (B-16) is independent of porosity because of two equal and opposite effects- as the porosity is increased the total volume of fluid that is injected increases (see Eq. (B-13)). At the same time, as the porosity is increased, the velocity of the fluid (for a given volumetric flow rate) is decreased proportionally. Thus in this special (homogenous) case, the two effects cancel and the advection velocity is independent of porosity. The total vertical distance traveled by the water is calculated by integrating the advection velocity, which can be written as,

$$z_a(t) = \frac{\beta_{w,th}}{A_{DBD}(\rho c_p)_m} Q(t) \tag{B-17}$$

Now that the equations have been developed, we insert some characteristic values to obtain estimates for the vertical escape velocity in this simplified scenario. The thermal expansion coefficient for water is plotted in Figure B-3.
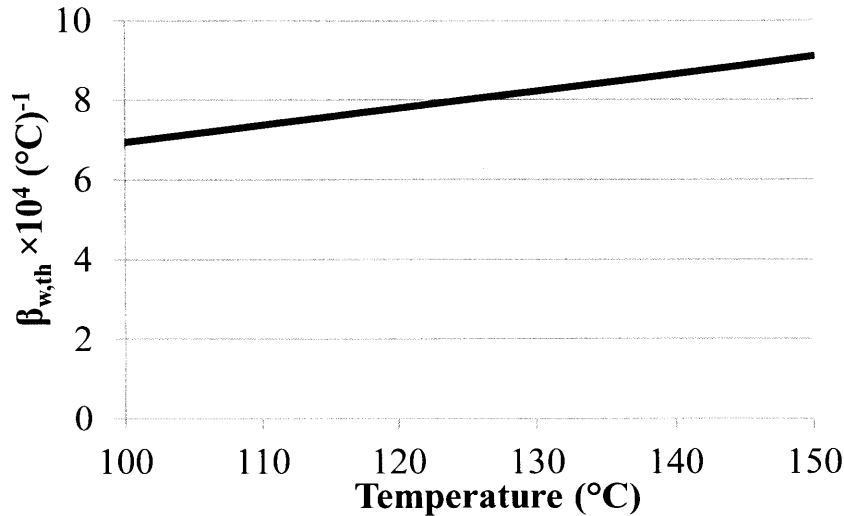
Figure B-3. Volumetric thermal expansion coefficient for water at 200 bar vs. temperature (evaluated from densities predicted by 1995 IAPWS formulation [290])

From Figure B-3, we see that the volumetric thermal expansion coefficient does not vary significantly over the temperature range that we are concerned with (it also does not have a strong dependence on the pressure). The average value over this temperature range is 8.42×10^{-4} $(°C)^{-1}$. Note that this is (conservatively) higher (by a factor of 3) compared to the volumetric thermal expansion coefficient of 2.8×10^{-4} $(°C)^{-1}$ developed by Kukkonen[114] for saline (NaCl) fluids between 0-100°C. Table B-1 summarizes the results of the equations presented thus far, for a homogeneous disposal zone.

Table B-1. Thermal energy and water volume expansion vs. time for a 2 km long disposal zone with 0.17 m hole radius in an infinite array of boreholes with spacing of 200 m.

	Disposal zone heat generation (W)	Cumulative thermal energy Q (J)	Cumulative water expansion V_{inj} (m³)	Water expansion rate $\dot{V}_{inj}$ (m³/s)	Darcy velocity v_D (m/s)	Advection velocity v_a (m/s)	Net Vertical Distance (m)
0	3.95×10^5	0	0	1.53×10^{-6}	3.83×10^{-11}	3.83×10^{-9}	0
10	3.07×10^5	1.09×10^{14}	424	1.19×10^{-6}	2.97×10^{-11}	2.97×10^{-9}	1.1
100	1.18×10^5	6.18×10^{14}	2390	4.58×10^{-7}	1.14×10^{-11}	1.14×10^{-9}	6.0
1,000	2.44×10^4	1.91×10^{15}	7390	9.44×10^{-8}	2.36×10^{-12}	2.36×10^{-10}	18.5
10,000	4410	4.33×10^{15}	1.678×10^4	1.71×10^{-8}	4.27×10^{-13}	4.27×10^{-11}	42.0
10^5	785	8.67×10^{15}	3.36×10^4	3.04×10^{-9}	7.60×10^{-14}	7.60×10^{-12}	83.9
10^6	140	1.64×10^{16}	6.35×10^4	5.41×10^{-10}	1.35×10^{-14}	1.35×10^{-12}	158.7

There are a few interesting conclusions from this analysis:

1. The total flow is proportional to the cumulative heat produced by the fuel.

2. Velocity is directly proportional to the total rate of heat production of the spent fuel.

3. Mass flow is not dependent on the spatial temperature distribution. This occurs because of the high hydraulic diffusivity of the rock which spreads out pressure spikes very rapidly (although the thermal diffusivity of the rock is ~5 orders of magnitude lower, which does result in significant spatial variations in temperature). It is also dependent on the assumption that the thermal expansion coefficient is constant with temperature.

4. Vertical transport time (determined by the advection velocity) is independent of both the porosity and permeability of the rock, (assuming the rock has radially uniform properties).

5. As long as the host rock (and plug) permeability are lower than $10^{-16}\,\text{m}^2$, the net vertical distance traveled by radionuclides will be insignificant (<200 meters). This is small compared to our reference design caprock thickness of at least 1 km.

6. Increasing the borehole spacing reduces the velocity by a squared factor.

B.4. Evaluation of leakage rate due to thermal expansion in a semi-closed system with a low permeability zone

In reality, the system will not have radially homogenous properties- for example if the plug and host rock have different properties. Plug design has been discussed in [137], where plug composition and properties were proposed. Although it was concluded to be technically feasible to achieve a plug permeability of 10^{-16} m^2 (approximately the same permeability as the host rock), it is important to evaluate failure scenarios and their consequences. Thus, the first logical step in adding heterogeneity to this model would be to assume that the plug has a significantly lower permeability than the host rock. A diagram of a failed plug within a homogenous host rock matrix is shown in Figure B-4.
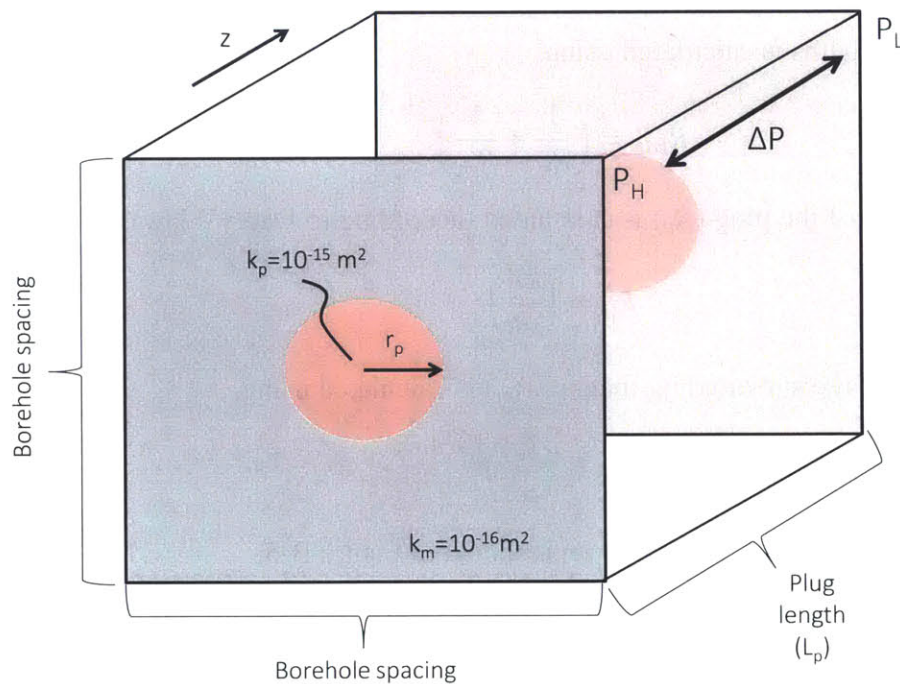
Figure B-4. Description of a failed plug scenario where the plug permeability is lower than the host rock permeability. The vertical direction (z) is indicated into the page.

In this simplified description, the plug zone spans what has been previously described as the caprock and overburden zones. The disposal zone elevates the pore water pressure at the top of the disposal zone to P_H, and the pressure is P_L at the surface which is the "ground" (in both the analogue to electric flow, and physical sense). Overall, if P_L is considered a zero potential point,

then P_H~ΔP, the potential that drives the flow through both the plug and the caprock. As a result of the assumption of high hydraulic diffusivity (and small radial gradients) in the caprock, the overpressure is uniform in the lateral/radial direction. Therefore, the relative ratio of flows between the two zones will balance such that the pressure drop is equal across the length of both zones (also similar to a parallel system of pipes subjected to a pressure difference). Neglecting variations in viscosity and compressibility, this can be treated as a resistance network described in the following series of equations,

$$I_{tot}\left(\frac{m^3}{s}\right) = \dot{V}_{inj}(t) = \frac{\Delta P}{R_{tot}}$$

(B-18)

Where I_{tot} is the analogous water current (flow rate) that is equal to $\dot{V}_{inj}(t)$. The total resistance of two parallel flow paths is calculated using,

$$R_{tot} = \left(\frac{1}{R_p} + \frac{1}{R_m}\right)^{-1}$$

(B-19)

where the resistance of the plug (R_p) is calculated (according to Darcy's law),

$$R_p = \left(\frac{kA}{\mu L}\right)_p^{-1}$$

(B-20)

and the resistance of the surrounding matrix (R_m) is calculated using,

$$R_m = \left(\frac{kA}{\mu L}\right)_m^{-1}$$

(B-21)

Schematically, this resistance analogy is represented in Figure B-5,

$$\dot{V}_{inj}(t) = I_{tot} = \frac{\Delta P(t)}{R_{tot}} = \frac{\Delta P(t)}{\left(R_p^{-1} + R_m^{-1}\right)^{-1}}$$
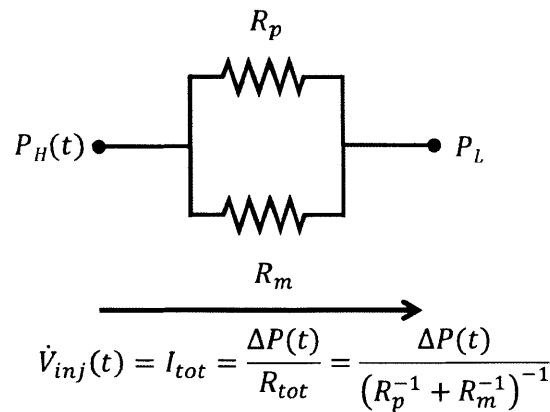
Figure B-5. Parallel resistance network representation of Darcy's law and vertical flow through the plug and matrix, subject to a given fluid injection rate.

The resulting time dependent overpressure $\Delta P(t)$ at the top of the disposal zone can be calculated by combining all equations from Eq. (B-18) to (B-21), resulting in Eq. (B-22),

$$\Delta P(t) = \dot{V}_{inj}(t)R_{tot} = \dot{V}_{inj}(t)\left(\left(\frac{kA}{\mu L}\right)_p + \left(\frac{kA}{\mu L}\right)_m\right)^{-1} \qquad \text{(B-22)}$$

If the plug is split into j portions with different permeabilities and lengths of δz_j, the total resistance of a series of resistors is the sum of the resistances of the j segments, which is represented by Eq. (B-23),

$$\left(\frac{kA}{\mu L}\right)_p = \frac{1}{\mu}\sum_1^j \left(\frac{kA}{\delta z}\right)_j \qquad \text{(B-23)}$$

The flow in each portion (plug or matrix), can be calculated by dividing the overpressure by the resistance of that flow path (i), as shown in Eq. (B-24),

$$I_i(t) = \Delta P(t)\left(\frac{kA}{\mu L}\right)_i \qquad \text{(B-24)}$$

The Darcy velocity is obtained by dividing the volumetric flow (or current) in Eq. (B-24) by the cross-sectional area of that rock path (A_i), which gives Eq. (B-25),

$$v_{D,i}(t) = \Delta P(t)\left(\frac{kA}{\mu L}\right)_i A_i^{-1} = \Delta P(t)\left(\frac{k}{\mu L}\right)_i \qquad \text{(B-25)}$$

Evaluating the Darcy velocity in the plug, the viscosity and length terms cancel, giving Eq. (B-26),

$$v_{D,p}(t) = \frac{\dot{V}_{inj}(t)\left(\frac{k}{\mu L}\right)_p}{\left(\left(\frac{kA}{\mu L}\right)_p + \left(\frac{kA}{\mu L}\right)_m\right)} = \dot{V}_{inj}(t)\left[\frac{k_p}{(kA)_p + (kA)_m}\right] \qquad \text{(B-26)}$$

The real or advection velocity in a region (i) is calculated by dividing Eq. (B-25) by the porosity ϕ, which gives Eq. (B-27),

$$v_{a,p}(t) = \dot{V}_{inj}(t)\left[\frac{k_p/\phi_p}{(kA)_p + (kA)_m}\right] \qquad \text{(B-27)}$$

The real or advection velocity in a region (i) can also be written in terms of the pressure drop created in the disposal zone, which gives Eq. (B-28),

$$v_{A,i}(t) = \Delta P(t) \left(\frac{k}{\mu L \phi} \right)_i \tag{B-28}$$

Assuming L_p=3000 meters, r_p=0.4 meters, k_p=10^{-15} m^2, k_m=10^{-16} m^2, a borehole spacing of 200 meters we obtain the a plug and matrix resistance of 1.193×10^{15} and 1.50002×10^{11} (Pa-s/m^3), respectively. Thus, the total resistance is 1.4998×10^{11}(Pa-s/m^3). Again, we stress that this assumes a rapid equilibration of radial pressure gradients. Plug lengths (or disposal depths) less than 3000 meters are discussed in the body of the thesis. Regardless of the length of the plug, from the analysis of resistances, it is apparent that the plug's permeability and area have a negligible effect on the total vertical flow and fluid overpressure. The plug permeability; however, still has a proportional effect on the advection distance within the plug. The advection distance is the integral of Eq. (B-28). Combining this with Eq. (B-13) which gave $V_{inj}(t)$, we obtain the expression for the advection distance vs. time in the plug, as shown in Eq. (B-29),

$$z_{A,p}(t) = \phi_p^{-1} \frac{R_{tot}}{R_p} \int_0^t \dot{V}_{inj}(t) dt = V_{inj}(t) \left[\frac{k_p}{(kA)_p + (kA)_m} \right] \phi_p^{-1} \tag{B-29}$$

This single expression couples and highlights the thermal behavior (encompassed by the V_{inj} term) and hydraulic behavior (encompassed by R_p/R_{tot}). Note that since the matrix resistance is the dominating term (i.e., $R_m \approx R_{tot}$) the advection distance in the surrounding matrix will be the same as previously estimated in Appendix A, Table B-2 summarizes the results of the equations presented thus far, for a time period of 1 million years.

Table B-2. Prediction of plug and matrix velocities within an inhomogeneous domain (k_p, k_m= $10^{-15}, 10^{-16}$ m^2). ϕ_m =0.01 as before, Plug porosity is left as a variable (ϕ_p)

Time	Total flow rate (m^3/s)	Overpressure (Pa)	Pressure gradient (Pa/m)	Matrix Darcy velocity $v_{D,m}$ (m/s)	Plug Darcy velocity $v_{D,p}$ (m/s)	$z_{A,m}$ (m)	$z_{A,p}$ (m)
0	1.53×10^{-7}	2.30×10^5	76.5	3.83×10^{-11}	3.83×10^{-10}	0	1
10	1.19×10^{-7}	1.78×10^5	59.4	2.97×10^{-11}	2.97×10^{-10}	1	11
100	4.58×10^{-8}	6.86×10^4	22.9	1.14×10^{-11}	1.14×10^{-10}	6	60
1,000	9.44×10^{-9}	1.42×10^4	4.72	2.36×10^{-12}	2.36×10^{-11}	18	185
10,000	1.71×10^{-9}	2560	0.854	4.27×10^{-13}	4.27×10^{-12}	42	420
10^5	3.04×10^{-10}	456	0.152	7.60×10^{-14}	7.60×10^{-13}	84	840
10^6	5.41×10^{-11}	81.1	2.71×10^{-2}	1.35×10^{-14}	1.35×10^{-13}	159	1,587

In this case, the plug porosity of 1% is quite low (the proposed plug design with sand and clay would have porosities approximately 10× higher than this, which would effectively make the vertical advection distance the same for both the plug and surrounding host rock. Note that the overpressure in this case is quite high (~2.3 bar). If the surrounding host rock permeability was even lower (10^{-18} m^2), the overpressure that drives this flow would be proportionally higher, probably resulting in excessively high pore pressures and geomechanical damage.

B.5. Calculation of penetration time in the plug

The time of plug penetration is an important parameter, as it determines the time and velocity at which contaminated fluids are first delivered to the receptor (presented in Appendix A). An analytical expression for the plug penetration time is also useful because it allows for rapid determination of the sensitivities of this important parameter to various inputs. The penetration time is obtained by setting the vertical penetration distance (which has just been derived as Eq. (B-29)) equal to the plug length (L_p ~2000-3000 meters), and solving for the time (τ_b). Thus we have,

$$z_{A,p}(\tau_b) = L_p = V_{inj}(\tau_b) \left[\frac{k_p}{(kA)_p + (kA)_m} \right] \phi_p^{-1} \tag{B-30}$$

Inserting the expression for $V_{inj}(t)$ from Eq. (B-13) at τ_b,

$$L_p = \frac{\phi_m}{\left(\rho c_p\right)_m \phi_p} \beta_{w,th} Q(\tau_b) \left[\frac{k_p}{(kA)_p + (kA)_m}\right] \qquad \text{(B-31)}$$

Inserting the cumulative heat production term $Q(\tau_b)$ from Eq. (B-9)

$$L_p = \frac{\phi_m}{\left(\rho c_p\right)_m \phi_p} \beta_{w,th} V_{disp} 4.10 \times 10^{10} \left[(\tau_b + t_c)^{0.25} - (t_c)^{0.25}\right] \left[\frac{k_p}{(kA)_p + (kA)_m}\right] \qquad \text{(B-32)}$$

Isolating the time terms,

$$\left(\frac{\rho c_p}{\phi}\right)_m \frac{\phi_p L_p}{\beta_{w,th} V_{disp} 4.10 \times 10^{10}} \left[\frac{(kA)_p + (kA)_m}{k_p}\right] + (t_c)^{0.25} = \left[(\tau_b + t_c)^{0.25}\right] \qquad \text{(B-33)}$$

Solving for the breakthrough time τ_b, we obtain Eq. (B-34),

$$\tau_b = \left(\left(\frac{\rho c_p}{\phi}\right)_m \frac{\phi_p L_p}{\beta_{w,th} V_{disp} 4.10 \times 10^{10}} \left[\frac{(kA)_p + (kA)_m}{k_p}\right] + (t_c)^{0.25}\right)^4 - t_c \qquad \text{(B-34)}$$

Note that if the plug permeability is within 4 orders of magnitude of the rock permeability, such that $(kA)_m \gg (kA)_p$ (which is expected) we may eliminate and group terms to simplify and approximate the final limiting case expression; as in Eq. (B-35),

$$\tau_b \sim \left(\left(\frac{\rho c_p kA}{\phi}\right)_m \left(\frac{L\phi}{k}\right)_p \frac{1}{\beta_{w,th} V_{disp} 4.095 \times 10^{10}} + (t_c)^{0.25}\right)^4 - t_c \qquad \text{(B-35)}$$

Although many of the variables are intuitive (e.g., high plug permeability decreases the breakthrough time) some of the others are not (e.g., a low matrix porosity, high specific heat, are beneficial). In addition, the origin of the fourth power dependence is not immediately apparent: it arises from the ¾ power dependence for the decay heat time variation.

Alternatively, the other bounding case occurs (which is not expected) when the plug permeability greatly exceeds the host rock $(kA)_p \gg (kA)_m$, it becomes the primary flow path (a

significant portion of injected volume is forced vertically through this single path). In this case, it is apparent that breakthrough time (and even velocity) in the plug are independent of permeability as shown in Eq.(B-36),

$$\tau_b = \left(\left(\frac{\rho c_p}{\phi} \right)_m \frac{(\phi AL)_p}{\beta_{w,th} V_{disp} 4.10 \times 10^{10}} + (t_c)^{0.25} \right)^4 - t_c = 0 \qquad \text{(B-36)}$$

In most cases then, the breakthrough time will clearly tend towards zero, as the left hand term is much smaller than the right hand term.

B.6. Evaluation of plug resistance with stochastic, axial variations in permeability

Note that the resistance analogy presented in section B.4 can be further refined by introducing axial variations in the plug (or even matrix) properties. This is particularly important given the sensitivity of the penetration time to the plug permeability and the inherent uncertainty and difficulty in predicting these values for man-made materials on geologic time scales. Schematically, the plug may be represented as a series of resistors with a total effective resistance as previously defined (R_p). Thus, the total resistance of the plug is the sum of all the resistances in series, calculated using Eq.(B-37),

$$R_p = \sum_{j=1}^{j=N} R_{p,j} = \left(\frac{k_j A}{L_j \mu} \right)_p^{-1} \qquad \text{(B-37)}$$

This is shown schematically for three resistive segments in series, of length (L_1, L_2, L_3) in Figure B-6.

$$R_{p,1} = \left(\frac{k_1 A}{L_1 \mu}\right)^{-1}_p \qquad R_{p,2} = \left(\frac{k_2 A}{L_2 \mu}\right)^{-1}_p \qquad R_{p,3} = \left(\frac{k_2 A}{L_2 \mu}\right)^{-1}_p$$

$$P_H(t) \bullet\!\!-\!\!\bigwedge\!\!\bigwedge\!\!\bigwedge\!\!-\!\!\bigwedge\!\!\bigwedge\!\!\bigwedge\!\!-\!\!\bigwedge\!\!\bigwedge\!\!\bigwedge\!\!-\!\!\bullet P_L$$

$$L_p = L_1 + L_2 + L_3$$

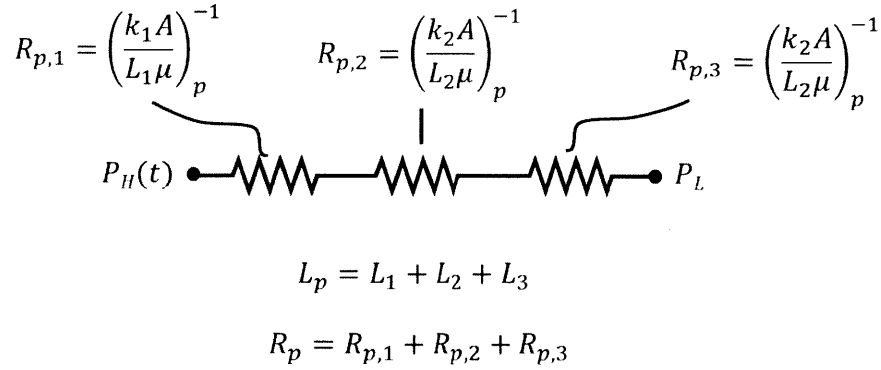$$R_p = R_{p,1} + R_{p,2} + R_{p,3}$$

Figure B-6. Hydraulic resistor analogy for an axially heterogeneous plug with three segments.

The solution for the total resistance can be simplified, since the area of the plug can be assumed to vary little compared to the other parameters,

$$R_p = \left[\left(\frac{\mu}{A}\right)\left(\frac{L_1}{k_1} + \frac{L_2}{k_2} + \frac{L_3}{k_3}\right)\right]_p \tag{B-38}$$

The effective resistance or permeability (k_{eff}) may be obtained from a length weighted average of the inverse of the permeability in each segment of the plug,

$$R_p = \left[\left(\frac{\mu}{A}\right)\left(\frac{L}{k_{eff}}\right)\right]_p \tag{B-39}$$

where the effective permeability k_{eff} is given in Eq. (B-40),

$$k_{eff} = L\left(\frac{L_1}{k_1} + \frac{L_2}{k_2} + \frac{L_3}{k_3}\right)^{-1} \tag{B-40}$$

It is now obvious that the segment(s) with the lowest permeability will dominate the effective permeability. In fact, if the permeability is higher by orders of magnitude in certain (failed) segment(s), then those portions will simply not contribute to the effective resistance. Thus, an instructive way to analyze plug permeability requirements is to calculate the length of intact segment with low resistance (representing the "successful" portion of the plug) necessary to

achieve the total or effective resistance. The effective plug permeability is related to the minimum permeability segment using Eq. (B-41),

$$k_{eff} = L \left(\frac{L_{min}}{k_{min}} \right)^{-1}$$

(B-41)

This example assumes that the remaining plug portion with length L-L_l has very high permeability and does not contribute to k_{eff}. Although 10^{-16} m^2 is an achievable goal for the deep borehole plug, values up to 10^{-14} m^2 are considered in this thesis. To give perspective on how difficult (or rather, easy) it is to achieve the conservative estimate of 10^{-14} m^2, the plug segment length and minimum permeability necessary to achieve an overall resistance equivalent to a plug with 10^{-14} m^2 (and length of 3000 meters) are shown in Table B-3.

Table B-3. Plug permeability and length required to achieve an effective permeability of 10^{-14} m^2 for a plug length of 3000 meters.

Permeability (k_l)	Intact length required (L_l)	Materials typically achieving this permeability
$\leq 10^{-18}$	≤ 30 cm	-Cement [291] or intact granite[41] (without cracks) -Natural shale [5] -Compacted bentonite[292] -50/50 mixtures of bentonite and sand (exposed to pure water) [293] -Bentonite/sepiolite mixtures exposed to brine[142].
10^{-17}	3 m	30/70 bentonite/sand mixtures exposed to water [294]
10^{-16}	30 m	Uncompacted bentonite exposed to brine [142].
10^{-15}	300 m	
10^{-14}	3000 m	Conservatively high estimate for permeability, assuming a poured bed of fine sand particles with diameter ~4.5 µm and porosity of 0.4.

Very short segments (30 cm to 30 meters) of various proposed plug materials achieve the desired k_{eff} of 10^{-14} m^2 over 3000 m. Only 30 m of what would already be considered a "failed" material (e.g., bentonite with a permeability increase due to brine exposure) is necessary. Thus, it is clearly unrealistic to assume that the plug would have an effective permeability significantly lower than 10^{-14} m^2 (although this has been done in previous sensitivity studies of deep boreholes [295]).

Given the very long length of the plug (>>100 meters), this analysis suggests that efforts or expenditures to achieve extremely low plug permeability will have rapidly diminishing benefits to the deep borehole confinement case. For other shallow repository designs with much shorter barrier lengths, such efforts may be required or justifiable. Note that the preceding analysis does not allow for cracks at the plug/host rock interface.

B.7. Probabilistic evaluation of plug resistance

It is also instructive to analyze the plug design goal using probabilistic or uncertainty analysis. Assuming the plug is made of three materials, each with presumably an independent probability distribution for permeability, we evaluate the effect of increasing the plug types on the mean and variance of the effective permeability. Assuming that each material's permeability (k_i in m^2) is described by a log-normal distribution as shown in Eqs. (B-42) and (B-43),

$$k_i = 10^{x_i} \hspace{3cm} \text{(B-42)}$$

where by definition,

$$Log(k_i) = x_i \hspace{3cm} \text{(B-43)}$$

and x_i are normally distributed random variables with mean μ_i and standard deviation of σ_i. In the simplest case, we assume that all three segments of the plug have the same length (1000 m) and normal distribution parameters ($\mu=-14$, $\sigma=.5$). Generating 10^5 random samples of x_1, x_2, x_3, (in MATLAB) the probability density for k_{eff} may be approximated by completing the calculation according to (B-42) and Eq. (B-44) and tallying the frequencies of results,

$$k_{eff} = 3000 \left(\frac{1000}{k_1} + \frac{1000}{k_2} + \frac{1000}{k_3}\right)^{-1} \hspace{2cm} \text{(B-44)}$$

The mean value and standard deviation of a lognormal distribution is not the same as the mean of the associated normal distribution used to create it. The results for statistical mean and standard deviation of x_1, x_2, x_3, k_1, k_2, k_3 and k_{eff} for 10^5 samples of each random variable are summarized in Table B-4.

Table B-4. Mean and standard deviation for 10^5 samples of x_1, x_2, and x_3 where $x_i(\mu, \sigma_i) = (-14, 0.5)$, producing corresponding probability distributions for k_1, k_2, k_3 and k_{eff}.

Random variable	Mean	Standard deviation
x_1	-13.999	0.4999
x_2	-13.9989	0.4989
x_3	-13.9978	0.5
k_1	1.943×10^{-14}	3.205×10^{-14}
k_2	1.937×10^{-14}	3.209×10^{-14}
k_3	1.950×10^{-14}	3.256×10^{-14}
k_{eff}	9.0317×10^{-15}	7.396×10^{-15}

The result for a normal distribution fitted to the histograms of k_1, k_2, k_3 and k_{eff} for the normal distribution means and standard deviations of -14 and 0.5, respectively, are shown in Figure B-7.
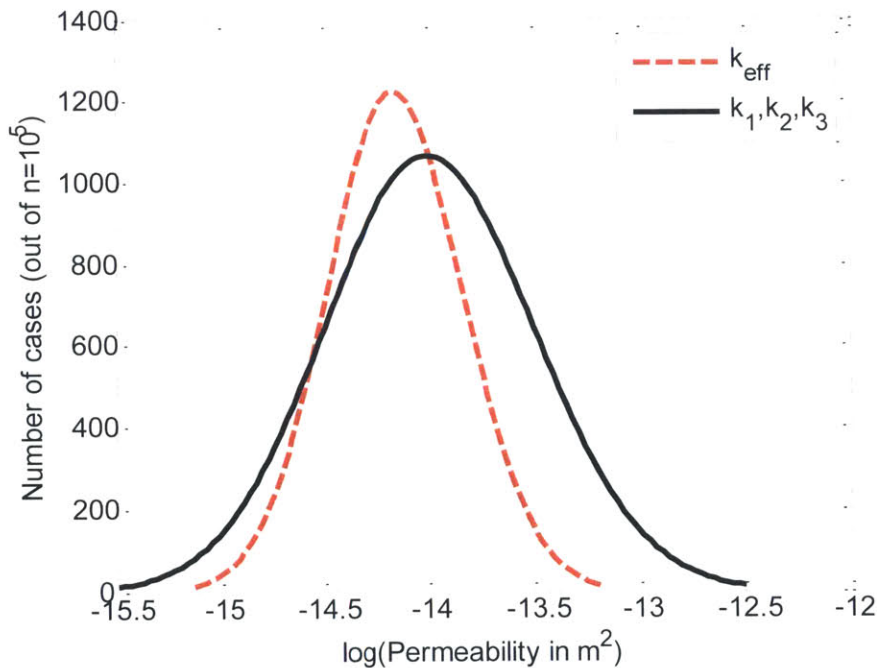

Figure B-7. Semi-log plot of permeability vs. # of cases for lognormal curve fits to the histograms of k_1, k_2, k_3 and k_{eff} generated by x_1, x_2, and x_3, where $x_i(\mu, \sigma_i) = (-14, 0.5)$.

In Figure B-7, the probability curves are not shown for k_2 and k_3 because they essentially overlap with k_1. The most important observation from these results is that k_{eff} of the plug has a both a smaller permeability and uncertainty compared to the three constituent components of the plug. Secondly, the probability distribution of k_{eff} also follows a lognormal distribution. Thus, this demonstrates that having three statistically independent materials (even with the exact same probability distribution for permeability) significantly decreases both the effective permeability (by a factor of ~2) and its associated standard deviation (by a factor of ~4).

273

As a second test case, the effect of increasing the uncertainty (standard deviation of the normal distributions) associated with the plug permeability is evaluated. For the sake of demonstrating this effect alone, the probability distributions for each portion of the plug are assumed to have the same mean, but higher standard deviation as compared to the previous case ($\mu=-14$, $\sigma=1$). In this case, to capture the larger variance, the number of samples is increased to 10^6. The results for statistical mean and standard deviation of x_1, x_2, x_3, k_1, k_2, k_3 and k_{eff} are shown in Table B-5 and Figure B-8.

Table B-5. Mean and standard deviation for 10^6 samples of x_1, x_2, and x_3 where $x_i(\mu, \sigma_i) = (-14, 0.5)$, producing corresponding probability distributions for k_1, k_2, k_3, k_{eff}.

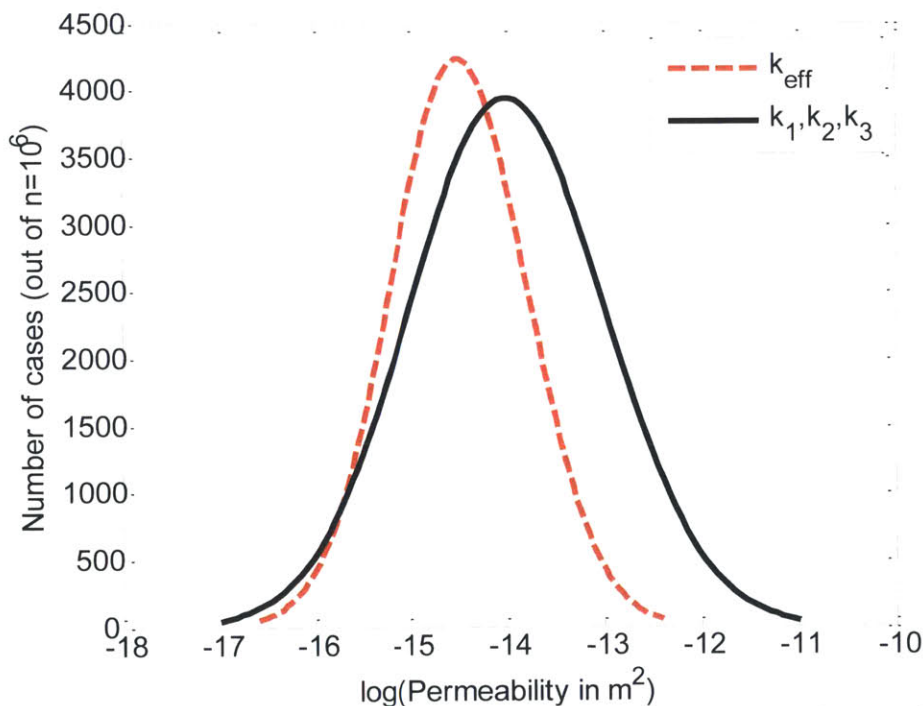| Random variable	Mean	Standard deviation
x_1	-14.001	0.999
x_2	-13.995	1.001
x_3	-14.000	0.9997
k_1	1.3949×10^{-13}	1.3721×10^{-12}
k_2	1.4112×10^{-13}	1.520×10^{-12}
k_3	1.4438×10^{-13}	1.979×10^{-12}
k_{eff}	1.0424×10^{-14}	2.798×10^{-14}

Figure B-8. Semi-log plot of permeability (k) vs. # of cases for lognormal curve fits to the histograms of k_1, k_2, k_3, and k_{eff} generated by x_1, x_2, and x_3, where $x_i(\mu, \sigma_i) = (-14, 1)$.

Although the standard deviation (i.e., spread) for the constituent plug permeabilities (k_1, k_2, k_3) has increased by a factor of 200 from the previous case, the standard deviation for k_{eff} has only increased by a factor of ~4. Again, the effective permeability is lower than the constituent mean permeabilities of the plug (by a factor of 14). This shows that the mean effective permeability is not very sensitive to the variability and uncertainty associated with the constituent materials.

In a final example, uncertainty parameters that may be characteristic of real plug materials are evaluated. Table B-6 presents a summary of reasonable modeling assumptions for the mean and standard deviation of three previously discussed and potential plug materials.

Table B-6. Mean and standard deviation for three different plug materials (sand, clay and concrete) with permeability determined by random distributions $x_1, x_2,$ and x_3.

Plug material	Length	Normal random variable	Mean	Standard deviation
Sand	L_1=1000 m	x_1	-14	0.5
Clay	L_2=1000 m	x_2	-16	1
Concrete	L_3=1000 m	x_3	-18	3

Here, sand is assumed to have the least variance (due to its plasticity, the fact that hydraulic resistance is created via simple phenomena (small and tortuous flow paths) which are relatively unaffected by fluid chemistry. Clay is modeled with a lower mean permeability, but higher variance due to the possibility of chemical interactions (e.g., salinity) that could increase permeability. Lastly, concrete or cements are modeled to have the lowest mean permeability (i.e., with respect to the normal variable x_3) due to the fact that concrete permeability measurements typically are extremely low. However, the possibility of fracturing and shrinking which can increase permeability by orders of magnitude [137] warrants the use of a higher standard deviation for concrete. Lognormal distributions are such that the long tails dictate the behavior of the mean, so higher standard deviations in the normal distributions used to create them result in a greater lognormal mean value. Table B-7 and Figure B-9 present the results of 10^7 simulations (increased because of the higher variability) for the statistical distributions presented in Table B-6.

Table B-7. Mean and standard deviation results from 10^7 samples of $x_1, x_2,$ and x_3 representing sand, clay and concrete, respectively, producing corresponding probability distributions for k_1, k_2, k_3 and k_{eff}.

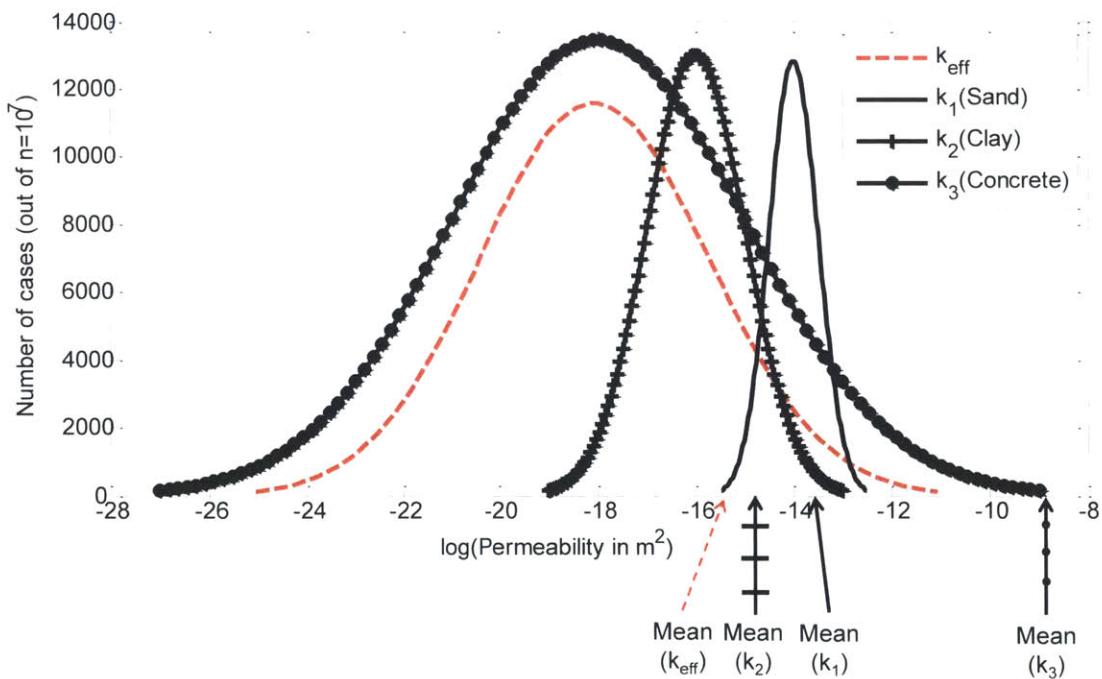|	Variable type	Random variable	Mean	Standard deviation	% k< 10^{-14}m^2
Sand	Normal	x_1	-14.0000	0.5000	
Clay	Normal	x_2	-16.0010	0.9999	
Concrete	Normal	x_3	-18.0019	3.0000	
Sand	Lognormal	k_1	1.9404×10^{-14}	3.2277×10^{-14}	50.00%
Clay	Lognormal	k_2	1.405×10^{-15}	1.6925×10^{-14}	97.77%
Concrete	Lognormal	k_3	1.020×10^{-9}	1.8068×10^{-6}	90.88%
Effective value for whole plug	Lognormal	k_{eff}	2.486×10^{-16}	1.4894×10^{-15}	99.68%

Figure B-9. Semi-log plot of permeability (k) vs. # of cases (out of 10^7) for normal density function fits to the histograms of log(k_1, k_2, k_3) and log(k_{eff}) generated by $x_1, x_2,$ and $x_3,$ representing sand, clay and concrete permeability probability distributions.

In Figure B-9, the approximate mean values (from Table B-7) are pointed out below the x axis for reference. Note that a semi-deterministic approach (which would insert the mean permeability from rows 5-7 of Table B-7 for each plug material into the expression Eq. (B-44)) predicts an effective permeability of 3.93×10^{-15}m^2. This is an incorrect method and clearly overly conservative compared to the probabilistic approach that gives a mean permeability of

2.486×10^{-16} m^2. The results so far add further support to the claim that 10^{-16} m^2 is an achievable plug permeability, in light of the large uncertainties that may exist for each of the plug materials on geologic time scales. The sixth column of Table B-7 also shows that the system performance of 99.68% (as measured by % of cases of having permeability lower than 10^{-14}m^2) is better than any of the constituent materials (even though some materials such as cement have a very high mean permeability due to their large standard deviation).

The results suggest that as more statistically independent layers are added to the system, the uncertainty and confinement performance of the plug increases. Thus, although only three layers have been modeled here, in reality more layers could be used (e.g., if different clay or cement types are used) and the performance and uncertainty of the system would benefit. In addition, the probability distributions used here are very approximate and created primarily to demonstrate the sensitivities of the system. In particular, the uncertainty and mean values used for clay are likely to be significantly lower.

B.8. Axially heterogeneous plug with radial flow

The assumption that there is no radial flow from the plug zone to the surrounding matrix is implicit in the derivation of the previous parallel resistance network analysis. This is only realistic if the borehole wall along the plug zone is assumed to be lined with a completely impermeable material (e.g., cement and steel). The effect of radial flow has very important implications on whether or not the impermeable liner should be a specific design goal.

In reality when there are axial differences in plug permeability as exemplified in Figure B-10, significant radial pressure differences between the plug and host rock will develop (if the system is not allowed to equilibrate due to an impermeable barrier between the plug and host rock).
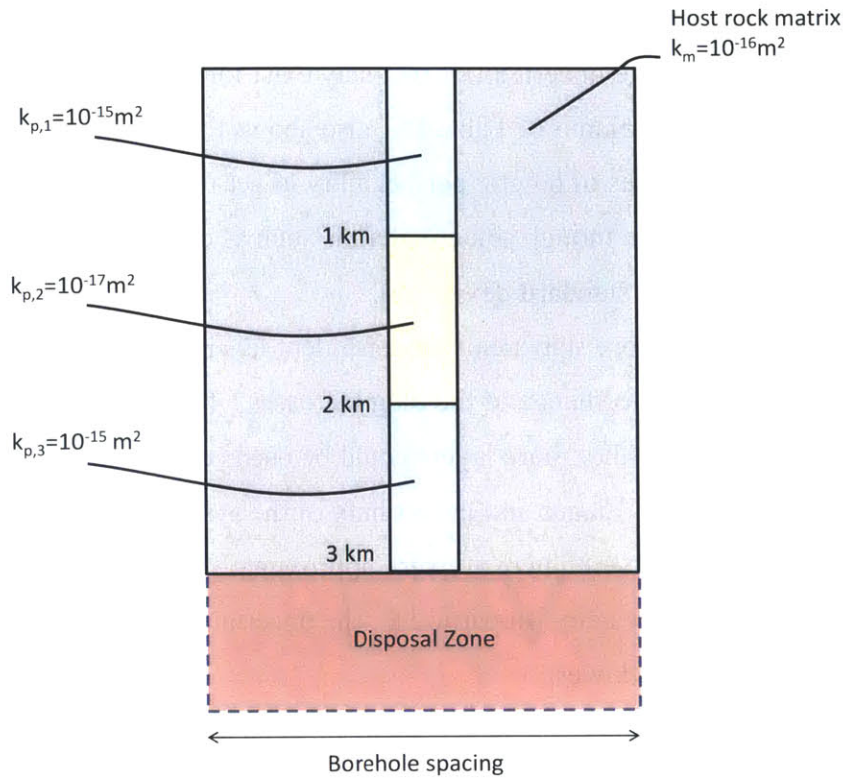
Figure B-10. Depiction of a plug with axial heterogeneity, which would result in radial flows between the plug and matrix zones.

If the borehole wall is permeable, the system will equalize pressures such that the entire system has the same pressure and pressure gradient, established by the surrounding host rock. Thus, when there are differences in permeability between the plug and host rock, there may be a radial flow of fluid which will equalize and eliminate the radial pressure difference, bringing the hatched line to the solid line, as depicted in Figure B-11.
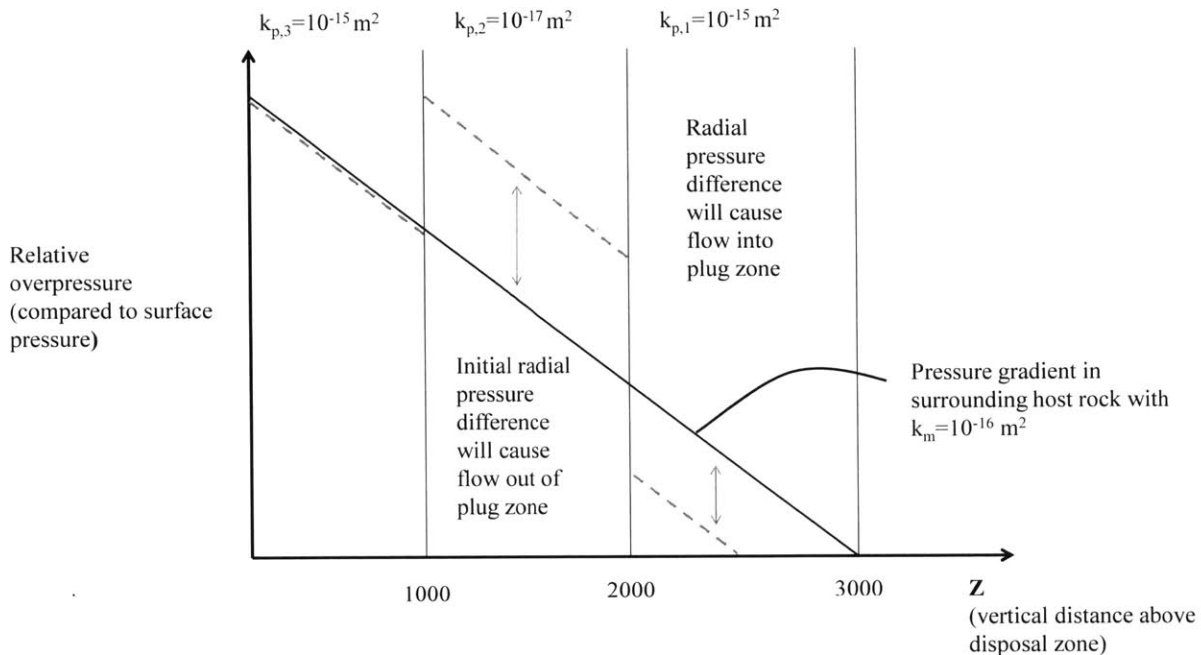
Figure B-11. Depiction of the radial pressure difference in a plug with axial heterogeneities (denoted by the hatched lines), which would subsequently be eliminated by radial flows between the plug and matrix zones.

Assuming equal porosities, in the deepest portion of the plug (with permeability denoted $k_{p,3}$), the vertical velocity of fluid is 10× higher than the surrounding host rock and the pressure gradient is thus equalized between the plug and the host rock (and there is no necessity for radial flow). However, if this high velocity and vertical transport rate are continued within the middle region (with much lower permeability denoted $k_{p,2}$) the pressure in the plug would be significantly higher than the surrounding rock. Thus, to have an equal pressure between this middle plug zone and surrounding host rock, there must be a significant reduction in the velocity of the fluid in the plug (by approximately factor of 100×) compared to its incoming value. As a result, at this point in the plug there will be a radial flow from the plug into the surrounding host rock. Conversely, in the uppermost zone (where the plug permeability denoted by $k_{p,1}$ is higher than that of the surrounding host rock) there must be a radial flow of fluid from the host rock into the plug, which would dilute the vertical pulse of radionuclides with uncontaminated water from the surrounding host rock.

In either case, the overall effect of having a permeable borehole wall and differences in permeability between the plug and host rock is to cause either a dilution (from inflow to the plug) or slowing of the radionuclides (from outflow to the matrix). Thus, we see that a

permeable liner (which allows radial flow between the plug and host rock) would benefit performance of the system by decreasing the vertical transport rate of radionuclides. In addition, if the liner is impermeable (from a chemical diffusion perspective) the beneficial effect of radial diffusion discussed in Section A.3 would be inhibited. Thus, there are both hydraulic and chemical benefits from promoting flow and diffusion of fluids and radionuclides from the plug to the surrounding host rock.

B.9. Permeability of an open cylindrical fracture

An open fracture in the plug or host rock represents a bounding scenario that provides minimal resistance to flow. The resistance to (laminar) flow in a cylindrical fracture is related to the friction factor given by Eq. (B-45),

$$f = \frac{64}{Re} = \frac{64\mu}{\rho v(2b)} \tag{B-45}$$

where $(2b)$ is the diameter of the cylindrical fracture in this case. The pressure drop per unit length due to flow in this configuration is given by Eq. (B-46),

$$\frac{\Delta P}{\Delta L} = \frac{1}{2}\rho v^2 \left(\frac{f}{2b}\right) \tag{B-46}$$

Inserting Eq. (B-45) into Eq. (B-46) gives Eq. (B-47),

$$\frac{\Delta P}{\Delta L} = \frac{1}{2}\rho v^2 \left(\frac{64\mu}{\rho v(2b)^2}\right) = \frac{32\mu v}{(2b)^2} \tag{B-47}$$

Relating this to the pressure drop in a Darcy's law expression with an equivalent permeability (k_{eq}),

$$Q = Av = \frac{k_{eq}A}{\mu}\frac{\Delta P}{\Delta L} \tag{B-48}$$

where the volumetric flow rate (Q) is related to the flow area (A) and the velocity of the fluid (v). Inserting Eq. (B-47) into Darcy's law,

$$v = \frac{k}{\mu}\frac{\Delta P}{\Delta L} = \frac{k}{\mu}\frac{32\mu v}{b^2} = k\frac{32v}{(2b)^2} \tag{B-49}$$

Solving for the equivalent permeability of the pipe/fracture, we obtain Eq. (B-50),

$$k_{eq} = \frac{(2b)^2}{32} \tag{B-50}$$

If the fracture is situated in a cylindrical plug (relatively impermeable), the effective permeability of the plug may be calculated by relating product of the permeability and area of the fracture and the plug, as seen in Eq. (B-51),

$$k_{eq}(\pi b^2) = k_{eff}(\pi r_p^2) \tag{B-51}$$

Thus, the effective permeability of the cylindrical fracture is written as Eq. (B-52),

$$k_{eff} = k_{eq}\left(\frac{b^2}{r_p^2}\right) = \frac{(2b)^2 b^2}{32 r_p^2} = \frac{b^4}{8 r_p^2} \tag{B-52}$$